Nanostructured Heterogeneous Catalysts
A Route to Higher Control of Active Sites

Skupien, Emmanuel

DOI
10.4233/uuid:d2d78316-806d-4de0-85c7-d859ef2828da

Publication date
2019

Document Version
Final published version

Citation (APA)
Skupien, E. (2019). *Nanostructured Heterogeneous Catalysts: A Route to Higher Control of Active Sites*. [Dissertation (TU Delft), Delft University of Technology]. https://doi.org/10.4233/uuid:d2d78316-806d-4de0-85c7-d859ef2828da

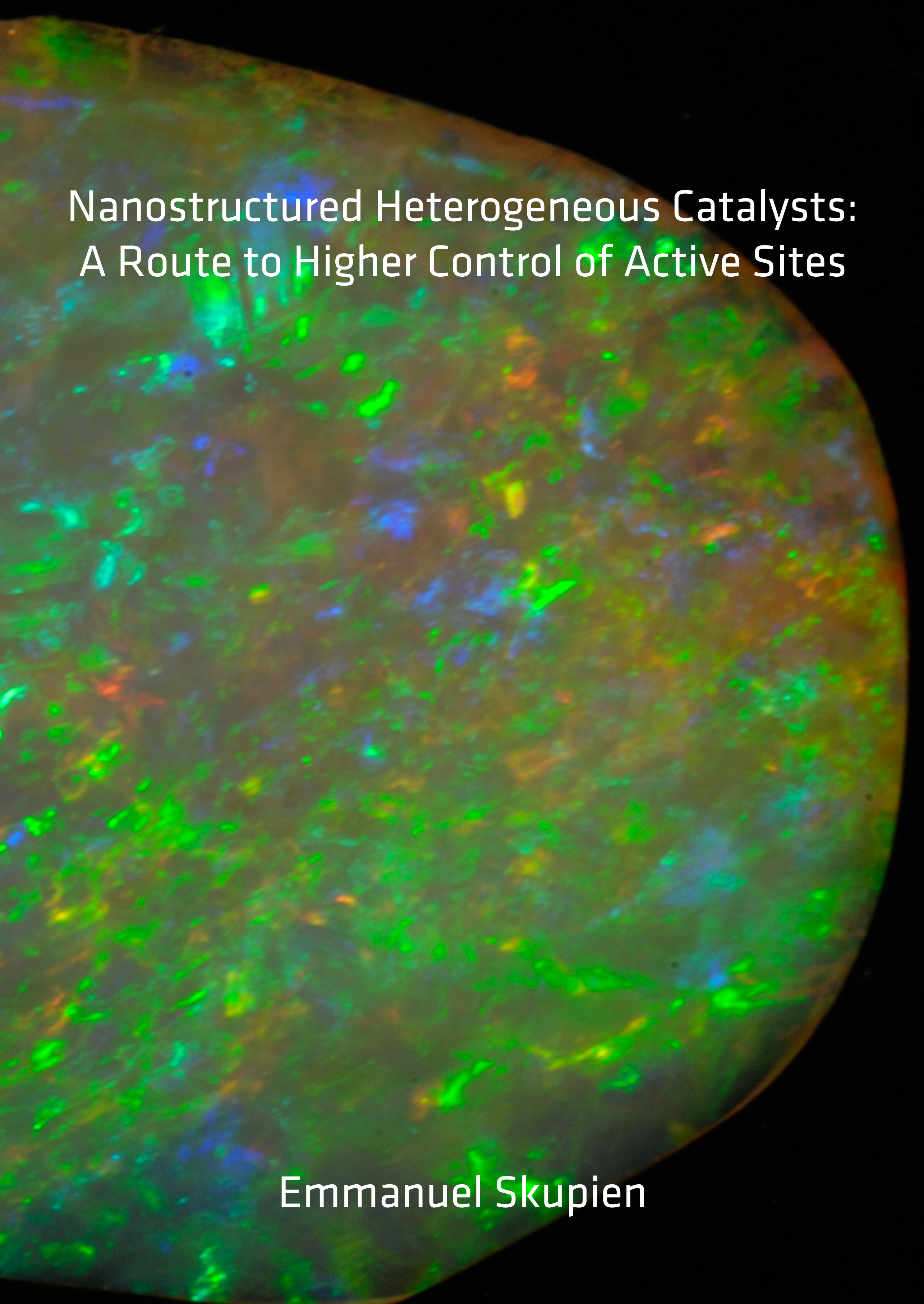

Nanostructured Heterogeneous Catalysts: A Route to Higher Control of Active Sites

Emmanuel Skupien

Nanostructured Heterogeneous Catalysts:
A Route to Higher Control of Active Sites

Emmanuel SKUPIEN

Nanostructured Heterogeneous Catalysts:
A Route to Higher Control of Active Sites

Dissertation

for the purpose of obtaining the degree of doctor

at Delft University of Technology

by the authority of the Rector Magnificus, Prof.dr.ir. T.H.J.J. van der Hagen,

chair of the Board for Doctorates

to be defended publicly on

Friday 1 November 2019

at 10:00 o'clock

by

Emmanuel SKUPIEN
Ingénieur diplomé de l'Ecole Nationale Supérieure de Chimie de Mulhouse
Master Sciences et Technologies, Université de Mulhouse
born in Bully les Mines, France

This dissertation has been approved by the promotors:
Prof. dr. Freek Kapteijn and Prof. dr. Patricia J. Kooyman

Composition of the doctoral committee:

Rector Magnificus	Chairperson
Prof. dr. F. Kapteijn	Delft University of Technology, promotor
Prof. dr. P. J. Kooyman	University of Cape Town, promotor
Prof. dr. ir. M. T. Kreutzer	Delft University of Technology, promotor

Independent members:

Prof. dr. E. J. R. Sudhölter	Delft University of Technology
Prof. dr. L. Lefferts	University of Twente
Prof. dr. G. Mul	University of Twente
Em. prof. dr. J. A. Moulijn	Delft University of Technology
Prof. dr. ir. J. R. van Ommen	Delft University of Technology (reserve)

The research reported in this thesis was conducted at the Catalysis Engineering section of the Chemical Engineering Department, Faculty of Applied Science, Delft University of Technology (Julianalaan 136, 2628 BL, Delft, the Netherlands), with financial support received from The Dutch National Research School Combination Catalysis Controlled by Chemical Design (NRSC-Catalysis).

Proefschrift, Technische Universiteit Delft
Met samenvattig in het Nederlands / Including summary in Dutch

ISBN: 978-94-6384-072-9

Printed by: Ipskamp Printing

Cover photo: Matthew Wood

FSC
www.fsc.org
MIX
Paper from responsible sources
FSC® C128610

Contents

Introduction

Nanostructured heterogeneous catalysts: a route to higher control of active sites

Introduction

1 – Motivation and concepts

Catalysis began as an experimental discipline, as although catalytic effects were relatively quickly reproduced and accepted, theoretical concepts had difficulties emerging [1]. However, scientists soon realized the importance of a very clean catalyst surface and identified the first catalyst poisons [1]. This triggered the emergence of the concept of adsorption which was picked up and explored in depth by Langmuir in 1915 from the earlier work by Haber [2]. Most of the advances that can be witnessed today boomed during the military context of the twentieth century, as demand for fuels and explosives was dramatically large. With the development of processes such as nitrogen fixation by ammonia synthesis, and fuel production by Fischer-Tropsch synthesis and catalytic cracking in the beginning of the twentieth century, the catalysis-based industry could meet this demand. Throughout the twentieth century, there is no doubt that the societal developments in terms of wealth and living standard would have been impossible without the development of the (petro)chemical industry and its strong foundation on catalysis, forming the energy-chemistry nexus [3]. Despite impressive industrial breakthroughs, also in fine chemistry and pharma, catalysis has remained a discipline strongly based on trial-and-error research, with high-throughput screenings of catalysts being the main workhorse technique.

As a logical result from the abundance of energy, commodities and wealth, the world population increased at an unprecedented rate, contributing to prospering industries. Unfortunately, this demographic increase was also translated to a stronger footprint of human civilization on the environment, to the point where it can no longer be neglected as it threatens society itself. In this context, concepts have surfaced such as the circular economy, where all commodities would be synthesized with negligible to zero footprint and all waste would be converted back to resources, in a Cradle to Cradle fashion. As heterogeneous catalysis is historically connected to large-scale (petro-)chemicals production at the root of the expansion of civilization, these societal and environmental pressures are directly transferred to this discipline. This results in the recent interest in modern catalysis in seeking cheaper processes and cleaner reactions [4].

There are a number of issues, such as the depletion of metal resources, urban pollution, depletion of crude oil or accumulation of plastic, for which a large part of the solution will come from new catalytic processes. These issues motivate catalysis research in e.g. renewable energy storage, fuel cells, solar fuels and renewable base chemicals synthesis.

Over the past decade, robust theoretical concepts such as density functional theory (DFT) have emerged as powerful prediction tools of catalytic activity and selectivity. Nørskov *et al*. have reviewed the topic of computational design of solid catalysts [5] and underlined the first examples of improvements generated from theoretical calculations of electronic structures. These include the stability improvement of steam reforming nickel catalysts by the addition of gold [6], the addition of mixed cobalt and molybdenum to ammonia synthesis catalysts [7], new mixed transition metal sulfides for hydro-desulfurization [8], new carbon monoxide-tolerant alloys for fuel-cell anodes [9], and near-surface alloys for hydrogen activation [10]. DFT calculates the thermodynamic energy diagrams of the different elementary steps of a given catalytic reaction from first principles. Important parameters such as the energies of adsorption and desorption, activation energies, bond breaking and bond forming energies are quantified and compared for a series of theoretical catalysts. Thus, DFT can be used as a powerful theoretical high throughput screening method [3], that can screen catalysts much faster and cheaper than experimental techniques. Therefore, it is increasingly used to dissect the challenging chemical reactions mentioned above.

In the catalysis field, DFT ultimately aims at the design of active sites at the atomic level, interacting with molecules and adsorbates [5]. Thus, transferring the knowledge to experimental studies requires the manipulation of matter at the atomic level. Materials and surface science have therefore naturally converged with catalysis science in an attempt to meet these requirements. Traditionally, heterogeneous catalysts are synthesized by methods such as impregnation-reduction, co-precipitation and deposition precipitation. Although these routes have the advantage to produce large scale quantities with little waste and competitive price, the resulting catalysts typically present a significant variety of metal particle size and shape, and as a consequence a variety of different active sites. The need to tailor a material at the atomic level requires nanostructuring, which is the concern of nanotechnology and materials science. Nanotechnology already allowed a number of significant improvements in fields such as electronics, with the utilization of semiconductor nanocrystals for the miniaturization of integrated circuits. In medicine, gold nanoparticles are used for targeted drug delivery and organ imaging [11]. In catalysis, the use of colloidal nanoparticles has mainly remained in the academic world, and industrial applications are scarce. The main reason is the scale of the industrial catalyst quantities, which translates into the challenge of economically tailoring bulk quantities of material, yet at the atomic level and with limited waste.

2 – Colloidal metal nanoparticles

Colloidal gold nanoparticles were first recognized by Faraday in 1857 [12]. In a pioneering synthesis method involving sodium tetrachloroaurate and phosphorous in carbon disulfide, he achieved the formation of what he called "ruby gold" and which he described as very finely divided metallic gold in suspension. No microscope was powerful enough to image the particles, but 100 years later, Turkevich et al. [13] analyzed samples prepared according to Faraday's methodology under an electron microscope and revealed that the dimensions of the gold nanoparticles were 6 nm on average. Turkevich created and investigated many other synthesis recipes, the most famous of which is the citrate reduction method. In his last publications, Turkevich summarized his findings on colloids [14, 15]. He described the role of citrate as the reductant of the gold salt, and the stabilizer forming the "Stern layer" on the colloidal particle. Such stabilizers are nowadays referred to as "capping agents" or "capping ligands", and the Stern layer is called the "double layer" in modern surface science.

Countless different recipes have since emerged for the preparation of colloidal metal nanoparticles [16, 17]. These usually involve a metal salt precursor, a reductant, a capping ligand and a solvent (See Figure i.1). In some studies, the same molecule serves as the reductant and capping ligand, or the capping ligand is reacted with a reductant prior to the introduction of the metal precursor, to form a reductive intermediate [18]. Other reports involve a solvent (e.g. ethylene glycol) that is thermally or chemically decomposed into a capping ligand upon its oxidation by the metal precursor which is simultaneously reduced [19]. There are also reports claiming "stabilizer free" colloidal syntheses, but these involve solvents such as dimethylformamide that are the actual stabilizer. A wide variety of chemical species can exhibit a capping ligand behavior, such as ions, small molecules, surfactants, polymers and dendrimers [16]. An excellent review by Ott *et al.* [20] about ranking stabilization effect and putative stabilizers brings a critical point of view of claimed stabilizers or claimed absence of stabilizers. It is clear that these nano-sized particles are not thermodynamically stable and that the bulk state is more stable. Therefore there is always, in one form or another, presence of a stabilizer if a synthesis route yields a colloidal dispersion. The metal nanoparticle stabilization is a key aspect for applications such as catalysis or sensing, as will become clear at the end of this section.

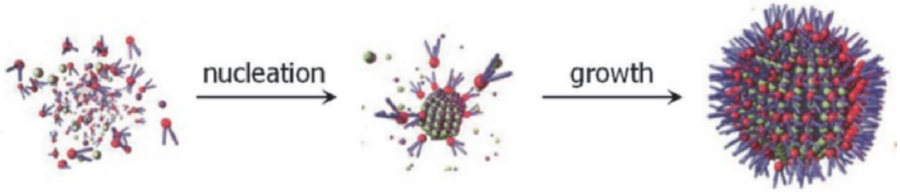

Figure i.1: Schematic of the nucleation of metal nanoparticles (green), and their stabilization by capping ligands (red and purple).

The biggest advantages of the colloidal route compared to the more traditional catalyst synthesis methods (e.g. impregnation-reduction) are the possibility to control precisely the particle size and shape without the influence of a support. Smaller nanoparticles are obtained when the capping ligand interacts strongly with the metal, thereby effectively slowing down particle growth. Ligands such as thiols easily yield nanoparticles below 5 nm diameter with narrow particle size distribution. Less strongly interacting ligands tend to yield bigger particles, in the range of 20 – 50 nm. Overcoming this limitation is possible in biphasic systems, because the transport of monomers to the growing nanoparticle is then also regulated by phase transfer rates or the finite amount of reactant in *e.g.* microemulsions. This is because the metal source is dissolved in the aqueous phase, and the capped nanoparticles are dispersed in the organic phase. Thus, the nanoparticles that are located in the organic phase receive less metal monomers, before protection by capping agent against further growth takes place, than if they would be dispersed in the same phase as the metal source. Tailored nanoparticle shape can also be induced by the capping ligand. This occurs when the ligand interacts more strongly with a particular crystal facet of the nanoparticle, yielding anisotropic growth of the other facets. The nanoparticle shapes usually encountered are spheres, cubes, octahedrons, truncated cuboctahedrons, tetrahexahedrons, (truncated) triangular platelets, and rods [21]. This variety of shapes is very interesting from a catalytic application point of view, because of the specific crystal facets exposed. For instance, given a fcc crystal structure, a metal nanocube has only (100) facets exposed to the outside, whereas an octahedron has only (111) facets exposed. Likewise, a truncated cuboctahedron has (100) facets exposed on its square faces and (111) facets exposed on its triangular faces. Furthermore, some ligands such as ionic surfactants are very good stabilizers for charged nanoparticles and some others induce a cationic character with a Lewis acid moiety. One can see arising the potential of building specific catalytic active sites, with atomic precision. Catalysts prepared via the colloidal route are thus an interesting way to experimentally verify the findings of theoretical studies, which suggest a particular active site to improve the catalytic properties.

Like any concept, the colloidal route for heterogeneous catalyst synthesis comes with some downsides or issues to consider. After immobilization of the preformed colloidal nanoparticles on the catalyst support, a significant amount of capping ligands remains on the surface of the nanoparticles. Methods for cleaning these comprise calcination or milder temperature treatment, extensive washing with solvents, and other chemical destruction, for instance with ozone. Calcination and heat treatment of large amounts of solid catalyst is already a routine operation in industry, since that is the way most currently applied catalysts are activated or regenerated. However, this might not be the most suitable way of removing the capping ligands present. As opposed to the nanoparticles obtained by impregnation methods, the immobilized colloidal nanoparticles are reported to have a higher surface mobility, probably due to the capping ligands present. These nanoparticles are therefore much more prone to aggregation and sintering upon high temperature treatments such as calcination. Mild temperature treatments have been devised to avoid particle growth but still remove the ligands [22]. However, particularly in the case of strongly interacting ligands, these milder temperature treatments are not sufficient and ligand residues tend to remain. Extensive washing of the ligands, even though proven effective, poses a problem of scalability. Industrial amounts of solvent waste constitute clearly a large expense in terms of cost of waste disposal and/or recycling. The same concern can be applied to the quantity and nature of the synthesis solvent with the same disposal/recycling problem. Syntheses routes involving water as solvent have been devised, but render the immobilization on the catalyst support more difficult. This is because the capping ligands involved in a water-based synthesis need to possess hydrophilic moieties in order to keep the dispersion stable, and the point of zero charge of the (hydrated) support needs to be adjusted to favor the immobilization of the nanoparticles. Thus, there are many more polar compounds present in a water-based colloidal synthesis, and these also interact with the nanoparticles, thereby lessening their interaction with the catalyst support. Another well-known problem, which also occurs with other catalyst synthesis routes, is the surface rearrangement of the nanoparticles. At the nano-scale, the material is very dynamic and quickly stabilizes its surface by rearrangement under influence of the environment. This can occur during any step of the synthesis, in particular when the capping ligands are eliminated, and even under catalytic reaction conditions. This phenomenon makes the convergence of theoretical and experimental studies even more challenging. Theoretical studies must now predict the optimal nanoparticle texture for a given catalytic reaction and at the same time assess the stability of this texture under catalytic conditions.

3 – Carbon nanotubes

Carbon nanotubes (CNTs) gained a huge interest after the pioneering work of Iijima [23] in 1991, although they were already observed by electron microscopy back in 1952 by Radushkevich and Lukyanovich [24]. These nanomaterials exhibit peculiar properties, such as high surface area, tensile strength, electronic conduction, with which they inspired important application perspectives in a variety of domains. CNTs are a special type of carbon nanofibers (CNFs), where the graphene sheets are rolled around the axis of the fiber, forming a hollow tube. Compared with the graphene cup stacks, ribbons or herring-bone structures found in CNFs, CNTs show a higher level of nanostructuring, less defects and therefore more stability. CNTs are well known for their exceptional mechanical properties, however, this short review focuses on the properties related to energy and (electro-)catalytic applications, such as specific surface area and electronic conductivity.

Surface properties, in particular the surface area, of CNTs strongly depend on their purity, wall number and the ratio of number of open end tubes versus that of overall tubes [25]. The maximum theoretical value for the BET area of isolated open-end single wall-CNTs (SWCNTs) is 2630 $m^2 \cdot g^{-1}$. The surface area of open-end multi wall-CNTs (MWCNTs) is inversely proportional to the number of walls. In practice, open-end MWCNTs with 8 walls and 30 nm diameter were experimentally found to have a surface area of 356 $m^2 \cdot g^{-1}$, close to the theoretical value of 329 $m^2 \cdot g^{-1}$ [25]. The surface area of most heterogeneous catalyst supports ranges from around 200 to more than 600 $m^2 \cdot g^{-1}$, thus, CNTs have potential as heterogeneous catalyst support [26].

Furthermore, this abundant surface is very stable chemically, so applicable under severe chemical treatments [27]. CNTs can be purified in air above 700 °C from amorphous carbon impurities, but oxidation by concentrated acids (e.g. 65 % HNO_3) is usually the preferred method. Largely applied for the removal of Ni or Fe nanoparticles synthesis residue from the inside of the CNTs, and removal of amorphous carbon impurities from the outside, after their synthesis, this oxidation treatment also affects the CNT surface. The hemispheres capping the end of the CNTs are more prone to oxidation than the tube itself, because of the presence of 5-carbon rings that are less stable. As a consequence, the oxidation treatment leads to the opening of these end-caps and gives access to the interior of the CNTs [28]. Surface moieties such as carboxyl, hydroxyl and carbonyl are introduced mainly on the open ends of the CNTs, and to a lesser extent on defect sites on the walls. Sulfur-containing moieties such as sulfate and sulfonate can also be introduced in a similar fashion with a mixture of concentrated sulfuric and nitric acid. These moieties can be used for further functionalization using amines for the amidation of carboxylic groups or alcohols for their esterification, as in classic organic chemistry. It is even possible to covalently join CNTs together via these condensation reactions. Fluorination of the side walls can be achieved in hydrofluoric acid between 250 and 400 °C, creating carbon sp^3 defects on the sp^2 carbon walls of the tubes. Alkyl chains can subsequently be grafted via the alkylation reaction using a Grignard reagent or an alkyl lithium. Thus, it is clear that almost any chemical functionality can be covalently attached to the surface of the CNTs. Larger nanostructures, such as Buckminsterfullerene C_{60} or even graphene "leaves" (nano-sheets) were also successfully grafted onto CNTs. Non-covalent functionalization is an effective way to manipulate the surface chemistry of CNTs without impeding their electronic conduction. Planar π moieties such as pyrenyl-containing molecules adsorb strongly on the outer walls of CNTs and open the way for surface functionalization by self-assembly. From a catalysis point of view, the acid-functionalized CNTs could find applications in acid catalysis for example, but their price and exceptional properties will probably bring them to more sophisticated applications. For instance, this surface chemical versatility brings up the potential of immobilizing homogeneous catalysts on the CNTs [29], which would save expensive recovery and purification of the homogeneous catalyst. The surface could also be tailored to stabilize metal nanoparticle catalysts, with moieties such as amines or sulfides that are usually good at stabilizing the nanoparticles in their colloidal suspension.

The electronic conductivity of CNTs is fundamentally governed by their lattice orientation with respect to the tube's axis [30]. As depicted in Figure i.2, the orientation of the roll-up vector $\mathbf{C}_h$ (the vector in the axis direction of the CNT) affects the overlap of the carbon π-orbitals and results in different conductivity behavior. If $n = m$, the CNT has metallic conduction, but if $n - m$ is a multiple of 3, the CNT shows semiconducting properties with a very small band gap. Other orientations make the CNT a moderate semiconductor. Synthesis methods do not yet result in the selective production of a particular type of CNT, but yield a mixture of metallic and semi-conductor CNTs [31], which is a major issue in the perspective of their application in electronic and electrochemical devices. Nevertheless, carrier mobilities in SWCNTs as high as $\sim 10\,000\ \mathrm{cm^2 \cdot V^{-1} \cdot s^{-1}}$ are reported [31], which is one order of magnitude higher than that of electrons in silicon and five orders of magnitude higher than that of conducting polymers. Furthermore, SWCNTs are able to carry current densities as high as $\sim 4 \times 10^9\ \mathrm{A \cdot cm^{-2}}$, which is three orders of magnitude higher than a typical metal. These electronic properties combined with

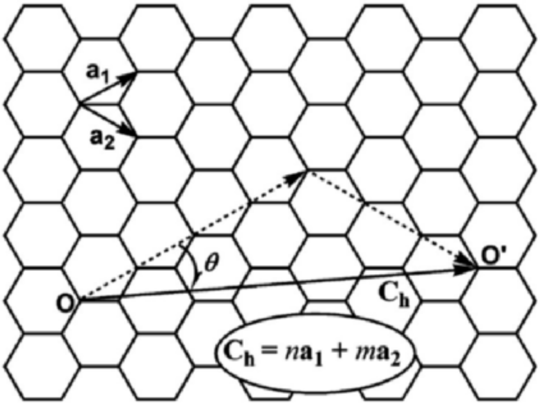

Figure i.2: Roll-up vector $\mathbf{C}_h$ ($\mathbf{C}_h = n\mathbf{a}_1 + m\mathbf{a}_2$) and chiral angle θ for a (n, m) SWCNT (for this special case, $n = 4$, $m = 3$), where $\mathbf{a}_1$ and $\mathbf{a}_2$ are the primitive vectors of a graphene sheet. Reproduced from [30].

their surface area properties logically make them attractive materials for batteries, sensors and electrocatalysis [32]. As is known to occur with conventional graphitic materials, Li can intercalate into the interstitial channels between tubes as well as inside their interior volume. Specific capacities of ~1000 $mA \cdot h \cdot g^{-1}$ have been reported using CNT composites as electrodes in Li-ion batteries, where graphite materials typically reach ~400 $mA \cdot h \cdot g^{-1}$. The performance is strongly depending on the purity, alignment, attachment procedure and surface modification, and is better with uncapped CNTs as they exhibit a higher surface area. CNTs have also been used in the fabrication of a variety of sensors [32], a field that is more related to electrocatalysis since it involves the selective chemisorption of a molecule, accompanied by an electron transfer. CNT-based sensors have been shown to lower the overpotential of electrode processes by promoting direct electron-transfer. The morphology of CNT arrays enables the access to the electroactive center of complex organic molecules such as proteins [33]. This is a direct benefit of the nanostructure of CNTs, and couldn't be attained solely with high electronic conductivity and surface area. Nevertheless, the latter results in exceptional sensitivity of CNT based sensors [34]. Finally, the unlimited surface functionalization possibilities discussed above enable very specific, i.e. selective, detection. For example, glucose oxidase was grafted onto the open tips of aligned carbon nanotubes, resulting in a glucose biosensor with 400 mV lower overpotential compared to the electrode not containing CNTs [35]. Detection limits as low as 10^{-10} $mol \cdot L^{-1}$ were reached for the sensing of free DNA sequences by functionalizing CNTs with the complementary DNA sequence. Incorporating CNTs into this sensor resulted in a tenfold improvement in detection sensitivity [36]. Carbon-based gas diffusion electrodes are widely applied in fuel cell research and CNTs have attracted attention in this area also in spite of their superior durability [37].

In view of their excellent tensile strength, CNTs have already made their way to various mechanical applications, e.g. reinforcing composites and coatings. These are among the most straightforward applications as they primarily rely on the good mixing of CNTs with the matrix. Applications aiming at utilizing CNTs exceptional conductivity are more delicate to tackle, as they require a better control over the CNTs, their purity and their lattice orientation. It is clear that CNTs will be employed in various electronic and electrocatalytic applications in the near future.

4 – Self-assembled nanostructures as heterogeneous catalysts

In a self-assembled nanostructure, atoms, molecules or even supramolecules or particles organize themselves via physico-chemical interactions into structures, driven towards a state of relative minimum Gibbs energy and maximum entropy [38]. This implies that if the building blocks are taken apart, and then mixed together again, they spontaneously re-assemble into the original nanostructure given favorable conditions. The inter-molecular interactions in play are Coulombic and Van der Waals interactions and the strong repulsion on short distance. Self-assembly generally implies a transition from dispersed (in gas phase or in solution) to condensed state, although rearrangements of nanostructures into others can also occur without dispersion of the building blocks. As opposed to the techniques of “pick and place” encountered in e.g. AFM, or the laser ablation techniques encountered in lithography, self-assembly of molecular components into a nanostructure allows the synthesis of nanomaterials in “one pot” and could be scalable to industrial amounts given the right conditions of mass and heat transport. This is the reason why the synthesis of colloidal metal nanoparticles was selected as a method of heterogeneous catalyst fabrication. However, the same industrial requirements of large quantities have to be considered, and a critical evaluation of the extra spending in precursors, energy, and waste treatment should not be avoided. In particular, the synthesis of colloidal metal nanoparticles can require expensive solvents, surfactants and sometimes even metal precursors. Some synthesis recipes rely on very diluted metal in order to effectively control the particle size, which would be a huge waste of solvent. Other recipes make use of complex micro-emulsions (another self-assembled nanostructure) involving a mixture of one or more organic solvents, some water and a large amount of surfactant [39]. In fact, such systems are better described as nanostructures made up of surfactant molecules, swelled by water and organic solvents. These have the advantage of concentrating the synthesis into a much smaller volume while still allowing control of the particle size, however, they require more expensive precursors and generate much more waste.

5 – Catalytic reactions

5 – 1 – Benzyl alcohol aerobic selective oxidation

Besides the widely studied carbon monoxide oxidation, alcohol selective oxidation to aldehyde is extensively studied to characterize the catalytic activity of gold-based catalysts in particular. This reaction is somewhat more demanding than carbon monoxide (total) oxidation, since it is a partial oxidation in liquid phase. Very active catalysts such as platinum-based catalysts tend to be poorly selective to aldehyde, and easily oxidize those further to carboxylic acid and even some carbon dioxide (See Figure i.3). The weak chemisorption of oxygen on gold surfaces also tends to favor a milder oxidation and hence, a higher selectivity to the aldehyde.

Benzaldehyde is a fine chemical that finds uses as flavoring agent (almonds), and as a building block for the plastic and pharmaceutical industries. It is currently being produced via the partial oxidation of toluene (heterogeneous catalysis) [40], and more commonly via alkaline hydrolysis of benzyl chloride (homogeneous catalysis) [41]. It is worth noticing that benzyl chloride is itself produced from toluene by chlorination, and therefore introduces chlorine into the production chain of benzaldehyde. Furthermore, the alkaline hydrolysis process involves strong bases that will also generate waste. Although this process is economically profitable, the informed chemist understands that chlorine is introduced to bring moieties on the specific methyl part of the toluene molecule, so that the alkaline hydrolysis only happens on this carbon atom, which is made more reactive. This means that maximizing selectivity is achieved, but at the expense of resource efficiency: the process uses chlorine as reactant and produces chloride waste. In order to be competitive, a chlorine-free catalytic process needs to meet this selectivity demand. The reasons for this are the relatively high cost of the chemical feedstock and all the costs related to separation and purification. However, when considering an alternative process, savings can be made on reducing the process temperature/pressure and using cheaper chemicals. For instance, aerobic oxidation of benzyl alcohol uses air as oxidizing agent, thereby drastically reducing chemical waste, and can be conducted at temperatures below 100°C, particularly using gold-based catalysts. Although benzyl

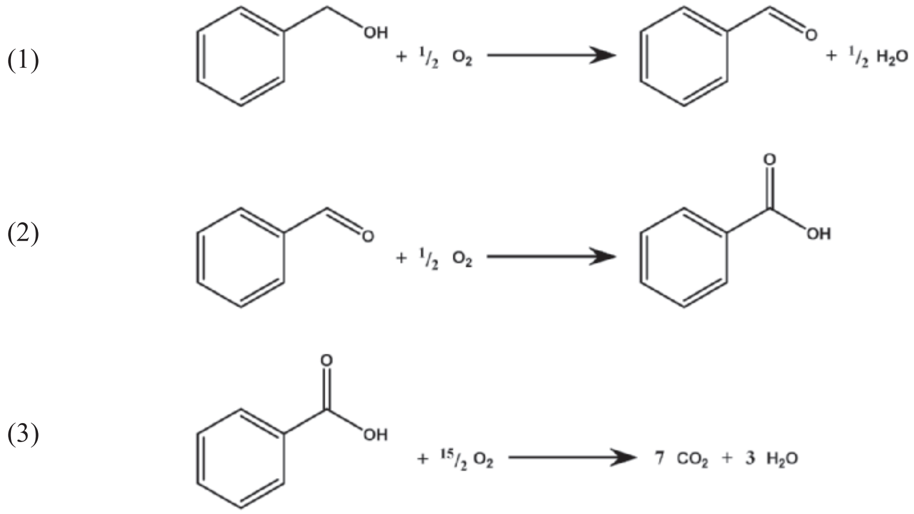

Figure i.3: Reaction equation of (1) Benzyl alcohol selective oxidation to Benzaldehyde (desired), (2) Benzaldehyde oxidation to Benzoic acid (undesired) and (3) Benzoic acid total oxidation to CO_2 (undesired).

alcohol is also mainly produced via chlorination of toluene, the same reasoning can be applied to this process and the partial oxidation of toluene could be considered.

Therefore, the aerobic oxidation of benzyl alcohol can be seen as an archetype of alternative chemical processes that use minimum chemical resources and energy, and produce minimum waste. Thus, it is not surprising that aerobic selective oxidation of benzyl alcohol has received particular interest. As emphasized before, selectivity is often more important than catalytic activity. This is reflected by the fact that it can be more economically interesting for a large-scale process to use a larger amount of catalyst rather than investing in down-stream processes of separation and purification. Gold-based catalysts are very selective to the aldehyde in alcohol oxidation with molecular oxygen [4]. Rodríguez-Reyez *et al*. [4] showed that this unusual selective behavior of gold catalysts is due to the interaction of molecular oxygen with gold surfaces that yields adsorbed atomic oxygen. Temperature programmed reaction spectroscopy (TPRS) experiments led to the conclusion that a low atomic oxygen coverage (up to 0.05 monolayer) favors high selectivity (>90%) to benzaldehyde, and benzyl benzoate is the main by-product. In contrast, high atomic oxygen coverage favors deeper oxidation and yields products of combustion, and carbon deposition. This means that it is not attractive to use a high molecular oxygen concentration in the gas mixture feeding oxygen to the reaction medium, explaining why the use of air instead of pure oxygen is also interesting from an engineering point of view, apart from an environmental and economic point of view. Cationic surface gold atoms, or low-coordinated atoms at edges and defects, are often seen as the active sites for the selective formation of aldehyde, because they possess Lewis acidity, allowing the formation of adsorbed alcoholates and hydrides [42]. It appears that similar active sites on other metals such as platinum tend to chemisorb the alcohol and the derived intermediates too strongly, and chemisorb atomic oxygen in much higher coverages (so-called over-oxidation of the metal). This results in deeper oxidation to benzoic acid and, even further to carbon dioxide [43].

From a catalyst design perspective, the focus is then placed on maximizing the amount of active sites that performs the desired reaction. The colloidal route for catalyst synthesis is therefore of particular interest for this goal, since it yields uniform nanoparticles with narrower particle size distributions compared to the impregnation methods. Catalysts made by employing this method already demonstrated activities and selectivities comparable to other catalysts prepared by traditional methods. Quintanilla et al. [18] prepared colloidal dodecylamine- and polyvinylpyrrolidone-stabilized gold nanoparticles, which were subsequently immobilized on alumina. These catalysts exhibited comparable activities and selectivities to those by a benchmark catalyst prepared via homogeneous deposition-precipitation. This kind of comparison to benchmark catalysts is essential to properly assess the relevance of any new catalyst, and is not often met in literature. It is clear that the costs of such a catalyst synthetic route will be higher, so improvements in activity and more importantly in selectivity and stability have to be demonstrated.

Not only the formation of the colloidal nanoparticles requires more chemicals (solvent, stabilizer/capping ligand), but also the post-synthesis treatments that are usually implemented to clean the resulting catalyst from capping ligands generate costs of energy and waste. Kuhn *et al.* [44] studied the effect of organic capping layers on platinum nanoparticles, and showed that heat treatment as a way to clean the nanoparticles results in carbonaceous deposits blocking the active sites. Higher temperature treatments tend to result in wider particle size distributions and the loss of the main advantage of the colloidal method.

5 – 2 – Carbon monoxide oxidation

Carbon monoxide oxidation is among the first examples of environmental catalysis, together with NO_x reduction. In this case, catalysis research efforts have been and still are placed for general public health rather than chemicals/fuels production. Carbon monoxide is mainly emitted by anthropogenic activities, including all carbon-based fueled transportation, non-transportation fuel combustion and industrial processes [45]. Natural sources also exist such as wildfires, but they remain a small contribution. Thanks to the development of the three-way catalytic converters, CO emissions in the USA were reduced by a factor of 3 between 1990 and 2011, according to the U.S. EPA [45]. This tremendous reduction, going from almost 150 to 50 million tons per year, has happened while the number of on-road motor vehicles kept increasing exponentially. This source is by far the largest of CO emissions and it was particularly this source that decreased by about a factor of 3, while emissions from other fuel combustion activities remained stable. Three-way catalytic converters perform CO oxidation, hydrocarbon total oxidation and NO_x reduction to N_2 in a single catalytic unit, which adds even more challenges to this accomplishment.

Apart from environmental catalysis, catalytic CO oxidation is relevant for the purification of gaseous hydrogen, mainly produced by steam reforming, which contains 30 to 60% CO depending on the feed and process. In H_2 production, the syngas H_2:CO ratio is increased up to 99:1 via the water-gas shift reaction, but energy-related applications such as fuel cells and ammonia synthesis are very intolerant to CO poisoning and require less than 10 ppm CO. Classically CO hydrogenation to methane is applied in the ammonia synthesis process, Alternatively, the purification can be conducted further via the preferential oxidation (PROX) of carbon monoxide over hydrogen in order to eliminate the last traces of CO.

The famous publication by Haruta in 1989 [46] changed the reputation of gold-based catalysts, which were regarded as poor catalysts due to the generally observed inertness of gold. It was then recognized that with gold nanoparticles smaller than 10 nm, catalytic activity starts to be appreciable, and was even impressive with particles smaller than 5 nm. Using nanoparticles as small as 4 nm, co-precipitated with iron oxide, extensive CO conversion was observed down to -70 °C. Gold catalysts have been reported to show activity for a myriad of redox reactions and in particular for selective partial oxidation reactions [47] such as glycerol oxidation to glyceric acid, hydrogen selective oxidation to hydrogen peroxide, hydrogenation of alkynes to alkenes and alcohol selective oxidation. However, it was also noticed that these catalysts are very sensitive to impurities such as chloride and alkali, and to the heat treatments employed for the removal of these impurities, resulting in difficulties regarding reproducibility. The involvement of the catalyst support in supplying oxygen to the gold nanoparticles is now well accepted. However, there is a large debate over the identification of the active gold species in very low temperature CO oxidation. Hutchings' group [48] claims that the active species responsible for 100% conversion around -70 °C are very small gold clusters of ~0.5 nm, containing around 10 gold atoms. On the other hand, Schüth's group [49] studied Au/$Mg(OH)_2$ and Au/MgO synthesized via the colloidal route, and observed an unusual U-shaped light-off curve over a temperature ranging from -89 °C to 275 °C. 100 % conversion was observed at -89 to 20 °C and above 230 °C. A minimum conversion of 73 % was observed at 90 °C, implying a negative apparent activation energy. CO titration on pre-oxidized catalysts supported the interpretation that atomic oxygen supplied from the support was depleting as the temperature increased, resulting in the apparent negative activation energy. Although not completely excluded, there was no evidence of the presence of gold clusters smaller than 1 nm. Corma's group [50] observed an induction period corresponding to the formation of Au_3-Au_5 and Au_3-Au_9 clusters from diluted gold salts, although it concerned other reactions than CO oxidation. The understanding of such a behavior has matured with the recent theoretical models by Nørskov *et al.* [51], explaining that the active gold species are Au atoms placed at the crystal corners of the nanoparticles and which possess the least complete coordination sphere. This satisfies the experimental observations since the amount of such corner atoms increases as particle size decreases.

We can see with the latter examples that research in CO oxidation by gold has reached a high level of detail, with scientists trying to build and identify the exact active site/species at the atomic level. The term "active site engineering" is emerging in catalysis science, suggesting the convergence of catalysis and nanotechnology.

5 – 3 – Carbon dioxide electrochemical reduction

Transforming carbon dioxide to useful chemicals is of course very attractive, provided that it can be done at the large scale and with abundant materials, and provided that the product of this transformation finds enough uses in the chemical industry to avoid accumulation. One immediately thinks of the relief this would bring regarding the greenhouse gas emission problem as it would close the carbon cycle. In addition, many chemicals derived from oil, such as monomers for the production of polymers or transportation fuels, will require new carbon sources as oil depletes. Therefore, CO_2 reduction to small molecules such as formic acid, carbon monoxide, methane or ethylene could establish a renewable source of base chemicals.

Formic acid finds a variety of uses in the industry, such as in food additives and in adhesives. It is also a valuable intermediate in the fine chemicals industry. The possibility to use formic acid in fuel cells instead of hydrogen would open up a large channel of formic acid consumption. This type of fuel cell releases carbon dioxide under operation, thus CO_2 reduction to formic acid would be a way to store hydrogen. Metals such as Pb, Hg, Tl, In, Sn, Cd and Bi are very selective towards the formation of formic acid [52]. These metals have the particularity to show a high activation overpotential for H_2 evolution, which could explain this behavior. Formic acid or formate is also observed as side product for a wide range of metals employed as a catalyst. The relatively small number of electron transfers necessary to reduce CO_2 to HCOOH is probably the reason why this compound is so easily formed.

Carbon monoxide is a very useful compound for the industry, since it is used in hydroformylation of alkenes to aldehydes, in methanol synthesis and it is also present in the production chain of acetic acid. Present in syngas, it is the feedstock of the Fischer-Tropsch process that enables the production of synthetic hydrocarbon fuels, particularly interesting for transportation, and lower olefins, interesting as chemical building blocks. Clearly, the channels of consumption of carbon monoxide are numerous and already implemented at the industrial scale. It is therefore a very attractive route to convert CO_2 to CO, or even to syngas directly, since H_2 formation by water splitting is hard to avoid as a byproduct of the electrochemical reduction, and can take a large part of the supplied energy. Metals such as Au, Ag, Zn, Pd and Ga produce predominantly CO [52], with a significant current efficiency to H_2. That behavior could be explained by the weak binding energy of these metals with CO. Recently, Hatsukade et al. [53] investigated metallic silver surfaces for CO_2 reduction and reached 90% current efficiency to CO at -1.1 V vs NHE. The other CO_2 reduction products were formic acid, and at very negative potentials (< -1.2 V vs. NHE) methane, methanol and ethanol started to appear, but only accounting for less than 0.1% of the current. Then, in the same group, Hahn et al. [54] investigated Au, Pd and AuPd alloy surfaces with a very sensitive electrochemical cell, and observed that pure Au was the most active and selective catalyst for CO production, with 90% current efficiency to CO at -0.45 V vs. RHE. Alloying with Pd increased the selectivity to formate and pure Pd showed the highest efficiency to formic acid.

Methane is an interesting compound that is mainly used as a fuel for domestic heating as well as for transportation. It has therefore large consumption channels. A renewable source of methane from carbon dioxide would logically take away a large part of the energy and CO_2 emission problems and would provide a direct source of fuel from CO_2. Ethylene is a very useful chemical building block, in particular for the polymer and fine chemical industries. It is currently obtained from crude oil, so the need for a renewable source is clear. Ethylene is often produced from CO_2 under similar electrocatalytic conditions as methane, but less selectively. These hydrocarbon formation reactions are associated with a high activation energy. The latter forces researchers to submit the catalytic material to very cathodic potentials at which the stability of the catalytic activity is difficult to maintain, as all sorts of reduction/deposition reactions are made possible with the impurities in the system. The reaction mechanism is still largely elusive, but there is no doubt that carbon monoxide is the central intermediate that yields hydrocarbons. Shibata *et al.* [55] revealed that this mechanism was even more puzzling than previously thought, with the observation of an Anderson-Schulz-Flory distribution of hydrocarbons up to C6. The result was difficult to reproduce, but more recently Kuhl *et al.* [56] even identified 16 different products of CO_2 reduction on a copper surface, thanks to the design of a very sensitive electrochemical cell. The elucidation of the reaction mechanism should in theory result in the identification of the rate-determining elementary step, but a principle surfaced that surpasses this approach: the scaling relationships between intermediate binding energies. This principle was emphasized by Nørskov's group [58-60] and Koper's group [61, 62] and is related to the Sabatier principle and becomes central as the amount of reaction intermediates increases. In short, according to the Sabatier principle, the best catalyst for a given reaction will have a binding energy of the reaction intermediate on the catalyst, that is high enough in order to chemisorb the compound and activate bonds, but low enough in order to allow desorption of the product and avoid inhibition. The reaction intermediate often chemically resembles the reactant and product, this results in a mathematical relation between their binding energies on given a catalyst surface. In a reaction involving a single intermediate, it is theoretically possible to find a catalyst that will conduct the reaction with zero activation energy: the top of the volcano plot. However, most reactions have a multi-intermediate mechanism and this ideal catalyst can only be approached. The binding energies of these intermediates on a catalyst surface scale with one another, so it is impossible to optimize a single active site for a given intermediate, without affecting its properties for another intermediate. The strategy Nørskov and Koper devised is to step away from uniform catalyst active sites, and introduce active site heterogeneity on the surface [58, 62]. This can be done with promoters, enzymes, co-catalysts and multimetallic catalysts.

This thesis aims at contributing to the approach of nanostructured catalyst design. A bottom-up approach as colloidal metal nanoparticle synthesis was selected as a promising candidate to apply atomically tailored materials as heterogeneous catalysts. A nanostructured catalyst support in the form of carbon nanotubes was selected for electrocatalytic studies in view of their large surface area combined with high electronic conductivity. The phenomenon of self-assembly is used for immobilization of nanoparticles on various supports. The resulting catalysts are then investigated in catalytic reactions relevant for the above-mentioned considerations such as selective oxidation of benzyl alcohol, carbon monoxide oxidation and electrocatalytic reduction of carbon dioxide.

Chapter 1 of this thesis covers the preliminary study of the benzyl alcohol oxidation reaction where an anomalous conversion curve was observed using a commercial gold-based catalyst. Although the initial conversion rate was in line with previous experiments, the conversion appeared to level off at longer reaction times. Besides, modeling and fitting such a behavior with reasonable reaction rates was not possible. This lead to an in-depth study of the catalyst stability by performing the reaction in the presence of its own reaction products and other compounds.

Chapter 2 of this thesis addresses catalytic support effects, by decoupling the gold nanoparticle size dependency from catalyst synthesis conditions, by employing the colloidal route and immobilizing the same gold nanoparticles on different metal oxide supports, the effects on the catalytic activity in benzyl alcohol oxidation and carbon monoxide oxidation are determined.

Chapter 3 of this thesis addresses the problem of capping ligand removal from immobilized gold colloidal nanoparticles. In view of the undesired effects of temperature treatments for that purpose, a room-temperature treatment was devised using ozone as strong oxidizer, in the same way zeolites are sometimes cleaned from structure directing agents. The effect of such a treatment on catalytic activity is assessed for benzyl alcohol oxidation and carbon monoxide oxidation.

Chapter 4 of this thesis explores the effects of nanostructuring the catalyst support on the catalytic activity. Employing different forms of carbon nanostructures such as carbon black or carbon nanotubes, palladium nanoparticles are deposited, resulting in a series of catalysts. Their catalytic activity for benzyl alcohol oxidation is investigated.

Chapter 5 of this thesis focuses on the scaling relationships between reaction intermediates of CO_2 reduction. Bimetallic copper-gold nanoparticles are synthesized via a colloidal route, and are immobilized on carbon nanotubes. The resulting catalysts are immobilized on gas diffusion cathodes and their catalytic activity and selectivity for CO_2 reduction are compared.

This thesis concludes with a summary and evaluation of the different chapters in the light of the objectives of this thesis.

References:

1. Lindström, B.; Pettersson, L.J. *Cattech 7,* **2003**, 130-138.
2. Langmuir, I. *J Am Chem Soc 37,* **1915**, 1139-1167.
3. Perathoner, S.; Centi, G.; Gross, S.; Hensen, E.J.M. *Science and Technology Roadmap on Catalysis for Europe - A Path to Create a Sustainable Future*; European Cluster on Catalysis, 2016.
4. Rodríguez-Reyes, J.C.F.; Friend, C.M.; Madix, R.J. *Surf Sci 606,* **2012**, 1129-1134.
5. Norskov, J.K.; Bligaard, T.; Rossmeisl, J.; Christensen, C.H. *Nat Chem 1,* **2009**, 37-46.
6. Besenbacher, F.; Chorkendorff, I.; Clausen, B.S.; Hammer, B.; Molenbroek, A.M.; Nørskov, J.K.; Stensgaard, I. *Science 279,* **1998**, 1913-1915.
7. Jacobsen, C.J.H.; Dahl, S.; Clausen, B.G.S.; Bahn, S.; Logadottir, A.; Nørskov, J.K. *J Am Chem Soc 123,* **2001**, 8404-8405.
8. Toulhoat, H.; Raybaud, P. *J Catal 216,* **2003**, 63-72.
9. Strasser, P.; Fan, Q.; Devenney, M.; Weinberg, W.H.; Liu, P.; Nørskov, J.K. *J Phys Chem B 107,* **2003**, 11013-11021.
10. Greeley, J.; Mavrikakis, M. *Nat Mater 3,* **2004**, 810-815.
11. Qian, X.; Peng, X.H.; Ansari, D.O.; Yin-Goen, Q.; Chen, G.Z.; Shin, D.M.; Yang, L.; Young, A.N.; Wang, M.D.; Nie, S. *Nat Biotechnol 26,* **2008**, 83-90.
12. Thompson, D.T. *Gold Bull 40,* **2007**, 267-269.
13. Turkevich, J.; Stevenson, P.C.; Hillier, J. *Discuss Faraday Soc 11,* **1951**, 55-75.
14. Turkevich, J. *Gold Bull 18,* **1985**, 86-91.
15. Turkevich, J. *Gold Bull 18* **1985**, 125-131.
16. Daniel, M.C.; Astruc, D. *Chem Rev 104,* **2004**, 293-346.
17. Pachón, L.D.; Rothenberg, G. *Appl Organomet Chem 22,* **2008**, 288-299.
18. Quintanilla, A.; Butselaar-Orthlieb, V.C.L.; Kwakernaak, C.; Sloof, W.G.; Kreutzer, M.T.; Kapteijn, F. *J Catal 271,* **2010**, 104-114.
19. Carroll, K.J.; Reveles, J.U.; Shultz, M.D.; Khanna, S.N.; Carpenter, E.E. *J Phys Chem C 115,* **2011**, 2656-2664.
20. Ott, L.S.; Finke, R.G. *Coordin Chem Rev 251,* **2007**, 1075-1100.
21. Cuenya, B.R. *Thin Solid Films 518,* **2010**, 3127-3150.
22. Puspitasari, I.; Skupien, E.; Kapteijn, F.; Kooyman, P.J. *Catalysts 6,* **2016**, 179.
23. Iijima, S. *Nature 354,* **1991**, 56-58.
24. Radushkevich, L.V.; Lukyanovich, V.M. *Zurn Fisic Chim 26,* **1952**, 88-95.

25. Dai, L. 12.4 Surface Characteristics of Carbon Nanotubes. In *Carbon Nanotechnology - Recent Developments in Chemistry, Physics,Materials Science and Device Applications*; Elsevier, **2006**.
26. Hu, M.; Yao, Z.; Wang, X. *Ind Eng Chem Res 56,* **2017**, 3477-3502.
27. Dai, L. 8. Functionalization and Applications of Carbon Nanotubes. In *Carbon Nanotechnology - Recent Developments in Chemistry, Physics,Materials Science and Device Applications*; Elsevier, **2006**.
28. Tsang, S.C.; Chen, Y.K.; Harris, P.J.F.; Green, M.L.H. *Nature 372,* **1994**, 159-162.
29. Giacalone, F.; Campisciano, V.; Calabrese, C.; La Parola, V.; Syrgiannis, Z.; Prato, M.; Gruttadauria, M. *ACS Nano 10,* **2016**, 4627-4636.
30. Lu, X.; Chen, Z. *Chem Rev 105,* **2005**, 3643-3696.
31. Hong, S.; Myung, S. *Nat Nano 2,* **2007**, 207-208.
32. Dai, L. 11. Electrochemical Properties of Carbon Nanotubes. In *Carbon Nanotechnology - Recent Developments in Chemistry, Physics,Materials Science and Device Applications*; Elsevier, **2006**.
33. Wang, J.; Li, M.; Shi, Z.; Li, N.; Gu, Z. *Anal Chem 74,* **2002**, 1993-1997.
34. Chen, R.J.; Franklin, N.R.; Kong, J.; Cao, J.; Tombler, T.W.; Zhang, Y.; Dai, H. *Appl Phys Lett 79,* **2001**, 2258-2260.
35. Ye, J.-S.; Wen, Y.; De Zhang, W.; Ming Gan, L.; Xu, G.Q.; Sheu, F.-S. *Electrochem Commun 6,* **2004**, 66-70.
36. Cai, H.; Cao, X.; Jiang, Y.; He, P.; Fang, Y. *Anal Bioanal Chem 375,* **2003**, 287-293.
37. Negro, E.; Latsuzbaia, R.; Dieci, M.; Boshuizen, I.; Koper, G.J.M. *Appl Catal B Environ 166-167,* **2015**, 155-165.
38. Zhang, J.; Wang, Z.; Liu, J.; Chen, S.; Liu, G. *Self-Assembled Nanostructures*; Springer US, **2006**.
39. Latsuzbaia, R.; Negro, E.; Koper, G.J.M. In *High yield synthesis of a durable platinum catalyst in bicontinuous microemulsion for PEMFC applications*, 5th European Fuel Cell Piero Lunghi Conference and Exhibition, EFC 2013, 2013; Cigolotti, V.; Barchiesi, C.; Chianella, M., Eds. ENEA: **2013**; 345-346.
40. Kroschwitz, J.I.; Seidel, A. *Kirk-Othmer Encyclopedia of Chemical Technology*; Wiley: **2006**.
41. Bruhne, F.; Wright, E. *Ullmann's Encyclopedia of Industrial Chemistry, 40 Volume Set*; Wiley: **2011**.
42. Abad, A.; Corma, A.; García, H. *Chem-Eur J 14,* **2008**, 212-222.
43. Davis, S.E.; Ide, M.S.; Davis, R.J. *Green Chem 15,* **2013**, 17-45.
44. Kuhn, J.N.; Tsung, C.K.; Huang, W.; Somorjai, G.A. *J Catal 265,* **2009**, 209-215.
45. Carbon Monoxide Emissions, Available online https://cfpub.epa.gov/roe/indicator_pdf.cfm?i=10 (03/03/2017)
46. Haruta, M.; Yamada, N.; Kobayashi, T.; Iijima, S. *J Catal 115,* **1989**, 301-309.
47. Hashmi, A.S.K.; Hutchings, G.J. *Angew Chem Int Edit 45,* **2006**, 7896-7936.
48. Herzing, A.A.; Kiely, C.J.; Carley, A.F.; Landon, P.; Hutchings, G.J. *Science 321,* **2008**, 1331-1335.
49. Jia, C.N.; Liu, Y.; Bongard, H.; Schüth, F. *J Am Chem Soc 132,* **2010**, 1520-1522.

50. Oliver-Meseguer, J.; Cabrero-Antonino, J.R.; Domínguez, I.; Leyva-Pérez, A.; Corma, A. *Science 338,* **2012**, 1452-1455.
51. Hvolbæk, B.; Janssens, T.V.W.; Clausen, B.S.; Falsig, H.; Christensen, C.H.; Nørskov, J.K. *Nano Today 2,* **2007**, 14-18.
52. Vayenas, C.G.; White, R.E.; Gamboa-Aldeco, M.E. *Modern Aspects of Electrochemistry 42*; Springer London, Limited: **2008**.
53. Hatsukade, T.; Kuhl, K.P.; Cave, E.R.; Abram, D.N.; Jaramillo, T.F. *Phys Chem Chem Phys 16,* **2014**, 13814-13819.
54. Hahn, C.; Abram, D.N.; Hansen, H.A.; Hatsukade, T.; Jackson, A.; Johnson, N.C.; Hellstern, T.R.; Kuhl, K.P.; Cave, E.R.; Feaster, J.T.; Jaramillo, T.F. *J Mat Chem A 3,* **2015**, 20185-20194.
55. Shibata, H.; Moulijn, J.A.; Mul, G. *Catal Lett 123,* **2008**, 186-192.
56. Kuhl, K.P.; Cave, E.R.; Abram, D.N.; Jaramillo, T.F. *Energ Environ Sci 5,* **2012**, 7050-7059.
57. Kuhl, K.P.; Hatsukade, T.; Cave, E.R.; Abram, D.N.; Kibsgaard, J.; Jaramillo, T.F. *J Am Chem Soc 136,* **2014**, 14107-14113.
58. Peterson, A.A.; Nørskov, J.K. *J Phys Chem Lett 3,* **2012**, 251-258.
59. Hansen, H.A.; Varley, J.B.; Peterson, A.A.; Nørskov, J.K. *J Phys Chem Lett 4,* **2013**, 388-392.
60. Nørskov, J.K.; Rossmeisl, J.; Logadottir, A.; Lindqvist, L.; Kitchin, J.R.; Bligaard, T.; Jónsson, H. *J Phys Chem B 108,* **2004**, 17886-17892.
61. Koper, M.T.M. *J Electroanal Chem 660,* **2011**, 254-260.
62. Koper, M.T.M. *Chem Sci 4,* **2013**, 2710-2723.

Chapter 1

Inhibition of a gold-based catalyst in benzyl alcohol oxidation: understanding and remediation

Benzyl alcohol oxidation was carried out in toluene as solvent, in the presence of the potentially inhibiting oxidation products benzaldehyde and benzoic acid. Benzoic acid, or a product of benzoic acid, is identified to be the inhibiting species. The presence of a basic potassium salt (K2CO3 or KF) suppresses this inhibition, but promotes the formation of benzyl benzoate from the alcohol and aldehyde. When a small amount of water is added together with the potassium salt, an even greater beneficial effect is observed, due to a synergistic effect with the base. A kinetic model, based on the three main reactions and four major reaction components, is presented to describe the concentration-time profiles and inhibition. The inhibition, as well as the effect of the base, was captured in the kinetic model, by combining strong benzoic acid adsorption and competitive adsorption with benzyl alcohol. The effect of the potassium salt is accounted for in terms of neutralization of benzoic acid.

This chapter is based on the publication:
Skupien, E.; Berger, R.J.; Santos, V.P.; Gascon, J.; Makkee, M.; Kreutzer, M.T.; Kooyman, P.J.; Moulijn, J.A.; Kapteijn, F., *Catalysts 4*, **2014**, 89-115

1 – Introduction

As far as the chemical industry is concerned, biomass is forecast to be one of the major successors of oil as a source of carbon for the production of organic molecules [1,2]. However, the chemistry of biomass-derived molecules differs significantly from oil-derived molecules [1,3]. Their higher oxygen content renders them more sensitive to oxidation, requiring milder conditions in selective oxidation processes. Furthermore, the solubility in water is enhanced when organics are oxygenated, which can be either problematic or advantageous. It is now widely recognized that the chemical industry will need to adapt to the new situation [1–3]. Once the catalytic abilities of gold had been discovered [4], its high activity for oxidation reactions at mild conditions, down to room temperature, was quickly noticed. This exceptionally low process temperature allows for a much better control over the selectivity, in particular in selective oxidations. These reactions play an important role in organic synthesis [1,5–11] and, as a consequence, much effort was put into studying and benchmarking gold-based catalysts for selective oxidation of alcohols, ketones, and carboxylic acids.

Benzyl alcohol (BnOH) selective oxidation to benzaldehyde (BnO) is one of these benchmark reactions used extensively to assess the catalytic activity of gold catalysts [1,5–9,11–13]. Alcohol selective oxidation is often carried out in the presence of a base as “promoter” or “co-catalyst” [1–3,7,8,11,12,14,15]. The base enhances the deprotonation of the alcohol, thereby ensuring that the rate-limiting step is the catalytic oxidation step [1,15]. Furthermore, alkaline conditions have also been reported to enhance the selectivity towards benzoic acid (BnOOH) [1,15]. However, the focus is usually on the initial turnover frequency (TOF) [5,7,12], whereas only a few reports mention issues of deactivation and re-usability [1,6,9,11,14].

Deactivation can arise either from catalyst degradation (e.g., sintering) or from catalyst poisoning or fouling [16]. Poisoning and fouling can sometimes be reversed by catalyst regeneration, mainly under oxidative conditions [9]. Sulfur-containing impurities are often responsible for poisoning of noble metal catalysts [16], and desulfurization catalysis has matured for decades to answer this problem, for instance by a combination of hydrodesulphurization (HDS) and guard beds. In a more general perspective, poisoning impurities in the feed can be eliminated by dedicated treatments. In selective oxidation over noble metal catalysts, deactivation can also occur due to the over-oxidation of Pt [14] and Pd [14,17] catalysts when an excess of (molecular) oxygen is present. This over-oxidation means that too much atomic oxygen (a reaction intermediate) is present on the catalytic sites, thereby blocking their accessibility for hydrocarbon adsorption. Because of this, catalysts tested in the oxygen mass-transfer limited regime can exhibit higher activity [1,11,14] than might be predicted based on data in the kinetic regime. It is generally accepted that gold-based catalysts are resistant to over-oxidation [1,3,11], making them promising candidates for oxidation reactions over extended periods of time. However, a reaction intermediate or the product itself can be an inhibiting entity. It should be noted that inhibition is reversible because the inhibition is remediated when the concentration of the inhibitor in the reaction medium is sufficiently reduced, whereas poisoning is irreversible at the reaction conditions [16]. This so-called product inhibition phenomenon is an even greater challenge, as the catalyst creates its own poison while performing the desired reaction. This has been frequently observed both in oxidation and dehydrogenation reactions. For instance, Dimitratos et al. [18] attributed deactivation of Au-Pd and Au-Pt catalysts in octanol oxidation to inhibition by the carboxylate formed. They also reported the alleviation of this inhibition when NaOH was present. Zope and Davis [3] reported similar effects for the selective oxidation of glycerol to glyceric acid. They performed the reaction in the presence of 19 different compounds: either products or intermediates in the glycerol oxidation reaction, or species that might be formed from condensation of intermediates and/or products. Ketones, condensation products of ketones or secondary alcohols (forming ketones upon oxidation) were found to be inhibiting compounds. In contrast, simple carboxylic acids such as acetic acid and propionic acid did not show appreciable inhibition, nor did diacids such as malonic or succinic acid, or primary alcohols such as methanol. To the best of our knowledge, and despite reviews mentioning the occurrence of product inhibition during the oxidation of alcohols on gold and platinum group metal catalysts in general [11,14], no detailed study of this phenomenon for BnOH oxidation over gold-based catalysts has been reported.

The current study concerns the Au-catalyzed partial oxidation of BnOH to BnO and benzyl benzoate (BnOOBn) in toluene over the commercial AUROlite™ Au/Al_2O_3 catalyst. BnOH, which is a primary alcohol, is oxidized to BnO and subsequently to BnOOH, while also BnOOBn can be formed (Figure 1.1). This system suffers from deactivation, which is particularly observed when the catalyst is re-used in batch-wise operation. This deactivation can be suppressed by the addition of an inorganic base. The aim of the current study is to analyze this deactivation process, identify the possible inhibiting species, elucidate the deactivation mechanism, and evaluate the beneficial effect of the inorganic base. To accomplish this, the reaction was carried out under various reaction conditions, including experiments in the presence of reaction products, bases, and water. Additionally, kinetic modeling was performed in order to confirm the reaction and deactivation mechanisms.

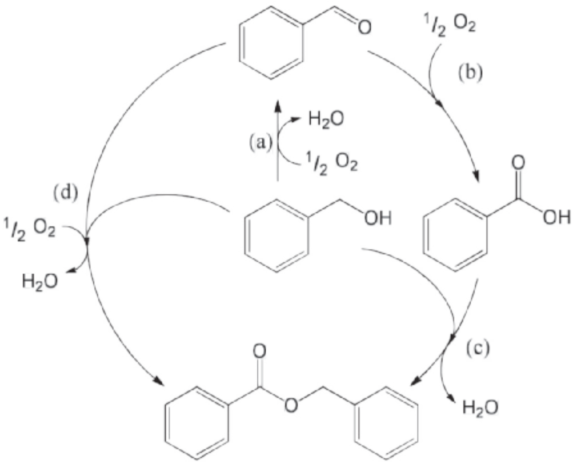

Figure 1.1: Reaction network: (**a**) oxidation of benzyl alcohol to benzaldehyde; (**b**) oxidation of benzaldehyde to benzoic acid; (**c**) esterification of benzyl alcohol and benzoic acid, and (**d**) esterification of benzyl alcohol and benzaldehyde under oxidative conditions to benzyl benzoate [19].

2 – Experimental Section

Toluene (anhydrous, 99.8%), benzyl alcohol (>99%), potassium carbonate (>99.0%), tetradecane (> 99%), potassium fluoride (>99.99%) and phosphorus pentoxide desiccant were supplied by Sigma Aldrich and were used without further purification. AUROlite™ catalyst (Au/Al_2O_3 1 wt.%, Au average particle size: 2–3 nm, specific surface area: 200–260 $m^2 \cdot g^{-1}$, from supplier specifications) was supplied by Strem Chemicals in the form of extrudates. The extrudates were crushed and sieved to a particle size <71 µm, thereby excluding diffusion limitations during catalytic experiments as verified using different catalyst particle sizes. The resulting powder was stored in a well-sealed container at 4 °C and in the dark. Catalytic testing under dry conditions was performed with this powder used as such. For the catalytic tests involving water, the desired amount of this powder was suspended in Milli-Q® water (18.2 MΩ·cm) under sonication for 30 min, and then vacuum filtered (using a Büchner funnel). The resulting moist catalyst was collected from the filter with a spatula and used as such for catalytic testing. The mass difference before and after this step indicates that around 0.5 g of water is adsorbed per gram of catalyst.

Catalytic experiments were carried out in a 100 mL round-bottom vessel, the inner diameter of which is 60 mm. The vessel was equipped with a reflux condenser and Teflon baffles, and mechanically stirred at 1300 rpm with a 4-blade Teflon impeller. Upon varying the catalyst quantity in preliminary tests, an initial reaction rate proportional to the catalyst quantity was observed, indicating that mass transport limitations were absent. In a typical catalytic test, 3.04 g of K_2CO_3 and 0.8 g of AUROlite™ are introduced in the vessel together with 80 mL of toluene. Two complementary tests were performed using 2.07 g of KF instead of K_2CO_3. The vessel was heated to 80 °C by means of an oil bath, and 200 mL·min^{-1} of air was bubbled through the reaction mixture via a glass frit. When the temperature was stabilized, 2.4 g of BnOH was introduced using a syringe, constituting the beginning of the test (t = 0 min). Small samples of 300 μL were taken at recorded times and filtered from catalyst and K_2CO_3 powders with a 13 mm syringe Teflon filter of 0.2 μm pore size (diameter: 13 mm; pore size: 0.2 μm; PTFE membrane; VWR International) and introduced in a GC sample vial together with 20 μL of tetradecane, the latter being used as internal standard.

GC analyses were performed using a Varian CP-3380 equipped with a FID detector and a CP-Sil 8 CB cat. no. 7453 column (length: 50 m; diameter: 0.25 mm; coating thickness: 0.25 μm). The initial temperature of the GC oven was 150 °C and was maintained for 4 min, then increased with 100 °C·min^{-1} to 220 °C and then maintained at 220 °C for 6.3 min. After testing, the catalyst was recovered by vacuum filtration, washed with 80 mL of toluene at room temperature and stored over P_2O_5 in an evacuated desiccator. In the case of the water treated catalyst samples, the catalyst was washed with 80 mL of toluene, followed by extensive washing with about 250 mL of Milli-Q® water (18.2 MΩ·cm) at room temperature.

Diffuse Reflectance Infra-Red Fourier Transform Spectroscopy (DRIFTS) spectra were recorded on a Nicolet model 8700 spectrometer, equipped with a high-temperature DRIFTS cell, and a DTGS-TEC detector. The spectra were recorded with 256 scans at 4 cm^{-1} resolution from 4000 to 500 cm^{-1} using potassium bromide (KBr) to perform background subtraction. The samples were pre-treated at 473 K for 1 hour in a helium flow of 20 mL·min^{-1}.

3 – Results and Discussion

3 – 1 – Catalyst Deactivation in Base-Free Conditions

Figure 1.2 displays the concentration profiles for two subsequent experiments performed under the same conditions and in the absence of a base. It should be noted that for all experimental data points, the mass balance of the 4 main components (BnOH, BnO, BnOOH and BnOOBn) closes to 100% within measurement errors, with rare exceptions where discrepancies up to 4% are present. Therefore, disproportionation and dehydration reactions, as reported by Alhumaimess et al. [5], can be neglected.

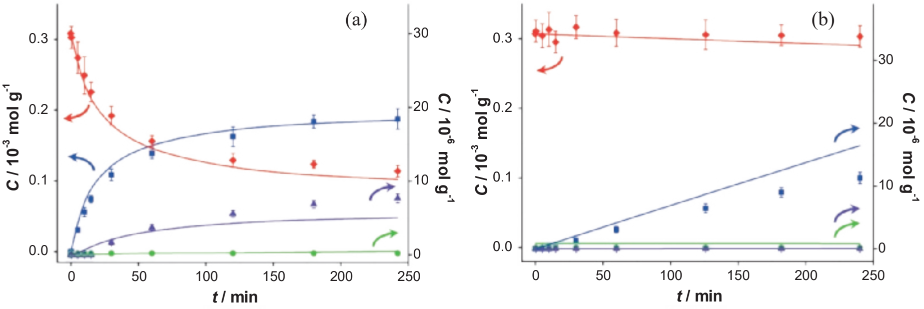

Figure 1.2: Catalyst performance in base-free conditions. Concentration of (♦) benzyl alcohol, (■) benzaldehyde, (●) benzoic acid and (▲) benzyl benzoate vs. reaction time for (a) first run using fresh AUROlite™ and (b) second run using spent AUROlite™. Reaction conditions: T = 80 °C, 0.8 g AUROlite™, $C_{\text{BnOH, t=0}}$ = 3.0 × 10−4 mol·g^{-1} in 80 mL of toluene, 200 mL·min^{-1} air flow. Concentrations are expressed in moles per unit mass of liquid in the reactor (mol·g^{-1}). The symbols with error bars are the experimental results and the lines represent the kinetic model.

In the first experiment, the initial TOF is 0.7 s^{-1} and conversion levels off at around 55–60% after about 120 min. The selectivity to BnO is 93%, as reported in Table 1.1. In view of the large discrepancies in TOF reported in literature [1], comparison of our data to previously published ones is not straightforward. It is satisfactory that the values of 0.6 to 0.8 s^{-1} reported in the present study are in the order of magnitude of those of 0.04 to 0.22 s^{-1} reported in the recent review by Davis et al. [1] for nanoparticulate gold and of 2.8 to 4.4 s^{-1} for a gold foil reported in the same review [1]. As indicated by Davis et al., the values span 2 orders of magnitude. The reason for this is most likely the wide range of reaction conditions used in different studies.

In the second experiment, which is identical to the first one but with re-use of the same catalyst sample after washing with toluene, virtually no conversion is observed, indicating that the catalyst was completely deactivated. Since no other reactants than toluene and benzyl alcohol were present in the reaction mixture, the deactivation must be caused either by catalyst deterioration or by an inhibitor formed during the first experiment. The potential presence of sulfur-containing impurities was investigated by analyzing the toluene and benzyl alcohol by gas chromatography (GC). No sulfur-containing compounds could be detected, implying that their concentration was below 50 ppb (the pulsed flame photometric detector (PFPD) detection limit). Accounting for the quantities of these chemicals introduced in the reaction mixture, this corresponds to 0.4 nmol of sulfur components at maximum in the reactor. That is five orders of magnitude lower than the total amount of gold present. Since similar concentration profiles as shown in Figure 1.2 were obtained when using reagents that were pre-treated with activated carbon to remove any strongly adsorbing impurities, we conclude that

Table 1.1: Benzyl alcohol conversion rate, turn over frequency (*TOF*), conversion at 240 min and selectivity to benzaldehyde at 60% conversion for AUROlite™ catalyst in different test conditions.

Catalytic system	**Figure**	***BnOH conversion rate*** [a] **/mmol·min^{-1}**	***TOF*** [b] **/s^{-1}**	***X* at 240 min** [c] **/%**	***Sel* to BnO** [d] **/%**
Base-free	2a	0.37 ± 0.02	0.7 ± 0.1	63 ± 3	93 ± 1
Base-free re-test	2b	0.06 ± 0.04	0.1 ± 0.1	1 ± 5	/
Base-free–BnO	3	0.09 ± 0.04	0.2 ± 0.1	20 ± 10	/
Base-free–BnOOH	4	0	0	2 ± 7	/
K_2CO_3	6a	0.5 ± 0.1	0.9 ± 0.4	78 ± 1	91 ± 1
K_2CO_3 re-test	6b	0.20 ± 0.02	0.4 ± 0.1	72 ± 1	85 ± 1
KF	7a	0.3 ± 0.1	0.6 ± 0.3	81 ± 1	91 ± 1
KF re-test	7b	0.5 ± 0.2	1.0 ± 0.5	95 ± 1	83 ± 1
K_2CO_3–BnOOH	10	0.10 ± 0.03	0.2 ± 0.1	61 ± 7	92 ± 1
K_2CO_3–H_2O	11	0.43 ± 0.03	0.8 ± 0.2	97 ± 1	86 ± 1
Base-free re-test–H_2O	12	0.03 ± 0.05	0.1 ± 0.1	1 ± 4	/

Concentrations are expressed in moles per unit mass of liquid in the reactor (mol·g^{-1}). [a] $BnOH\ conversion\ rate = \frac{\Delta C_{BnOH}}{\Delta t} \times w_{liq}$, where $\frac{\Delta C_{BnOH}}{\Delta t}$ is the conversion rate of benzyl alcohol (mmol·g^{-1}·min^{-1}), calculated by linear regression of the concentration values between 0 and 15 min and w_{liq} is the total mass of liquid (g); [b] $TOF = \frac{\Delta C_{BnOH}}{\Delta t} \times \frac{0.001}{60} \times w_{liq} \times \frac{M_{Au}}{w_{cat} \times 0.01 \times 0.22}$, where $\frac{w_{cat} \times 0.01}{M_{Au}}$ is the total amount of gold in the reactor (mol) and 0.22 is the amount of edge + corner atoms per amount of gold for 2.5 nm gold nanoparticles [20] (mol·mol^{-1}); [c] $X = \frac{C_{BnOH,t=0} - C_{BnOH,t=240\min}}{C_{BnOH,t=0}} \times 100\%$; [d] $Sel_{BnO} = \frac{C_{BnO,\,X=60\%}}{C_{BnO,\,X=60\%} + C_{BnOOH,\,X=60\%} + 2 \times C_{BnOOBn,\,X=60\%}} \times 100\%$ In parallel and series reaction networks, selectivities have to be compared at the same conversion levels. 60% is chosen here, as it is the level in the base free experiment after 240 min.

feed contaminants, including sulfur compounds, are not responsible for the observed

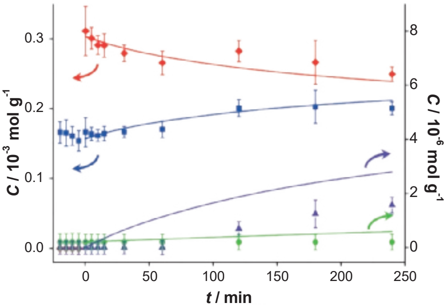

Figure 1.3: Catalyst performance after pre-addition of benzaldehyde. Concentration of (♦) benzyl alcohol, (■) benzaldehyde, (●) benzoic acid and (▲) benzyl benzoate *vs.* reaction time for catalytic reaction over fresh AUROlite™. Benzaldehyde was introduced 20 min before benzyl alcohol was added. Reaction conditions: $T = 80$ °C, 0.8 g AUROlite™, $C_{\text{BnOH}, t=0} = 3.0 \times 10{-}4$ mol·g^{-1}, $C_{\text{BnO}, t<0} = 1.7 \times 10{-}4$ mol·g^{-1}, in 80 mL of toluene, 200 mL·min^{-1} air flow. Concentrations are expressed in moles per unit mass of liquid in the reactor (mol·g^{-1}). The symbols with error bars are the experimental results and the lines represent the kinetic model.

deactivation. As a consequence, activated carbon cleaning was deemed not to be necessary and was omitted for the experiments reported here.

These results thus suggest that products or intermediates formed cause the observed deactivation. In order to investigate whether product inhibition is indeed taking place, an experiment was performed with fresh catalyst, where BnO was added to the reactor 20 min prior to the actual start of the catalytic reaction under the same reaction conditions, i.e., before the introduction of BnOH. The 20 min exposure time was selected based on the results of Figure 1.1a where it can be seen that BnOOBn was already formed at that reaction time, thereby ensuring that all potentially inhibiting products were present.

The results in Figure 1.3 show a very low conversion of 20%, confirming strong product inhibition. It is striking that despite the appreciable amount of BnO introduced at $t < 0$, neither BnOOBn nor BnOOH could be detected until the BnOH was introduced at $t = 0$. Clearly the sites for the sequential reactions of BnO (Figure 1.1a,b) are fully blocked without the presence of alcohol. It should be noted that for $t < 0$ the BnO concentration shows a slight decrease, indicating that a small amount of BnO is consumed without producing a detectable amount of BnOOH in the liquid phase. We conclude that some product is formed which remains on the catalyst and inhibits further turnovers. Carboxylic acid moieties are well known to interact strongly with gold nanoparticle surfaces, even allowing the stabilization of small gold clusters in colloidal systems [21]. BnOOH is therefore suspected to be the inhibitor, since it is the logical

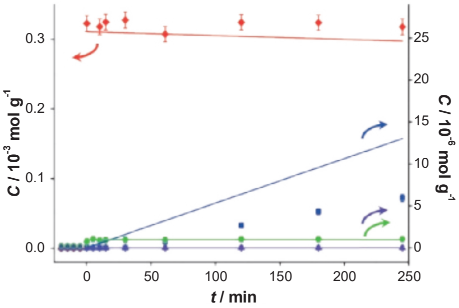

Figure 1.4: Catalyst performance after pre-addition of benzoic acid. Concentration of (♦) benzyl alcohol, (■) benzaldehyde, (●) benzoic acid and (▲) benzyl benzoate *vs.* reaction time for catalytic reaction over fresh AUROlite™. Benzoic acid was introduced 20 min prior to the beginning of the reaction. Reaction conditions: T = 80 °C, 0.8 g AUROlite™, $C_{\mathrm{BnOH},\, t=0} = 3.0 \times 10^{-4}$ mol·g^{-1}, $C_{\mathrm{BnOOH},\, t<0} = 4.1 \times 10^{-6}$ mol·g^{-1}, in 80 mL of toluene, 200 mL·min^{-1} air flow. Concentrations are expressed in moles per unit mass of liquid in the reactor (mol·g^{-1}). The symbols with error bars are the experimental results and the lines represent the kinetic model.

product of BnOH oxidation, although its concentration in the solution stayed below the GC detection limit of 0.20 µmol·g^{-1}. In order to evaluate the effect of BnOOH, a similar experiment was performed in which BnOOH was added 20 min prior to the actual start of the test. The concentration profiles are shown in Figure 1.4. In this experiment, approximately 40 times less acid was introduced compared to the amount of aldehyde introduced for the experiment in Figure 1.3. Nevertheless, an even more dramatic inhibiting effect was observed: hardly any conversion of BnOH occurred. The concentration of BnOOH measured by GC at $t < 0$ is 1 µmol·g^{-1}, which is about 25% of what was added, suggesting a strong interaction of BnOOH with the catalyst. The slight increase in concentration of BnOOH upon addition of BnOH at $t = 0$ is attributed to competitive adsorption between the alcohol and the acid. No ester was present at the beginning of the reaction, nor was it detected during the course of the reaction. This suggests that the inhibiting product is either BnOOH or a compound formed from BnOOH. Therefore, product inhibition particularly occurs on catalysts on which BnO can react further to BnOOH. This interpretation is confirmed by a nanostructured gold-based catalyst synthesized in our lab exhibiting 100% selectivity to BnO not showing deactivation for 4 consecutive runs [22].

3– 2 – Influence of a Base on Catalyst Deactivation

Figure 1.5 shows the reaction mechanism, in basic conditions, of the oxidation of alcohol to aldehyde and the sequential oxidation to carboxylic acid [1,15,23–25]. Au* indicates an active site on the gold surface. A dashed line represents a chemical

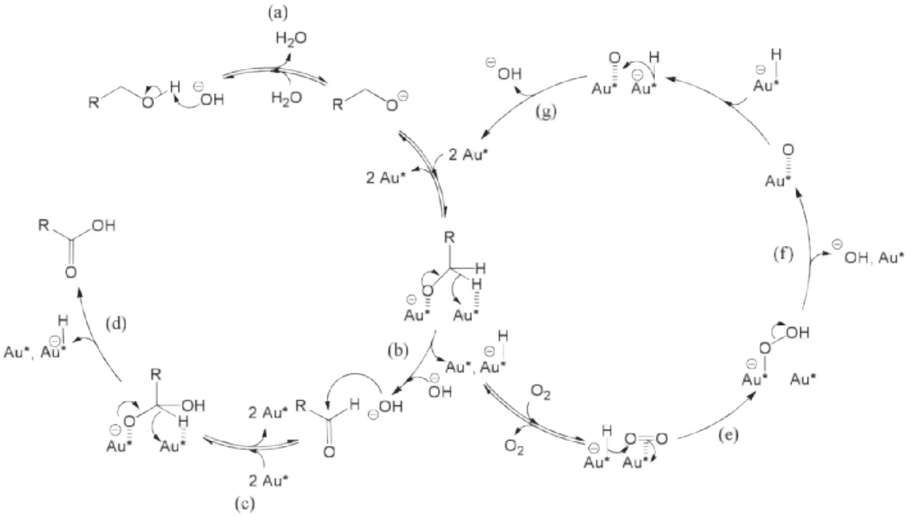

Figure 1.5: Reaction mechanism of benzyl alcohol oxidation to benzaldehyde and sequential oxidation to benzoic acid over a gold catalyst, co-catalyzed by the base HO^- [1,15,23–25].

interaction of a species with an adsorption site on the gold surface. Electron transfers corresponding to bond cleavage or formation are indicated by curved arrows. As indicated in Figure 1.5, reaction step a, the role of the base is to deprotonate the alcohol, thereby ensuring that the rate limiting step is the reaction on the gold surface, presumably the β-hydride elimination forming the aldehyde (step b yielding R-CH=O) or the carboxylic acid (step d yielding R-COOH) [1,15,23–25]. However, basic conditions have also been reported to enhance the selectivity towards carboxylic acid, by favoring the conversion of aldehyde to the corresponding geminal diol [1,15] as depicted by reaction step c (The diol is shown as R-CH(OH)O−, partially deprotonated and adsorbed on Au*). In parallel, the gold site that carries the hydride (Au*-H−) is regenerated by adsorbed molecular oxygen (Au*||||O2) via a peroxyl intermediate (step e yielding Au*-O-OH) [1,15], or via dissociated oxygen from the catalyst support [25]. This also regenerates an OH− (steps f and g) [15] and closes the catalytic cycle as shown on the right-hand side of Figure 1.5. For stoichiometric reasons, it is clear that two hydrides species must react per O_2 molecule. However, it is unclear whether the second hydride reacts after the O-O bond dissociation (step f), or if the O-O is assisted by the second hydride (in the latter case, step f and g would bond dissociation be simultaneous). The question arises if the presence of a base has an influence on the catalyst stability. The catalytic reaction was carried out in the presence of two different bases: potassium carbonate (pK_{b1} = 3.68) and potassium fluoride (pK_b = 10.8). Although the pK_b values (defined in aqueous environment) are not directly transferable

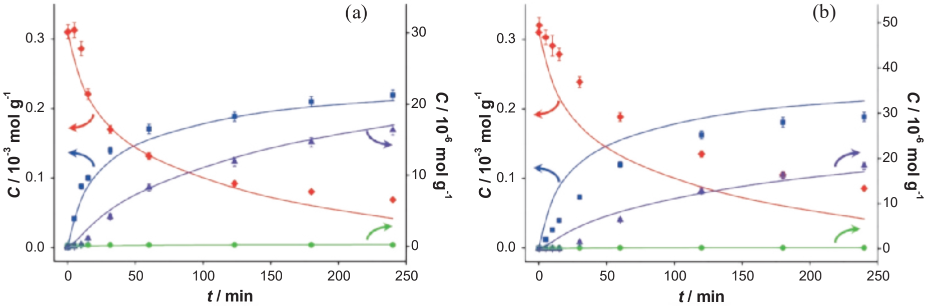

Figure 1.6: Catalyst performance in the presence of K_2CO_3. Concentration of (♦) benzyl alcohol, (■) benzaldehyde, (●) benzoic acid and (▲) benzyl benzoate *vs.* reaction time for catalytic reaction over fresh AUROlite™ in the presence of K_2CO_3. (a) First run using fresh AUROlite™ (b) second run using spent AUROlite™. Reaction conditions: $T = 80$ °C, 0.8 g AUROlite™, 3.04 g K_2CO_3, $C_{\mathrm{BnOH},\ t=0} = 3.0 \times 10^{-4}$ mol·g^{-1}, in 80 mL of toluene, 200 mL·min^{-1} air flow. Concentrations are expressed in moles per unit mass of liquid in the reactor (mol·g^{-1}). The symbols with error bars are the experimental results and the lines represent the kinetic model.

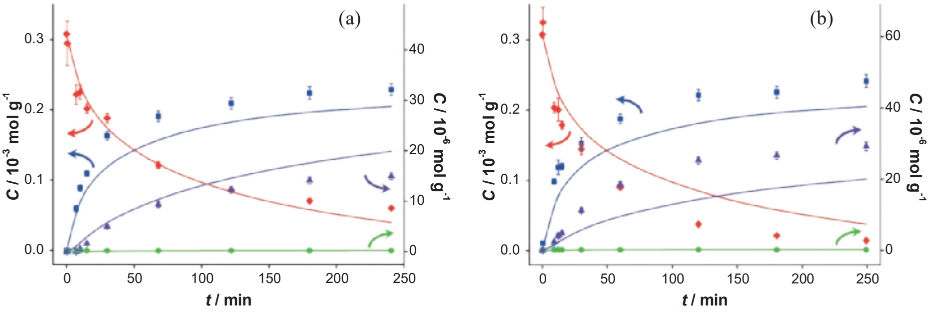

Figure 1.7: Catalyst performance in the presence of KF. Concentration of (♦) benzyl alcohol, (■) benzaldehyde, (●) benzoic acid and (▲) benzyl benzoate *vs.* reaction time for catalytic reaction over fresh AUROlite™ in the presence of KF. (a) First run using fresh AUROlite™ and 2.1 g KF (b) second run using spent AUROlite™ and ~3 g KF. Reaction conditions: $T = 80$ °C, 0.8 g AUROlite™, $C_{\mathrm{BnOH},\ t=0} = 3.0 \times 10^{-4}$ mol·g^{-1}, in 80 mL of toluene, 200 mL·min^{-1} air flow. Concentrations are expressed in moles per unit mass of liquid in the reactor (mol·g^{-1}). The symbols with error bars are the experimental results and the lines represent the kinetic model.

to aprotic solvent (toluene), and these bases hardly dissolve in toluene, the pK_b values still indicate the relative basicity of both bases used.

The spent catalysts were also re-used. A significant loss of KF was observed during the recovery of the catalyst after the first test, which was compensated for by the addition of another 2.1 g of KF to the spent catalyst, resulting in an estimated total amount of KF present during the second experiment with the spent catalyst of about 3 g. The concentration profiles of these experiments are presented in Figures 1.6 and 1.7, respectively. The results of the first run are similar to those for the base-free experiments, although a slight increase in the initial *TOF*, from 0.7 to 0.9 s^{-1}, is observed (Table 1.1). Increased activity upon addition of a base has already been reported [1] and is probably due to the enhanced deprotonation of BnOH. The conversion at 240 min is also higher: 78% compared with 63% in base-free conditions. The selectivity to BnO does not change significantly (93% when no base is present *vs.* 91% in the presence of potassium carbonate). However, it should be noted that more ester is formed in the presence of K_2CO_3 (at 240 min: 16 $\mu mol \cdot g^{-1}$ compared to 8 $\mu mol \cdot g^{-1}$ in base free conditions), and the amount of BnOOH remains below detection limit. The most striking difference, when compared to base-free conditions, is the largely maintained activity when re-using the spent catalyst. The initial *TOF* is lower than that of the fresh catalyst (0.4 s^{-1} compared with 0.9 s^{-1}), but the conversion at 240 min is comparable (72% compared with 78%). This shows that the addition of a base to the reaction medium largely remediates the strong product inhibition observed under base-free conditions. When K_2CO_3 is replaced by an equimolar amount of KF, the results are similar. *TOF* is slightly lower (0.6 s^{-1}) although the difference is within the measurement error. The conversion is 81% after 240 min when KF is used, and 78% when K_2CO_3 is used (Table 1.1). Apparently, the strength of the base does not affect the activity of the fresh catalyst. Upon re-using the spent catalyst however, a higher initial reaction rate is observed (1.0 s^{-1}) and the final conversion even reaches 95%. This increase is attributed to the additional potassium fluoride added. The preserved catalytic activity proves that no other deactivation mechanism than product inhibition (e.g., sintering or poisoning) is taking place. It is clear that the bases largely neutralize the acid responsible for product inhibition. As this alleviation of the inhibition is always accompanied by an increase of selectivity towards BnOOBn, apparently ester formation is faster in the presence of a base. However, direct esterification of the carboxylic acid with the alcohol catalyzed by a base is mechanistically not likely. After deprotonation of the BnOOH by a base, nucleophilic attack of the alcohol (R-CH2-OH) on the functional carbon of carboxylate anion ($R\text{-}COO^{-}$) is highly unlikely as this would imply that a nucleophile (also seen as a Lewis base) would have to react with an electron rich species. This is illustrated in Figure 1.8 (steps d and e). The classic acid-catalyzed esterification between carboxylic acid and alcohol is depicted on the left hand-side of Figure 1.8 for comparison. It shows that under acidic conditions, the functional carbon becomes positively charged (Figure 1.8 step a, yielding $R\text{-}C(OH)^{2+}$) and thus more prone to nucleophilic attack. Another pathway involving base-catalyzed ester formation from an alcohol and an aldehyde has been suggested by Rodríguez-Reyes *et al.* [19]. This pathway is illustrated in Figure 1.9, and can explain why in our system a higher ester production is observed under basic conditions.

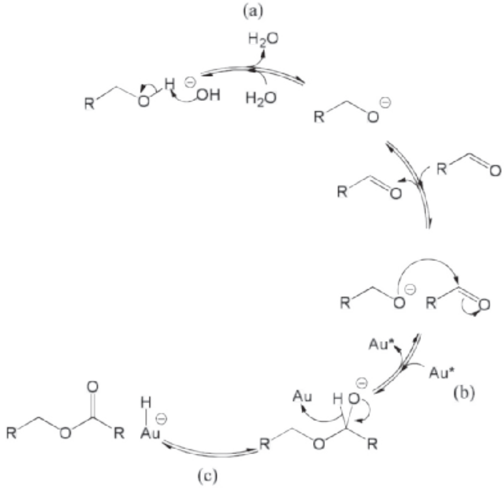

Figure 1.8: Reaction mechanism of base-catalyzed ester formation from alcohol and aldehyde, adapted from [19]. (**a**) alcohol deprotonation, (**b**) nucleophilic attack of alcoholate on carbonyl, followed by (**c**) β-hydride elimination yields the corresponding ester. The rest of the catalytic cycle consists of the oxidation of the hydride left on the gold surface by molecular oxygen, which also regenerates the base as depicted in Figure 1.5 (steps f and g).

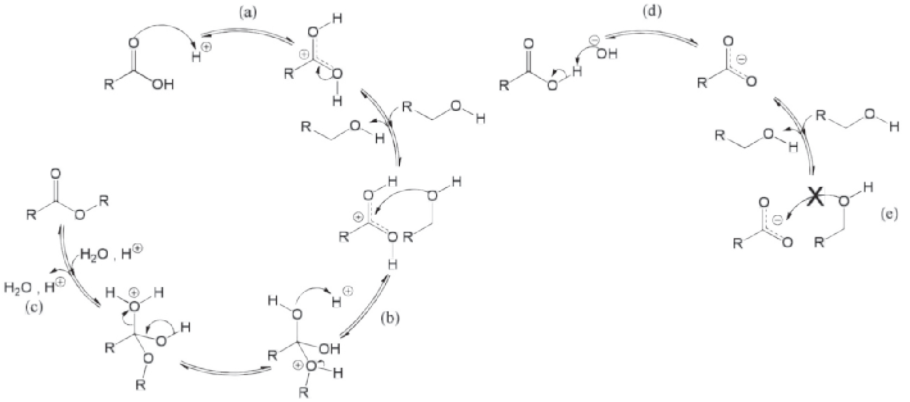

Figure 1.9: Reaction mechanism of acid catalyzed esterification of carboxylic acid and alcohol. (a) protonation of carbonyl oxygen yielding an electrophilic carbocation; (b) nucleophilic attack of the alcohol and (c) dehydration yielding the corresponding ester. (d) deprotonation of the carboxylic acid by a base yielding a carboxylate anion; (e) the nucleophilic attack of the alcohol is then greatly disfavored.

To further elucidate the role of the base on product inhibition, an experiment was performed with potassium carbonate and pre-addition of BnOOH. The concentration profiles are shown in Figure 1.10 and are directly comparable with the ones shown in Figure 1.6a where K_2CO_3 was present but no inhibitor was pre-added, and with Figure

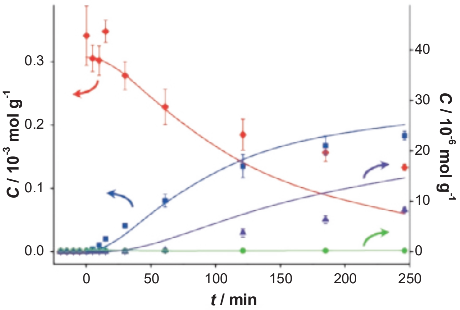

Figure 1.10: Catalyst performance in the presence of K_2CO_3 after pre-addition of benzoic acid. Concentration of (♦) benzyl alcohol, (■) benzaldehyde, (●) benzoic acid and (▲) benzyl benzoate *vs.* reaction time for catalytic reaction over fresh AUROlite™ where benzoic acid was introduced prior to the beginning of the reaction. Reaction conditions: $T = 80$ °C, 0.8 g AUROlite™, 3.04 g K_2CO_3, $C_{\mathrm{BnOH},\, t=0} = 3.0 \times 10^{-4}$ mol·g^{-1}, $C_{\mathrm{BnOOH},\, t<0} = 4.1 \times 10^{-6}$ mol·g^{-1}, in 80 mL of toluene, 200 mL·min^{-1} air flow. Concentrations are expressed in moles per unit mass of liquid in the reactor (mol·g^{-1}). The symbols with error bars are the experimental results and the lines represent the kinetic model

1.4 where no base was present but BnOOH was pre-added. In comparison with Figure 1.6a where no BnOOH was added, the initial TOF is lower: 0.2 s^{-1} (Table 1.1). The conversion after 240 min is 61% and the selectivity to BnO is 92%. When compared with the results in Figure 1.4 (no carbonate added), we can conclude that even though inhibition is still observed, the presence of potassium carbonate greatly reduces it. Based on our interpretation, the presence of a base results in (partial) neutralization of the BnOOH, thereby alleviating inhibition. In parallel, basic conditions also enhance the subsequent ester formation depicted in Figure 1.9, leading to more ester production and decreasing aldehyde selectivity. An effect of the amount of potassium on the inhibition is also suspected based on Figure 1.7a,b, but this has not been further quantified.

3 – 3 – Influence of Water on Catalyst Deactivation

Water was already recognized to be crucial for Au-catalyzed gas phase CO oxidation by Daté et al. [26], who demonstrated its great beneficial role. The mechanism was later proposed by Daniells et al. [27]. In many of the reaction mechanisms discussed above, water plays a role. It is produced in an amount equimolar to BnO (see Figures 1.1a and 1.5a). The mechanism of the oxidation of aldehyde to carboxylic acid involves a base-catalyzed hydration of aldehyde to geminal diol. Water is also a byproduct of the equilibrium-limited esterification. Yang et al. [28] studied the influence of different water contents on the kinetics of oxidation and determined that water has a promoting effect. They observed higher conversions of BnOH and higher selectivities to BnO

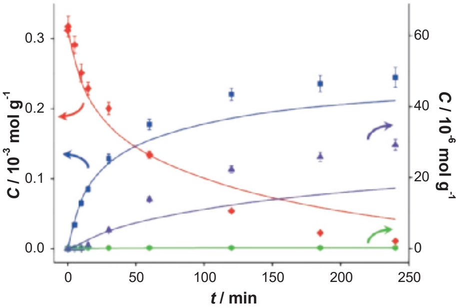

Figure 1.11: Catalyst performance in the presence of K_2CO_3 and a small amount of water. Concentration profiles of (♦) benzyl alcohol, (■) benzaldehyde, (●) benzoic acid and (▲) benzyl benzoate *vs.* reaction time for catalytic reaction over fresh AUROlite™ in the presence of water. Reaction conditions: $T = 80$ °C, 0.8 g AUROlite™, 3.04 g K_2CO_3, ~0.4 g H_2O, $C_{BnOH,\,t=0} = 3.0 \times 10^{-4}$ mol·g^{-1}, in 80 mL of toluene, 200 mL·min^{-1} air flow. Concentrations are expressed in moles per unit mass of liquid in the reactor (mol·g^{-1}). The symbols with error bars are the experimental results and the lines represent the kinetic model.

when an optimal amount of water was used. More recently, Chang and coworkers [29] conducted a computational study to better understand this effect on methanol dehydrogenation/oxidation. They concluded that the promoting effect originates from a facilitated peroxyl formation from O_2 by transfer of hydrogen from the water itself or from the alcohol via the water, where hydrogen bonds are reported to play a key role in this mechanism. Therefore, water could play a role in the deactivation of the catalyst in the present study. With this in mind, the reaction was carried out in the presence of the small amount of water that adheres to the catalyst after immersion in water and filtration. The mass difference before and after this treatment indicates about 0.5 g of water per gram of catalyst, which corresponds to around 550 mol of water per mol of gold. The results of this experiment are presented in Figure 1.11. Compared with the dry conditions of Figure 1.6a the initial TOFs are equal within the experimental error, being 0.8 s^{-1} in moist conditions and 0.9 s^{-1} in dry conditions. We do not observe the kinetic effect of water found by Yang et al., but in the presence of water our catalyst does not deactivate and the final conversion is close to 100%. The water thus positively influences the catalyst stability. A possible explanation could be that water interacts with the inhibiting product, thereby diminishing its interaction with the catalyst. However, since potassium carbonate was also present in the reactor, a synergistic effect of base and water cannot be excluded. To address this question, the deactivated catalyst obtained after the experiment of Figure 1.2b (where no base was present) was tested again in the presence of water and without the addition of any base. Concentration profiles of this experiment are displayed in Figure 1.12. Clearly, catalytic activity could not be recovered by this treatment. Thus, water alone does not remove the species

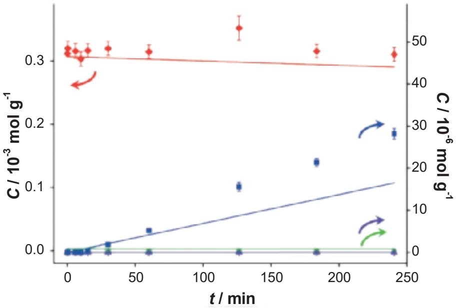

Figure 1.12: Catalyst performance of the water-washed spent catalyst in base-free conditions from Figure 1.2 in the presence of water. Concentration of (♦) benzyl alcohol, (■) benzaldehyde, (●) benzoic acid and (▲) benzyl benzoate *vs.* reaction time for catalytic reaction spent AUROlite™ in the presence of water. Reaction conditions: $T = 80$ °C, 0.8 g AUROlite™, ~1 g H_2O, $C_{BnOH,\ t=0} = 3.0 \times 10^{-4}$ mol·g^{-1}, in 80 mL of toluene, 200 mL·min^{-1} air flow. Concentrations are expressed in moles per unit mass of liquid in the reactor (mol·g^{-1}). The symbols with error bars are the experimental results and the lines represent the kinetic model.

responsible for deactivation, and the beneficial influence of water observed in Figure 1.11 is due to a synergistic effect with the potassium carbonate, e.g., by an enhanced dissolution of the inorganic base. It should also be noted that adding more water than used in these experiments provoked phase separation in which the catalyst agglomerated in the water phase, thereby eliminating the dispersion of the catalyst powder in the organic phase and causing the reaction to proceed in a mass- transport limited regime.

In order to further assess which hypothesis holds, the spent catalyst was analyzed by DRIFTS before and after washing in boiling water for 12 h (Figure 1.13). The fresh catalyst barely shows any features. In contrast, both the spent catalyst and the spent catalyst after boiling in water show clear absorption features. The catalyst tested in the presence of KF, which did not deactivate after two runs, exhibited different features. Identification of the species on the surface of the catalysts was based on reference spectra recorded of the compounds present in the reactor adsorbed on alumina. The band at 1200 cm^{-1} is attributed to C_{arom}–CHO or C_{arom}–CH_2OH stretching vibrations [30] and originates only from BnOH and BnO. Interestingly, this band is only present for the catalyst tested with KF. A small absorption band at 1390 cm^{-1} is seen in practically all cases and corresponds to the bending vibration of O–H bonds; thus, it cannot be used to differentiate the components of interest. The sharp absorption at 1450 cm^{-1} is due to in-plane bending vibrations of protons at a primary alcohol carbon and is specific to BnOH. Unfortunately, this band is often masked by a broader one due to other O–H vibrations at the same wavenumber. Absorptions between 1500 and 1600 cm^{-1} are attributed to C_{sp2}=C_{sp2} stretching vibrations present in all the compounds of

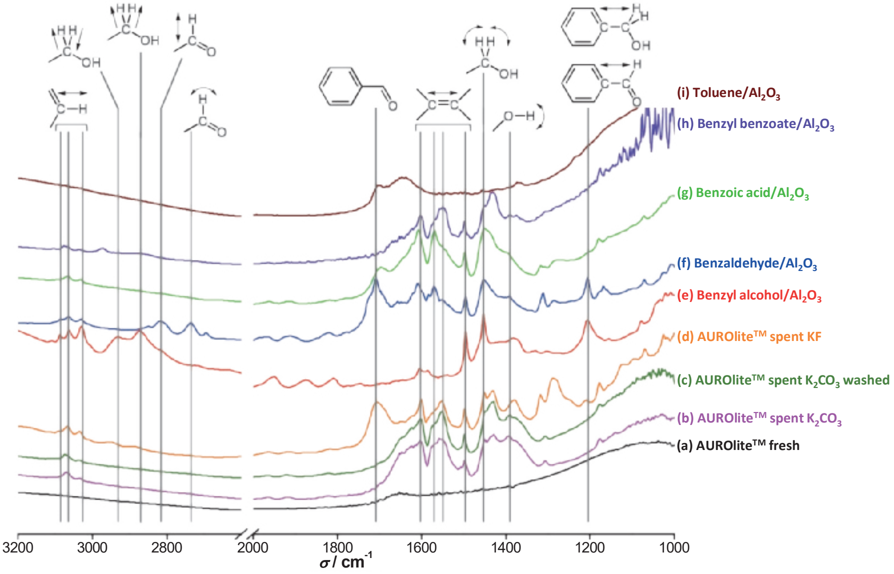

Figure 1.13: DRIFT spectra of (**a**) fresh AUROlite™ catalyst; (**b**) used with K_2CO_3; (**c**) used with K_2CO_3 and washed in boiling water; (**d**) used with KF, (**e**)–(**i**) reference compounds adsorbed on alumina. Catalyst samples were pretreated under He at 473 K before recording.

interest. The broad band at 1710 cm^{-1} is specific to benzaldehydes and is due to π-conjugation of bonds throughout the entire molecule. Again, this characteristic feature is only present for the catalyst tested with KF. A smaller feature is also observed for BnOOH for the same reasons, but the carboxyl moiety seems to alter it drastically. The bending mode of water, which should appear at around 1600–1800 cm^{-1}, is hardly visible due to the pre-treatment of the samples at 473 K. Some features are also observed at higher wavenumbers. The small bands centered at around 2740 cm^{-1} and 2820 cm^{-1} arise from wagging and stretching vibrations respectively of the BnO carbonyl proton, but these bands are not detected on any of the spent catalysts. The symmetric and anti-symmetric stretching vibrations of primary alcohol methylene group protons give rise to absorptions at 2870 and 2930 cm^{-1}, respectively. The three bands between 3030 and 3090 cm^{-1} are assigned to C_{sp2}–H vibrations, which stem from any aromatic compound in the reaction medium.

Figure 1.13 clearly demonstrates that water does not visibly wash off the species involved in the reaction from the catalyst surface. Even after 12 h in boiling water, the intensities of the absorption bands corresponding to aromatic species and oxygenated aromatic species do not show any sign of decrease. Therefore, combined with the results of Figure 1.12, the hypothesis that water remediates the product inhibition by enhancing desorption of the inhibiting product is refuted. The absorption features on the catalyst tested in the presence of K_2CO_3 are very similar to those of BnOOH and BnOOBn, although the observed bands are not specific to these compounds. In contrast, the catalyst tested in the presence of KF shows absorption features similar to those of BnO, in particular the characteristic band at 1710 cm^{-1}. Since this catalyst did not deactivate whereas the catalyst tested with K_2CO_3 showed some deactivation, the attribution of the inhibitor being BnOOH or one of its products is supported. However, in view of the low degree of deactivation shown by the catalyst tested in the presence of K_2CO_3, a signal corresponding to BnO would be expected. It remains unclear why BnO seems to be absent from this catalyst surface despite the fact that KF and K_2CO_3 have similar beneficial effects.

3 – 4 – Kinetic Modeling

Since our experiments show that the BnOOH concentration in solution is very low at all times and that the ester formation increases in the presence of a base, it is assumed that the esterification runs entirely through the reaction of BnO with BnOH by H abstraction. The reactions involved in the model are:

$$C_6H_5CH_2OH + \tfrac{1}{2}O_2 \longrightarrow C_6H_5CHO + H_2O \qquad (1)$$

$$C_6H_5CHO + \tfrac{1}{2}O_2 \longrightarrow C_6H_5COOH \qquad (2)$$

$$C_6H_5CHO + C_6H_5CH_2OH + \tfrac{1}{2}O_2 \longrightarrow C_6H_5COOCH_2C_6H_5 + H_2O \qquad (3)$$

The reaction model is accordingly assumed to consist of the set of surface reactions shown in the following set of equations, in which $*$ stands for a catalytic oxidation site:

BnOH adsorption $$C_6H_5CH_2OH + * \rightleftharpoons C_6H_5CH_2OH* \qquad (4)$$

BnO adsorption $$C_6H_5CHO + * \rightleftharpoons C_6H_5CHO* \qquad (5)$$

BnOH oxidation $$C_6H_5CH_2OH* + * \longrightarrow C_6H_5CHOH* + H* \qquad (6)$$

$$H* \xrightarrow[fast]{\frac{1}{4}O_2} * + \tfrac{1}{2}H_2O$$

$$C_6H_5CHOH* \xrightarrow[fast]{O_2*} C_6H_5CHO* + HO_2*$$

$$HO_2* \xrightarrow[fast]{} \tfrac{1}{2}H_2O + \tfrac{3}{4}O_2$$

BnO hydration $$C_6H_5CHO* \underset{-H_2O}{\overset{H_2O}{\rightleftharpoons}} C_6H_5CH(OH)_2* \qquad (7)$$

BnO oxidation $C_6H_5CH(OH)_2* + * \longrightarrow C_6H_5CHO(OH)* + H*$ (8)

$$H* \xrightarrow[fast]{\frac{1}{4}O_2} * + \tfrac{1}{2}H_2O$$

$$C_6H_5CHO(OH)* \xrightarrow[fast]{O_2*} C_6H_5COOH* + HO_2*$$

$$HO_2* \xrightarrow[fast]{} \tfrac{1}{2}H_2O + \tfrac{3}{4}O_2$$

BnOOH adsorption $C_6H_5COOH + * \rightleftharpoons C_6H_5COOH*$ (9)

BnOOBn adsorption $C_6H_5COOCH_2C_6H_5 + * \rightleftharpoons C_6H_5COOCH_2C_6H_5*$ (10)

BnOOBn formation $C_6H_5CHO* + C_6H_5CH_2OH* \longrightarrow C_6H_5COOCH_2C_6H_5* + 2H*$ (11)

$$2H* \xrightarrow[fast]{\frac{1}{2}O_2} * + H_2O$$

It is assumed that all three surface oxidation reactions are irreversible. These reactions require two adjacent sites, one for the adsorbed species originating from the BnOH or BnO and one empty site that was regenerated by the oxygen or, for the esterification, adjacently adsorbed BnOH or BnO. It is also assumed that the hydride species, H*, and the peroxy species. HO_2*, are quickly removed in the excess of oxygen present, leading to the assumption that the occupancy of both species is always very low. Adsorption of water and oxygen is assumed not to inhibit the reaction. The surface reactions are described by the surface species reaction rates shown in the following equations:

BnOH adsorption $r_{BnOH} = k_{BnOH}C_{BnOH}N_T\theta_* - k_{-BnOH}N_T\theta_{BnOH*}$ (12)

BnO adsorption $r_{BnO} = k_{BnO}C_{BnO}N_T\theta_* - k_{-BnO}N_T\theta_{BnO*}$ (13)

BnOOH adsorption $r_{BnOOH} = k_{BnOOH}C_{BnOOH}N_T\theta_* - k_{-BnOOH}N_T\theta_{BnOOH*}$ (14)

BnOOBn adsorption $r_{BnOOBn} = k_{BnOOBn}C_{BnOOBn}N_T\theta_* - k_{-BnOOBn}N_T\theta_{BnOOBn*}$ (15)

BnOH oxidation $r_1 = k_1^{'}N_T\theta_{BnOH*}\theta_*s$ (16)

BnO oxidation $r_2 = k_2^{'}N_T\theta_{BnO*}\theta_*s$ (17)

BnOOBn formation $r_3 = k_3^{'}N_T\theta_{BnO*}\theta_{BnOH*}s$ (18)

Where: r_i = reaction rate (mol·g_{cat}^{-1}·s^{-1})
k_i = reaction rate constant (unit according to equations)
C_i = concentration (mol·g^{-1})
θ_i = occupancy of the surface sites (-)

N_T = total number of surface oxidation sites per unit catalyst mass (g_{cat}^{-1})
s = number of adjacent sites per site (-)

The hydration of BnO followed by the sequential oxidation of the diol species has been lumped here into a single step (17), as the equilibrium constant of the reversible hydration will be highly correlated with the rate constant of the oxidation step.

In general, adsorption reactions are at *quasi*-equilibrium, while the surface reactions are rate-limiting steps. This allows expression of the surface coverages as functions of the concentrations and the adsorption constants:

BnOH adsorption $\theta_{BnOH*} = K_{BnOH} C_{BnOH} \theta_* \text{ with } K_{BnOH} = k_{BnOH} / k_{-BnOH}$ (19)

BnO adsorption $\theta_{BnO*} = K_{BnO} C_{BnO} \theta_* \text{ with } K_{BnO} = k_{BnO} / k_{-BnO}$ (20)

BnOOH adsorption $\theta_{BnOOH*} = K_{BnOOH} C_{BnOOH} \theta_* \text{ with } K_{BnOOH} = k_{BnOOH} / k_{-BnOOH}$ (21)

BnOOBn adsorption $\theta_{BnOOBn*} = K_{BnOOBn} C_{BnOOBn} \theta_* \text{ with } K_{BnOOBn} = k_{BnOOBn} / k_{-BnOOBn}$ (22)

Where: K_i = adsorption constant of compound i on a gold active site (g·mol^{-1})

After substitution of all the surface coverage expressions in the site balance:

$$\theta_{BnOH*} + \theta_{BnO*} + \theta_{BnOOH*} + \theta_{BnOOBn*} + \theta_* = 1 \tag{23}$$

$$\theta_* = \frac{1}{\left(1 + K_{BnOH} C_{BnOH} + K_{BnO} C_{BnO} + K_{BnOOH} C_{BnOOH} + K_{BnOOBn} C_{BnOOBn}\right)} \tag{24}$$

The kinetic parameter estimation based on the full model showed that not all adsorption constants could be estimated properly due to a too weak sensitivity. It appeared that only the adsorption term of the most polar species present, BnOOH, was significant allowing the estimation of its adsorption constant and neglecting the adsorption terms of the BnOH, the BnO and the BnOOBn. Since it was experimentally observed that the presence of a base, *i.e.*, K_2CO_3 or KF, results in significant ester formation, it was assumed that this reaction is base-catalyzed. Since hardly any ester is formed in absence of base, it is concluded that the condensation reaction of BnOOH and BnOH does not occur to any significant extent.

By elimination of the coverages of the surface species, the following reaction rate expressions are obtained:

$$r_1 = \frac{k_1}{\left(1 + K_{BnOOH} C_{BnOOH}\right)^2} C_{BnOH} \qquad \text{With:} \quad k_1 = k_1^{'} K_{BnOH} N_T s \qquad (25)$$

$$r_2 = \frac{k_2}{\left(1 + K_{BnOOH} C_{BnOOH}\right)^2} C_{BnO} \qquad \text{With:} \quad k_2 = k_2^{'} K_{BnO} N_T s \qquad (26)$$

$$r_3 = \frac{S_{base}\ k_3}{\left(1 + K_{BnOOH} C_{BnOOH}\right)^2} C_{BnO} C_{BnOH} \qquad \text{With:} \quad k_3 = k_3^{'} K_{BnO} K_{BnOH} N_T s \qquad (27)$$

Where: r_i = reaction rate (mol·kg_{cat}^{-1}·s^{-1})
k_i = lumped rate constant (unit according to equations)
C_i = concentration (mol·g^{-1})
S_{base} = base strength (K_2CO_3 or KF) (-)

In the two catalytic experiments in which BnOOH was added prior to the BnOH (Figures 1.4 and 1.10), it was observed that the catalyst support Al_2O_3 adsorbs BnOOH more strongly than BnOH. In the first experiment (Figure 1.4), it was observed that the molar quantity of BnOOH in the liquid was much lower (16 μmol) than that originally added (780 μmol). The amount of BnOOH in solution increased only slightly (to 74 μmol) after subsequent addition of the 22 mmol of BnOH, demonstrating that BnOOH is adsorbed more strongly than BnOH. In the second experiment (Figure 1.10), it was observed that despite the addition of a similar amount of BnOOH (712 μmol yielding a theoretical concentration of 10.3 μmol·g^{-1}), the concentration in solution remained below detection limit (0.20 μmol·g^{-1}) for the entire reaction. Since the total amount of gold present in the reactor is in all cases 41 μmol, we conclude that adsorption on the catalyst support is responsible for the missing quantities of BnOOH. The adsorption on the support is captured by site coverages assuming to follow Langmuir behavior:

$$\theta_{BnOH,\ Al_2O_3} = \frac{K^{ads}_{BnOH,\ Al_2O_3} C_{BnOH}}{1 + K^{ads}_{BnOH,\ Al_2O_3} C_{BnOH} + K^{ads}_{BnOOH,\ Al_2O_3} C_{BnOOH}} \qquad (28)$$

$$\theta_{BnOOH,\ Al_2O_3} = \frac{K^{ads}_{BnOOH,\ Al_2O_3} C_{BnOH}}{1 + K^{ads}_{BnOH,\ Al_2O_3} C_{BnOH} + K^{ads}_{BnOOH,\ Al_2O_3} C_{BnOOH}} \qquad (29)$$

Where: $\theta_{i,\ Al_2O_3}$ = occupancy of the surface sites (-)

$K^{ads}_{i,\ Al_2O_3}$ = adsorption constant of compound *i* on the support (g·mol^{-1})

From these experimental data the adsorption constants $K^{ads}_{BnOH,\ Al_2O_3}$ and $K^{ads}_{BnOOH,\ Al_2O_3}$

were estimated to be 18.1 g·mol^{-1} and 2.47 × 10^4 g·mol^{-1}, respectively, and the total adsorption site density was found to be 1.12 mmol·g$_{cat}$$^{-1}$. With a specific surface area of 230 m^2·g^{-1} and using Avogadro's number, the corresponding site density on the support is equivalent to 2.92 sites per nm^2, which is in good agreement with Matulewicz *et al.* [31] who report a value of 2 sites/nm^2 for their γ-alumina. This yields a relation between the overall acid concentration in the vessel, $C_{\mathrm{BnOOH,tot}}$, and the actual acid concentration in the liquid phase, C_{BnOOH}:

$$C_{BnOOH} = C_{BnOOH,\,tot} - \sigma_{OH,\,Al_2O_3}\frac{w_{cat}}{w_{liq}}\frac{K^{ads}_{BnOOH,\,Al_2O_3}C_{BnOOH}}{1+K^{ads}_{BnOH,\,Al_2O_3}C_{BnOH}+K^{ads}_{BnOOH,\,Al_2O_3}C_{BnOOH}} \qquad (30)$$

Where: $C_{BnOOH,\,tot}$ = BnOOH concentration if no adsorption would take place (mol·g^{-1})
$\sigma_{OH,\,Al2O3}$ = adsorption site concentration on the catalyst (mol·g$_{cat}$$^{-1}$)
w_{cat} = amount of catalyst in the reactor (g$_{cat}$)
w_{liq} = amount of liquid in the reactor (g)

Since the amount of BnOH in the liquid phase is about three orders of magnitude larger than the amount of surface adsorption sites, the influence of BnOH adsorption on the concentration in the liquid phase is neglected. The actual acid concentration in the liquid phase can therefore be calculated directly from this quadratic equation with respect to C_{BnOOH}:

$$C_{BnOOH} = \frac{1}{2}\left(T+\sqrt{T^2+\frac{4C_{BnOOH,\,tot}\left(1+K^{ads}_{BnOH,\,Al_2O_3}C_{BnOH}\right)}{K^{ads}_{BnOOH,\,Al_2O_3}}}\right) \qquad (31)$$

Where: $$T = C_{BnOOH,\,tot} - \frac{\left(1+K^{ads}_{BnOH,\,Al_2O_3}C_{BnOH}\right)}{K^{ads}_{BnOOH,\,Al_2O_3}} - \sigma_{OH,\,Al_2O_3}\frac{w_{cat}}{w_{liq}}$$

The strong adsorption of BnOOH could be the main cause of the very low activity of catalysts reused for the same experiment after a test in absence of a base, since it was observed that this acid remains on the catalyst during rinsing with toluene and also during boiling in water (Figure 1.13). The amount of BnOOH that remains on the catalyst in these 'second runs' (Figures 1.2b, 1.6b, 1.7b and 1.12) is not known but an estimate can be made. Assuming that the BnOOH concentration in the liquid equals its detection limit of 0.20 µmol·g^{-1}, a coverage of 0.88 is found from our simulations. Thus, it is tentatively concluded that although the amounts of acid formed in the previous runs is very low (often below the detection limit), the coverage is close to 1. Since the inhibition with a reused catalyst was very small or negligible in the presence of K_2CO_3 or KF, it was assumed for simplicity that in these cases all acid was removed, which seems acceptable in view of the time (approximately half an hour, the time needed for heating plus temperature stabilization) that the catalyst particles were in the close vicinity of the K_2CO_3 or KF crystals at reaction conditions (80 °C and well mixed) before the BnOH was added.

The model also accounts for the time allowed between adding the BnO or the BnOOH to the reactor and adding the main reactant BnOH, in all cases about 20 min at reaction conditions (additionally from the heating time). In the case of BnO this causes the formation of significant amounts of BnOOH, inhibiting the reaction (Figure 1.3).

Besides the three rate constants k_1, k_2, k_3, and the three adsorption equilibrium constants, K_{BnOOH}, $K^{ads}_{BnOH\,,\,Al_2O_3}$ and $K^{ads}_{BnOOH\,,\,Al_2O_3}$, there are several other unknown parameters, which are related to the effect of the base present. The experimental results show that the main effects of either K_2CO_3 or KF are (i) a decrease of the inhibition and (ii) an increase in formation of the BnOOBn ester.

In order to account for effect (i), it is assumed that the bases react to potassium benzoate with the BnOOH formed. Although acid-base reactions are typically instantaneous reactions, a finite rate is assumed to account for the transport from the catalyst pores to the insoluble crystals of K_2CO_3 or KF. The reaction rate is assumed to be first-order with respect to the acid and independent of the catalyst concentration:

$$r_{AcBase} = k_{AcBase} C_{BnOOH} \tag{32}$$

Effect (ii) is accounted for by defining parameters to describe the strength of either K_2CO_3 or KF in the catalysis of the esterification of BnO with BnOH:

$$\text{No base: } S_{base} = 1 \tag{33}$$

$$\mathrm{K_2CO_3} : S_{base} = 1 + S_{K_2CO_3} \tag{34}$$

$$\mathrm{KF} : S_{base} = 1 + S_{K_2CO_3}\, S_{KF/K_2CO_3} \tag{35}$$

S_{K2CO3} is defined as the base strength of K_2CO_3 and $S_{KF/K2CO3}$ as the relative base strength of KF compared to K_2CO_3.

Since the experiments were performed in batch operation in a vessel that is assumed to be ideally stirred, the reactor model used to describe the process is the batch reactor model:

$$\frac{dC_{i,L}}{dt} = C_{cat} \sum_j v_{i,j} r_j \qquad (36)$$

Where: $C_{i,L}$ = concentration of component i in the liquid phase (mmol·g^{-1})
t = time (s)
C_{cat} = catalyst concentration (mg·g^{-1})
$v_{i,j}$ = stoichiometric coefficient of component i in reaction j (-)
r_j = reaction rate of reaction j (mmol·mg$_{cat}^{-1}$·s^{-1})

The complete experimental dataset used for the parameter estimation contains 140 experimental data points obtained in 14 batch experiments at various conditions. The parameter estimation was carried out using the software package Athena Visual Studio [32], applying Bayesian estimation for multiresponse experiments using the full covariance matrix [33]. The concentrations (expressed in mol·g^{-1}) of the four measured liquid components were used as the input for the objective function to be minimized. Since the concentrations of the BnOOH and the ester were typically up to two orders of magnitude smaller than those of the BnOH and BnO, the weight of BnOOBn was set at 10 and that of BnOOH at 100. For experiments with a very low conversion rate of BnOH, the weight of BnO was increased to 10 as well.

With the exception of the experiment of Figure 1.4, BnOOH concentrations were mostly below the detection limit of 0.20 μmol·g^{-1}. Since the model predictions are very sensitive to the acid concentration, it was necessary to estimate acid concentrations for experiments where these were not detectable. In those cases, acid concentrations were arbitrarily assumed to be half of the detection limit.

These data lead to fits of the seven kinetic parameters to the experimental dataset and the results are shown in Table 1.2

While relatively good fits of predicted concentrations of BnOH, benzaldehyde and BnOOBn with time are evident in Figures 1.2a and 6a for first batch runs with and without K_2CO_3, relatively poor fits of benzaldehyde concentration are observed for second-time runs (Figures 1.2b and 1.6b) and the first run with KF (Figure 1.7a). The poorer fit of the second runs in the presence of K_2CO_3 is understandable since it was assumed in the model that all BnOOH was removed by the base in between the experiments, which is probably not completely justified, indicating that some acid or another inhibiting species remains on the catalyst. In all other experiments, approximate fits of concentrations of one or both products or of all three species (alcohol, aldehyde and ester) are observed (see Figures 1.3, 1.4, 1.7b,

Table 1.2: Optimal estimates of the kinetic parameters using all experimental data.

Parameter	**Unit**	**Estimate**	**95% confidence range**	
			Value	**Relative /%**
k_1	$/\mathrm{g \cdot mg_{cat}^{-1} \cdot s^{-1}}$	2.69×10^{-3}	$\pm 5.0 \times 10^{-4}$	± 19
k_2	$/\mathrm{g \cdot mg_{cat}^{-1} \cdot s^{-1}}$	2.37×10^{-4}	$\pm 5.9 \times 10^{-5}$	± 25
k_3	$/\mathrm{g^2 \cdot mmol^{-1} \cdot mg_{cat}^{-1} \cdot s^{-1}}$	6.6×10^{-4}	$\pm 3.5 \times 10^{-4}$	± 54
k_{AcBase}	$/\mathrm{s^{-1}}$	0.71	± 0.15	± 21
K_{BnOOH}	$/\mathrm{g \cdot mmol^{-1}}$	1.23×10^{4}	$\pm 1.5 \times 10^{3}$	± 12
$K^{ads}_{BnOH,\ Al_2O_3}$	$/\mathrm{g \cdot mmol^{-1}}$	18.1	fixed	
$K^{ads}_{BnOOH,\ Al_2O_3}$	$/\mathrm{g \cdot mmol^{-1}}$	2.47×10^{4}	fixed	
S_{K2CO3}	/-	1.39	± 0.81	± 58
$S_{KF/K2CO3}$	/-	1.37	± 0.39	± 29
SSR*	/-	0.414	-	-

(*) $SSR = \sum_{i=1}^{v} w_i \sum_{k=1}^{n} \left(C_{i,k,\exp} - C_{i,k,\mathrm{mod}}\right)^2$ (sum of the squared residuals) (w_i = weight factor for response i, v = number of responses, $C_{i,k,exp}$ = experimental response of component i in experiment k, $C_{i,k,mod}$ = model response of component i in experiment k, n = number of experiments (samples).

and 1.10–1.12). Thus, variations in how well the fit follows the data are a logical consequence of attempting to simulate in a single model a wide range of concentrations with and without base and in the absence and presence of strongly inhibiting aldehyde and acid product species. Moreover, the model did not include effects of water and was limited to the three most important reactions and four most important species. The 54% and 58% relative confidence intervals for k_3 and S_{K2CO3} originate from the strong correlation between these two parameters, which is discussed later in this section. The approximate nature of the model can be attributed to:

Table 1.3: Correlation matrix between all the parameters estimated using the optimized kinetic model.

Parameter	k_1	k_2	k_3	k_{AcBase}	K_{BnOOH}	S_{K2CO3}	$S_{KF/K2CO3}$
k_1	1						
k_2	0.52	1					
k_3	0.06	−0.13	1				
k_{AcBase}	0.12	−0.17	−0.02	1			
K_{BnOOH}	0.51	−0.30	0.09	0.64	1		
S_{K2CO3}	0.02	0.12	−0.97	0.06	−0.01	1	
$S_{KF/K2CO3}$	−0.01	−0.02	0.33	−0.05	−0.01	−0.45	1

(1) Assumptions that are only approximately valid, e.g., (a) arbitrary estimates of benzoic acid concentration, and (b) the assumption that benzoic acid is completely removed from the catalyst by interaction with insoluble K_2CO_3 or KF crystals.

(2) By practical necessity, the limited scope of the mechanistic scheme, e.g., (a) neglecting effects of adsorption or inhibition of some species such as coverages of BnOH of BnOOBn and (b) neglecting the positive effect of water.

Nevertheless, the model provides (1) accurate predictions of initial reaction rate for oxidation of BnOH to BnO on a gold/alumina catalyst and (2) approximate predictions of the effects of BnOOH inhibition and the neutralizing effect of potassium salts to alleviate this inhibition.

The value of the rate constant for the reaction of the BnOOH with the base to potassium benzoate, k_{AcBase}, represents the characteristic time for the transport of BnOOH from a catalytic site to the K_2CO_3 or KF crystals. The order of magnitude can be compared with an estimate of the characteristic time for diffusion [34] of BnOOH through the catalyst pores to the liquid bulk, obtained from a typical diffusion distance (one third of the catalyst particle size 50 μm, estimated from the sieve mesh size) and an effective diffusivity of 4.8×10^{-10} $m^2 \cdot s^{-1}$ (estimated using Wilke and Chang's relationship [35], using porosity-tortuosity ratio of 0.14, based on data of similar aluminas and catalysts):

$$\tau_{diff,\,BnOOH} = \frac{\left(\frac{1}{3} d_p\right)^2}{2 \times D_{eff,\,BnOOH}} \tag{37}$$

Where: $\tau_{diff,BnOOH}$ = diffusion time (s)
d_p = catalyst particle diameter (m)
$D_{eff,\,BnOOH}$ = effective diffusivity ($m^2 \cdot s^{-1}$)

This yields a typical diffusion time of 0.3 s, which is about 4.8 times smaller than the typical time $(k_{AcBase})^{-1} = 1.41$ s. The latter seems a plausible value in view of the additional transport resistance that might be caused by the transfer from the external catalyst surface towards the K_2CO_3 or KF crystals.

The correlation matrix for the estimated parameters, shown in Table 1.3, shows that the strongest correlation occurs between k_3 and S_{K2CO3} with a correlation coefficient of −0.97, which is in line with our conclusion that the ester formation in our system is base-catalyzed. All correlations between the parameters justify maintaining all parameters in the model since these do not exceed the value of 0.99, which is accepted as the limit for a proper parameter estimation [36].

4 – Conclusions

Our study shows that benzoic acid or compounds formed from benzoic acid cause catalyst inhibition in benzyl alcohol oxidation in toluene and in absence of a base. The introduction of a potassium salt as a base prevents this inhibition by neutralizing the benzoic acid formed. Basic conditions result in a decrease in selectivity to benzaldehyde and in an increase of ester production. The enhanced ester formation probably occurs via condensation of alkoxy species (formed by alcohol deprotonation by the base) with benzaldehyde under oxidative conditions, and is not the result of an increased benzoic acid production followed by esterification, as might be expected under acidic conditions. Water appears to have no influence on inhibition, but may enhance the effect of the base described above by improved dissolution. Although effects of water were not modeled, a kinetic effect for water cannot be excluded.

The concentration *versus* time data of the batch experiments in this study, which covered a wide range and included effects of acid inhibition and base, were fitted to a comprehensive kinetic model for (1) the primary reaction, oxidation of benzyl alcohol to benzaldehyde; (2) secondary oxidation of benzaldehyde to benzoic acid; and (3) secondary esterification of benzyl alcohol and benzaldehyde to benzyl benzoate. Effects of base (potassium salts) were also included in the model. The resulting model predicts concentration-time trends approximately well, including inhibition by benzoic acid and the neutralization of benzoic acid by potassium salts, forming potassium benzoate. A precise fit of the model to experimental data was observed in two first batch runs, with and without K_2CO_3. Variations in how well the fit follows the data are a logical consequence of attempting to simulate in a single model a wide range of concentrations with and without base and in the absence and presence of product species such as aldehyde and strongly inhibiting acid. Moreover, the model did not include effects of water and was limited to the three most important reactions and four most important species.

Nevertheless, the model provides (1) accurate predictions of initial reaction rate for oxidation of benzyl alcohol to benzaldehyde on a gold/alumina catalyst and (2) approximate predictions of the effects of benzoic acid inhibition and the neutralizing effect of a potassium base to alleviate this inhibition.

References

1. Davis, S.E.; Ide, M.S.; Davis, R.J. *Green Chem 15,* **2013**, 17–45.
2. Lilga, M.A.; Hallen, R.T.; Gray, M. *Topics Catal 53,* **2010**, 1264–1269.
3. Zope, B.N.; Davis, R.J. *Green Chem 13,* **2011**, 3484–3491.
4. Haruta, M.; Yamada, N.; Kobayashi, T.; Iijima, S. *J Catal 115,* **1989**, 301–309.
5. Alhumaimess, M.; Lin, Z.; Weng, W.; Dimitratos, N.; Dummer, N.F.; Taylor, S.H.; Bartley, J.K.; Kiely, C.J.; Hutchings, G.J. *ChemSusChem 5,* **2012**, 125–131.
6. Deplanche, K.; Mikheenko, I.P.; Bennett, J.A.; Merroun, M.; Mounzer, H.; Wood, J.; MacAskie, L.E. *Topics Catal 54,* **2011**, 1110–1114.
7. Guo, H.; Kemell, M.; Al-Hunaiti, A.; Rautiainen, S.; Leskelä, M.; Repo, T. *Catal Commun 12,* **2011**, 1260–1264.
8. Guo, H.; Al-Hunaiti, A.; Kemell, M.; Rautiainen, S.; Leskelä, M.; Repo, T. *ChemCatChem 3,* **2011**, 1872–1875.
9. Hao, Y.; Hao, G.P.; Guo, D.C.; Guo, C.Z.; Li, W.C.; Li, M.R.; Lu, A.H. *ChemCatChem 4,* **2012**, 1595–1602.
10. Heeskens, D.; Aghaei, P.; Kaluza, S.; Strunk, J.; Muhler, M. *Phys Status Solidi A 250,* **2013**, 1107–1118.
11. Mallat, T.; Baiker, A. *Chem Rev 104,* **2004**, 3037–3058.
12. Quintanilla, A.; Butselaar-Orthlieb, V.C.L.; Kwakernaak, C.; Sloof, W.G.; Kreutzer, M.T.; Kapteijn, F. *J Catal 271,* **2010**, 104–114.
13. Sá, J.; Taylor, S.F.R.; Daly, H.; Goguet, A.; Tiruvalam, R.; He, Q.; Kiely, C.J.; Hutchings, G.J.; Hardacre, C. *ACS Catal 2,* **2012**, 552–560.
14. Mallat, T.; Baiker, A. *Catal Today 19,* **1994**, 247–283.
15. Zope, B.N.; Hibbitts, D.D.; Neurock, M.; Davis, R.J. *Science 330,* **2010**, 74–78.
16. Moulijn, J.A.; van Diepen, A.E.; Kapteijn, F. *Appl Catal 212,* **2001**, 3–16.
17. Keresszegi, C.; Bürgi, T.; Mallat, T.; Baiker, A. *J Catal 211,* **2002**, 244–251.
18. Dimitratos, N.; Villa, A.; Wang, D.; Porta, F.; Su, D.; Prati, L. *J Catal 244,* **2006**, 113–121.
19. Rodríguez-Reyes, J.C.F.; Friend, C.M.; Madix, R.J. *Surf Sci 606,* **2012**, 1129–1134.
20. Fang, W.; Chen, J.; Zhang, Q.; Deng, W.; Wang, Y. *Chem A Eur J 17,* **2011**, 1247–1256.
21. Kimling, J.; Maier, M.; Okenve, B.; Kotaidis, V.; Ballot, H.; Plech, A. *J Phys Chem B 110,* **2006**,

15700–15707.

22. Juan-Alcañiz, J.; Ferrando-Soria, J.; Luz, I.; Serra-Crespo, P.; Skupien, E.; Santos, V.P.; Pardo, E.; Llabrés i Xamena, F.X.; Kapteijn, F.; Gascon, J. *J Catal 307,* **2013**, 295–304.
23. Fristrup, P.; Johansen, L.B.; Christensen, C.H. *Catal Lett 120,* **2008**, 184–190.
24. Abad, A.; Corma, A.; García, H. *Chem A Eur J 14,* **2008**, 212–222.
25. Pina, C.D.; Falletta, E.; Rossi, M. *Chem Soc Rev 41,* **2012**, 350–369.
26. Daté, M.; Okumura, M.; Tsubota, S.; Haruta, M. *Angew. Chem Int Ed 43,* **2004**, 2129–2132.
27. Daniells, S.T.; Overweg, A.R.; Makkee, M.; Moulijn, J.A. *J Catal 230,* **2005**, 52–65.
28. Yang, X.; Wang, X.; Liang, C.; Su, W.; Wang, C.; Feng, Z.; Li, C.; Qiu, J. *Catal Commun 9* **2008**, 2278–2281.
29. Chang, C.R.; Yang, X.F.; Long, B.; Li, J. *ACS Catal 3,* **2013**, 1693–1699.
30. Socrates, G. *John Wiley & Sons Ltd: Heidelberg, Germany*, **2004**; pp. 50–167.
31. Matulewicz, E.R.A.; Kerkhof, F.P.J.M.; Moulijn, J.A.; Reitsma, H.J. *J Colloid Interface Sci 77,* **1980**, 110–119.
32. Athena Visual Studio, Software for Modeling, Estimation and Optimization, Version 14.2. Available online: www.AthenaVisual.com 1997–2009 (accessed 25 September **2013**).
33. Stewart, W.E.; Caracotsios, M.; Sorensen, J.P. *AIChE J 38,* **1992**, 641–650.
34. Atkins, P.W. *W.H. Freeman: New York, NY, USA*, **1994**.
35. Perry, R.H.; Green, D.W. *McGraw-Hill: New York, NY, USA*, **1997**.
36. Stewart, W.E.; Caracotsios M. *John Wiley & Sons, Inc., Hoboken, NJ, USA*, **2008**.

Chapter 2

Synthesis of similar Au-nanoparticles on different supports: support catalytic effects in the oxidation of benzyl alcohol and carbon monoxide

The colloidal deposition method was successfully employed to prepare gold-based catalysts, in order to suppress the influence of the support during the preparation on the final gold particle size distribution. This approach resulted in rather similar Au particle size distributions on four different oxide supports (Al_2O_3, CeO_2, SiO_2, ZrO_2) as evidenced by TEM. The support surface area was taken into account for the colloidal deposition, resulting in identical average surface concentration of the Au nanoparticles. TPR experiments show strong differences in reducibility of the different oxide supports, CeO_2 being the most reducible, followed by ZrO_2, whereas Al_2O_3 and SiO_2 didn’t show any reducibility. NH_3-TPD shows that support acidity increases in the order: $SiO_2 < Al_2O_3 < ZrO_2 < CeO_2$. The catalytic performance was evaluated for the liquid phase oxidation of benzyl alcohol and the gas phase oxidation of carbon monoxide. The presence of remaining capping ligands led to significant leaching of the gold nanoparticles from the SiO_2 support during benzyl alcohol oxidation, and a hysteresis in the first light-off cycle during carbon monoxide oxidation over the ceria and zirconia based catalysts. Although both are oxidation reactions, the catalysts' performances for these reactions rank in opposite order. Low support acidity leads to a high performance for benzyl alcohol oxidation, whereas high support acidity is favourable for carbon monoxide oxidation. Likewise, low support reducibility yields a good performance in benzyl alcohol oxidation, whereas the opposite holds for carbon monoxide oxidation. Even though it is acknowledged that the catalytic performance reflects an overall combination of active phase and support-related (and unrelated) effects, the observed behaviours are mainly attributed to the different mechanisms of the studied reactions.

1 – Introduction

The catalyst support is well known to affect the catalytic properties of heterogeneous catalysts. This can occur indirectly, when a reactant first adsorbs on the support and surface-diffuses to the metal nanoparticles or other active centers. In this case, the reactant-support affinity is a key parameter to tune the catalytic properties. It can also happen directly, when the support actively takes part in the reaction mechanism (bifunctionality) and supplies reaction intermediates to the active phase via spill-over. In this case, the support shows catalytic properties as much as e.g. the metal nanoparticles, and both determine the overall catalytic performance. For instance, when the support supplies intermediates to the metal nanoparticles, which then are selectively transformed into the end product, the rate of the support process(es) should not be limiting in order for the catalyst to show its best performance. The opposite is true when, alternatively, a product is formed on the support from intermediates supplied from the metal nanoparticles, such as occurs in hydroisomerization [1]. Support properties often pointed out in literature are reducibility, oxygen availability (in case of oxide supports) and acidity/basicity [2-4]. These are pure chemical properties that operate directly on the reagents during the catalytic reaction in a co-catalyst fashion. However, other support properties such as metal nanoparticle-support interaction can affect the overall catalytic properties indirectly. This interaction governs how strongly bound the nanoparticles are, which in turn influences their oxidation state and their morphology [2]. Additionally, this interaction controls the perimeter length between the nanoparticles and the support, of which the role as active site has been recognized in many studies [2, 3]. Thus, the support exerts an influence on the nanoparticles that translates to an influence on the catalytic properties. With this taken into account, it becomes evident that isolating one support property to unravel its catalytic effect is not straightforward if at all possible.

Heterogeneous catalysts are usually synthesized by the well-established methods of impregnation, ion exchange, homogeneous deposition precipitation or co-precipitation. Although the simplicity of these routes allows for large-scale production of catalysts at relatively low costs, the support-metal salt and/or support-metal affinities play an important role in determining the morphology of the final catalyst, in particular the metal nanoparticle size distribution. Studying the support effects using these catalyst synthesis methods implies that the observed effects are a combination of real catalytic properties (as discussed in the previous paragraph) plus the influence of the support during the synthesis on the final morphology of the catalyst.

In the present study, catalysts were prepared via a colloidal route, in order to suppress the influence of support-metal precursor interactions on the morphology and performance of the final catalysts. Colloidal gold nanoparticles, prepared separately, were immobilized on zirconia, silica, alumina and ceria and the catalytic properties of the resulting catalysts were assessed for benzyl alcohol aerobic oxidation and carbon monoxide oxidation. Schüth *et al.* already applied this concept in detail for CO-oxidation with gold-based catalysts on various supports in several studies and presented their results in an extensive review [2, 5]. Using a polyvinyl alcohol (PVA)-based colloidal synthesis, followed by deposition on various supports and heat treatment (typically at 300 °C) to remove the residual capping ligands, the resulting catalysts show identical particle size distributions on practically all the supports. However, in some cases, upon removal of the ligand, thereby allowing the nanoparticle-support interface to seek equilibrium, particle shape/morphology presented differences. Therefore, although all precautions were taken to obtain exactly the same gold nanoparticles on different supports, it was unavoidable that these nanoparticles ultimately adapted to each support, once the final step of cleaning off the ligands was performed. Nevertheless, the colloidal route for catalyst synthesis seems to be the best way to obtain catalyst nanoparticles as identical as possible on different supports, in order to study the catalytic effects of the latter. In CO oxidation the temperature at 50% conversion under the applied conditions, $T_{X=50\%}$ spanned 200 °C for the various supports studied. The factors that most likely explain the differences in activity are identified to be the nanoparticle morphology (number of facets and defect concentration), different amounts of available support oxygen, and the presence of active molecular oxygen on the support. It remains unclear, however, how these factors exert their influence, and "a unique explanation for the extraordinary catalytic activity of gold-based catalysts appears improbable" [2]. As suggested by a theoretical study by Nørskov [6], it is rather a combination of factors that contributes to enhancing the catalytic properties of gold nanoparticles and that this combination of factors varies from one catalytic system to another.

In this chapter, this approach is applied to another catalytic reaction: the aerobic selective oxidation of benzyl alcohol, and compared with the CO oxidation. These two reaction systems vary considerably in terms of reaction conditions: solvent phase vs. gas phase, low temperature (80 °C) vs. high temperature (typically from 100 to 600 °C) and also in terms of reaction: selective oxidation of a primary alcohol to its corresponding aldehyde vs. total oxidation of CO to CO_2.

Figure 2.1: Reaction scheme of dodecylaminomethanol formation from dodecylamine and formaldehyde.

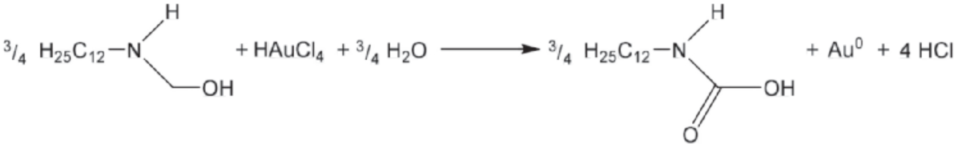

Figure 2.2: Reaction scheme of chloroauric acid reduction by dodecylaminomethanol, forming metallic gold and dodecylcarbamic acid.

Figure 2.3: Dodecylcarbamic acid decomposition into dodecylamine and carbon dioxide. Dodecylamine interacts with gold nanoparticle surfaces and stabilizes them.

2 – Experimental

2 – 1 – Catalyst synthesis

Au nanoparticles were synthesized following the colloidal route developed by Chen *et al.* [7] and later used by Quintanilla *et al.* [8]. 0.75 g of dodecylamine (99.5%, Sigma Aldrich) was dissolved in 25 mL of cyclohexane (anhydrous, 99.5%, Sigma Aldrich). 6 mL of formaldehyde solution (37 wt.% in H_2O, 10-15% methanol as stabilizer, Sigma Aldrich) was then added in order to form the reductive intermediate dodecylaminomethanol, as described in Figure 2.1. This reaction was allowed to proceed for 30 min at room temperature. The mixture was allowed to phase separate in a decantation funnel and the cyclohexane phase (top) containing the reductive intermediate was recovered. 10 mL of an aqueous solution of 4 $g \cdot L^{-1}$ of $HAuCl_4$ (99.999%, Sigma Aldrich) was then added to the dodecylaminomethanol solution under vigorous stirring at room temperature. The aminomethanol forms a carbamic acid upon its oxidation by chloroauric ions (Figure 2.2), thereby reducing the latter to metallic gold and leading to nucleation of nanoparticles. The carbamic acid is unstable and decomposes back to dodecylamine, thereby releasing CO_2, as described in Figure 2.3.

These simultaneous reactions were allowed to proceed for 1 h at room temperature, under vigorous stirring. The gold nanoparticle growth is regulated by the supply of gold from the water phase to the cyclohexane phase and by the adsorption of dodecylamine on the surface of the nanoparticles (capping effect). The color of the mixture after addition of the gold precursor changed gradually from white to brown and finally turned deep red. The resulting gold nanoparticles were dispersed in the cyclohexane phase in a colloidal fashion, dodecylamine being the capping agent and the dispersant. Aqueous and organic phases were again separated using a decantation funnel, and the cyclohexane colloidal solution was recovered. A purification step was carried out, where the cyclohexane was first evaporated using a rotary evaporator, followed by the introduction of 50 mL acetone to dissolve the excess dodecylamine as well as any synthesis residues. This mixture was centrifuged at 10000 rpm (Hermle Z323) for 5 min, and the clear acetone was disposed of. The addition of 50 mL cyclohexane to the nanoparticle sediment provoked its re-dispersion to a colloidal suspension.

ZrO_2 was supplied by Alfa Aesar (CAS 43814, monoclinic), SiO_2 was supplied by Fuji Silysia Chemicals and γ-Al_2O_3 (99.98%) was supplied by Akzo Chemicals. CeO_2 was synthesized by calcination of $Ce(NO_3)_3$;$6H_2O$ (99%, Sigma Aldrich) in stagnant air. The temperature was increased by $2°C \cdot min^{-1}$ to 500°C and was maintained for 6 h. These catalyst supports were ground and sieved to a particle size below 71 μm. Preliminary experiments on an AUROlite™ benchmark catalyst with varying catalyst particle size determined this particle size to be small enough to avoid internal mass transport limitations during the catalytic experiments (see Figure 2.9). A calcination step at 500°C in static air for 6 h followed for Al_2O_3, SiO_2 and ZrO_2 to ensure a clean surface. The powders, including CeO_2, were stored in an evacuated desiccator containing a bed of P_2O_5 (desiccant grade, Sigma Aldrich).

The various metal oxide supports were added to colloidal, 5 nm gold nanoparticles, which resulted in their immobilization on the surface. The amount of support introduced into the colloidal solution was adjusted to obtain a similar amount of nanoparticles per unit of support surface area, to eliminate this variable. The target gold content was 25 $\mu g_{Au} \cdot m^{-2}{}_{support}$ ($7.6 \cdot 10^{16}$ Au atoms per m^2 of catalyst support). Table 2.1 summarizes the quantities involved in the synthesis of the catalysts.

2 – 2 – Catalyst characterization

Temperature-programmed reduction experiments were performed on a packed bed of catalyst placed between two SiC beds of 100 mg each, in a reactor of 6 mm inner diameter. 30 $mL \cdot min^{-1}$ of 10 vol% H_2 in Ar were passed through the catalyst bed as the

Table 2.1: Quantities involved in Au catalyst syntheses, target Au content and Au content revealed by ICP.

Support	$m_{support}$ (g)	S_{BET} support ($m^2 \cdot g^{-1}$)	colloidal Au concentration ($g \cdot L^{-1}$)	$V_{colloidal\ solution}$ (mL)	Au content ($\mu g_{Au}/m^2_{support}$)	Target Au content (wt.%)	Au content by ICP (wt.%)
Al_2O_3	1.56	252	0.50	17.0	21.6	0.54	0.40
CeO_2	3.52	106	0.50	18.7	25.1	0.27	0.25
SiO_2	1.36	276	0.49	19.0	25.0	0.69	0.12
ZrO_2	3.73	100	0.51	18.3	25.2	0.25	0.24

temperature was increased from room temperature to 550°C at a rate of $10°C \cdot min^{-1}$. The H_2 consumption in the effluent gas was monitored using a TCD detector, calibrated based on Copper (II) oxide. The TCD signal was corrected for the sample quantity and surface area (mass × surface area) for a fair comparison.

Temperature programmed desorption of ammonia (NH_3-TPD) was performed using a Micromeritics Autochem II 2920 to determine the acidity of the catalyst supports. The quantity of sample was adjusted to keep the total sample surface equal to 50 m^2. The samples were first degassed in a flow of 25 $mL \cdot min^{-1}$ He at 550°C for 1 h. Subsequently, ammonia was allowed to adsorb on the sample bed at 80°C or 200°C for 1 h, under 25 $mL \cdot min^{-1}$ of 10% NH_3 in He. The temperature was then ramped from room temperature to 550°C at $10°C \cdot min^{-1}$ under 25 $mL \cdot min^{-1}$ helium, and the ammonia concentration in the effluent gas was monitored by a TCD detector.

The BET area of the different catalyst supports was determined using a Quantachrome Autosorb-6B. The samples were first pre-treated at 200°C in vacuum ($P < 0.1$ mbar) for 17 h. N_2 adsorption was done at -196°C and the relative pressure was varied from 0.01 to 0.99. The multipoint BET method was used to calculate the specific surface area including 21 points and using a value of 0.162 nm^2 for the molecular area of adsorbed N_2 [9]. The BET areas of the studied catalyst supports are reported in Table 2.1.

X-ray photoelectron spectra (XPS) of all fresh and used catalysts were recorded on an Al K-alpha spectrometer (Thermo Scientific, Al $K\alpha = 1486.6$ eV). The binding energy scale of the spectra was calibrated based on the sp^3 carbon 1*s* signal at 284.8 eV. The background signal due to inelastic processes was corrected using the "Smart" method (Thermo Scientific, Avantage software). A fixed Lorentzian:Gaussian shape function of 0.3 was used to deconvolute the overlapping peaks of the Au 4*f* signal.

Transmission electron microscopy (TEM) was performed using either an FEI Tecnai TF20 with a field emission gun as the source of electrons operated at 200 kV (Al_2O_3 and SiO_2), or a JEOL JEM1400S (CeO_2 and ZrO_2) with an LaB6 filament as the source of electrons operated at 120 kV. Samples were mounted on Quantifoil® microgrid carbon polymer supported on a copper grid by placing a few droplets of a suspension of ground sample in ethanol on the grid, followed by drying at ambient conditions.

2 – 3 – Catalytic experiments

The catalytic activity for benzyl alcohol aerobic oxidation was investigated in a stirred-tank reactor in a semi-batch arrangement. The reactor consisted of a round bottom vessel of 60 mm inner diameter equipped with baffles and was mechanically stirred at 1200 rpm. In a typical experiment, a quantity of catalyst equivalent to 5 mg gold was introduced in the reactor together with 3 g potassium carbonate and 80 mL toluene. The reactor was continuously purged with 200 mL·min^{-1} air and heated to 80°C using an oil bath. After a steady temperature was reached, 2.4 g (22 mmol) benzyl alcohol was injected into the stirred slurry and the reaction started. The reaction mixture liquid was regularly sampled with a syringe to follow its composition over time. Liquid samples were analysed using a Varian CP-3380 gas chromatograph equipped with a FID. Helium was used as carrier gas through a CP-SIL 8 CB column (Chrompack) of 50 m in length, 0.25 mm diameter and 0.25 μm coating thickness. The initial temperature of the GC oven was 150 °C and was maintained for 4 min, then increased with 100 °C·min^{-1} to 220 °C and then maintained at 220 °C for 6.3 min. In the assessment of catalytic activity, the *TOF* values were calculated according to:

$$TOF = \frac{M_{\text{Au}} \times n_{\text{BnOH},t=0}}{m_{\text{cat}} \times Au_{\text{content (ICP)}}} \times \frac{dX}{dt} \tag{1}$$

Where M_{Au} is the molar mass of gold (196.97 g·mol^{-1}), $n_{\text{BnOH,t=0}}$ (mol) is the amount of benzyl alcohol introduced in the reactor at t = 0 min, m_{cat} (g) is the mass of catalyst present in the reactor, $Au_{\text{content(ICP)}}$ (wt.%) is the content of gold in the catalyst and $\frac{dX}{dt}$ (%·min^{-1}) is the conversion rate of the benzyl alcohol.

The catalytic activity for carbon monoxide oxidation was investigated in a continuous flow packed-bed reactor. The reactor consisted of a quartz tube of 4 mm inner diameter equipped with a quartz frit. The catalyst quantity was adjusted to keep the gold content constant at 0.15 mg throughout the series of experiments and was physically mixed with 100 mg of SiC. The catalyst bed was placed between two SiC packed beds of 50 mg each. 35 $mL \cdot min^{-1}$ of 1% CO and 0.5% O_2 in He was fed to the reactor at 2 bar while the temperature was increased step-wise from room temperature to the temperature where the catalyst showed 100% conversion. The outlet stream was analysed by a Chrompack CP 9001 gas chromatograph equipped with a TCD. Helium was used as carrier gas through a dual column system consisting of a Parabond Q column (Chrompack, 25 m length, 0.53 mm diameter and 10 μm coating thickness) and a Molsieve 5A column (Chrompack, 10 m length, 0.53 mm diameter and 50 μm coating thickness). Conversion data were recorded at a particular temperature value once steady state was reached. In most cases, steady state is achieved within 46 minutes, which correspond to 2 GC runs of 23 min (see Figure 2.12).

3 – Results and discussion

3 – 1 – TPR

Figure 2.4 shows the results of the TPR experiments on the bare catalyst supports. Al_2O_3 and SiO_2 are not reducible, although a slight H_2 consumption appears in case of the Al_2O_3 at around 720 K. In their detailed TPR study of CoO/Al_2O_3, Arnoldy and Moulijn [10] detected a small H_2 consumption at 1120 K in the Al_2O_3 TPR, which they attributed to the reduction of adsorbed trace impurities. In view of the very small intensity of H_2 consumption in Figure 2.4, it is reasonable to also attribute this to trace impurities. Literature data on TPR of SiO_2 are scarcer, but most studies agree on the non-reducible character of SiO_2 [11]. The case of ZrO_2 is less conclusive in the present results, where the TCD signal oscillates strongly throughout the studied temperature range. Wang *et al.* [12] studied the reducibility of pure ZrO_2 and of an Au/ZrO_2 catalyst by a similar TPR method. Pure ZrO_2 did not show any detectable reduction signal between 520 and 1270 K. Only when nanoparticulate Au was present on the surface of ZrO_2 did two reduction peaks appear at around 770 and 1150 K. It is generally concluded that ZrO_2 under the conditions of our TPR experiments is non-reducible [13, 14]. Kouva *et al.* [15] reviewed extensively the surface reactivity of monoclinic ZrO_2. They reported that even at 1173 K and 900 Torr H_2, the ZrO_2 surface was non-reducible. Activation treatments above 873 K generate some Zr^{3+} and Zr^{4+} sites, that can subsequently react with H_2 heterolytically to form Zr^{4+} and Zr-H, respectively. In comparison, our thermal treatment was conducted at only 773 K, excluding the formation of such oxygen vacancies. The authors also

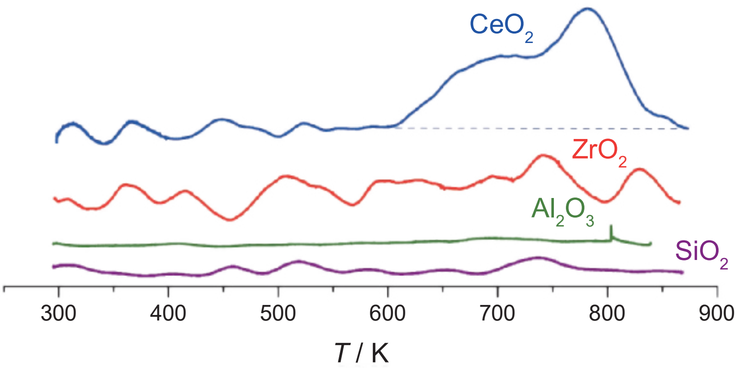

Figure 2.4: Temperature programmed reduction profiles of — Al_2O_3, — CeO_2, — SiO_2 and — ZrO_2. 30 mL·min^{-1} of 10 vol% H_2 in Ar flows through the reactor heated at 10 K·min^{-1}.

emphasized that the 820 – 880 kJ/mol theoretically necessary to form surface oxygen vacancies on ZrO_2, is much higher than the 530 – 580 kJ/mol necessary for TiO_2, a reducible oxide. Therefore bare ZrO_2 is also considered non-reducible in this study. We attribute the oscillating signal in Figure 2.4 to the noise related to the amplified detector signal of our equipment.

In contrast, CeO_2 clearly shows reducibility above 620 K. Trovarelli reviewed the behaviour of ceria in H_2 [16], and in particular TPR experiments reported in various publications. In most cases, two H_2 consumption peaks are observed around 770 K and 1100 K (10 K·min^{-1} heating rate) where the peak area shows a strong correlation with the surface area of the material. Quantification of the total amount of reacted hydrogen corresponds to the bulk reduction of CeO_2 to Ce_2O_3. This quantification supports Trovarelli's interpretation that the peak at 770 K corresponds to the removal of 25% of the surface oxygen as the reduction from Ce IV in CeO_2 to Ce III in Ce_2O_3 takes place. According to Trovarelli [16], the 1100 K peak corresponds to the removal of 25% of the bulk oxygen according to the same reaction. The bulk oxygen has to diffuse to the surface before it can be eliminated, explaining a shift to higher temperature. This interpretation was recently supported by Hakeem *et al.* [17] in their TPR experiment of nanoparticulate CeO_2 supported on ZrO_2. This sample showed only one reduction peak at 753 K, with a peak area corresponding to the reduction of CeO_2 to Ce_2O_3. Thus, although the reduction of Cerium IV oxide to Cerium III oxide can take place around 750 – 770 K, the reduction of the bulk oxide is hampered by restricted diffusion through the crystal lattice, and can only take place quantitatively when the temperature is sufficiently high (~1100 K). From their temporal analyses of products (TAP) on $DeNO_x$ catalysis, Wang *et al.* [18] also agreed that the surface of ceria is more prone to reduction than the bulk. More evidence of such a mechanism is available in a study by Beckers and Rothenberg [19] where the surface area of ceria was monitored (*ex-situ*) after heat treatments under different atmospheres (H_2, CO, H_2O, CO_2 and vacuum). In particular, the decreasing surface area indicated a complete collapse of the structure at temperatures above 920 K in H_2 or 1120 K in vacuum, due to a major rearrangement of the solid. Therefore, we conclude that the H_2 consumption peak observed for CeO_2 in Figure 2.4 corresponds to the removal of the surface oxygen, resulting in the reduction of Ce IV oxide to Ce III oxide at the surface.

In a quantitative analysis of TPR data, many phenomena should be taken into consideration. In particular, the TPR signal could be flawed by the reduction of impurities and the desorption of carbonates. The model developed by Johnson and Mooi [20] is simple: it does not take into account different CeO_2 crystallographic planes, a constant O-ion radius of 0.14 nm is assumed, and cell expansion with temperature is ignored. Perrichon *et al.* [21] completed the study of Johnson and Mooi, using magnetic susceptibility measurements to accurately quantify the extent of reduction of CeO_2 to Ce_2O_3 (the Ce^{3+} ion being paramagnetic). They found great discrepancies between TPR data and Johnson and Mooi's model, but a better agreement was found between the model and the magnetic susceptibility measurements. Apparently, TPR does not give a quantitative picture. The accuracy of quantitative TPR measurements is hampered by the above mentioned artefacts, particularly the elimination of bulk carbonate impurities which greatly distort the reduction peak of surface CeO_2, and furthermore the major solid rearrangement leading to considerable loss of surface area in H_2 above 920 K. Therefore, although the hydrogen consumption during the reduction of surface CeO_2 in TPR experiments correlates well with the BET area, it is bound to show discrepancies from theoretical modelling due to the nature of the measurement itself. Following the model by Johnson and Mooi [20], the number of terminating oxide ions on the surface is calculated according to:

$$O_c = 6n^2 - 12n + 8 \tag{2}$$

Where O_c is the number of terminating oxygen ions (-) on cubic ceria crystallites and n is the number of oxygen ions on the side of such a cubic crystallite (-). n is calculated according to:

$$n = \frac{a}{2r_O} \tag{3}$$

Where a is the crystallite size (Å), and r_O is the radius of the oxygen ion (1.40 Å), Finally, a is obtained from the following relation:

$$a = \frac{60000}{A \times d} \qquad (4)$$

Table 2.2: Evaluation of H_2 consumption in TPR of CeO_2 compared with the theoretical prediction from Mooi's model [20] and with the empirical relation from Perrichon [21].

	Absolute value	Fraction of theoretical value
S_{BET} CeO_2 ($m^2 \cdot g^{-1}$)	106	N/A
Corresponding amount of surface oxide (Mooi's model) ($mmol_{Os} \cdot m^{-2}$)	$1.98 \cdot 10^{-2}$	N/A
Theoretical H_2 consumption (Mooi's model) ($mmol \cdot m^{-2}$)	$4.96 \cdot 10^{-3}$	100%
H_2 consumption based on Perrichon's empirical regression ($mmol \cdot m^{-2}$)	$3.1 \cdot 10^{-2}$	57%
TPR derived H_2 consumption ($mmol \cdot m^{-2}$)	$6.58 \cdot 10^{-4}$	13%

Where A is the surface area of CeO_2 ($m^2 \cdot g^{-1}$) assuming cubic particles, d is the density of bulk CeO_2 (7.13 $g \cdot cm^{-3}$) and 60000 includes the number of faces of a cube and conversion factors for the length dimension homogeneity (Å), given the units of A and d. In our CeO_2 sample with a surface area of 106 $m^2 \cdot g^{-1}$, the numerical application of equation (3) yields a crystallite size a of 79.4 Å (TEM image analysis gives 88.0 Å), of which the number of oxygen ions along the side of a cubic CeO_2 particle n is 28 (equation (2)) and the number of oxygen ions terminating the surface of such a particle O_c is 4491 ions (equation (1)). The area of the surface of such a particle is $6 \times \left(a \times 10^{-10}\right)^2$ (m^2), which corresponds to $3.78 \cdot 10^{-16}$ m^2. So the amount of capping oxide ions per unit surface area is $1.98 \cdot 10^{-2}$ $mmol_{Oc} \cdot m^{-2}$. This number corresponds to 12 ions per nm^2, a physically realistic number.

Table 2.2 summarizes the theoretical H_2 consumption as predicted by Mooi [20], the empirical value as derived from Perrichon's regression of H_2 consumption vs. S_{BET} and our experimental value. Upon reduction of the surface CeO_2 to Ce_2O_3, the stoichiometry of the reaction predicts a removal of 1/4 of the surface oxide ions, which is $4.96 \cdot 10^{-3}$ $mmol_{Oc} \cdot m^{-2}$, and which should yield a H_2 consumption of $4.96 \cdot 10^{-3}$ $mmol \cdot m^{-2}$. The integration of the H_2 consumption peak in Figure 2.4 yields a value of $6.58 \cdot 10^{-4}$ $mmol \cdot m^{-2}$, which is 13% of the theoretical value. So the observation by Perrichon *et al.* [21] that the TPR H_2 consumption underestimates the amount of terminating oxide as predicted for cubic CeO_2 particles is also evidenced here. For comparison, the empirical regression of their experimental data (H_2 consumption as a function of S_{BET})

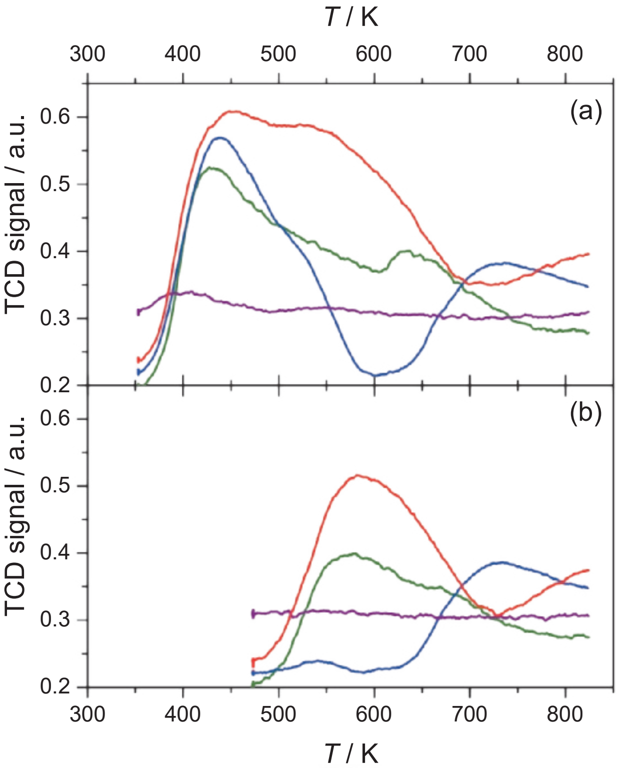

Figure 2.5: Ammonia temperature programmed desorption of — Al_2O_3, — CeO_2, — SiO_2 and — ZrO_2, (a) NH_3 adsorbed at 353 K and (b) at 473 K. Temperature ramp is 10 K·min^{-1}.

led to a H_2 consumption corresponding to 57% ($3.1 \cdot 10^{-3}$ mmol·m^{-2}) of that predicted by Johnson and Mooi's model ($54 \cdot 10^{-4}$ mmol·m^{-2}) (Table 2.2). It remains unclear why a lower value was obtained (13%) in the present data. The reason could be a higher amount of oxygen vacancies resulting from our synthesis, prior to the TPR. The theoretical consideration of exclusively cubic particles showing (111) facets could also explain a discrepancy from the model's side.

3 – 2 – NH_3 TPD

The results of the ammonia temperature programmed desorption experiments are plotted in Figure 2.5. In view of the many shoulders observed on the NH_3 desorption peaks in the case of Al_2O_3, CeO_2 and ZrO_2 when NH_3 was adsorbed at 353 K (Figure 2.5 (a)), it was decided to repeat the experiments while adsorbing NH_3 at 473 K to simplify the interpretation (Figure 2.5 (b)). Katada and Niwa [22] reviewed NH_3-TPD of zeolitic and non-zeolitic materials, and demonstrated that low temperature desorption

(400 – 500 K) originates from ammonia either adsorbed on non-acidic sites (e.g. ion exchange sites) or physisorbed. In the present results, when NH_3 is adsorbed at 473 K instead of 353 K, the desorption peaks below 500 K are not present. The weakly adsorbed NH_3 desorbing below 500 K can therefore be attributed to non-acidic sites or physisorption and can be ignored when acidic character is of interest.

In Figure 2.5 (a), Al_2O_3 shows a clear desorption peak at 430 K with a large tail and a second one at 635 K. When NH_3 was adsorbed at 473 K (Figure 2.5 (b)), a desorption peak at 575 K is revealed with a shoulder at around 650 K corresponding to the peak at 635 K of Figure 2.5 (a). Similar NH_3-TPD profiles are reported in literature [23-25]. Abello *et al.* [23] modelled experimental NH_3-TPD data with Monte Carlo simulations, thereby correlating desorption temperatures with interaction energies of ammonia and a commercial γ-Al_2O_3. Their data show a desorption peak at 395 K (when the alumina acid sites are fully saturated with ammonia), with a large tail until 900 K. These results are very similar to our findings, except that the shoulder we observe at 635 – 650 K is absent in their data. Dosing the amount of adsorbed ammonia and performing the desorption revealed the acid site strength distribution, divided into six types of acid sites. They conclude that ammonia desorbing at temperatures below 500 K (desorption energy 25 kcal·mol^{-1}) corresponds to 2 types of sites where ammonia is physisorbed and weakly chemisorbed, whereas desorption above 500 K is assigned to 4 types of sites with strong modes of ammonia interaction. Their findings are in good agreement with those by Joly *et al.* [24], who measured similar NH_3 desorption profiles. The peak temperature at maximum NH_3 coverage was 380 K and a large tail up to 800 K was also observed. Lower amounts of adsorbed ammonia revealed stronger acid sites releasing NH_3 at 635 to 708 K, corresponding to the shoulders we observe at 635 – 650 K. They conclude that ammonia adsorbs on alumina in 5 different modes, corresponding to 5 types of acid sites. The weaker sites release NH_3 at 380 K whereas the stronger ones, ascribed to Lewis sites (Al^{3+}) and acid-base pairs (Al^{3+}-O^{2-}), allow desorption only above 400 K. Thus, we can conclude that the peak we observe at 430 K in Figure 2.5 (a) corresponds to weakly adsorbed NH_3 on sites of very low acidity, where the desorption energy is similar to that of physisorbed ammonia. The peaks at 575 K and 635 – 650 K in Figure 2.5 (b) are assigned to strong acid sites, where ammonia truly chemisorbs. In view of the modelling results shown by Abello *et al.* [23] and Joly *et al.* [24], it is clear that many different types of acid sites contribute to each of these peaks.

CeO_2 releases a NH_3 peak at 440 K with a shoulder at 525 K in Figure 2.5 (a). When NH_3 is adsorbed at 473 K (Figure 2.5 (b)), the first peak disappears to leave a much smaller peak at 540 K, probably corresponding to the shoulder at 525 K in Figure 2.5 (a). A strong desorption peak appears at 740 K which is of the same intensity whatever the adsorption temperature of NH_3, resulting from high desorption energy and therefore corresponding to strong acidity. Most studies report desorption peaks around 420 K and 520 K, in agreement with our results [4, 26-29]. In these reports, NH_3 desorption can also be seen around 650 K, but only in very small amounts, except Miao *et al.* [27] who observed a more significant peak at 650 K which could correspond to our observation at 740 K. This illustrates again the strong impact that the source of the CeO_2 (and other solids) has on its surface properties.

In the case of SiO_2, only a very small amount of NH_3 adsorbs on the surface compared with the other 3 samples. Figure 2.5 (a) shows a low intensity peak at 400 K and a very small one around 550 K. Furthermore, no NH_3 seems to adsorb at 473 K, leaving a flat signal during TPD. In their NH_3-TPD study, Dias *et al.* [30] analysed silicas from two different manufacturers. The two samples showed significantly different TPD profiles: two NH_3 desorption peaks were observed at 360 and 715 K for the first sample, whereas only one peak at 375 K was observed for the second one. The adsorption temperatures used in the present study are too high to observe these lower-temperature peaks, which correspond to very weak acidity or even non-acidic sites (physisorption). Verhaak *et al.* [31] observed a NH_3 desorption peak at 350 K and two very low intensity peaks at 450 K and 600 K. In contrast, Wu *et al.* [25] did not detect any desorbing ammonia in their TPD study. The large differences in NH_3-TPD profiles across different reports stem from a strong dependency of SiO_2 acid properties on morphology and preparation method. Therefore, we conclude that no acid sites are present on the surface of our SiO_2 and that the profile shown in Figure 2.5 (a) corresponds to physisorbed ammonia, which does not exist after adsorption at 473 K as shown in Figure 2.5 (b).

In contrast, ZrO_2 shows intense NH_3 desorption peaks. In Figure 2.5 (a), two convoluted peaks at 450 K and 530 K are observed. When NH_3 is adsorbed at 473 K (Figure 2.5 (b)), the first peak disappears leaving only one at 590 K, smaller than the one at 530 K in Figure 2.5 (a). In both Figure 2.5 (a) and (b) the signal rises above 700 K with the same intensity. Using a water vapour treatment method, Katada and Niwa [22] showed that the peak at 450 K corresponds to ion-exchange sites rather than acidic sites: when water vapour was introduced after ammonia adsorption, ammonia on this type of sites was replaced by water (although water is less basic than ammonia). Since the polarity of an O-H bond is stronger than that of an N-H bond, Katada and Niwa conclude that polarity governs the interaction with these sites, not acidity. As their water vapour treatment eliminated this peak at 450 K, a smaller NH_3 desorption peak at 575 K was

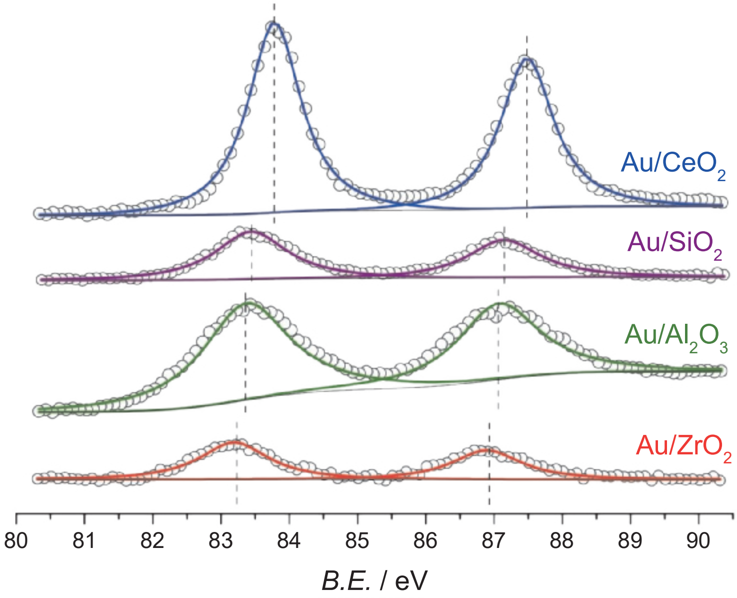

Figure 2.6: XPS spectra of Au 4*f* for — Au/Al$_2$O$_3$, — Au/CeO$_2$, — Au/SiO$_2$ and — Au/ZrO$_2$.

revealed, which was attributed to acid sites. We conclude that adsorbing NH_3 at 473 K has the same effect as the water vapour treatment, and that the NH_3 desorption peak we observe at 590 K in Figure 2.5 (b) corresponds to acid sites on ZrO_2. However, it is unclear whether the signal rising above 700 K is due to NH_3 desorption, or a chemical conversion e.g. decomposition of nitrides that could form at lower temperature.

3 – 3 – XPS

The XPS spectra of the studied catalysts are plotted in Figure 2.6 and the measured Au 4*f* binding energies are reported in Table 2.3. The usual reference binding energy for Au 4*f* 7/2 photoelectrons is 84.00 eV [8, 32-34], although numerous measurements of lower values for elemental gold have been reported, even for bulk (i.e. non-nanoparticulate) gold [8, 32, 33, 35]. In the present study, for all four systems the observed binding energy is lower than the reference value. The negative shift is largest (-0.7 eV) for Au/ZrO_2 and lowest (-0.2 eV) for Au/CeO_2. The reasons for positive or negative shifts in XPS spectra are a subject of debate [33, 34]. Besides the presence of charges or dipoles, a number of effects related to sample morphology also plays an important role, in particular for nanomaterials. The Au particle size has a strong influence on the observed binding energy, and when it is around 5 nm or smaller, initial and final state effects start to play a significant role. Initial state effects provoke a

Table 2.3: XPS peak binding energies of Au 4*f* 7/2 and Au 4*f* 5/2 of the catalysts.

catalyst	Au 4*f* 7/2 B.E. (eV)	Au 4*f* 5/2 B.E. (eV)
Au/Al_2O_3	83.36	87.06
Au/CeO_2	83.78	87.48
Au/SiO_2	83.45	87.15
Au/ZrO_2	83.29	86.99

decrease in *BE* as particle size decreases, because of the higher fraction of surface Au atoms. Since the coordination of these surface atoms is relatively low, their surface valence band is narrower, making the Au 5*d* electrons more localized. In turn, these localized valence electrons better screen the hole created by the photo- electric effect, which eases the escape of the Au 4*f* photoelectron, translating into a lower *BE* for the latter [33]. Final state effects yield an increase in *BE* as particle size decreases, because the hole created by the photo-electric effect is less screened as the number of neighbouring atoms decreases. Thus, the escaping photoelectron will experience a higher *BE* [33]. Initial state effects arise from the surface atoms, whereas final state effects arise from atoms below the surface, but both effects become stronger as particle size decreases. The binding energies observed here are likely a convolution of both initial and final state effects [34]. Other interpretations involve the creation of dipoles due to Au nanoparticle-support interaction [8] or Au nanoparticle surface-adsorbate interaction [36]. Nanoparticle-support interaction usually yields cationic Au species [8] which are thought to be the active sites of Au catalysts. On the other hand, Alloway *et al.* [36] studied the effect of thiolated organic monolayers on Au substrates by UV photoemission and demonstrated the ability to create $Au^{\delta+}$-$RSH^{\delta-}$ and $Au^{\delta-}$-$RSH^{\delta+}$ dipoles depending on the substituents present on the alkyl chain of the thiols.

In this study, the gold nanoparticles are ~5 nm in size, making the initial and final state effects significant. They are immobilized on metal oxide supports, which can induce dipoles. Furthermore, they were synthesized using a colloidal route involving fatty amine stabilizers and no drastic cleaning was attempted to completely clean these from the Au nanoparticle surface. As we demonstrate by DRIFTS in chapter 3 of this thesis, some dodecylamine remains on the nanoparticles when no cleaning procedure is applied.Thus, all the above-mentioned explanations for the observed XPS shift in Au 4*f* binding energy apply for these catalysts, and we are probably observing the superposition of all of them. Therefore, no firm conclusions can be drawn for the observed increase in *BE* for the support range of zirconia, alumina, silica to ceria.

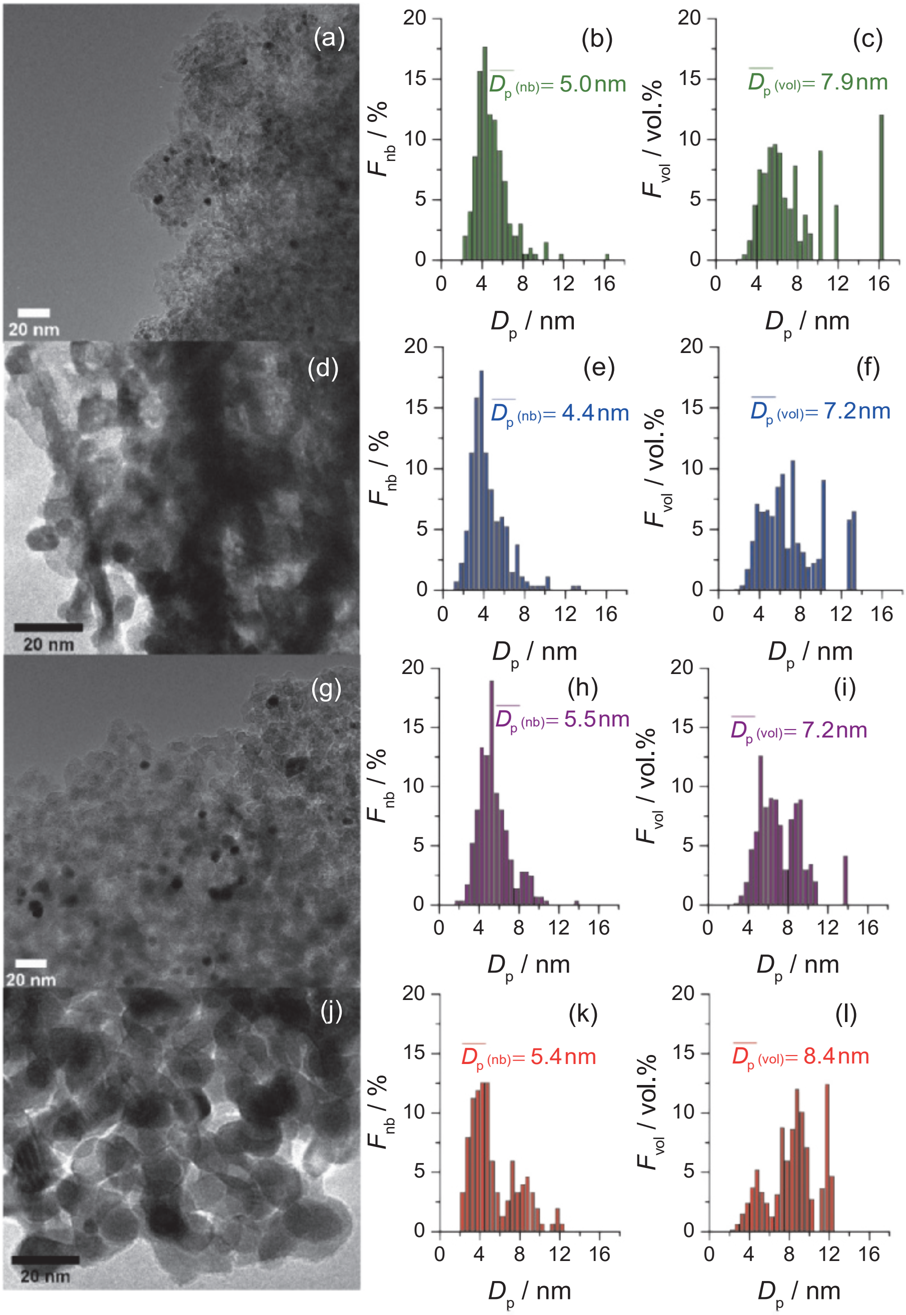

Figure 2.7: Representative TEM micrographs, nb- and vol- particle size distributions of (a), (b), (c) Au/Al_2O_3; (d), (e), (f) Au/CeO_2; (g), (h), (i) Au/SiO_2 and (j), (k), (l) Au/ZrO_2.

3 – 4 – TEM

Representative TEM micrographs as well as number- and volume-based particle size distributions (nb-PSD and vol-PSD, respectively) are depicted in Figure 2.7. The particle size is in good agreement with those reported by Quintanilla *et al.* [8] and by Chen *et al.* [7], who first reported this synthesis route. Overall, our strategy to obtain the same gold nanoparticles by employing the colloidal route is successful, though the Au particle size distribution of Au/ZrO_2 deviates slightly, as is discussed in detail below. A general tendency in scientific publications concerning colloidal nanoparticle synthesis is to represent the particle size distribution in percentage of the number of particles measured (nb, number based) [8, 37-41]. We find this view incomplete since the amount of material contained in a (spherical) particle increases with the third power of its diameter. In other words, a 10 nm diameter particle contains 8 times more material than a 5 nm diameter particle and 1000 times more material compared with a 1 nm diameter particle. To illustrate this, we include both nb-PSD and vol-PSD in Figure 2.7. vol-PSD depicts the volume-based fraction of the total amount of analysed material for each diameter interval. Such a distribution gives a more complete view in the outcome of the colloidal synthesis, therefore, it will be considered for the evaluation of the synthesis used here. In the case of Al_2O_3, CeO_2 and SiO_2, the nb-PSD is narrow (standard deviation 1.7 – 1.8 nm) and the (number-based) average particle size is around 5 nm. Although the nb-PSD of Au/ZrO_2 yields an average particle size of 5.4 nm, similar to those of Al_2O_3, CeO_2 and SiO_2, the standard deviation is relatively large (2.4 nm compared to 1.8 nm). The vol-PSDs of Au/Al_2O_3, Au/CeO_2 and Au/SiO_2 are also rather similar, with a volume-based average size of 7.2 – 7.9 nm, while the vol-PSD of Au/ZrO_2 shows a larger proportion of bigger particles (6 – 10 nm), which translates in a volume-based average size of 8.4 nm. It remains unclear why the colloidal Au nanoparticles show a different behaviour on ZrO_2 than on the three other supports, despite our precautions to obtain exactly the same particles on the different supports.

Table 2.4 summarizes the observations and conclusions of the different characterization techniques. Overall, our TEM results show that the Au nanoparticle size distributions are essentially the same for the four studied catalysts, particularly in view of the standard deviation (σ) of the distributions. We can therefore conclude that the differences in catalytic activity are originating from support properties and not from differences in gold particle size. Furthermore, the XPS results do not allow a clear conclusion concerning the Au nanoparticle-support interaction. This aspect should be investigated more in depth in a separate study. In contrast, clear differences in support reducibility were established, with CeO_2 being the most reducible support, followed by

Table 2.4: Summary of the observations and conclusions of the characterization techniques.

	Au/Al_2O_3	Au/CeO_2	Au/SiO_2	Au/ZrO_2
TPR	Not reducible	CeO_2 to Ce_2O_3 reduction at the surface above 600K, labile oxygen allowing creation of oxygen vacancies	Not reducible	Bare ZrO_2 not reducible. Au on ZrO_2 induces some ZrO_2 reducibility
NH_3 TPD	NH_3 desorption at 575 K and 650 K, second least acid support of the series	NH_3 desorption at 540 K, most acid support of the series	No NH_3 adsorption, least acid support of the series	NH_3 desorption at 590 K, second most acid support of the series
XPS	Au 4*f* 7/2 B.E. at 83.36 eV	Au 4*f* 7/2 B.E. at 83.78 eV	Au 4*f* 7/2 B.E. at 83.45 eV	Au 4*f* 7/2 B.E. at 83.29 eV
	Reference Au 4*f* 7/2 B.E. = 84.00 eV [8] Initial state effects due to small particle size: induces negative shift. Final state effects due to small particle size: induces positive shift. Interaction of Au with oxide support: induces positive shift. Interaction of Au with remaining dodecylamine: induces positive or negative shift, depending on the polarization direction of Au···N dipole. Convolution of all these effects does not allow firm conclusion.			
TEM	$D_{p\,(nb)} = 5.0$ nm $\sigma = 1.8$ nm	$D_{p\,(nb)} = 4.4$ nm $\sigma = 1.8$ nm	$D_{p\,(nb)} = 5.5$ nm $\sigma = 1.7$ nm	$D_{p\,(nb)} = 5.4$ nm $\sigma = 2.4$ nm
	The nb-PSDs for all the catalysts are essentially the same. Au nanoparticle size cannot account for the differences in catalytic performance.			

ZrO_2, whereas Al_2O_3 and SiO_2 didn't show any reducibility. Following the order of NH_3 desorption temperatures, it is established that CeO_2 is the most acidic of the support series, followed by ZrO_2 and then Al_2O_3. No NH_3 adsorbed on SiO_2, making it the least acid support of the series. Thus, we are able to clearly distinguish the different catalysts supports on two properties: reducibility and acidity.

3 – 5 – Benzyl alcohol oxidation activity

Figure 2.8 shows the reaction scheme of the benzyl alcohol oxidation to benzaldehyde.

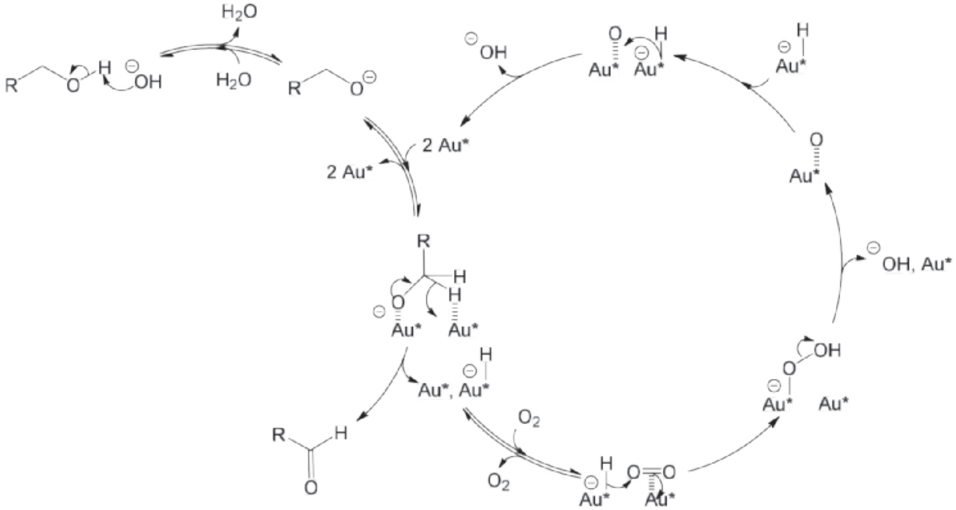

Figure 2.8: Kinetic scheme of the benzyl alcohol selective oxidation to benzaldehyde.

The deprotonation of the alcohol takes place via an acid-base reaction with a strong base (K_2CO_3 in our experiments). The adsorption of the alcoholate and the elimination of the β-hydride require the gold nanoparticles to have an electrophilic character (or Lewis acidity). This might be induced by the interaction of the gold nanoparticles with the catalyst support.

Mass transport limitations were verified to be absent with the benchmark catalyst (AUROlite™) by varying quantity and particle size. Figure 2.9 shows that when using catalyst particles between 50 and 70 µm or smaller than 40 µm the reaction rate is the same, thus demonstrating the absence of intra-particle diffusion limitations as long as the catalyst particles are smaller than 70 µm. Since the AUROlite™ catalyst was more active than the 4 studied catalysts, and since all catalysts particle sizes are below 70 µm, we tentatively conclude that the catalysts studied operate in the kinetic regime under the applied conditions. Thereby it is assumed that the effective diffusivities of the catalysts are similar.

The catalytic activity of the four studied catalysts is plotted in Figure 2.10 and the *TOF* values are summarized inTable 2.5. Au/Al_2O_3 shows the best activity for this reaction as well as reasonable stability (*TOF* = 13.7 min $^{-1}$ in run 1 and 10.4 min^{-1} in run 2). Although Figure 2.10 (c) shows a very low conversion for Au/SiO_2, the low gold loading (0.12 wt.%) makes its *TOF* the second highest of this catalyst series (*TOF* = 6.7 min^{-1}, run 1). The SiO_2-supported catalyst completely deactivates during the first run, showing no conversion during the second run (*TOF* = 0.2 min^{-1}). Since upon

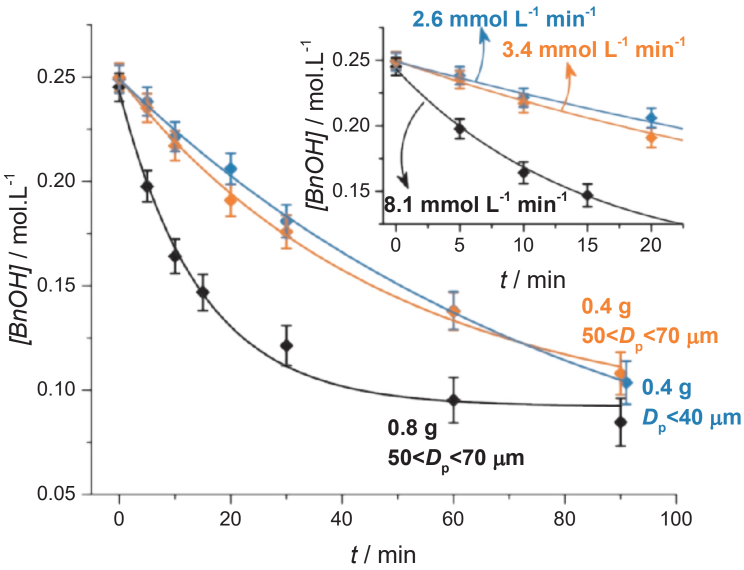

Figure 2.9: Benzyl alcohol concentration during selective oxidation over AUROlite™ benchmark catalyst. (—◆—) 0.8 g catalyst of 50 – 70 µm particle size, (—◆—) 0.4 g catalyst of 50 – 70 µm particle size and (—◆—) 0.4 g catalyst of <40 µm particle size. Inset shows initial reaction rates. The error bars are the [BnOH] measurement uncertainties that propagated from the GC, the weighing scale and the volumetric glassware.

filtration of the catalyst at the end of run 1 both a strong discoloration of the catalyst and a pink colour of the filtrate were observed, it can be concluded that the deactivation was caused by the loss of almost all the gold nanoparticles into the solvent (toluene) of the reaction. Additionally, the target gold loading (0.7 wt.%) couldn't be reached during the synthesis: only 0.12 wt.% was achieved. Therefore, we conclude that the Au-SiO_2 interaction is very weak. Au/CeO_2 and Au/ZrO_2 show similar performance in terms of activity (TOF = 1.8 and 3.2 min^{-1} respectively in run 1) and stability (TOF = 1.2 and 1.9 min^{-1} respectively in run 2), but are significantly less active than Au/Al_2O_3.

Al_2O_3 and SiO_2 are the least reducible materials of this series (Figure 2.4) and CeO_2 is the most reducible. In this respect, our results suggest that high support reducibility is detrimental for the catalytic oxidation of benzyl alcohol to benzaldehyde. ZrO_2 and CeO_2 are also the most acidic supports of this series (Figure 2.5), which should then also be regarded as detrimental for the catalytic activity. This can be understood considering the first elementary step of the reaction, which requires a base for the deprotonation of the alcohol. No clear correlation appears between Au 4*f* binding energies in XPS (Figure 2.6) and catalytic activity. As stated above, many phenomena contribute to the XPS signal, which makes it difficult to draw clear conclusions. The

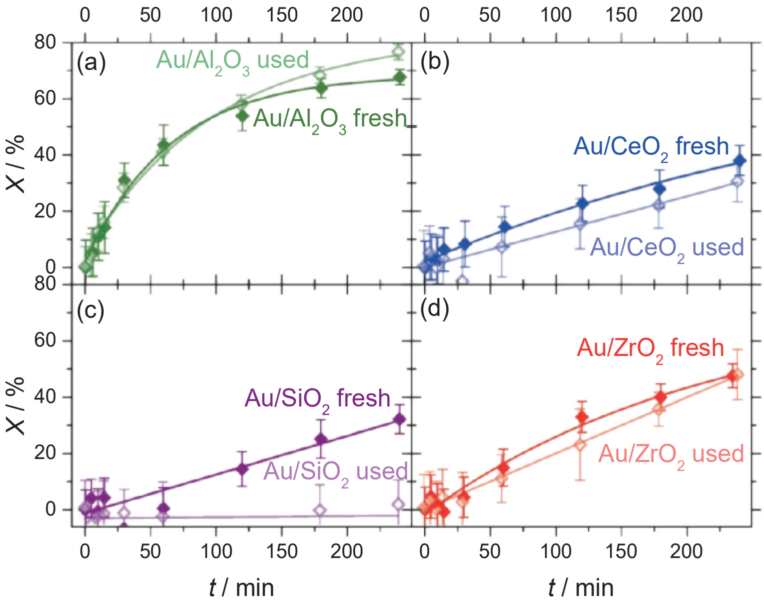

Figure 2.10: Conversion vs time for the aerobic oxidation of benzyl alcohol over (◆) Au/Al_2O_3 fresh, (◇) Au/Al_2O_3 used, (◆) Au/CeO_2 fresh, (◇)Au/CeO_2 used, (◆) Au/SiO_2 fresh, (◇) Au/SiO_2 used, (◆) Au/ZrO_2 fresh, (◇) Au/ZrO_2 used. Reaction conditions: 5 mg Au, 3 g K_2CO_3, 80 mL toluene, T=80°C, 200 mL·min^{-1} air, stirring at 1200 rpm.

goal of obtaining the same Au nanoparticles on the different supports has been reached, and for a similar average Au nanoparticle size and surface concentration (Figure **2.7**) the observed catalytic activity differed considerably.

The benzyl alcohol oxidation mechanism is discussed in detail in chapter 1 of this thesis. It consists of alcoholic proton abstraction by a strong basic site, followed by β-hydride elimination by a gold site, thereby forming the aldehyde. This mechanism implies that basic sites should be present on the catalyst and that the gold nanoparticles should be of oxidative character. The latter property is achieved with positively charged nanoparticles/surface Au atoms and/or with very small nanoparticles, presenting abundant edge and corner atoms which are less coordinated and therefore more oxidative. The *TOF* values in Table 2.5 are ranked in the opposite order (Al_2O_3 > SiO_2 > ZrO_2 > CeO_2) with respect to the NH_3 desorption temperatures in Table 2.4. We conclude that the acidity of the catalyst support is the most important parameter for the aerobic oxidation of benzyl alcohol to benzaldehyde, and that the presence of basic sites and a low acidity, such as encountered on MgO or hydrotalcite, are the desired support properties.

Table 2.5: Quantities involved in catalytic benzyl alcohol oxidation experiments, conversion rates and turn-over frequencies.

Catalyst	m_{cat} (g)	$Au_{content(ICP)}$ (wt.%)	$n_{benzyl\ alcohol,\ t=0}$ (mol)	$dX/dt_{t=0}$ (%·min^{-1})	*TOF* (min^{-1})
Au/Al_2O_3 fresh	0.8028	0.40	0.022	1.03	13.7
Au/Al_2O_3 used	0.8279	*	0.022	0.80	10.4
Au/CeO_2 fresh	1.8981	0.25	0.022	0.20	1.8
Au/CeO_2 used	1.7810	*	0.022	0.13	1.2
Au/SiO_2 fresh	0.7312	0.12	0.022	0.14	6.7
Au/SiO_2 used	0.7483	**	0.022	0.004	0.2
Au/ZrO_2 fresh	2.0086	0.24	0.022	0.34	3.2
Au/ZrO_2 used	1.9896	*	0.022	0.20	1.9

* The Au content of the used catalysts was assumed to be the same as that of fresh catalysts, as it was not possible to separate the catalyst powder from the potassium carbonate after the first run. ** Au/SiO_2 lost a large amount of Au during the first run, resulting in an underestimation of the *TOF* value.

3 – 6 – Carbon monoxide oxidation activity

Figure 2.11 shows the reaction scheme of the CO oxidation reaction. Dioxygen dissociation on gold surfaces is strongly disfavoured and the oxide support usually assists in supplying atomic oxygen to Au sites, in particular at the Au-support perimeter interface [14]. Therefore, a strong oxygen lability of the catalyst support is required for this reaction. Carbon monoxide is a strong Lewis base, so the adsorption of CO on Au sites requires them to have an electrophilic character. Besides, the carbon of the CO_2 molecule carries a Lewis acidity, which means that its desorption is favoured from an electrophilic site as their interaction is poor. A strong gold-support interaction might induce this electrophilic character.

Figure 2.12 illustrates the evolution to steady state for different temperatures for Au/CeO_2. Some noise is observed; the steady-state was considered attained after the third GC run for a given temperature. CO oxidation catalytic activities for the catalysts are plotted in Figure 2.13 and the temperatures at 50% conversion are reported in Table 2.6. Au/CeO_2 is the most active of the series ($T_{X=50\%}$ = 154 °C and 89 °C), followed by Au/ZrO_2 ($T_{X=50\%}$ = 223 °C and 136 °C) and then Au/Al_2O_3 ($T_{X=50\%}$ = 395 °C and 383 °C). The least active of the series is Au/SiO_2 which only reaches 28 % conversion at 595 °C.

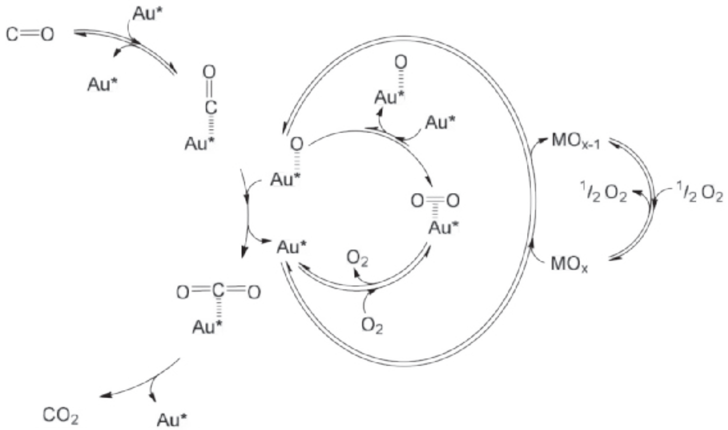

Figure 2.11: Kinetic scheme of the CO oxidation reaction. The dioxygen dissociation on Au surfaces is strongly disfavoured and the metal oxide support (MO_x) usually assists in supplying atomic oxygen to Au sites.

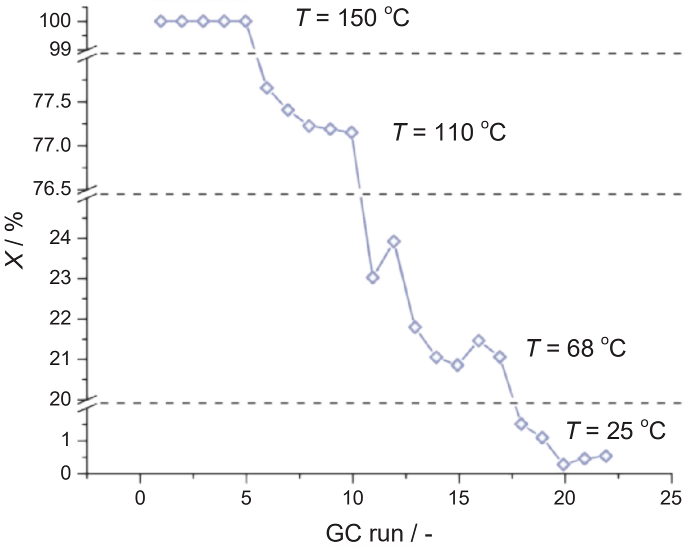

Figure 2.12: CO conversion at given T vs. successive GC runs in the course of cooling for Au/CeO_2 (Figure 2.13 (b), 2). Reaction conditions: 15 mg of Au is present in the reactor and 35 $mL\cdot min^{-1}$ of 1% CO and 0.5% O_2 in He was fed to the reactor at 2 bara. GC runs are spaced by 23 min.

CeO_2 is the most reducible support of the series, followed by ZrO_2 which shows some reducibility provided that Au nanoparticles are present on its surface [12]. Al_2O_3 and SiO_2 did not show any significant reducibility in TPR (Figure 2.4). The present results suggest that support reducibility is favourable in the catalytic oxidation of CO. CeO_2

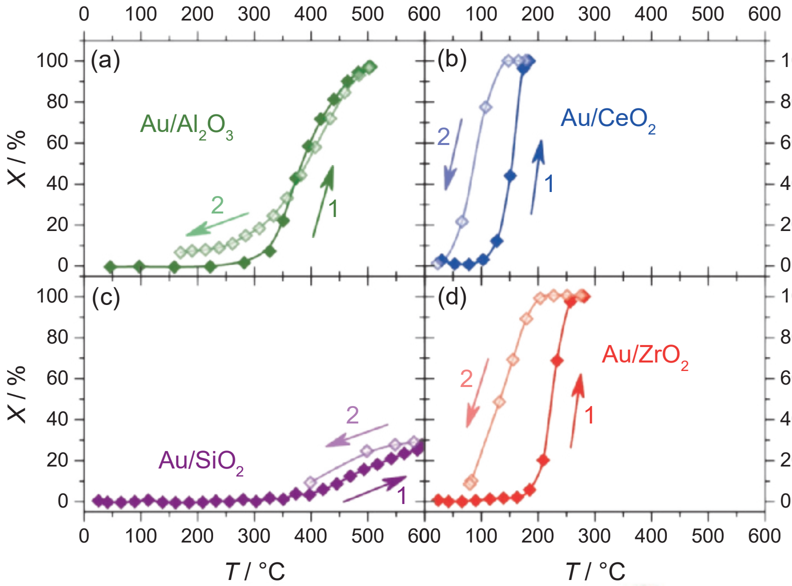

Figure 2.13: CO conversion vs. Temperature for (a) Au/Al_2O_3 (1, ◆) heating up, (2, ◇) cooling down; (b) Au/CeO_2 (1, ◆) heating up, (2, ◇) cooling down; (c) Au/SiO_2 (1, ◆) heating up, (2, ◇) cooling down and (d) Au/ZrO_2 (1, ◆) heating up, (2, ◇) cooling down. Reaction conditions: 15 mg of Au are present in the reactor and 35 mL·min^{-1} of 1% CO and 0.5% O_2 in He was fed to the reactor at 2 bar.

and ZrO_2 are also the most acidic supports of this series followed by Al_2O_3; SiO_2 does not show any acidity. The trend in activity seems also to follow the one in acidity, and it is concluded that high support acidity is beneficial for this reaction. As we explained for the benzyl alcohol oxidation, it is not possible to correlate the trend in activity with the XPS analysis.

In CO oxidation, O_2 dissociates on the support and elemental O spills over to the metal nanoparticles where it binds to the chemisorbed CO to form CO_2. Reducibility has long been pointed out to be the key factor for this reaction because a reducible support exhibits more oxygen vacancies on its surface [2, 11, 14, 18]. Those vacancies dramatically favour O_2 chemisorption and dissociation. Therefore, the trend observed in this study is not surprising. The correlation of catalytic activity with acidity is not obvious since no acid-base elementary step is involved in CO oxidation. Since a Lewis acid site is an electrophilic site, which can also be viewed as an oxidizer, the trend could be explained in terms of Lewis acidity the same way it is explained in terms of reducibility. The hysteresis observed in the light-off curves for Au/ZrO_2 and Au/CeO_2 can be explained by the combustion of the remaining capping ligands from the Au nanoparticles, thereby clearing more active surface of the catalyst. For Au/Al_2O_3 the

Table 2.6: Amount of catalyst loaded in the reactor, Au content and temperature at 50% CO conversion at heating up and cooling down operations.

catalyst	m_{catalyst} (mg)	Au content (wt.%)	Total m_{Au} in the reactor (µg)	$T_{X=50\%}$ (°C)
Au/Al_2O_3 heat up / cool down	24.8	0.404	100	385 / 395
Au/CeO_2 heat up / cool down	55.0	0.253	139	155 / 90
Au/SiO_2 heat up / cool down	22.5	0.121	27	595 / 595*
Au/ZrO_2 heat up / cool down	61.5	0.236	145	225 / 135

* Au/SiO_2 only reached $X = 28\%$ conversion in the studied temperature range.

cooling curve points only to a slightly more active catalyst in the cooling run. Au/Al_2O_3 was exposed to a maximum temperature of 500 °C during the catalytic experiment, and Au particle agglomeration and sintering is often reported when the temperature exceeds 300 – 400 °C [42]. Therefore, the beneficial effect of capping agent removal being countered by the increase in Au particle size is a reasonable hypothesis. Schüth [2] also observed that the Au nanoparticles equilibrate with the support surface upon removal of the capping ligands after immobilization of the nanoparticles on ZrO_2, TiO_2 and $MgFe_2O_4$ supports. Particles that were spherical in colloidal dispersion showed faceting after immobilization and subsequent capping agent removal [2]. This behaviour makes the Au nanoparticle morphology support-dependent again, although this is less strongly influenced by the usually applied impregnation/precipitation preparation routes. Even though the influence from the synthesis method is minimized, the colloidal route for studying pure catalytic support effects shows its limitations.

The most striking observation in this study is the opposite trend in catalytic activity between benzyl alcohol oxidation and carbon monoxide oxidation. Even though both reactions are oxidations, *i.e.* in both cases one carbon has its oxidation state increased, their mechanism is very different. Therefore, a priori, it is not to be expected that the ideal catalytic properties would be the same for both reactions. Furthermore, it should be noted that there was no attempt to completely eliminate the capping ligand after immobilisation, which was therefore still present during the catalytic experiments.

Some capping ligands probably remain on the catalyst after benzyl alcohol oxidation, but are most probably removed during carbon monoxide oxidation, resulting in the observed hysteresis. Our results suggest that strong support basicity is beneficial for benzyl alcohol oxidation, but is detrimental to or has no effect on carbon monoxide oxidation. Alcohol deprotonation by a base explains the trend in benzyl alcohol oxidation, whereas carbon monoxide adsorbs as a weak base on an electrophilic site such as a gold edge/corner [43]. On the other hand, support reducibility is strongly beneficial for carbon monoxide oxidation whereas it is detrimental for benzyl alcohol oxidation. As the support supplies oxygen to the reaction, and since reducibility often induces mobility, the carbon monoxide oxidation mechanism explains the observed correlation of activity with support reducibility. As the alcohol deprotonation could be impeded by high support acidity, thereby disfavouring the adsorption of the alcoholate, the negative correlation of activity and support acidity for the benzoyl oxidation can be explained. Our results also suggest that support acidity has a beneficial effect for carbon monoxide oxidation, although this does not really reflect on the mechanism as CO is considered to adsorb on gold sites directly. These observations should however be rationalized taking into account that other support effects, not addressed in this study, could be playing a role. In particular the Au nanoparticle-support interaction has been shown to be important [2]. This is for instance, the most probable culprit for the very low activity of the Au/SiO_2 in the benzyl alcohol oxidation, where significant leaching was observed. Although leaching is not an issue in the gas-phase CO oxidation, the Au-SiO_2 interaction is probably very weak and could be an explanation for the low activity. The Au nanoparticle size is also often pointed out to be of crucial importance in the catalytic activity [5, 6, 44]. The particle size distributions of the catalysts studied here are very similar, except for Au/ZrO_2 where the nanoparticles are substantially larger. This makes the colloidal route for catalyst synthesis a suitable way of studying catalytic support effects that are not, or a lot less, influenced by the catalyst preparation [2].

Finally, it should be acknowledged that all these support properties are playing their beneficial/detrimental role in concert with the active phase during the catalytic reaction. It is therefore hard to eliminate the support influences completely and draw conclusions on their individual contributions. Theoretical modelling might allow changing one property only and determine its particular effects.

Conclusions

The colloidal synthesis route for gold provides a way to achieve similar particle size distributions on different catalyst supports and allows eliminating this factor in studying the support influence in catalytic reactions. By adjusting the amount of Au colloidal nanoparticles to the support surface area, it proved possible to prepare a series of catalysts with very similar morphology, and varying only chemically.

In benzyl alcohol oxidation, the basicity of the support has a positive influence on the catalytic activity. Support reducibility does play a large role, and if present, it is detrimental for this reaction. The deprotonation of benzyl alcohol being the first elementary step, the observed correlation with basicity is logical from a mechanistic point of view. The observation of significant leaching of Au nanoparticles from SiO_2 after the first catalytic experiment shows that the Au-SiO_2 interaction is very weak. This could be due to the fact that removing the capping ligand after the immobilisation of the nanoparticles was not attempted.

In carbon monoxide oxidation, in all cases the catalyst activates upon the increase of reaction temperature, leading to hysteresis upon decreasing temperature. This hysteresis effect is attributed to the removal of the capping ligand at increasing temperature, introducing more gold-support interaction, resulting in more active surface available for catalysis. The presence of acid support sites is beneficial for the catalytic activity. Support reducibility appears to be the most important property promoting catalytic activity in carbon monoxide oxidation, as is often reported. O_2 chemisorption, dissociation and surface diffusion are facilitated on strongly reducible supports because of the high oxygen mobility and vacancies it provides on the surface.

This study shows that despite both reactions being oxidations, the required catalyst properties are very different, which is explained by the largely differing reaction mechanisms.

References

1. Soualah, A.; Lemberton, J.L.; Pinard, L.; Chater, M.; Magnoux, P.; Moljord, K. *Appl Catal A-Gen 336,* **2008**, 23-28.
2. Schüth, F. *Phys Status Solidi B 250,* **2013**, 1142-1151.
3. Chen, M.S.; Goodman, D.W. *Catal Today 111,* **2006**, 22-33.
4. Tomishige, K.; Yasuda, H.; Yoshida, Y.; Nurunnabi, M.; Li, B.; Kunimori, K. *Green Chem 6,* **2004**, 206-214.
5. Liu, Y.; Jia, C.N.; Yamasaki, J.; Terasaki, O.; Schüth, F. *Angew Chem Int Edit 49,* **2010**, 5771-5775.
6. Remediakis, I.N.; Lopez, N.; Nørskov, J.K. *Angew Chem Int Edit 44,* **2005**, 1824-1826.
7. Chen, Y.; Wang, X. *Mater Lett 62,* **2008**, 2215-2218.
8. Quintanilla, A.; Butselaar-Orthlieb, V.C.L.; Kwakernaak, C.; Sloof, W.G.; Kreutzer, M.T.; Kapteijn, F. *J Catal 271,* **2010**, 104-114.

9. De Lange, M.F.; Vlugt, T.J.H.; Gascon, J.; Kapteijn, F. *Micropor Mesopor Mat 200,* **2014**, 199-215.
10. Arnoldy, P.; Moulijn, J.A. *J Catal 93,* **1985**, 38-54.
11. Hernández, W.Y.; Romero-Sarria, F.; Centeno, M.A.; Odriozola, J.A. *J Phys Chem C 114,* **2010**, 10857-10865.
12. Wang, X.; Hao, Y.; Keane, M.A. *Appl Catal A-Gen 510,* **2016**, 171-179.
13. Noronha, F.B.; Fendley, E.C.; Soares, R.R.; Alvarez, W.E.; Resasco, D.E. *Chem Eng J 82,* **2001**, 21-31.
14. Widmann, D.; Liu, Y.; Schüth, F.; Behm, R.J. *J Catal 276,* **2010**, 292-305.
15. Kouva, S.; Honkala, K.; Lefferts, L.; Kaverno, J. *Catal Sci Technol 5*, **2015**, 3473-3490
16. Trovarelli, A. *Catal Rev Sci Eng 38,* **1996**, 439-520.
17. Hakeem, A.A.; Rajendran, J.; Kapteijn, F.; Makkee, M. *Catal Today 242,* **2015**, 168-177.
18. Wang, Y.; Posthuma de Boer, J.; Kapteijn, F.; Makkee, M. *ChemCatChem 8,* **2016**, 102-105.
19. Beckers, J.; Rothenberg, G. *Green Chem 12,* **2010**, 939-948.
20. Johnson, M.F.L.; Mooi, J. *J Catal 103,* **1987**, 502-505.
21. Perrichon, V.; Laachir, A.; Bergeret, G.; Fréty, R.; Tournayan, L.; Touret, O. *J Chem Soc, Faraday Transactions 90,* **1994**, 773-781.
22. Katada, N.; Niwa, M. *Catal Surv Asia 8,* **2004**, 161-170.
23. Abello, M.C.; Velasco, A.P.; Gorriz, O.F.; Rivarola, J.B. *Appl Catal A-Gen 129,* **1995**, 93-100.
24. Joly, J.P.; Khalfallah, M.; Bianchi, D.; Pajonk, G.M. *Appl Catal A Gen 98,* **1993**, 61-70.
25. Wu, S.K.; Lai, P.C.; Lin, Y.C.; Wan, H.P.; Lee, H.T.; Chang, Y.H. *ACS Sustain Chem Eng 1,* **2013**, 349-358.
26. Shen, Y.; Zhu, S.; Qiu, T.; Shen, S. *Catal Commun 11,* **2009**, 20-23.
27. Miao, J.Y.; Yang, L.F.; Cai, J.X. *Surf Interface Anal 28,* **1999**, 123-125.
28. Watanabe, S.; Ma, X.; Song, C. *J Phys Chem C 113,* **2009**, 14249-14257.
29. Yi, T.; Zhang, Y.; Li, J.; Yang, X. *Chinese J Catal 37,* **2016**, 300-307.
30. Dias, C.R.; Zãvoianu, R.; Portela, M.F. *React Kinet Catal L 77,* **2002**, 317-324.
31. Verhaak, M.J.F.M.; van Dillen, A.J.; Geus, J.W. *Appl Catal A-Gen 105,* **1993**, 251-269.
32. Powell, C.J. *NIST X-ray Photoelectron Spectroscopy Database*, Version 4.1. Available online: http://srdata.nist.gov/xps/ (13/06/**2016**),
33. Zwijnenburg, A.; Goossens, A.; Sloof, W.G.; Crajé, M.W.J.; van der Kraan, A.M.; Jos de Jongh, L.; Makkee, M.; Moulijn, J.A. *J Phys Chem B 106,* **2002**, 9853-9862.
34. Chusuei, C.C.; Lai, X.; Luo, K.; Goodman, D.W. *Top Catal 14,* **2001**, 71-83.
35. Andrulevičius, M.; Tamulevičius, S.; Gnatyuk, Y.; Vityuk, N.; Smirnova, N.; Eremenko, A. *Mater Sci-Medzg 14,* **2008**, 8-14.
36. Alloway, D.M.; Hofmann, M.; Smith, D.L.; Gruhn, N.E.; Graham, A.L.; Colorado, R.; Wysocki, V.H.; Lee, T.R.; Lee, P.A.; Armstrong, N.R. *J Phys Chem B 107,* **2003**, 11690-11699.
37. Daniel, M.C.; Astruc, D. *Chem Rev 104,* **2004**, 293-346.
38. Wang, Y.; Biradar, A.V.; Wang, G.; Sharma, K.K.; Duncan, C.T.; Rangan, S.; Asefa, T. *Chem-Eur J 16,* **2010**, 10735-10743.
39. Lang, H.; May, R.A.; Iversen, B.L.; Chandler, B.D. *J Am Chem Soc 125,* **2003**, 14832-14836.
40. Das, D.D.; Sayari, A. *J Catal 246,* **2007**, 60-65.
41. Alhumaimess, M.; Lin, Z.; Weng, W.; Dimitratos, N.; Dummer, N.F.; Taylor, S.H.; Bartley, J.K.; Kiely, C.J.; Hutchings, G.J. *ChemSusChem 5,* **2012**, 125-131.
42. Jia, C.-J.; Liu, Y.; Schwickardi, M.; Weidenthaler, C.; Spliethoff, B.; Schmidt, W.; Schüth,

F. *Appl Catal A-Gen 386,* **2010**, 94-100.

43. Hvolbæk, B.; Janssens, T.V.W.; Clausen, B.S.; Falsig, H.; Christensen, C.H.; Nørskov, J.K. *Nano Today 2,* **2007**, 14-18.
44. Haruta, M.; Yamada, N.; Kobayashi, T.; Iijima, S. *J Catal 115,* **1989**, 301-309.

Chapter 3

Au Capping Agent Removal Using Plasma at Mild Temperature

To prevent sintering, ozone treatment at mild temperature is used to remove the capping agent from supported Au nanoparticles. The Au nanoparticles are first synthesized as a colloidal solution and then supported on alumina. Fourier Transform Infra Red (FTIR) shows the capping agent is removed completely. Transmission Electron Microscopy (TEM) and catalytic test reactions show that the Au does not sinter significantly upon low temperature ozone treatment.

This chapter is based on the publication:
Puspitasari, I.; Skupien, E.; Kapteijn, F.; Kooyman, P.J.; *Catalysts 6*, **2016**, 179

1 – Introduction

Synthesis of metallic nanoparticles has been the subject of intensive research due to their potential interesting applications [1]. These particles can be applied in chemical and biological fields such as nanoparticles for catalysis, chemical sensors, drug delivery, bio-sensing, etc [2-4]. In the preparation of metal nanoparticles, capping agents are commonly used [5-7]. The function of the capping agent is to avoid aggregation of the nanoparticles in the solution and to control the size as well as the shape of the nanoparticles [8-11]. The size and shape of the nanoparticles are important factors in catalytic activity and selectivity. At the end of the preparation steps, the capping agent is still attached to the surface of the nanoparticles.

When the metal nanoparticles are used in catalytic reactions, the presence of the capping agent can affect the catalytic activity and selectivity because it hinders the chemical and physical access to the metal particle surface, and modifies the surface chemistry of the metal surface [12]. Therefore, methods to remove the capping agents are important issues. Washing with chemicals (acid, base or salt solution) [13-15], calcination [16-19], and combination of UV and ozone treatments [20-23] have been reported to remove the capping agents. But these techniques require special equipment and sometimes the morphology of the nanoparticles is not preserved due to harsh treatment conditions. Clearly, low temperature capping agent removal is important to prevent agglomeration of the nanoparticles.

Ozone has been used to remove unwanted organic compounds from inorganic surfaces [24,25]. In this method, a sample is contacted with an oxygen/ozone mixture at a certain temperature where ozone decomposes into atomic oxygen and radical species, which are highly reactive [26,27]. Kuhn et al. used ozone treatment at 200 °C to remove the DD3R template from zeolites in a 38 h detemplation process [24]. In comparison with the ozone treated samples, the synthesised samples were also calcined at 550-700 °C for 6-16 h. They reported that the porosity characteristics of the ozone treated samples were equal to those of the calcined samples, which verifies that the ozone treatment at low temperature is a powerful detemplation method.

In the 1980s, Haruta showed that oxide-supported gold nanoparticles with particle size smaller than 5 nm have a remarkable catalytic activity even at low temperatures. Since then gold nanoparticles have been recognised as catalysts for many reactions, including oxidation of propene [28,29], CO oxidation [30], NO_x reduction [31,32], selective hydrogenation of acetylene [33,34], and the water-gas shift reaction [35,36]. Gold nanoparticles have been successfully prepared using several capping agents. Dodecylamine (DDA) is one of the most commonly used capping agents [37-39] and has been used for the current study. The capping agent removal was performed by an ozone treatment [12].

CO oxidation is one of the structure-sensitive catalytic reactions that is widely used to test the activity of gold catalysts. The rate and selectivity of this reaction are defined by three factors: the size and structure of the Au nanoparticles and the selected support [40]. Clearly, the Au catalyst preparation is an important step. In this investigation, the gold nanoparticles were prepared using a colloidal method and deposited on γ-Al_2O_3 support at room temperature condition. With this route, the desired particle size and shape were obtained. The γ-Al_2O_3, which was chosen as the support material, is expected to have an influence on the activity [12,41].

In this chapter, we report on the DDA capping agent removal from the surface of Au nanoparticles by ozone treatment in relation to their catalytic performance. The experiments were conducted at mild conditions to prevent structural and morphological changes as well as agglomeration of the nanoparticles. Catalyst characterisation was performed using Transmission Electron Microscopy (TEM), Fourier Transform Infrared Spectroscopy (FTIR), and X-ray Photoelectron Spectroscopy (XPS). CO oxidation and selective oxidation of benzyl alcohol to benzaldehyde were selected to study the catalytic performance before and after capping agent removal in a gas phase and a liquid phase reaction.

2 – Experimental

2 – 1 – Catalyst preparation

The gold catalysts were prepared following the methodology described by Chen [7] and Quintanilla [12]. 0.75 g of DDA (99.5% Sigma-Aldrich) was dissolved in 25 mL of cyclohexane (anhydrous, 99.5% Sigma-Aldrich). Then 6 mL of formaldehyde solution (37 wt% in water, 10-15% methanol as stabiliser, Sigma-Aldrich) was added to the mixture. The mixture was then stirred at room temperature for 30 minutes. The reactions depicted in Figure 2.1, 2.2 and 2.3 were allowed to take place.

Two phases of suspensions were separated by decantation. The top phase (transparent) was the cyclohexane phase and contained the desired dodecylaminomethanol. The bottom phase (white) was the water phase, also containing the excess formaldehyde. Then 10 mL of 4 g/L $HAuCl_4$ (0.04 g $HAuCl_4$ (Sigma-Aldrich) in 10 mL of Milli-Q water) was added into the cyclohexane phase under stirring at room temperature. Soon after addition, the suspension colour turned yellow. The -$NHCH_2OH$ was oxidised to -NHCOOH by Au^{3+} which at the same time was reduced to Au^0. The -NHCOOH was not stable and decomposed into -NH_2 and CO_2. Then the -NH_2 was released and adsorbed on the Au^0 nanoparticle surface. After stirring for at least 1 h, the colour changed to ruby red, indicating the formation of small gold particles.

The mixture had two separated phases. The top part (ruby red colour) was the cyclohexane phase, which contained the Au-DDA, and the bottom part was the water phase. The suspension was left overnight in a separator funnel until the separation of the two phases was completed. The result was a ruby red suspension of Au-DDA colloid in cyclohexane. The Au-DDA colloid was washed using acetone. The acetone (about 3x the colloid volume) was added to the colloid suspension, and then the mixture was centrifuged for 5 minutes at 10,000 rpm to precipitate the nanoparticles. After the supernatant was removed, the nanoparticles were redispersed in 25 mL of cyclohexane. The Au nanoparticles were immobilised on γ-Al_2O_3. 1.5 g γ-Al_2O_3 (previously calcined at 500 °C, 6 h, < 7.1 µm, Akzo Chemical) was added to the cyclohexane mixture under vigorous stirring. The stirring was left overnight. The suspension was filtered resulting in a pink catalyst powder (Au-DDA/γ-Al_2O_3). The powder was washed with 100 mL cyclohexane and 100 mL acetone, then left to dry in a vacuum desiccator at room temperature overnight.

DDA/γ-Al_2O_3 was also prepared for blank experiments. 0.9 g DDA was dissolved in 25 mL cyclohexane. 0.9 g γ-Al_2O_3 was then added to the mixture and stirred overnight. The suspension was filtered and left to dry overnight in a vacuum desiccator.

2 – 2 – Capping agent removal

The removal of the capping agent from the supported catalyst was conducted by loading the 1% Au-DDA/γ-Al_2O_3 catalyst into a U-tube glass reactor, which was installed in the ozone detemplation setup (Figure 3.1). Oxygen from a gas cylinder was passed through a Corona discharge ozone generator (A2Z Ozone Systems, SOZ -16GLAB). The check valves (CV1 and CV2) prevent back flow of the ozone to the mass flow controllers (MFC1 and MFC2). The ozone concentration at the outlet was monitored using an ozone detector (Lenntech, BMT 964), after which it was sent through a manganese dioxide / copper oxide catalytic ozone destructor. The U-tube glass reactor was placed inside the oven (Binder FP53) equipped with a temperature controller. The experiment was conducted at 30 °C while the ozone concentration was 7 g/Nm^3 (0.35%). The reaction time was varied from 6-10 h.

2 – 3 – Catalyst characterisation

The morphological characterisation of the gold catalysts was performed using a FEI TECNAI F20 transmission electron microscope (TEM) operated at 200 kV with a Field

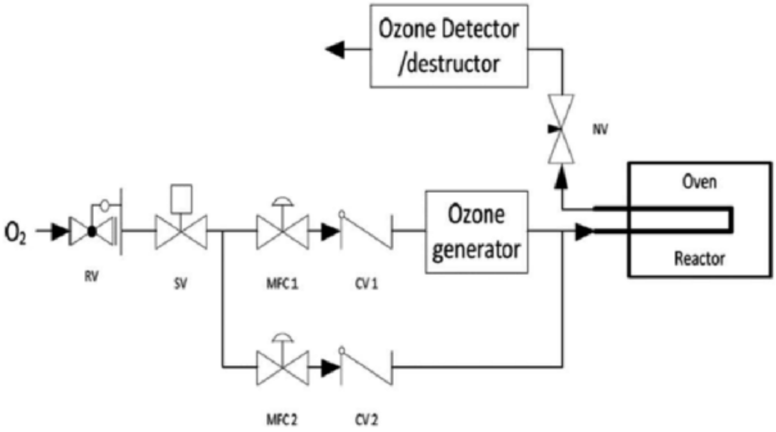

Figure 3.1: Process flow diagram of the ozonication set-up.

Emission Gun (FEG) and a Gatan ultra scan camera.

The samples were prepared by depositing one drop of washed gold colloid onto a microgrid Quantifoil® carbon film supported on a copper TEM grid and left to dry at room temperature. In case of the powder catalysts (as-synthesised Au-DDA/γ-Al_2O_3 and ozone treated catalyst), a finely crushed catalyst suspension in ethanol was used. A drop of the suspension was deposited on a Quantifoil® covered copper TEM grid and left to dry at room temperature. The particle size distributions and average particle sizes were determined from the TEM images by measuring the size of 300 particles from each sample.

The infrared spectra of the catalysts were recorded using a Thermo Scientific Nicolet Fourier Transform Infrared (FTIR) spectrophotometer. Prior to the FTIR characterisation, the background spectrum of the pure KBr pellet was recorded under He flow at room temperature. Then about 0.050 g catalyst was evenly spread on top of the KBr powder. The KBr background spectrum was automatically subtracted from the spectrum obtained from the measurement, resulting in the sample spectrum only.

The catalyst oxidation states were studied using a Thermo Scientific K-Alpha X-ray photoelectron spectrometer (XPS). The measurements were done by using a line scan at four areas with each area having a spot size of 400 μm at ambient temperature and chamber pressure of about 10^{-7} mbar. The binding energy of the XPS spectra was calibrated using the C 1*s* peak (binding energy = 285.1 eV). The spectra were analysed and processed using Thermo Avantage v5.903 software (Thermo Fischer Scientific).

The peaks were fitted using a Lorentzian-Gaussian product function. A Shirley type background was then subtracted from the spectra and the Au 4f spectra were deconvoluted.

2 – 4 – Catalytic test

The CO oxidation reaction was chosen to test the catalyst activity. Approximately 25 mg catalyst (as-synthesised Au-DDA/γ-Al_2O_3 or ozone treated catalyst) was placed in a flow glass tube reactor (inner diameter ~0.4 mm). The reactor was first loaded with SiC (~ 50 mg) then a mixture of catalyst (25 mg) and SiC (~100mg) was added on top of it. The dilution with SiC is to facilitate heat removal, preventing hot spots. The last layer was again SiC (~ 50 mg) and quartz wool. The gas mixture used in the experiment was 0.5% O_2, 1% CO and 98.5% He at 35 mL min^{-1}. The reactor was at a total pressure of 2 bar during the test. The reaction temperature was increased fast (5 °C min^{-1}) from room temperature to 300 °C, then increased slowly (1 °C min^{-1}) from 300 °C to 500 °C. After maintaining the temperature at 500 °C for 1 h, the reactor was cooled down to 330 °C (1 °C min^{-1}). The setup was connected to a Chrompack CP 9001 GC equipped with a TCD detector, sampling every 12 minutes. Helium was used as carrier gas through a dual column system consisting of a Parabond Q column (Chrompack, 25 m in length, 0.53 mm in diameter and 10 µm of coating thickness) and a Molsieve 5A column (Chrompack 10 m in length, 0.53 mm in diameter and 50 µm of coating thickness). The CO oxidation using a reference catalyst (1% AUROlite™ from Strem Chemicals) and blank experiments (using γ-Al_2O_3 and DDA/γ-Al_2O_3) were also performed as comparison.

A reaction to evaluate catalytic performance in the liquid phase was the benzyl alcohol oxidation. In a round-bottom flask (60 mm inner diameter, equipped with baffles and stirrer shaft), approximately 0.6 g catalyst (as-synthesised Au-DDA/γ-Al_2O_3 or ozone treated catalyst) was mixed with 3.04 g K_2CO_3 (>99.0%, Sigma-Aldrich). 80 mL Toluene (anhydrous, 99.8% Sigma Aldrich) was added to disperse the mixture. The flask was stirred at 1200 rpm and heated to 80 °C. 200 mL min^{-1} of air was bubbled through the mixture. When the temperature was stable, 22 mmol (2.4 g) of benzyl alcohol was added (t = 0 min). Small samples of 300 µL were taken at recorded times and filtered from catalyst and K_2CO_3 powders with a 13 mm syringe Teflon filter of 0.2 µm pore size (diameter: 13 mm; pore size: 0.2 µm; PTFE membrane VWR international) and introduced in a GC sample vial together with 20 µL of tetradecane, the latter being used as internal standard. They were analysed by a Varian CP-3380 GC equipped with FID. Helium was used as carrier gas through a CP-SIL 8 CB column (Chrompack) of 50 m in length, 0.25 mm in diameter and 0.25 µm of coating thickness.

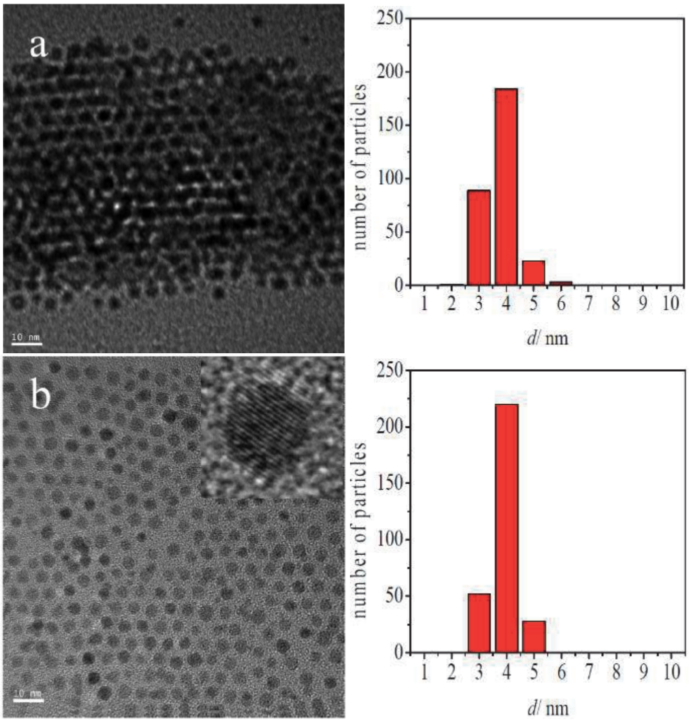

Figure 3.2: TEM images and particle distribution of (a) unwashed Au-DDA colloid and (b) washed Au-DDA colloid.

In the chromatograms, the main product (benzaldehyde) and the consecutive products (benzoic acid and benzyl benzoate) were detected in the product mixture. Previous work showed that no conversion of benzyl alcohol occurs over pure γ-Al_2O_3 [12], therefore no blank experiment was performed.

The turnover frequency (*TOF*) was calculated as follows:

$$TOF = \frac{\Delta n_{BnOH}}{\Delta t} \times \frac{M_{Au}}{w_{cat} \times x_{Au}} \qquad (1)$$

Where $\frac{\Delta n_{BnOH}}{\Delta t}$ is the benzyl alcohol reaction rate (mol h^{-1}), M_{Au} is the molar mass of gold (g mol^{-1}), w_{cat} is the amount of catalyst in the reactor (g), and x_{Au} is the gold loading of the catalyst (wt.%).

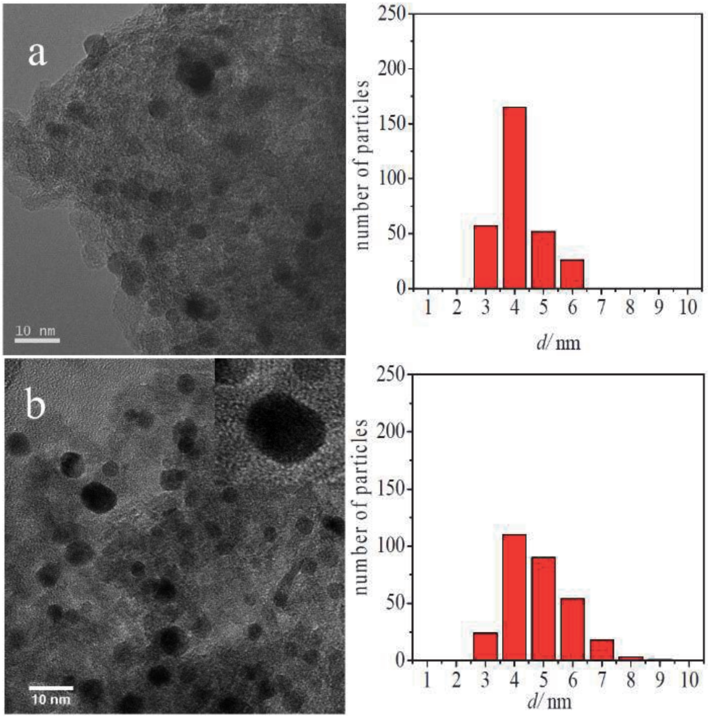

Figure 3.3: TEM images (left) and particle size distributions (right) of (a) Au-DDA/γAl_2O_3, and (b) Au-DDA/γAl_2O_3 (O_3 8h). The inset in the TEM image (b) shows the crystallinity of a Au nanoparticle.

3 – Results and discussion

3 – 1 – Catalyst characterisation

The use of capping agent yields a uniform particle shape as shown in Figure 3.2. The unwashed Au-DDA colloid showed severe carbon contamination under the TEM beam because the excess of DDA was still present in the colloid (Figure 3.2a). The average particle size of the unwashed colloid is 3.3 nm (St.Dev. = 0.5). Figure 3.2b shows a TEM image and particle size distribution of the washed colloid. The average particle size is 3.8 nm (St.Dev. = 0.5). The inset in figure 3.2b shows that the Au nanoparticles are monocrystalline as reported by Quintanilla and coworkers [12]. As expected, the immobilisation of the catalyst on γ-Al_2O_3 support does not drastically change the particle size (Figure 3.3a) because the gold particles had been produced before the deposition and the deposition process should not alter the particle sizes and distributions [41]. The average particle size of as-prepared supported particles and after capping

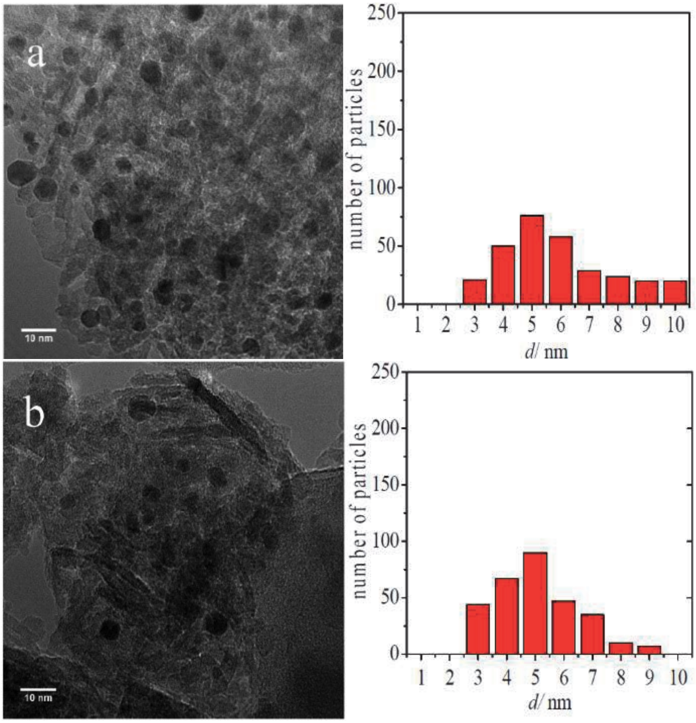

Figure 3.4: TEM images (right) and particle size distributions (left) of post-CO oxidation of (a) Au-DDA/γAl_2O_3, and (b) Au-DDA/γAl_2O_3 (O_3 8h)

agent removal using ozone treatment (Au-DDA/γ-Al_2O_3 (O_3, 8 h)) at 30 °C was 4.0 nm (St.Dev. = 0.8) and 4.3 nm (St.Dev. = 1.0) respectively (Figure 3.3a-b). Even though the average particle size before and after ozone treatment are similar, the broadening of the particle size distribution after ozone treatment shows that some sintering occurred. However, since the ozone treatment is at mild temperature, the agglomeration is less than at high temperatures [42]. For a sulphur-containing capping agent, Menard et al. showed a tripling of the nanoparticle size (from 0.8 to 2.7 nm) upon calcination at 400 °C, whereas the particle size increase was limited to 1.2 nm after ozone treatment [22]. Figure 3.3b (inset) shows lattice fringes on the Au nanoparticles, indicating that the ozone treatment does not change the Au nanoparticle crystallinity.

The TEM images of the catalysts after CO oxidation (Figure 3.4a-b) show that the high temperature CO oxidation caused sintering. However, the particle size does not change drastically. After use, the average particle size is 5.5 nm (St.Dev. = 1.9) for the as-prepared catalyst and 4.7 nm (St.Dev. = 1.3) for the ozone treated catalyst.

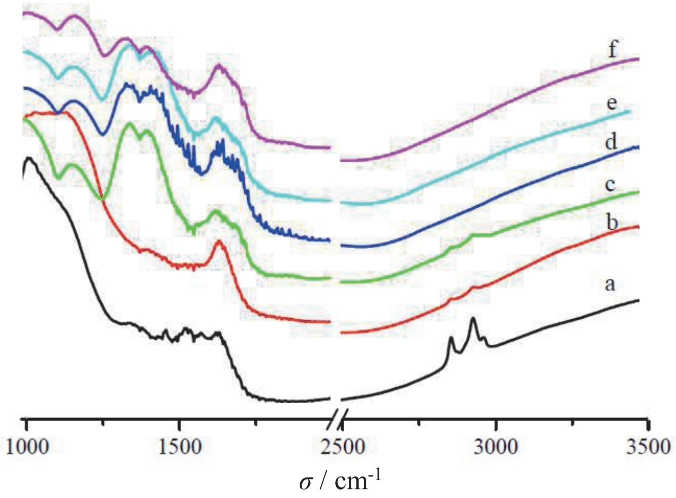

Figure 3.5: FTIR spectra of (a) DDA/γAl_2O_3, (b) Au-DDA/γAl_2O_3, (c) Au-DDA/γAl_2O_3 (O_3 6h), (d) Au-DDA/γAl_2O_3 (O_3 7h), (e) Au-DDA/γAl_2O_3 (O_3 8h) and (f) Au-DDA/γAl_2O_3 (O_3 10h)

Figure 3.5 shows infrared spectra of Au-DDA/γ-Al_2O_3 after different duration of ozone treatment. The changes in the absorbance below 1600 cm^{-1} are due to water vapour interactions on the surface of the γ-Al_2O_3 support. The DDA/γ-Al_2O_3 spectrum was used to determine the vibration energy signals of -CH_2- and -CH_3 groups from the DDA at the wavenumbers 2858 cm^{-1} and 2930 cm^{-1} [43,44] (Figure 3.5a). The intensity of these peaks disappeared after 7 h of treatment, showing that the DDA has been removed. But to make sure that all of the DDA have been removed, 8 h of treatment was chosen as the experimental time to remove the DDA. Combining the information from TEM and FTIR, we conclude that DDA has been removed from the surface of the Au nanoparticles after 8 h ozone treatment at 30 °C without drastically changing the diameter of the Au particles.

XPS was used to study the oxidation state of the gold. Figure 3.6 shows the Au 4*f* photoelectron spectra from as-prepared Au-DDA/γ-Al_2O_3 and ozone treated catalysts. For the ozone treated catalyst, the peaks shifted to higher binding energies. The deconvolution of these peaks leads to the FWHM measurement which indicates that the Au in the as-prepared catalyst is metallic (Au^0, binding energy 836 and 871 eV), while after ozone treatment the Au is cationic ($Au^{\delta+}$, binding energy 841 and 878 eV). The results are in line with previous studies, which concluded that surfactant-encapsulated

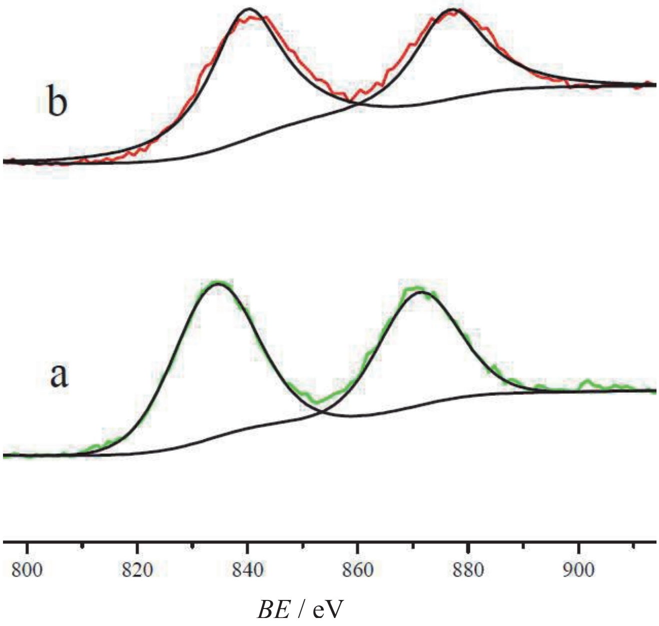

Figure 3.6: XPS spectra of the Au 4*f* binding energy region for (a) Au-DDA/γ-Al_2O_3 as prepared and (b) after O_3 treatment for 8 h (30 °C)

gold and platinum nanoparticles surface act as metals while supported nanoparticles are cationic [12,45-47].

3 – 2 – Catalytic tests

Figure 3.7 shows the CO conversion against temperature for several samples. The blank samples (γ-Al_2O_3 and DDA/γ-Al_2O_3) show very low conversion because the active phase for this reaction is the nanoparticulate Au, and the Au nanoparticle-support interface enhances the activity of the Au nanoparticles [40,48]. As expected the conversion increases after introduction of Au nanoparticles, but no significant conversion changes can be seen between the as-prepared Au-DDA/γ-Al_2O_3 and ozone treated catalysts. This can be explained by the similarity in Au particle size and crystallinity. The 1% AUROlite™ catalyst (reference catalyst, average particle size 2-3 nm [49]) gives the highest CO oxidation activity. This result was due to the presence of chloride (from the Au precursor during catalyst preparation) on the surface of the Au nanoparticles which lowers the catalytic activity by stimulating the agglomeration of

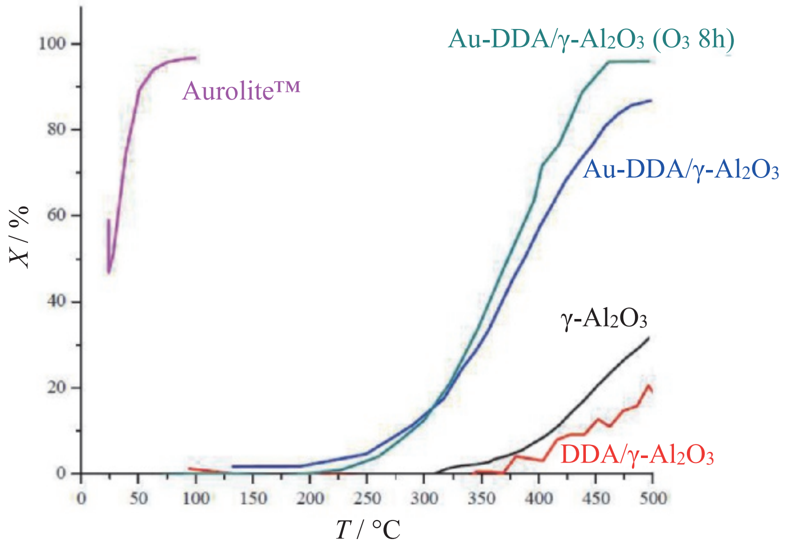

Figure 3.7: CO conversion vs. Temperature for — γ-Al_2O_3, — DDA/γ-Al_2O_3, — Au-DDA/γ-Al_2O_3, — Au-DDA/γ-Al_2O_3 (O_3 8h) and — Aurolite™

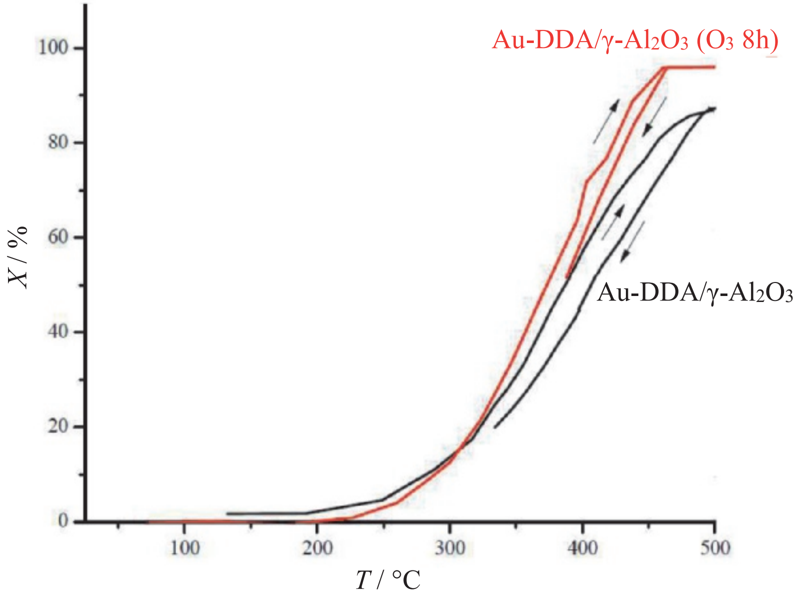

Figure 3.8: CO oxidation vs. Temperature during heating and cooling for — Au-DDA/γ-Al_2O_3 and — Au-DDA/γ-Al_2O_3 (O_3 8h)

Au nanoparticles during the heat treatment (> 100 °C) and hinders the reduction of Au

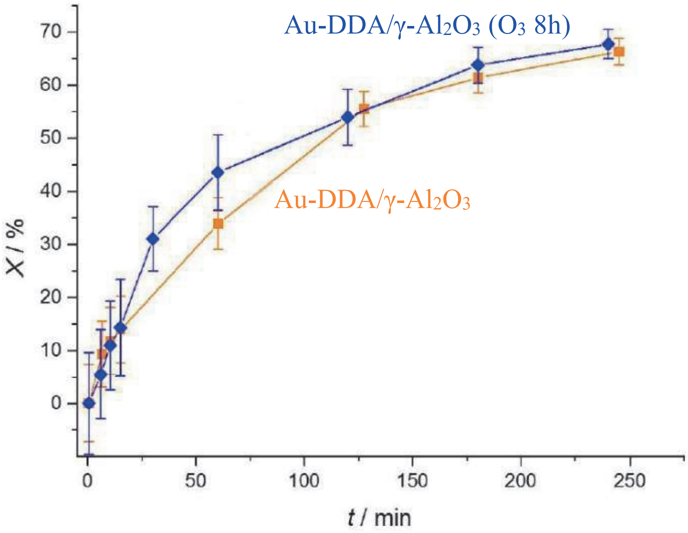

Figure 3.9: Benzyl alcohol conversion vs. time for — Au-DDA/γ-Al_2O_3 and — Au-DDA/γ-Al_2O_3 (O_3 8h)

cations by poisoning [50-52]. Figure 3.8 shows the CO oxidation performance of the as-prepared Au-DDA/γ-Al_2O_3 and Au-DDA/γ-Al_2O_3 ozone treated for 8h catalysts during heating and cooling cycling. The CO conversion during cooling is slightly lower than during heating, which is attributed to some sintering, as witnessed by TEM observations.

The benzyl alcohol oxidation reaction is presented in Figure 1.1. The main product is benzaldehyde while the side products, benzoic acid and benzyl benzoate, are formed in consecutive reactions. The as-prepared Au-DDA colloid is not active for this reaction while supported Au-DDA is slightly active as reported in a previous study [12]. This confirms the influence of a metal-support interaction, which contributes to the catalyst activity. After capping agent removal, the interaction is stronger, therefore the activity is slightly higher than for the as-prepared sample. Similar to the CO oxidation results, the as-prepared Au-DDA/γ-Al_2O_3 and the ozone-treated samples present a similar activity with *TOF* = 894 h^{-1} for Au-DDA/γ-Al_2O_3 and *TOF* = 1106 h^{-1} for Au-DDA/γ-Al_2O_3 O_3 8h. The benzyl alcohol conversions at 240 min are in the range of 65-70% (Figure 3.9). For comparison, the benzyl alcohol conversion over AUROlite™ at 240 min is 78% and its *TOF* 682 h^{-1} [49].

The activity of the supported gold catalyst is often attributed to cationic gold species in the catalyst [12]. Quintanilla and coworkers reported that the Au-DDA colloid is not catalytically active, but after immobilisation it appears to be slightly active because some cationic Au species are formed. The alumina support induces the formation of cationic Au and more surface Au atoms. The concentration of the cationic Au species in the catalyst is responsible for the activity of the catalyst during the catalytic reaction. The Au-DDA/γ-Al_2O_3 shows activity during CO oxidation and benzyl alcohol oxidation despite the XPS results showing that the Au is in the metallic state, which is also what Quintanilla et al. concluded [12]. The Au cationic species might also be present in small concentrations in the catalyst. Then it increases after ozone treatment, resulting in the shift of the XP spectrum and a slight increase of the catalyst activity.

4 – Conclusions

Ozone treatment at mild temperature was shown to remove the capping agent from the surface of supported gold nanoparticles. The average particle size, shape, and crystallinity of the gold nanoparticles hardly changed after capping agent removal. Due to the mild temperature of the ozone treatment, sintering was minimised and stable catalytic particles were obtained. The ozone treated catalysts did not sinter significantly even during the high temperature CO oxidation reaction, whereas the as-prepared capping agent containing catalyst was affected by sintering and, thus, showed lower activity. The activity for benzyl alcohol oxidation with molecular oxygen of the ozone-treated Au-DDA-Al_2O_3 was slightly increased compared to that of the as-prepared catalyst, probably due to the increased concentration of Au cationic species on the surface of the catalyst after the ozone treatment. Repeated catalytic tests are required to analyse the possibility of long-term deactivation processes due to sintering on both catalysts.

References

1. Hutchings, G. J., Haruta, M. *Appl. Catal A 291,* **2005**, 2-5.
2. Bond, G. C., Louis, C., Thompson, D. T. *Catalysis by Gold.*, (Imperial College Press, **2006**). ISBN: 978-1860946585.
3. Otieno, B. A., Krause, C. E., Latus, A., Chikkaveeraiah, B. V., Faria, R. C., Rusling, J. F. *Biosens Bioelectron 53,* **2014** 268-274.
4. Nagelli, E., Naik, R., Xue, Y., Gao, Y., Zhang, M., Dai, L. *Nanotechnology* 24, **2013,** 444010
5. Lee, I., Morales, R., Albiter, M. A., Zaera, F. *PNAS* **2008**, *105*, 15241-15246, ISSN: ISSN-0027-8424.
6. Polavarapu, L., Xu, Q. H. *Nanotechnology 20,* **2009**, 185606.
7. Chen, Y., Wang, X. *Mater Lett 62,* **2008**, 2215-2218.

8. Sun, Y., Mayers, B., Herricks, T., Xia, Y. *Nano Lett 3*, **2003**, 955-960.
9. Sun, Y., Xia, Y. *Science 298,* **2002**, 2176-2179.
10. Bratlie, K. M., Lee, H., Komvopoulos, K., Yang, P., Somorjai, G. A. *Nano Lett 7,* **2007**, 3097-3101.
11. Tao, A. R., Habas, S., Yang, P. *Small 4,* **2008**, 310-325.
12. Quintanilla, A., Butselaar-Orthlieb, V. C. L., Kwakernaak, C., Sloof, W. G., Kreutzer, M. T., Kapteijn, F. *J Catal 271,* **2010**, 104-114.
13. Naresh, N., Wasim, F. G. S., Ladewig, B. P., Neergat, M. *J Mat Chem A 1,* **2013**, 8553-8559.
14. Mazumder, V., Sun, S. *JACS 131,* **2009**, 4588-4589.
15. Nalajala, N., Gooty Saleha, W. F., Ladewig, B. P., Neergat, M. *Chem Comm 50,* **2014**, 9365-9368.
16. Lange, C., De Caro, D., Gamez, A., Storck, S., Bradley, J. S., Maier, W. F. *Langmuir 15,* **1999**, 5333-5338.
17. Yu, R., Song, H., Zhang, X. F., Yang, P. *J. Phys Chem B 109,* **2005**, 6940-6943.
18. Joo, S. H., Park, J. Y., Tsung, C. K., Yamada, Y., Yang, P., Somorjai, G. A. *Nat Mater 8,* **2009**, 126-131.
19. Kim, C., Min, M., Chang, Y. W., Yoo, K. H., Lee, H. *J. Nanosci Nanotech 10,* **2010**, 233-239.
20. Aliaga, C., Park, J. Y., Yamada, Y., Lee, H. S., Tsung, C. K., Yang, P., Somorjai, G. A. *J Phys Chem C 113,* **2009**, 6150-6155.
21. Crespo-Quesada, M., Andanson, J. M., Yarulin, A., Lim, B., Xia, Y., Lioubov, K. W. *Langmuir 27,* **2011**, 7909-7916.
22. Menard, L. D., Xu, F., Nuzzo, R. G., Yang, J. C. *J. Catal 243,* **2006**, 64-73.
23. Niu, Z., Li, Y. *Chem Mater 26,* **2014**, 72-83.
24. Kuhn, J., Gascon, J., Gross, J., Kapteijn, F. *Micropor Mesopor Mat 120,* **2009**, 12-18.
25. Heng, S., Lau, P. P. S., Yeung, K. L., Djafer, M., Schrotter, J. C. *J. Membrane Sci 243,* **2004**, 69-78.
26. Benson, S. W., Axworthy, A. E. *J Chem Phys 42,* **1965**, 2614-2615.
27. Benson, S. W., Axworthy Jr, A. E. *J Chem Phys 26,* **1957**, 1727-1733.
28. Nijhuis, T. A., Sacaliuc, E., Beale, A. M., van der Eerden, A. M. J., Schouten, J. C., Weckhuysen, B. M. *J Catal 258,* **2008**, 256-264.
29. Delannoy, L., Fajerwerg, K., Lakshmanan, P., Potvin, C., Méthivier, C., Louis, C. *Appl Catal B Environ 94,* **2010**, 117-124.
30. Valden, M., Lai, X., Goodman, D. W. *Science 281,* **1998**, 1647-1650.
31. Go, M. J., Lee, B. K., Kumar, P. A., Lee, W. K., Joo, O. S., Ha, H. P., Lim, H. B., Hur, N. H. *Appl Catal A Gen 370,* **2009**, 102-107.
32. Miquel, P., Granger, P., Jagtap, N., Umbarkar, S., Dongare, M., Dujardin, C. *J Mol Catal A Chem 322,* **2010**, 90-97.
33. Sárkány, A. *React Kinet Catal Lett 96,* **2009**, 43-54.
34. Gluhoi, A. C., Bakker, J. W., Nieuwenhuys, B. E. *Catal Today 154,* **2010**, 13-20.
35. Mohamed, M., Khairou, K. S. *Energ Fuel 23,* **2009**, 4413-4419.
36. Rodriguez, J. A. *Catal Today 160,* **2011**, 3-10.

37. Osmic, M., Kolny-Olesiak, J., Al-Shamery, K. *Cryst Eng Comm 16,* **2014**, 9907-9914.
38. Lee, H., Kim, C., Yang, S., Han, J. W., Kim, J. *Catal Surv Asia 16,* **2012**,14-27.
39. Kremser, G., Rath, T., Kunert, B., Edler, M., Fritz-Popovski, G., Resel, R., Letofsky-Papst, I., Grogger, W., Trimmel, G. *J Coll Interf Sci 369,* **2012**, 154-159.
40. Haruta, M. *J. New Mater Electrochem Syst 7,* **2004**, 163-172.
41. Comotti, M., Li, W. C., Spliethoff, B., Schüth, F. *JACS 128,* **2006**, 917-924.
42. Quintanilla, A., Butselaar-Orthlieb, V. C. L., Kwakernaak, C., Sloof, W. G., Kreutzer, M. T., Kapteijn, F. *Poster presentation at 6th World Congress on Oxidation Catalysis*, **2009** July 5-10, Lille, France.
43. Mo, L., Liu, D., Li, W., Li, L., Wang, L., Zhou, X. *Appl Surf Sci 257,* **2011**, 5746-5753.
44. Dablemont, C., Lang, P., Mangeney, C., Piquemal, J. Y., Petkov, V., Herbst, F., Viau, G. *Langmuir 24,* **2008** 5832-5841.
45. Leff, D. V., Brandt, L., Heath, J. R. *Langmuir 12,* **1996**, 4723-4730.
46. Borodko, Y., Habas, S. E., Koebel, M., Yang, P., Frei, H., Somorjai, G. A. *J Phys Chem B 110,* **2006**, 23052-23059.
47. Calla, J. T., Davis, R. J. *Catal Lett 99,* **2005**, 21-26.
48. Liu, X., Liu, M. H., Luo, Y. C., Mou, C. Y., Lin, S. D., Cheng, H., Chen, J. M., Lee, J. F., Lin, T. S. *JACS 134,* **2012**, 10251-10258.
49. Skupien, E., Berger, R., Santos, V., Gascon, J., Makkee, M., Kreutzer, M. T., Kooyman, P. J., Moulijn, J. A., Kapteijn, F. *Catalysts 4,* **2014**, 89-115.
50. Oxford, S.M., Henao J.D., Yang J.H., Kung M.C., Kung H.H. *Appl Catal Lett A 339,* **2008**, 180-186.
51. Oh. D.H., Yang J.H., Costello C.K., Wang Y.M., Bare S.R., Kung H.H., Kung M.K. *J Catal 210,* **2002**, 375-386.
52. Lina C.H., Lina S. D., Lee J.F. *Catal Lett 89,* **2016**, 235-242.

Chapter 4

Synthesis of highly dispersed Pd nanoparticles supported on multi-walled carbon nanotubes and their excellent catalytic performance for oxidation of benzyl alcohol

Narrow sized and highly homogeneous dispersed Pd nanoparticles have been synthesized on nitric acid-functionalized multi-walled carbon nanotubes (CNTs) without a capping agent. The TEM images show that the extremely small Pd nanoparticles with an average size of about 1.5 nm were homogeneously dispersed on the surface of the CNTs. The characterization results indicate that the pretreatment with nitric acid not only improved the dispersion of Pd, but also enhanced the strong interaction between the Pd nanoparticles and the CNTs, thereby preventing their agglomeration and leaching in the liquid phase. With HNO_3 pretreatment, it is possible to generate more acidic groups on the surface of CNTs without a significant change in textural properties. The catalytic performance of the aforementioned material was investigated for selective oxidation of benzyl alcohol. Pd/CNTs exhibits high activity (~98% conversion) and selectivity (~90%) to benzaldehyde with excellent reusability. The high activity of the catalyst was attributed to the small size and high dispersion of Pd nanoparticles and higher accessibility of reactants. A careful analysis of the kinetic data suggests that there are different sites for the disproportionation and oxidation reactions. The excellent reusability of Pd/CNT catalysts makes this material a promising candidate for selective benzyl oxidation. Furthermore, the results of the present study show that it is possible to synthesize uniformly dispersed Pd nanoparticles on various carbon supports without a capping agent.

This chapter is based on the publication:
Shinde, V.M.; Skupien, E.; Makkee, M., *Catal Sci Technol 5*, **2015**, 4144-4153

1 – Introduction

Noble metal nanoparticles supported on carbon nanotubes as heterogeneous catalysts have gained increasing interest due to their one-dimensional morphology and synergistic effects [1]. It has been reported that the noble metal nanoparticles supported on carbon nanotubes exhibit an improved catalytic activity. The catalytic properties of the nanoparticles are highly sensitive to the size, morphology, composition, and dispersion of the noble metal particles [2–4]. For the synthesis of highly dispersed and stable catalyst, a strong interaction between the metal precursor and the support is essential [5]. However, the uniform dispersion of the noble metal nanoparticles on carbon support is difficult due to its chemical inertness. High temperature treatment with concentrated acid or of doping with heteroatoms is usually used to functionalize the surfaces CNTs [6–8]. These pretreatments can often control the hydrophobicity of CNTs and introduce active sites on the CNT surface [9–11]. The concentration, distribution, and nature of the functional groups also influence the dispersion of noble metals. Furthermore, the functionalization of supports can prevent the sintering of supported nanoparticles [12]. In addition, functional groups on the support render a strong metal–support interaction which averts the problem of leaching of the active phase in liquid phase reactions.

There are several methods to synthesize noble metal nanoparticle/CNT composites, including impregnation, the colloidal synthesis method, and the polyol method [13–16]. Among these methods, the polyol method is a promising alternative to synthesize nanoparticles due to its ability to control particle size and size distribution, high dispersion, and precisely tuneable bimetallic composition. However, it has been shown that there is a large variation of the resulting mean particle size with the final catalyst composition [17]. In general, the ultrafine Pd nanoparticles are vulnerable to serious aggregation [18, 19] therefore, the capping agents (surfactants or polymeric stabilizers) are commonly used to stabilize the nanoparticles [20, 21]. However, in most cases, the removal of the capping agent is required to activate the catalyst. This is usually accomplished by washing and/or heat treatment [20, 21]. However, most of the time, the complete removal of the capping agents is difficult due to either a strong interaction between the nanoparticles and the capping agent or due to the aggregation tendency of the nanoparticles at high temperatures. Therefore, it remains a great challenge to synthesize nanoparticles without any capping agent [22]. An improved method has been later developed without the addition of a capping agent which involves refluxing of the carbon nanotubes in a mixture of concentrated nitric and sulfuric acids to create surface functional groups, such as carbonyl (–CO), hydroxylic (–COH) and carboxylic (–

COOH). The acid treated CNTs were then used for the deposition of metal nanoparticles. Ethylene glycol was used as a solvent and reducing agent to reduce the metal precursor [23, 24] at 120 °C or by heating with microwave radiation [25, 26]. Although no capping agent was used during the synthesis, it was difficult to remove the oxidation products of ethylene glycol at elevated temperatures and it remained adsorbed on the Pd nanoparticles.

Recently, a facile method for the synthesis of nanoparticles using CO as a gaseous stabilizer has been reported for a Pt–Ni bimetallic alloy [27]. The unique role of the CO molecule, as a size confining molecular adsorbate, due to its size-dependent coverage and chemisorption energy, in the restriction of the mean particle size of the alloy at 4 nm regardless of the Ni content, has been illustrated. Therefore, it was anticipated that the direct reduction of a Pd precursor in the presence of gaseous molecules such as CO or H_2, should be able to control the growth of Pd nanoparticles due to their strong adsorption on metallic Pd. A physical adsorption technique was used for the deposition of Ru nanoparticles on CNTs in which the Ru precursor was first impregnated on CNTs and then was reduced to metallic Ru nanoparticles [28]. The resulting metal nanoparticles had a mean size in the range of 3–7 nm and metal loadings were lower than 0.2 wt.%. To the best of our knowledge, a simple synthesis method for a highly dispersed Pd nanoparticle on CNTs at high metal loading without a capping agent has not been reported in the literature.

The selective oxidation of alcohols to their corresponding carbonyl compounds is a subject of growing interest. Noble metal-supported catalysts such as Pd, Pt, Ru, and Au are active for the selective oxidation of alcohols [29–31]. Among these, Pd-supported catalysts show a relatively high activity and selectivity [29]. These studies reveal that the aldehyde selectivity is close to 60–80% over the Pd-supported catalysts [32]. In particular, the addition of Au to Pd catalysts improves not only the catalytic activity, but also the selectivity to the aldehyde [33]. Thus, bimetallic catalysts are promising candidates for transformation and offer greater flexibility not only in chemical composition but also in interatomic arrangement compared to monometallic catalysts [34]. However, they need a very careful synthesis procedure in order to avoid any segregation or inhomogeneity that weakens the synergistic effects of the bimetallic catalysts [35]. In this study, we describe a convenient approach to synthesize highly and uniformly dispersed Pd nanoparticles on CNTs without a capping agent. The CNTs were first functionalized with nitric acid to create the surface O functional groups for the deposition of metal nanoparticles and then the Pd precursor, $PdCl_2$, was impregnated on the surface of CNTs followed by drying and subsequent reduction of metal precursor in the presence of H_2. The results show that the functionalization of the CNTs demonstrated a uniform deposition of Pd nanoparticles on CNTs at relatively high loading of 3 wt%. The synthesized Pd/CNTs exhibited an average size of 1.5 nm and a narrow particle size distribution. Pd catalysts supported on the various form of carbons such as carbon black, activated carbon, and graphite were also synthesised using the aforementioned approach. The catalytic performance of all these materials was investigated for the selective oxidation reaction of benzyl alcohol to benzaldehyde. The Pd/CNTs showed a better activity, selectivity, and reusability than the Pd nanoparticles supported on the other form of carbons.

2 – Experimental

2 – 1 – Synthesis and characterization

Four carbon supports, namely: multi-walled CNTs (Cheap Tubes Inc., USA), carbon black (Cabot Corporation, USA), activated carbon (Fluka Analytical, Netherlands), and graphite (Alfa Aesar, Germany) were used. All the Pd-supported catalysts were prepared using an impregnation–reduction method. The supports were first functionalized with a pretreatment of concentrated nitric acid. Typically, 2 g of carbon material were suspended in 150 mL of concentrated HNO_3 (68 wt%) and refluxed at 120 °C for 6 h. After cooling to room temperature, the mixture was filtered and washed with demineralized water for several times until the pH of filtrate reached 7, and was subsequently dried in air oven at 120 °C for 2 h. The required amount of $PdCl_2$ (Sigma Aldrich, Netherlands) for 3 wt% Pd loading was dissolved in 20 mL of demineralized water (a small amount of HCl was added to ensure the complete solubility of $PdCl_2$). After stirring for 30 min, the CNTs were dispersed into the above solution and stirred for 6 h at room temperature until a paste-like mixture was obtained upon evaporation of water. Finally, the mixture was dried at 120 °C and subsequently reduced in 5% of H_2 in N_2 flowing at 100 mL min^{-1} at 350 °C in a flow reactor for 2 h. The same procedure was followed to synthesize all other Pd-supported catalysts.

X-ray diffraction (XRD) patterns were recorded on a Phillips X'Pert diffractometer using Co Kα radiation (k = 0.1788 nm) operated at 40 kV and 30 mA. The scans were recorded at a rate of 0.5° min^{-1}. The peaks were identified with reference to the JCPDS database. The transmission electron microscopy (TEM) images were recorded on a JEOL JEM-2010F instrument operated at 200 kV. The sample was dispersed in ethanol and dried on a carbon-coated copper grid (300 mesh). The TEM images were recorded in different regions of the Cu grid. The size distribution of the Pd nanoparticles were obtained by measuring around 150–200 particles in arbitrarily chosen areas of the image. X-ray photoelectron spectroscopy (XPS) was used to examine the electronic properties of the catalysts. The XPS spectra were recorded on a Thermo Scientific Multilab equipped with an Al anode (Al K-alpha = 1486.6 eV). The XPS spectra were calibrated using a binding energy of C 1*s* observed at 284.6 eV. The background due to inelastic process was corrected using the Shirley method. A fixed Gaussian–Lorentzian shape function was used to deconvolute the overlapping peaks. The normalized peak intensities (corrected with the atomic sensitivity factors) were used to estimate the relative concentration of the Pd^0 and Pd^{2+} states on the various carbon supports.

Temperature programmed desorption (TPD) of the catalysts was performed to study surface oxygen mobility in a fixed bed reactor connected to a mass spectrometer. 100 mg of a sample was heated from room temperature to 900 °C at a heating rate of 10 °C min^{-1} in He flowing at 30 mL min^{-1}. The mass spectrometer was calibrated using calcium oxalate as a reference. The evolution of the species such as CO and CO_2 was measured as function of temperature.

N_2 adsorption–desorption isotherms were measured with a Quantachrome Autosorb-6B unit gas adsorption analyser (Micromeritics, USA) using a continuous adsorption procedure. The BET method was used to calculate the specific surface areas of the sample. Prior to N_2 adsorption, the sample was degassed at 200 °C for 12 h in vacuum. Pd content of the carbon catalysts was determined by ICP-OES analyses (Micro Analytical Laboratory Kolbe, Germany).

2 – 2 – Catalytic activity measurements

The benzyl alcohol oxidation reaction was carried out in a 100 mL round-bottom stirred vessel equipped with a condenser. In a typical experiment, 50 mL of xylene (a mixture of isomers) and 300 mg of catalyst were introduced into the reactor. Toluene, frequently used as a solvent in the literature, was not used as it was suspected to be one of the (oxidation) products of the reaction. The vessel was heated to 90 °C using an oil bath. The reaction mixture was stirred at 900 rpm and an air flow rate of 100 mL min^{-1} was continuously bubbled through the reaction mixture. After stabilization of the reactor temperature at 90 °C, 2.4 g of benzyl alcohol was introduced using a syringe (t = 0 min). The samples were collected in a regular interval and analysed by GC (Varian CP-3380 with a 50 m CP-Sil 52 CB column), equipped with an FID detector. The initial temperature of the GC oven was programmed from 150 °C (held for 6 min) to 350 °C at a heating rate of 20 °C min^{-1}. An external standard was used to quantify the amount of reactants consumed and products formed during the reaction. It was observed that no reaction occurred either in the absence of Pd catalyst or in the presence of the support. The rate of reaction was linearly proportional to the catalyst amount and independent of the speed of stirring, indicating that mass transport limitations were absent. For the reusability test, the catalyst was recovered after the test by vacuum filtration and washed with xylene at room temperature. The conversion of benzyl alcohol, the selectivity to benzaldehyde, and the quasi-turnover frequency are defined as follows:

Conversion (%) $$X = \frac{\text{moles of reactant converted}}{\text{moles of reactant in feed}} \times 100 \qquad (1)$$

Selectivity (%) $$S = \frac{\text{moles of product formed}}{\text{moles of reactant converted}} \times 100 \qquad (2)$$

quasi-turnover frequency (h^{-1}) $$qTOF = \frac{\text{moles of reactant converted}}{\text{moles of Pd sites} \times \text{reaction time}} \qquad (3)$$

3 – Results and discussion

3 – 1 – Structural studies

Table 4.1 summarizes the results of textural analysis of HNO_3 treated and non-acid treated Pd/CNTs. There was no dramatic change observed in the textural properties of CNTs after HNO_3 treatment. The BET surface area and microporous volume of the sample are slightly modified after the acid pretreatment which is probably due to the removal of impurities blocking the pore channels of CNTs. Figure 4.1 shows the XRD patterns of the Pd-supported catalysts. A broad diffraction peak at 31° was observed for all carbon-supported catalysts which is a characteristic peak of “graphitic” carbon [36]. Two specific features of graphitic carbon were observed at 31° and 64.6° for the graphite-supported catalyst, while a broad peak was observed at 31° for all other carbon-supported catalysts. The diffraction peaks at 46.9°, 54.7°, and 81.1° are indexed to the palladium face-centered cubic (fcc) phase indicating the formation of metallic Pd particles. The crystalline size of Pd was calculated using the Scherrer formula and found to be in the range of 4–6 nm. Since the crystallite size calculated using the Scherrer formula is influenced by many factors and may be misleading for nanoparticles, the particle sizes were also measured by TEM [37].

Figure 4.2(a) and (b) display the TEM images of acid treated and non-acid treated Pd/CNTs along with their particle size distributions. It can be seen from the TEM images that the Pd nanoparticles are spherical and uniformly distributed over acid treated Pd/CNTs. The particle size distribution shows that the monodispersed ultrafine

Table 4.1: Physical properties of various Pd-supported catalysts

Catalyst	Pd loading (%)[a]	Pore volume (cm^3 g^{-1})	Pd cluster size (nm)[b]	Surface area (m^2 g^{-1})	CO/CO_2 ratio[c]
CNTs	2.39	0.553	1.5	150	0.99
CNTs without HNO_3	2.39	0.5	5.5	131	3.27
Carbon black	2.84	0.026	2.6	160	2.07
Graphite	2.87	—	1.5–2.5	5	2.21
Activated carbon	3.08	0.632	3.5	1551	1.73

[a] determined by ICP. [b] Average particle size observed by TEM.
[c] Measured by TPD. [d] Measured by XPS.

Pd particles are deposited on CNTs. The average size of the Pd nanoparticles was found to be 1.5 nm for the acid pretreated sample. The comparison between acid treated and non-acid treated Pd catalysts were also performed in order to understand the effect of acid functionalization on the particle size distribution. It has been observed from the TEM images that there was a significant difference in the Pd particle size between the acid treated and the non-acid treated samples. Relatively large and less dispersed Pd clusters were observed on the surface of CNTs without HNO_3 pretreatment. The average size of the Pd particles was found to be 5.5 nm for the non-acid treated sample. The XPS results (see Figure 4.4) suggest that the surface carboxylic acid groups were generated during acid pretreatment and these sites probably act as the anchoring sites which prevent agglomeration of Pd nanoparticles. It is well-known that the oxidizing treatments can functionalize the carbon surface mainly through the formation of carboxylic acids and phenolic groups. These functional groups often decrease the hydrophobicity of the support and increase the adsorption capacity of organic compounds [38,39]. Since the Pd nanoparticles were uniformly dispersed over the acid treated CNTs, it seems that the surface carboxylic acid groups are homogeneously formed throughout the surface of CNTs. The hydrogen of the carboxyl group can exchange with various kinds of metal cations and complexes. It has been reported that there is a strong correlation between the Pt deposited and the concentration of surface carboxylic groups on Pt/carbon black [40]. In the present study, the interaction between the surface carboxylic acid groups and Pd precursor are more likely to affect the dispersion of the Pd nanoparticles over CNTs and this is indeed observed after acid pretreatment. Therefore, the acid pretreatment in liquid phase favours the formation of

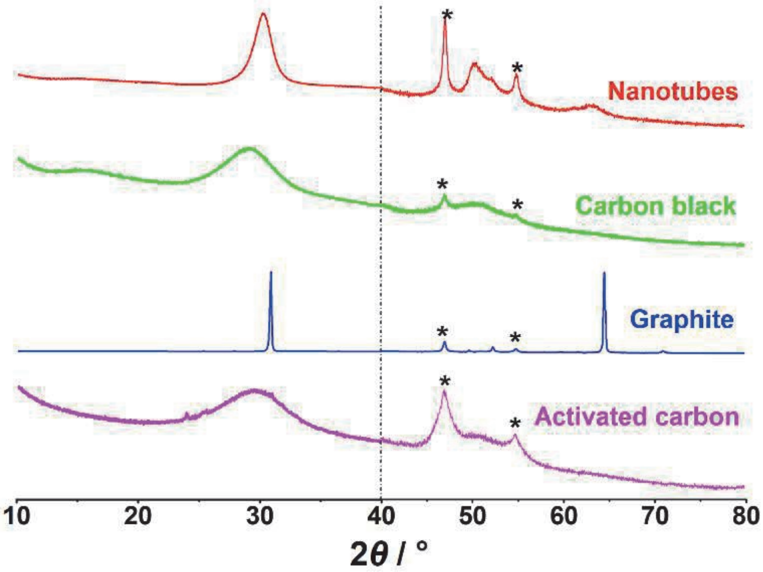

Figure 4.1: XRD diffraction patterns of (—) Pd/CNT, (—) Pd/Carbon Black, (—) Pd/Graphite, (—) Pd/Activated Carbon

carboxylic groups which control and stabilize the growth of Pd nanoparticles on CNTs.

In order to emphasize the importance of the artificially generated functional groups in stabilizing Pd nanoparticles, the functionalization was also performed to synthesize Pd supported on various carbon forms. Figure 4.2(c)–(e) display the TEM images of Pd supported on 4 structures of carbon along with their particle size distributions. All catalysts exhibited very narrow particle size distribution irrespective of the support used. The average size of Pd nanoparticle for various catalysts is given in Table 4.1. The average particle size of Pd supported on nanotubes, carbon black, and graphite are similar and smaller than the average size of Pd supported on activated carbon. This indicates that there is no correlation between the particle size and surface area of the support but rather the nature of the surface functional groups on the support influences the particle sizes and their distribution [41–43]. Therefore, a simple impregnation–reduction method with the functionalization of the carbon support can effectively be used to synthesize ultrafine Pd particles on the carbon supports.

In general, the acid treatment introduces the oxygen/nitrogen functionality which improves the metal–support interactions and hence the activity and stability of the catalyst [44]. There is a correlation between surface oxygen availability and activity. The higher the surface oxygen content, the higher the activity of the catalyst. Therefore, TPD was used to study the surface chemistry of carbon supports [45–47] by monitoring the CO and CO_2 desorption as a function of the temperature. It also provides the information about the type and amount of O-containing functional groups present on

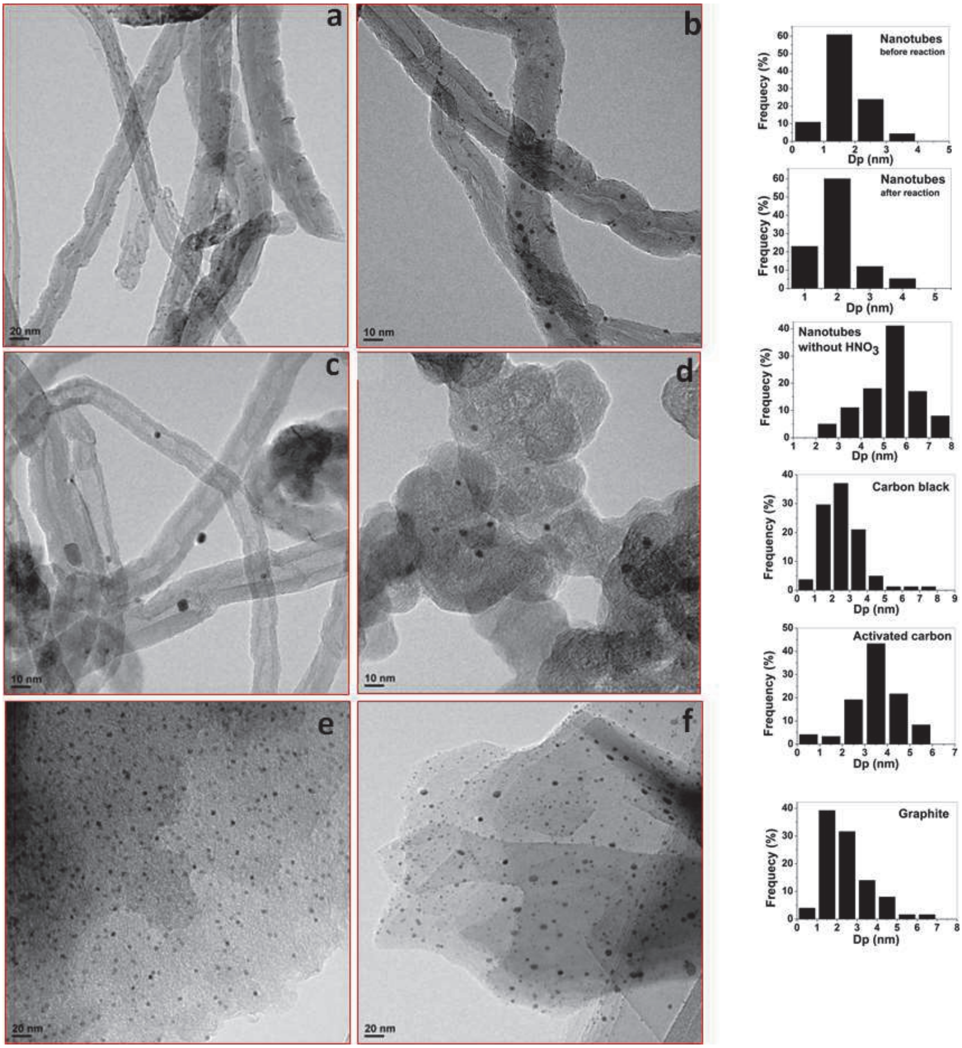

Figure 4.2: Bright field images and corresponding particle size distributions of the studied Pd supported catalysts: (a) nanotubes with HNO_3 pretreatment, (b) nanotubes after the reaction (with HNO_3 pretreatment) (c) nanotubes without HNO_3 pretreatment, (d) carbon black (e) activated carbon, and (f) graphite.

the carbon support [45–47]. The origin of CO_2 evolution at low temperature (150–450 °C) is due to the decomposition of carboxylic acids, while at high temperature (600–800 °C) it is due to the decomposition of lactones. The decomposition of carboxylic anhydrides produces both CO and CO_2 (400–650 °C), whereas the decomposition of phenols (600–800 °C), carbonyls and quinones (750–1000 °C) results in the formation of CO [45–47]. The TPD profiles for CO and CO_2 for the various Pd-supported catalysts

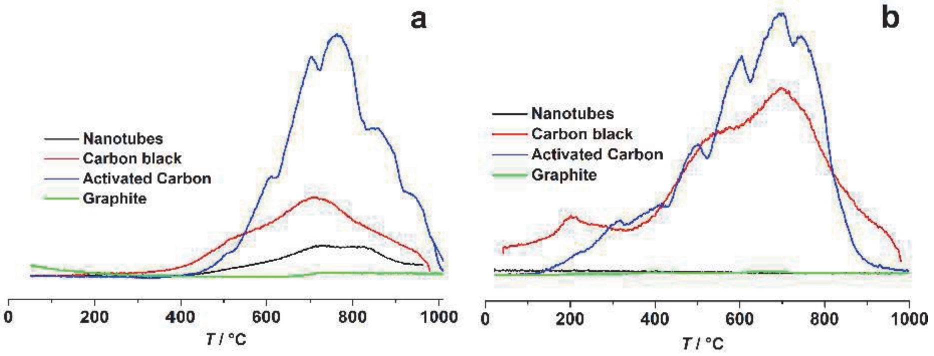

Figure 4.3: TPD for (a) CO and (b) CO_2 over various Pd supported catalysts. Experimental conditions: 100 mg catalyst; heating rate 10ºC/min; He flow rate of 30 mL/min.

are shown in Figure 4.3. The area under the curve of CO and CO_2 were used to calculate the amount of oxygen-containing functional groups and it follows the order: activated carbon > carbon black > nanotubes > graphite. In the case of graphite, very small peaks for CO and CO_2 were observed indicating that the concentration of oxygen-containing functional groups is very small. In case of the nanotubes, a small CO desorption peak between 400 and 900 °C indicated the existence of phenol and carbonyl/quinone functional groups on the surface. The CO peak observed between 350 °C and 940 °C for carbon black corresponds to the decomposition of anhydrides and carbonyls/quinones and the weak CO_2 signal at 610 °C and 860 °C is assigned to the dissociation of lactones. For the activated carbon, the CO desorption peak above 750 °C is due to the presence of the carbonyl/quinone groups, while the CO_2 desorption below 400 °C is attributed to the presence of carboxylic acids. The simultaneous desorption of CO and CO_2 around 700 °C also indicates the presence of the carboxylic anhydrides. However, the presence of CO_2 desorption peak around 600 °C shows that the contribution due to some lactones cannot be ruled out. The ratio of CO/CO_2 is usually used as an indicator of acid–base properties of the carbonaceous material [48,49]. A high CO/CO_2 ratio indicates a higher basic character of the carbon support. Table 4.1 shows that the nanotubes are more acidic while the graphite is the least acidic in nature.

The XPS was used to identify the nature of functional groups on acid pretreatment and the oxidation state of Pd-supported catalysts. Figure 4.4 shows the C 1*s* spectra of the acid pretreated and non-pretreated CNTs. For the acid pretreated sample, a small peak at 290 eV was observed in addition to the main peak of carbon at 284.6 eV. This small peak can be assigned to the oxygen-containing groups such as the carboxylic groups. The absence of such peak for non-acid pretreated CNTs confirms that the oxygen was incorporated into the surface of the oxidized CNTs and the role of the carboxylic groups in the improvement of the Pd dispersion cannot be ruled out.

Figure 4.5 shows the XPS spectra of the Pd supported on the various carbon supports

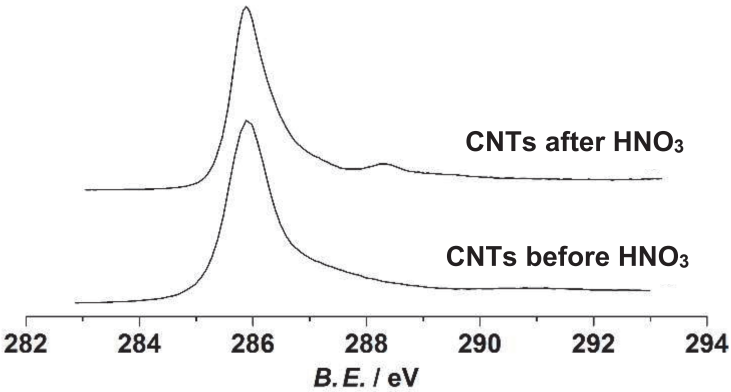

Figure 4.4: XPS spectra of C(1*s*) for CNTs before and after HNO_3 treatment

before the reaction. The Pd spectra for all catalysts were wide indicating either multiple oxidation states of the Pd species or several different interactions of the oxidized carbon support. The binding energies of Pd 3*d* observed at 335.5 and 337 eV correspond to metallic Pd^0 and PdO species, respectively. The spectra were also deconvoluted to obtain the contribution of the individual oxidation states and the relative concentration of Pd^0 for each catalyst is given in Table 4.1. The small amount of the Pd^{2+} state was observed for all catalysts before the reaction. The XPS spectra of the catalyst after the reaction were also analysed to observe if there is any change in the oxidation state of Pd. The XPS spectra of the used catalyst show that there is a large amount of Pd^{2+} (~67%) present after the reaction. However, the activity of the used catalyst (without washing of the catalyst) is very similar to that of the fresh catalyst. Therefore, the observed difference in the activity of catalysts cannot be attributed to the oxidation state of Pd.

It is well-known that the highly dispersed Pd^0 nanoparticles are susceptible to re-oxidation upon contact with air (or oxygen) [50]. The XPS measurement was performed to determine the oxidation state of Pd in the samples after reduction at 350 °C and subsequent storage in air at room temperature. The deconvolutions of the XPS spectra show that 75% of Pd was present as Pd^0 in the non-acid treated Pd/CNT sample, whereas 85–90% of Pd was present as Pd^0 in the HNO_3 pretreated Pd/CNTs sample. The high amount of metallic Pd in the acid treated Pd/CNTs is also consistent with the highly dispersed nanoparticles observed by TEM. Thus, the XPS results show that the introduction of oxygen-containing functional groups on the carbon support stabilize the Pd nanoparticles and prevent them from oxidation upon exposure to the air at room temperature. The selected preparation method leads to reproducible, almost monodisperse Pd nanoparticles with an average particles size of 1.5 nm.

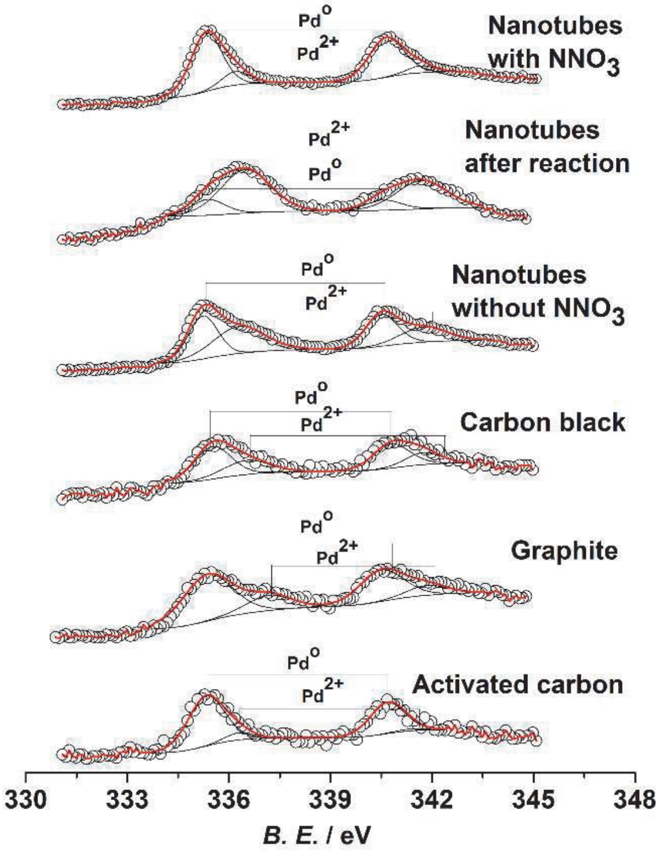

Figure 4.5: XPS spectra of Pd (3*d*) for the various Pd supported catalysts

3 – 2 – Alcohol oxidation activity

The catalytic performance of Pd supported on the various carbon supports was studied and the online profiles of benzyl alcohol conversion are depicted in Figure 4.6. The blank experiments without Pd loading exhibit a negligible benzyl alcohol conversion (<7% at 90 °C and 6 h reaction time) for all studied carbon supports. However, in the presence of the Pd catalyst, the benzyl alcohol conversion increases monotonically with time. The benzyl alcohol conversion using Pd over nanotubes, carbon black, and activated carbon reaches nearly complete conversion within 2 h, while the conversion using the graphite-supported catalyst increases continuously (50% conversion after 6 h) with time. This shows that the Pd/CNT catalyst is highly active, while the Pd/graphite catalyst is the least active under similar experimental conditions. Table 4.2 shows the catalytic performance of the various Pd-supported catalysts in the selective oxidation of benzyl alcohol. The order of the reaction rate is: nanotubes > carbon black > activated

Table 4.2: Catalytic performance of the studied Pd supported catalysts

Catalyst	Reaction rate (mol/g of Pd/ min)	Conversion (%)	$TOF^{\#}$ (h^{-1})	$S_{Aldehyde}$ (%)	$S_{Toluene}$ (%)
Pd/CNTs	1.618	98	2552	89	8
Pd/CNTs without HNO_3	0.422	95	1256	88	7
Pd/Carbon black	0.227	97	628	89	6
Pd/Activated carbon	0.073	83	445	92	5
Pd/Graphite	0.044	51	125	96	4

Reaction conditions: 300 mg catalyst; 2.4 g benzyl alcohol in 50 mL xylenes; air flow rate of 100 mL/min; 90oC; 6 h reaction time; carbon balance 98.5%.3. # TOF was calculated after 15 min.

carbon > graphite. The final product mixtures, for all catalysts, consist of benzaldehyde (>89%), toluene (<10%) and minor side products (<1%) such as benzene, benzoic acid and benzyl benzoate. The main oxidation product, benzaldehyde, is formed by oxidation of benzyl alcohol and the major side product, toluene, is mainly initially formed by disproportionation of benzyl alcohol into toluene and benzaldehyde. It should be noted that during the experiment, toluene is oxidized to benzyl alcohol at a much slower rate than that of oxidation of benzyl alcohol to benzaldehyde. The selectivity to benzaldehyde is high for all catalysts and it slightly decreases with time due to subsequent oxidation of benzaldehyde into benzoic acid. The highest production rate of benzaldehyde was observed for CNTs, while a low rate of benzyl alcohol oxidation was found for the graphite catalyst. The present finding contradicts the results reported in the literature where it has been reported that the Pd/CNTs showed lower activity than that of Pd/activated carbon which was attributed to the lower metal dispersion on CNTs [44]. However, our results demonstrate that it is possible to tune the surface chemistry of the support by specific chemical treatment and, thereby, change the activity of the catalytic surface.

In order to understand the high catalytic activity of the Pd/CNTs, several factors need to be considered. Firstly, the effect of support material on particle size distribution and/or the mode of anchoring of Pd nanoparticles onto the support should be taken into account. The TEM images and the particle size distribution data show that there is no large difference in size of the Pd nanoparticles, which range from 1.5 to 4 nm. Despite having similar metal loading and Pd particle size, particularly for carbon black- and activated carbon-supported catalysts, a large variation in the catalytic activity for the oxidation of benzyl alcohol was observed. The slight variation in overall particle size distribution alone cannot account for the observed catalytic behaviour. Furthermore, the

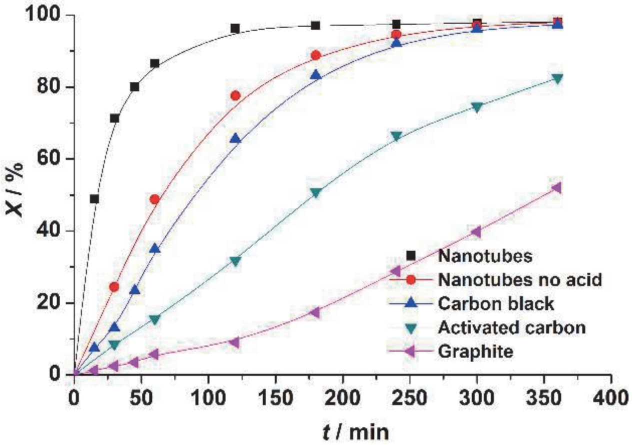

Figure 4.6: Conversion profile for benzyl oxidation with Pd-supported catalysts.

TEM images also show that the dispersion of Pd nanoparticles over the activated carbon and graphite supports is relatively higher than that over the CNTs. However, their catalytic performance for the benzyl oxidation reaction is very poor compared to that of Pd/CNT catalyst. The enhanced activity of Pd/CNTs could be attributed to the unique structure of CNTs which significantly enhances the diffusion and the accessibility of the reactants to the catalytic sites. Secondly, the presence of the surface oxygen species, such as carboxylic acid and phenolic groups on the carbon support could be considered because the catalytic activities of the carbon support are closely related to the presence of such oxygen containing species. Frequently, the availability of the surface oxygen species is used to explain a superior catalytic performance of carbon-supported catalysts [51,52]. Our TPD results showed that the total amount of O-containing functional groups for CNTs is much less than that of the activated carbon. This observation is, however, not in line with the activity ranking, implying that the amount of oxygen-containing functional groups are not the determining factor for the activity of CNT-supported Pd catalyst. Nevertheless, the role of O-functionality such as carboxylic acid groups cannot be ruled out in improving the metal dispersion and the stabilization of the nanoparticles. In order to understand the role of the carboxylic acid groups, Pd/CNT catalysts were also synthesized without nitric acid pretreatment. The Pd/CNTs without acid pretreatment showed lower reaction rate than those of the acid treated Pd/CNT catalysts (see Figure 4.6 and Table 4.2). This indicates that the O-containing functional groups, mainly carboxylic groups, render a strong metal–support interaction which increases the dispersion of the Pd nanoparticles. Therefore, the physical and chemical properties of the carbon support play an important role in determining the catalytic activity. From the activity trend observed for the various carbon-supported Pd catalysts, it is expected that several interlocked factors such as structure and size, support and steric hindrance for reactants, determine the overall catalytic activity [53]. The contribution due of each individual factor is difficult to analyse. Thus, the higher activity of Pd/CNTs can mainly be collectively attributed to the higher accessibility of the CNTs surface in combination with the narrow range Pd nanoparticles.

3 – 3 – Reusability of the catalyst

The recycling of the catalyst is very important for industrial application. If the active phase is not properly anchored onto the support, leaching can occur during the reaction, resulting in loss of activity in the subsequent runs. In addition, a strong inhibition due to adsorption of the products on the surface of the catalyst was observed in our previous study and the catalyst showed no activity in subsequent runs [54]. Therefore, the reusability of the catalyst for the aerobic oxidation of benzyl alcohol was evaluated, and the results are shown in Figure 4.7(a). The catalyst was reused with and without solvent washing. After completion of the reaction, fresh benzyl alcohol was injected into the reaction mixture (without washing of the catalyst). Similar conversion of benzyl alcohol and yield of benzaldehyde were observed with the absence of the initial disproportionation of benzyl alcohol into toluene and benzaldehyde. This confirms that the inhibition due to the products is most likely absent. Furthermore, in order to check the leaching of Pd (if any) in the liquid phase, the catalyst from the previous run was washed with xylene and dried in vacuum at room temperature for 6 h before the next run (washing of the catalyst). A similar reaction rate for benzyl alcohol up to ~98% conversion was observed. This shows a strong metal–support interaction which prevents the leaching of Pd nanoparticles during the reaction. A long term recyclability of the catalyst was also investigated for six successive runs. Each time the fresh benzyl alcohol was injected into the reaction mixture after the completion of reaction without washing the catalyst. The catalyst exhibited high selectivity for benzyl alcohol oxidation even after the fifth run. However, a minor decrease in the initial reaction rate is visible after in the fifth run (Figure 4.7c). Nevertheless, it is interesting to note that the catalyst showed more than 90% conversion after 4 h in all runs. Furthermore, the catalyst was also regenerated to understand the loss of initial activity. The used catalyst was calcined at 300 °C and reused again under similar experimental conditions. The catalyst showed an increase in the activity in the sixth run compared to that of the fifth run. However, the activity of the catalyst in the sixth run was still in some extent lower than that of the fresh catalyst. The increase in the activity of the catalyst in the sixth run (after calcination) confirms that the organic species were adsorbed onto the surface of catalyst thereby inhibiting the active sites during recycle test. Thus, the calcination treatment has a positive effect on the regeneration of the catalyst, as the active sites were cleaned by removal of the strongly adsorbed species. Furthermore, the TEM analysis of the spent catalyst shows that the size and particle size distribution were similar to that of the fresh catalyst and no sintering of the Pd nanoparticles were observed after the reaction (Figure 4.2b). Therefore, the above results demonstrate that Pd/CNTs is a promising catalytic material in the benzyl alcohol oxidation reaction with high activity, selectivity, and stability.

The selectivity to toluene for each run is also plotted in Figure 4.7(c) to understand if

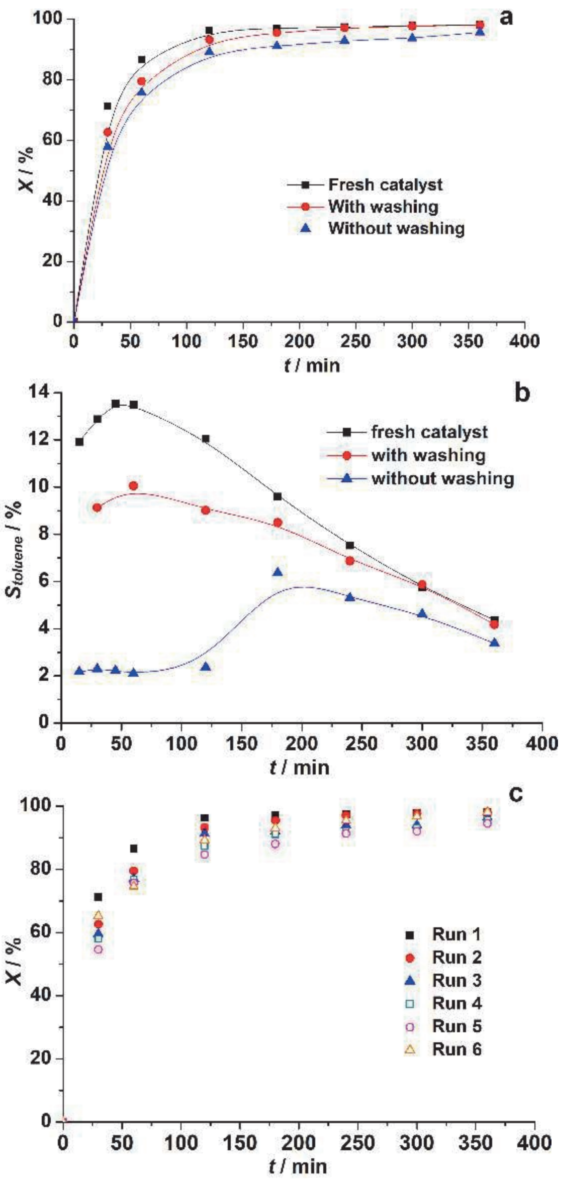

Figure 4.7: Conversion profile (a), Selectivity to Toluene with and without catalyst washing (b), and Conversion profiles for six consecutive cycles (c).

the nature of the active sites changes in the subsequent runs. Figure 4.7(c) shows that the initial rate of disproportionation of benzyl alcohol is high and it goes through a maximum. The maximum in toluene concentration is explained by further oxidation of toluene into benzyl alcohol and benzaldehyde. It should also be noted that the rate of disproportionation of benzyl alcohol using the fresh catalyst is higher than that using the spent catalyst (with washing). However, the rate of benzaldehyde formation is similar for both catalysts (not shown). This means that there are different active sites for the disproportionation and the oxidation reactions. The disproportionation sites are easily poisoned by the presence of the products. This observation is further confirmed by the fact that practically no toluene was observed initially over the spent catalyst (without washing). Further research is necessary to distinguish the nature of these two active sites. The understanding of the nature of these sites helps to develop a more active, selective, and stable catalyst for the selective oxidation of benzyl alcohol into benzaldehyde.

4 – Conclusions

A controlled design of self-assembling Pd nanoparticles on the surface of functionalized CNTs without capping agent is reported. The synthesized Pd/CNTs has a uniform dispersion and narrow size distribution around 1.5 nm. The synthesized Pd/CNTs shows an excellent catalytic activity towards the selective oxidation of benzyl alcohol which is collectively attributed to highly dispersed, uniform and nanosized Pd nanoparticles on CNTs. In addition, the peculiar morphology of the carbon nanotubes significantly improves the diffusion of the reactant and products and the accessibility to the catalytic sites. The complete reusability of the catalyst without Pd leaching shows that the functionalization of the carbon support yielded a strong metal–support interaction. Meanwhile, this synthesis approach was not only limited to the structural form of carbon (nanotube), but can also be used to synthesize a wide variety of carbon-supported catalysts with controlled Pd nanoparticle size distribution. The catalytic activities for the selective aerobic oxidation of benzyl alcohol significantly depend on the nature of the supports, and follow the order: nanotubes > carbon black > activated carbon > graphite with a high selectivity to benzaldehyde (>89%). Furthermore, this study shows that there is no correlation between the amount of oxygen-containing functional groups and the activity of Pd-supported catalysts. The excellent activity and reusability of Pd/CNTs, demonstrated in this study, make it a promising candidate for the selective oxidation of benzyl alcohol. On the fresh and thoroughly washed catalysts, significant disproportionation is observed, indicating a two-site reaction mechanism, one of disproportionation and one of oxidation. The disproportionation sites are very rapidly deactivated by the reaction products.

References

1. Y. Xing, J. *Phys Chem B 108,* **2004**, 19255–19259.
2. C. C. de Paula, A. Garcia Ramos, A. C. da Silva, E. Cocchieri Botelho and M. C. Rezende, *Carbon 40,* **2002**, 787–788.
3. B. Yoon and C. M. Wai, *J Am Chem Soc 127,* **2005**, 17174–17175.
4. J.-P. Tessonnier, L. Pesant, G. Ehret, M. J. Ledoux and C. Pham-Huu, *Appl Catal A 288,* **2005**, 203–210.

5. Y. Zhang, Y. Liu, G. Yang, Y. Endo and N. Tsubaki, *Catal Today 142,* **2009**, 85–89.
6. Z. Jian, P. Liu, F. Li, P. He, X. Guo, M. Chen and H. Zhou, *Angew Chem Int Ed 53,* **2014**, 442–446.
7. S. Akbayrak and S. Özkar, *ACS Appl. Mater. Interfaces 4,* **2012**, 6302–6310.
8. C. Chen, J. Zhang, B. Zhang, C. Yu, F. Peng and D. Su, *Chem Commun 49,* **2013**, 8151–8153.
9. R. Singh and A. Singh, *Carbon 47,* **2009**, 271–278.
10. J. Xu and T. Zhao, *J. Power Sources 195,* **2010**, 1071–1075.
11. T. Koh, H. M. Koo, T. Yu, B. Lim and J. W. Bae, *ACS Catal 4,* **2014**, 1054–1060.
12. A. Tavasoli, R. M. M. Abbaslou, M. Trepanier and A. K. Dalai, *Appl Catal A 345,* **2008**, 134–142.
13. S. Wang, X. Wang and S. P. Jiang, *Langmuir 24,* **2008**, 10505–10512.
14. T. Fujigaya and N. Nakashima, *Adv Mater 25,* **2013**, 1666–1681.
15. S.-A. Park, D.-S. Kim, T.-J. Kim and Y.-T. Kim, *ACS Catal 3,* **2013**, 3067–3074.
16. X. Chen, Y. Hou, H. Wang, Y. Cao and J. He, *J Phys Chem C 112,* **2008**, 8172–8176.
17. A. Quintanilla, V. Butselaar-Orthlieb, C. Kwakernaak, W. Sloof, M. Kreutzer and F. Kapteijn, *J Catal 271,* **2010**, 104–114.
18. D. Astruc, F. Lu and J. R. Aranzaes, *Angew Chem Int Ed 44,* **2005**, 7852–7872.
19. R. J. White, R. Luque, V. L. Budarin, J. H. Clark and D. J. Macquarrie, *Chem Soc Rev 38,* **2009**, 481–494.
20. Z.-P. Sun, X.-G. Zhang, H. Tong, R.-L. Xue, Y.-Y. Liang and H.-L. Li, *Appl Surf Sci 256,* **2009**, 33–38.
21. V. Mazumder and S. Sun, *J Am Chem Soc 131,* **2009**, 4588–4589.
22. W. Li, X. Zhao and A. Manthiram*, J Mater Chem A 2,* **2014**, 3468–3476.
23. V. Lordi, N. Yao and J. Wei, *Chem Mater 13,* **2001**, 733–737.
24. R. Yu, L. Chen, Q. Liu, J. Lin, K.-L. Tan, S. C. Ng, H. S. Chan, G.-Q. Xu and T. A. Hor, *Chem Mater 10,* **1998**, 718–722.
25. W. X. Chen, J. Y. Lee and J. Z. Liu, *Chem Commun*, **2002**, 2588–2589.
26 Z. Liu, L. Hong, M. P. Tham, T. H. Lim and H. Jiang, *J Power Sources 161,* **2006**, 831–835.
27 C. Cui, L. Gan, M. Neumann, M. Heggen, B. Roldan Cuenya and P. Strasser, *J Am Chem Soc 136,* **2014**, 4813–4816.
28. J. Planeix, N. Coustel, B. Coq, V. Brotons, P. Kumbhar, R. Dutartre, P. Geneste, P. Bernier and P. Ajayan, *J Am Chem Soc 116,* **1994**, 7935–7936.
29. X. Wang, G. Wu, N. Guan and L. Li, *Appl Catal B 115-116,* **2012**, 7-15.
30. A. Abad, A. Corma and H. Garcia, *Chem Eur J 14,* **2008**, 212–222.
31. C. Zhou, Y. Chen, Z. Guo, X. Wang and Y. Yang, *Chem Commun 47,* **2011**, 7473–7475.
32. A. Villa, M. Plebani, M. Schiavoni, C. Milone, E. Piperopoulos, S. Galvagno and L. Prati, *Catal Today 186,* **2012**, 76–82.
33. J. Feng, C. Ma, P. Miedziak, J. K. Edwards, G. L. Brett, D. Li, Y. Du, D. J. Morgan and G. J. Hutchings, *Dalton Trans 42,* **2013**, 14498–14508.
34. N. Dimitratos, A. Villa, D. Wang, F. Porta, D. Su and L. Prati, *J Catal 244,* **2006**, 113–121.
35. A. Villa, N. Janjic, P. Spontoni, D. Wang, D. S. Su and L. Prati, *Appl Catal A 364,* **2009**, 221–228.
36. X. Yu, Y. Huo, J. Yang, S. Chang, Y. Ma and W. Huang, *Appl Surf Sci 280,* **2013**, 450–455.
37. E. Antolini, F. Cardellini, L. Giorgi and E. Passalacqua, *J Mater Sci Lett 19,* **2000**, 2099–2103.

38. J. Rangel-Mendez and M. Streat, *Water Res 36,* **2002**, 1244–1252.
39. Y. Li, C. Lee and B. Gullett, *Fuel 82,* **2003**, 451–457.
40. K. Yasuda and Y. Nishimura, *Mater Chem Phys 82,* **2003**, 921–928.
41. A. Villa, G. M. Veith, D. Ferri, A. Weidenkaff, K. A. Perry, S. Campisi and L. Prati, *Catal Sci Technol 3,* **2013**, 394–399.
42. E. G. Rodrigues, S. A. Carabineiro, J. J. Delgado, X. Chen, M. F. Pereira and J. J. Órfão, *J Catal 285,* **2012**, 83–91.
43 N. E. Kolli, L. Delannoy and C. Louis, *J Catal 297,* **2013**, 79–92.
44. A. Villa, D. Wang, P. Spontoni, R. Arrigo, D. Su and L. Prati, *Catal Today 157,* **2010**, 89–93.
45. J. L. Figueiredo, M. F. Pereira, M. M. Freitas and J. J. Órfão, *Ind Eng Chem Res 46,* **2007**, 4110–4115.
46. E. G. Rodrigues, M. F. Pereira, X. Chen, J. J. Delgado and J. J. Órfão, *J Catal 281,* **2011**, 119–127.
47. J. Figueiredo, M. Pereira, M. Freitas and J. Orfao, *Carbon 37,* **1999**, 1379–1389.
48. Y.-C. Chiang, W.-H. Lin and Y.-C. Chang, *Appl Surf Sci 257,* **2011**, 2401–2410.
49. C. Moreno-Castilla, M. Lopez-Ramon and F. Carrasco-Marın, *Carbon 38,* **2000**, 1995–2001.
50. A. F. Lee, S. F. Hackett, J. S. Hargreaves and K. Wilson, *Green Chem 8,* **2006**, 549–555.
51. J. L. Figueiredo and M. F. R. Pereira, *Catal. Today 150,* **2010**, 2–7.
52. J. Zhu, S. A. Carabineiro, D. Shan, J. L. Faria, Y. Zhu and J. L. Figueiredo, *J Catal 274,* **2010**, 207–214.
53. D. Wang, A. Villa, D. Su, L. Prati and R. Schlögl, *ChemCatChem 5,* **2013**, 2717–2723.
54. E. Skupien, R. J. Berger, V. P. Santos, J. Gascon, M. Makkee, M. T. Kreutzer, P. J. Kooyman, J. A. Moulijn and F. Kapteijn, *Catalysts 4,* **2014**, 89–115.

Chapter 5

Bimetallic CuAu Electrocatalysts on Multi-Walled Carbon Nanotubes and their Application in CO_2 Reduction

Following the recommendations from the enlightening studies of Nørskov's and Koper's teams, bimetallic copper-gold catalysts of various Cu:Au ratios were investigated in an attempt to confirm the predicted break in the scaling relationships between the intermediates' binding energies in the CO_2 electrocatalytic reduction reaction. A colloidal route based on the reduction of $CuCl_2$ by ethylene glycol was employed to obtain monodisperse Cu nanoparticles that were subsequently immobilized on multi-walled carbon nanotubes (MWCNTs). The bimetallic catalysts of controlled Cu:Au ratios were obtained from Cu/MWCNT by galvanic replacement of a fraction of the metallic Cu by $HAuCl_4$. Thermogravimetric analyses combined with XRD confirm that Au was incorporated into the catalyst, but no evidence is found that Au and Cu are mixed at the atomic level. The catalytic performance for CO_2 reduction suggests contributions of separated Au and Cu phases. With decreasing Cu:Au ratios, the CO production increases, while the hydrocarbon production either decreases or is unaffected. No benefit of Au addition on the activation overpotential for hydrocarbon production was detected, whereas the activation overpotential for CO production using bimetallic catalysts decreases as more Au is present. The monometallic Au/MWCNT catalyst has the lowest activation overpotential for CO production, showing that the scaling relationships are still in play in these systems.

1 – Introduction

The relevance of the electrocatalytic reduction of CO_2 is more and more recognized as realistic and feasible on the large scale, provided that the performance of the electrocatalyst makes it economically viable. A satisfactory performance comes with severe requirements, such as strong selectivity to a particular product, long term stability, and acceptable energy efficiency. Copper has been mainly studied in its bulk form, and it is the only metal capable of producing hydrocarbons from CO_2, albeit with low Faraday efficiencies (H_2 is the main product). CO_2 electrocatalytic reduction studies involving heterogeneous catalysts such as those encountered in the bulk chemical and petrochemical industries are becoming more abundant. These materials usually consist of metal nanoparticles on a high surface area support, and are almost always more active than the corresponding bulk metals.

Catalysis science/engineering and electrochemistry have to be combined to tackle this difficult reaction. Particular focus is placed on the activation overpotential, which directly impacts the energy efficiency of the overall system, imposing a larger cell voltage than would be required according to thermodynamics. This would result in a drastic energy loss in a large scale process and would strongly impede its economic feasibility. Nørskov *et al.* [1-3] and Koper *et al.* [4, 5] studied theoretical and experimental aspects in depth, and were able to explain the poor activities and high activation energy (or activation overpotential) with the scaling relationships between the binding energies of the many reaction intermediates. In short, according to the famous Sabatier principle [6], the best catalyst for a given reaction will have a binding energy of the reaction intermediate on the catalyst high enough in order to chemisorb the compound and activate bonds, but low enough in order to desorb the product and avoid inhibition. The reaction intermediate often chemically resembles the reactant and product, and, as a consequence, the binding energies of reaction intermediates will be close to each other and related to each other on a given catalyst surface. In a reaction involving a single intermediate, it is theoretically possible to find a catalyst that will conduct the reaction with zero activation energy. However, most reactions have a multi-intermediate mechanism and this ideal catalyst can only be approached. The binding energies of these intermediates on a catalyst surface scale with one another, so it is impossible to optimise a single active site for a given intermediate without degrading its properties for another intermediate. The strategy Nørskov and Koper devise is to step away from uniform active catalyst sites, and introduce active site heterogeneity on the surface. This can be done using promoters, enzymes, co-catalysts and multi-metallic catalysts. The latter option is explored in this study, with a focus on copper and gold.

Copper-gold alloys were already studied in 2012 by Christophe *et al.* [7] in the form of metal sheets. Four alloy compositions (Au_1Cu_{99}, Au_1Cu_9, Au_1Cu_4, and Au_1Cu_1) were benchmarked against pure Cu and pure Au. Electrocatalytic CO_2 reduction was performed in a 0.1 M phosphate buffer for 3 h. In summary, increasing the Au content in the electrode yielded a strong enhancement of CO production and a near complete suppression of hydrocarbon production compared to a pure Cu electrode. The electrode with Au_1Cu_1 produced more CO than the pure Au electrode by approximately 80%. The authors explain this behaviour with the slow desorption of CO from Cu, whereas it desorbs faster from Au. This is believed to provoke CO spill-over from Cu sites to Au sites before hydrogenated species can be formed, Au being inactive for hydrocarbon production. Likewise, compared to pure Cu, the amount of adjacent Cu sites supposedly necessary for the formation of C-C bonds is lower on Au_1Cu_1, explaining the absence of higher hydrocarbons in the CO_2 reduction products on this electrode. Kim *et al.* [8] conducted a similar study involving nanoparticulate Au-Cu alloys synthesized via a colloidal method. Their results show that at -1.1 V vs. RHE, Au_3Cu_1 and Au_1Cu_1 have the highest activity for CO production (~5% increase relative to pure Au). This contrasts with the study by Christophe *et al.* [7] and might be explained by the difference in the applied potentials. It underlines again the strong structure and process sensitivities of the CO_2 reduction reaction. At increasing Au content the hydrocarbon production was drastically reduced [8], which was also observed by Christophe *et al.* [7]. 5% of the current was still used for producing CH_4 at -1.1 V vs. RHE on AuCu, but no hydrocarbons were detected at any potential when Au:Cu increased further (Au_3Cu and Au). In line with the reasoning of Christophe *et al.* [7], Kim *et al.* [8] attributed the activity gain in CO production to a combination of geometric and electronic effects in relation with the position and neighbouring of the Au and Cu atoms.

In a more recent study by Jovanov *et al.* [9], bimetallic sheets of Au-Cd alloy were explored both theoretically and experimentally. A DFT-based study identified Au_3Cd (211) as the ideal active site for CO_2 reduction to CO. However, implementing a Au_3Cd sheet for CO_2 reduction showed catalytic properties (activity and selectivity) very similar to those of pure Au. The authors argue that surface rearrangement under electrocatalytic conditions must be occurring to explain the observations. Such a rearrangement was indeed observed by Kim *et al.* [10] on catalysts derived from colloidal Cu nanoparticles. SEM analyses revealed that the 7 nm spherical nanoparticulate Cu turned into cubic structures of various sizes up to 40 nm.

In this chapter the catalytic properties of CuAu bimetallic nanoparticles of various compositions are investigated. They were prepared via a combined colloidal and galvanic route and immobilized on multi-walled carbon nanotubes. The goal is to find a suitable composition to break the scaling relationships, which might lead to a lower activation overpotential and higher productivities in CO_2 reduction.

2 – Experimental

2 – 1 – Catalyst preparation

Multi-walled carbon nanotubes (MWCNTs) (≥ 95%, CheapTubes.com) were used as electrocatalyst support without purification. The supplied MWCNTs contain 1.5 wt% nickel from their preparation. Their outer diameter is 30-50 nm, their inner diameter is 5-10 nm and their length is 10-20 µm. The surface area is 60 $m^2 \cdot g^{-1}$ and the electrical conductivity is > 100 $S \cdot cm^{-1}$. Figure 5.1 shows a TEM image of the MWCNTs as supplied. MWCNTs were surface-functionalized by immobilization of pyrene carboxylic acid (PCA, 97%, Sigma-Aldrich) through π-π interactions, following Simmons' methodology [12] developed for single-walled carbon nanotubes (SWCNTs). The supplied MWCNTs were added to deionized water and sonicated for 15 minutes in a Eumax ultrasonic bath (UD50SH-2L, 50W) at room temperature. In parallel, 1 mg PCA per 3 mL methanol (99.8% Sigma-Aldrich) was sonicated in the same ultrasonic bath for 15 min to completely dissolve it, yielding a 1.35 mM solution. That solution was then added to the water suspension of MWCNTs (1:2 volume ratio, PCA in methanol/MWCNT in water), in order to obtain a PCA loading on MWCNTs of 10 wt%. This suspension was further sonicated for approximately 30 min at room temperature. The resulting PCA-MWCNTs were filtered and washed with MilliQ water repeatedly to remove methanol.

Colloidal Cu nanoparticles were prepared similarly to the procedure described by Oh *et al.* [13] for Pt nanoparticles. $CuCl_2.2H_2O$ (≥99.99%, Sigma-Aldrich) was used as the Cu source. 100 mg $CuCl_2.2H_2O$ was dissolved in 50 mL ethylene glycol (EG). 200 mg NaOH pellets (≥97.0%, Sigma-Aldrich) were added resulting in a 0.1 M concentration. The resulting suspension was sonicated for 15 minutes. The pH adjustment with H_2SO_4

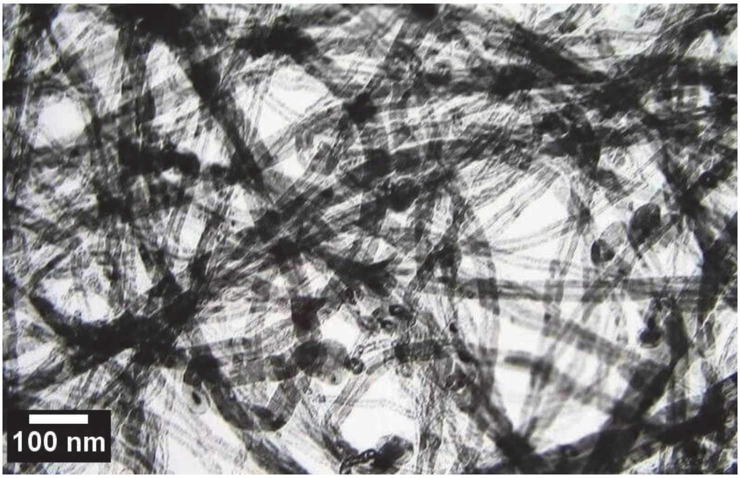

Figure 5.1: TEM image of the MWCNTs as supplied by CheapTubes.com [11]

after the nanoparticle formation, as reported by Oh *et al.*, was skipped because it provoked re-oxidation and re-dissolution of the Cu nanoparticles during preliminary trials. In order to keep the total metal loading (Cu + Au) on the MWCNTs at 10 wt.% after galvanic replacement while varying the Cu:Au ratio, the initial Cu loading needed to be adjusted. Different amounts of PCA-MWCNTs were introduced to the Cu colloidal suspension and were sonicated for 15 minutes in the same bath. The quantities involved and the target metal loadings are summarized in Table 5.1. The suspension was then stirred and purged with 20 $mL \cdot min^{-1}$ nitrogen gas for 1 h and was refluxed at 160 °C for 3 h under nitrogen gas. The suspension was allowed to cool down to room temperature and vacuum-filtered over a Magna nylon filter (0.45 μm thick, 47 mm in diameter, Maine Manufacturing) and washed 5 times with ethanol (anhydrous, VWR international) to remove all the EG. The resulting carbon-supported Cu catalyst was dried in air for 3 h at 80 °C. The resulting (chunky) material was then ground to a fine powder. This polyol synthesis was studied by Caroll *et al.* [14] who proposed the reaction mechanism presented in Figure 5.2. According to these authors, ethylene glycol functions both as solvent and reducing agent and in addition, it forms a capping agent in the form of polyethylene glycol (PEG). The hydroxide reacts with the polyol forming water and a glycolate ion. This forms a complex with copper as it exchanges with chloride. Another hydroxide then reacts with this complex to form water, metallic copper, a glycolate ion and a glycoaldehyde molecule. At these reaction conditions the EG is also polymerizing to PEG, which regulates nanoparticle growth and encapsulates them.

Table 5.1: Precursor quantities involved in the synthesis of (bi-)metallic catalysts.

Cu NP colloidal synthesis and immobilization on PCA-MWCNT				Galvanic replacement of Cu by Au			
Cu:Au (mol:mol)	**w_{CuCl2} (mg)**	**$w_{PCA\text{-}MWCNT}$ (mg)**	**Cu initial theoretical loading (wt.%)**	**$w_{Cu/PCA\text{-}MWCNT}$ involved in galvanic exchange (mg)**	**w_{HAuCl4} introduced to 250 mg of Cu/MWCNT (mg)**	**(Cu+Au) theoretical loading (wt.%)**	**theoretical Cu:Au (mol:mol)**
1:0	103	337	10.2	248	0	10.2	1:0
98:2	99	345	9.7	252	4	10.0	97:3
70:30	105	478	7.6	255	30	10.3	71:29
50:50	101	551	6.4	252	42	10.3	47:53
0:1	99	691	5.1	253	55	10.1	0:1

In the colloidal synthesis, $CuCl_2$ was dissolved in 50 mL EG together with 200 mg NaOH. In the galvanic exchange, $HAuCl_4$ was dissolved in 30 mL ethanol before adding the Cu/PCA-MWCNT. The theoretical loading and the theoretical Cu:Au ratio are calculated based on the stoichiometry of oxidation of Cu^0 by Au^{3+} (3 Cu for 2 Au).

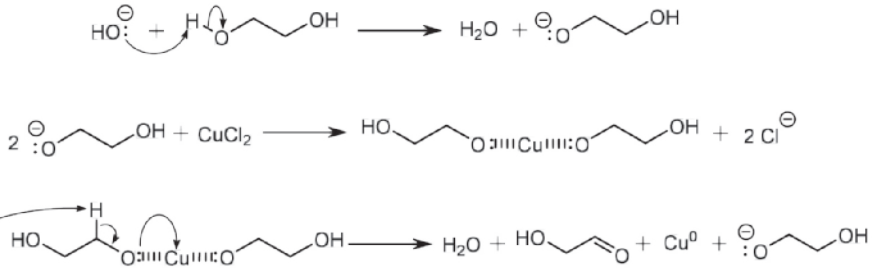

Figure 5.2: Reaction mechanism of the reduction of Cu^{2+} by EG under NaOH, as proposed by Caroll *et al.* [14]. IIIII symbolises the coordination bonds of the Cu-EG complex.

In order to obtain bimetallic CuAu nanoparticles of similar particle size distribution, galvanic replacement of Cu by Au was performed. $HAuCl_4$ was dissolved in 30 mL ethanol, resulting in a yellow solution. 250 mg Cu/MWCNT was added and sonicated for 15 min to fully disperse them. This mixture was stirred for 12 h at room temperature to ensure reaction completion. The mixture was filtered under vacuum and washed 5 times with 25 mL ethanol. The filtrate turned green, indicating the presence of $CuCl_2$ complex. The filtered material was dried in an oven at 80°C. Different copper-gold compositions were made by varying both the amount of Au^{3+} introduced and the initial

$$2\,Au^{3+} + 3\,Cu^{0} \longrightarrow 2\,Au^{0} + 3\,Cu^{2+}$$

Figure 5.3: Reaction scheme of the galvanic replacement of Cu by Au.

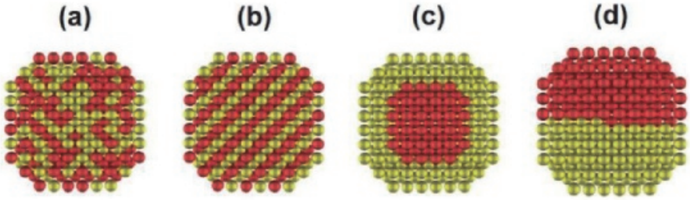

Figure 5.4: Bimetallic nanoparticles structures generally encountered. (a) random alloy, (b) ordered alloy, (c) core-shell, (d) Janus-like, from [20].

loading of Cu on MWCNTs, according to the stoichiometry of the reaction (Figure 5.3). A complete replacement has also been performed, to verify that the reaction was quantitative and that the amount of copper replaced is really controlled by the amount of $HAuCl_4$ introduced. TGA and XRD analyses confirmed that this was the case. The other Cu:Au target compositions were 98:2, 70:30 and 50:50. Table 5.1 summarizes the quantities involved in the Cu/MWCNT synthesis and in the galvanic exchange.

The formation of bimetallic nanoparticles can lead to different structures as depicted in Figure 5.4. In case the two metals have a strong affinity for each other, diffusion leads to an alloy which can be random (Figure 5.4-a) or ordered (Figure 5.4-b) depending if a crystal structure corresponds with a thermodynamic minimum. In case the affinity between the two metals is smaller, they tend to remain in segregated phases such as the core-shell or the Janus-like structure (Figure 5.4-c and d, respectively). In the case of Cu and Au, the regular intermetallic compounds (Figure 5.4-b) Cu_1Au_3, Cu_1Au_1 and Cu_3Au_1 have been reported [15-19] and their XRD data are available from the ICDD, so these crystallographic phases could form in our system.

The catalysts were applied onto a 7 x 3 cm conductive carbon cloth (415 μm thickness, 10% PTFE, Quintech) using the spraying methodology commonly encountered in fuel cell technology [21]. 190 mg catalyst was dispersed by sonication (30 min) in 64 mL ethanol to form an ink suspension of 3 $mg{\cdot}mL^{-1}$. Nafion is added to this suspension and serves as a binder and later as a proton conductor. 1.6 g Nafion solution (PFSA 5 wt.% in ethanol, Quintech) was added, which corresponds to a 7:3 composition of catalyst:Nafion. The carbon cloth was placed on an 80°C hot plate and the suspension was sprayed onto it with an air brush (Anest Iwata HP-SB Plus) under 2 bar N_2 pressure, resulting in a uniform distribution. However, large losses were observed in preliminary experiments (up to 50%), because some catalyst was sprayed next to the cloth or was entrained by the fume hood ventilation. Therefore, the amount of catalyst ink was adjusted in order to reach the target of 5 mg per cm^2 of carbon cloth. The catalyst loading (mg·cm^{-2}) on the electrode is measured by weighing the electrode before and after spraying. A blank electrode, containing only PCA-MWCNT and Nafion binder, was also prepared to assess the catalytic activity of the nanotubes themselves.

2 – 2 – Catalyst characterization

Particle size distributions of the prepared catalysts were determined from/using transmission electron microscopy (TEM) using an FEI Tecnai TF20 electron microscope with a field emission gun operated at 200 kV as source of electrons. Samples were mounted on Quantifoil microgrid carbon polymer supported on a metal grid by placing a few droplets of a suspension of ground sample in ethanol on the grid, followed by drying at ambient conditions.

Cu and (Cu+Au) loadings on PCA-MWCNT were determined by thermo-gravimetric analysis (TGA) (TGA/SDTA851^e, Mettler Toledo). The heating profile was set from 25 to 750 °C with a rate of 10 °C·min^{-1} in a flow of 100 mL·min^{-1} air. Weight losses observed at around 150 and 250 °C were attributed to the evaporation of H_2O and EG respectively. Therefore, the initial mass considered for the calculation of Cu and (Cu+Au) loadings was the mass present at 300 °C. It was assumed that the copper was completely oxidized to Cu_2O at the end of the TGA experiment and the residual mass was corrected to calculate the Cu loading. In the case of CuAu bimetallics, as it was determined that the galvanic replacement reaction was quantitative, the gold content was calculated from the quantity of $HAuCl_4$ used for that reaction, and used to deduce the copper content. Combined results of TGA and TEM-EDX of as-supplied MWCNT revealed a residual mass corresponding to 1.5 wt.% nickel (or 1.9 wt.% NiO), thus the loading was also corrected in this respect.

The metal particles were examined by powder X-ray diffraction (XRD) using a Bruker 2D phaser with a Cu $K\alpha$ radiation source (λ = 1.54184 Å). The 2θ Bragg angles were scanned over a range of 20-80 ° at a rate of 0.4 °·min^{-1} with a 0.02° angular resolution. Bragg's law was used to convert the x-axis from 2θ degrees to d spacing (Å). In order to precisely index the reflections of Au (111), Au_3Cu (111), AuCu (111) $AuCu_3$ (111) and Cu (111) and to accurately compare them with ICSD references, the C (002) reflection was set to 3.395 Å [22] for all diffraction patterns.

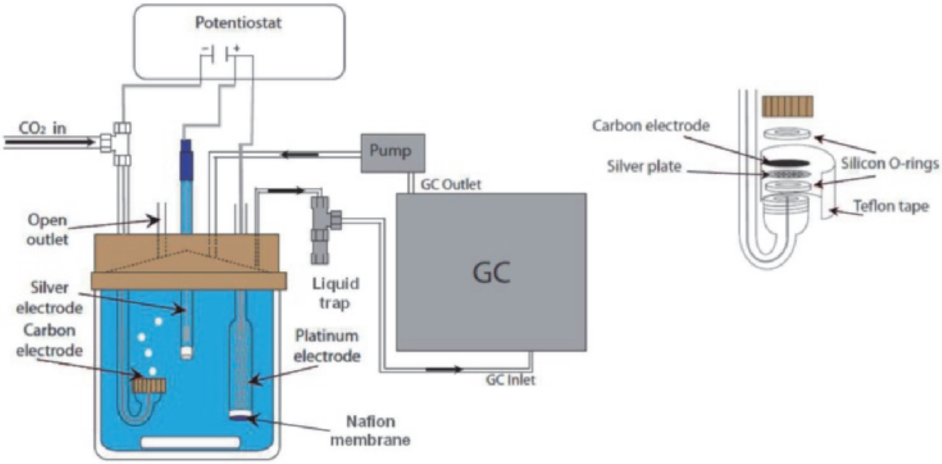

Figure 5.5: Schematic of the 3-electrode cell used in the electrocatalytic experiments (left) and schematic of the Gas Diffusion Electrode (GDE) assembly on the glass tube (right).

2 – 3 – Catalytic performance assessment

The performance of the catalysts was evaluated using a continuous, 3-electrode electrocatalytic flow cell. A schematic overview is presented in Figure 5.5. The cell is a 3-electrode system comprising a Ag/AgCl reference electrode and a platinum counter electrode in a small compartment separated with a Nafion membrane. The working electrode was a catalyst-loaded Gas Diffusion Electrode (GDEs) described in the experimental section. This was mounted on a U-shaped glass tube, on top of a silver perforated plate (current collector), and sealed with O-rings and Teflon tape as depicted in Figure 5.5. The GDE exposed area is a disk of 1 cm in diameter (0.8 cm^2). Electronic contact with the potentiostat was made via a silver wire placed through the glass tube. This set-up allowed supplying CO_2 directly through the GDE, thereby avoiding mass transport limitations and keeping a high concentration of CO_2 in the vicinity of the GDE. The volume of the headspace (between the surface of the liquid electrolyte and the lid) was minimized to circa. 15 mL to keep the response time of the set-up as short as possible. This headspace was connected to the gas chromatograph (GC) and via a closed loop the gas was continuously circulated at 10 $mL\cdot min^{-1}$, ensuring a similar composition, and providing simultaneous stirring of the head space. A small liquid trap was placed between the gas sampling port of the cell and the GC in order to avoid flooding the sampling line of the GC.

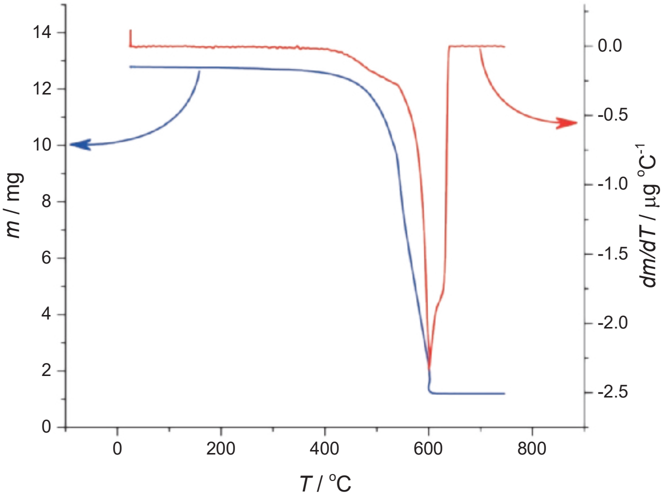

Figure 5.6: TGA of Cu/MWCNT 5.1 wt.% used for complete galvanic replacement with Au. (—) sample mass vs temperature and (—) its first derivative representing mass loss rate vs temperature. Temperature was increased at a rate of 10 °C·min^{-1} under 100 mL·min^{-1} synthetic air. The major mass loss is due to oxidation of the carbonaceous support.

A pH 7 solution of 0.1 mol·L^{-1} phosphate buffer was used (KH_2PO_4, ≥99.995%, Sigma-Aldrich and K_2HPO_4, ≥99.999%, Sigma-Aldrich) as supporting electrolyte. The cell was purged with 20 mL·min^{-1} CO_2 (99.995%, Linde gas) while the electrolyte was stirred at 400 rpm, to strip air and to saturate the solution with CO_2. The extent of CO_2 saturation and the presence of O_2 were monitored by the GC. Once saturated, the flow of CO_2 through the GDE was set to 0.5 mL·min^{-1}. Potentiostatic electrolysis (Autolab PGSTAT302N) was performed during 2 h at potentials between -0.2 and -2.0 V vs. SHE to measure the catalytic activity. The data from the potentiostat and GC were synchronised to correlate the current input to the productivity for a given time. The time resolution of the potentiostat is 1 second, whereas that of the GC is 6 min. The current is therefore averaged with a 6 minute-resolution (box-car averaging). The productivity for each potential value is calculated from the average productivity over at least 30 min (5 GC analyses), once steady state was reached.

3 – Results & discussion

3 – 1 – Catalyst characterization

Figure 5.6 gives an example of the TGA patterns, here for the sample aiming at complete galvanic replacement of Cu by Au. The combustion of the support results in the observed mass loss and a copper(I) oxide residue. The data given in Table 5.2 (last

Table 5.2: Quantification by TGA of the metal loading on MWCNT before and after galvanic replacement.

Cu:Au (theoretical)	theoretical Cu initial loading (wt.%)	Cu initial loading TGA (wt.%)	(Cu+Au) theoretical loading (wt.%)	(Cu+Au) loading TGA (wt.%)	Cu:Au (TGA)
1:0	10.2	8.4	10.2	8.4	1:0
97:3	9.7	9.6	10.0	9.8	97:3
71:29	7.6	6.5	10.3	7.9	62:38
47:53	6.4	5.6	10.3	8.0	32:68
0:1	5.1	6.4	10.1	12.1	0:1

The Cu:Au ratio is calculated assuming that 100% of $HAuCl_4$ has reacted during the galvanic replacement. Theoretical values based on synthesis quantities are given for comparison.

row) show that the reaction is quantitative: Cu loading (5.1 wt.% theoretical) before replacement was determined to be 6.4 wt.% (± 0.7 wt.%) or 0.064 g_{Cu}/g_{MWCNT} (Table 2), which corresponds to $1.01 \cdot 10^{-3}$ mol_{Cu}/g_{MWCNT}. Following the reaction stoichiometry, complete galvanic replacement should yield $6.71 \cdot 10^{-4}$ mol_{Au}/g_{MWCNT}, which corresponds to 0.132 g_{Au}/g_{MWCNT}, or 13.2 wt.%. The Au loading determined using TGA after galvanic replacement is 12.1 wt.% (± 0.7 wt.%), which is in good agreement with the prediction in view of the TGA experimental uncertainty. Likewise, XRD analysis does not show any Cu reflections after galvanic replacement, in agreement with the assumption that the galvanic replacement proceeds until all $HAuCl_4$ has reacted. Thus, the introduced amount of $HAuCl_4$ can be used to estimate the Cu:Au ratios of the prepared catalysts. It should be noted that it is assumed that in the residual mass Cu is present as Cu_2O. The results for all samples are given in Table 5.2, together with the theoretical values from the synthesis quantities. Table 5.2 shows that the Cu loading is generally lower than expected, except for Cu:Au = 0:1 (6.4 wt.% Au measured against 5.1 wt.% theoretical). This difference is, however, not significant in view of the experimental uncertainty of the TGA method (0.7 wt.%). It should be noted that the TGA results reveal that in all cases the galvanic replacement yielded a higher Cu loss than expected, as is evidenced by the Cu:Au ratios determined by TGA that are lower than the Cu:Au ratio expected from the quantities involved in the reaction. In fact, recalculating the molar ratio of $Cu_{reacted}$ to $Au_{introduced}$ gives a value between 1.64 and 1.72, where the stoichiometry of the reaction in Figure 5.3 predicts a value of 1.5. This can be explained by the fact that the surface of the Cu nanoparticles was probably

$$2\,Au^{3+} + 3\,Cu_2O + 6\,H^+ \longrightarrow 2\,Au^0 + 6\,Cu^{2+} + 3\,H_2O$$

Figure 5.7: Reaction scheme of the galvanic replacement of Cu_2O by Au.

Table 5.3: Catalyst loadings and metal loadings on the gas diffusion electrodes (GDE).

Catalyst	Catalyst loading ($mg \cdot cm^{-2}$)	(Cu + Au) loading on the GDE ($mg \cdot cm^{-2}$)
Cu/MWCNT	4.7	0.50
$Cu_{97}Au_3$/MWCNT	4.9	0.50
$Cu_{62}Au_{38}$/MWCNT	4.2	0.35
$Cu_{32}Au_{68}$/MWCNT	4.0	0.41
Au/MWCNT	4.5	0.58
MWCNT	7.5	0.11

oxidized to some extent to Cu_2O. The galvanic replacement of Cu_2O by Au follows a different stoichiometry (Figure 5.7) and more Cu atoms are replaced by one Au atom. Therefore, we conclude that the galvanic replacement went mostly through replacement of metallic Cu, as shown in Figure 5.3, and partially of oxidized Cu according to the reaction in Figure 5.7. The catalyst loadings on the electrodes, determined by mass difference before and after the spraying step, are summarized in Table 5.3.

Figure 5.8 shows the XRD patterns of the studied catalysts and of the MWCNT. The latter shows reflections at 3.395 Å and 2.11 Å [22]. These reflections of the MWCNTs are assigned to (002) and (100) reflections, corresponding to the interlayer spacing of the nanotubes and the *d*-spacing between carbon atoms of a given nanotube respectively [23]. As mentioned in the experimental section, nickel nanoparticles are present in the as-supplied MWCNTs, as can be seen at 2.03 Å (Ni (111)), 1.77 Å (Ni (200)) and 1.22 Å (Ni (222)) in Figure 5.8. These nanoparticles are fully encapsulated in the MWCNTs and do not contribute to the catalytic properties, as can be concluded form the fact they are still present even after the complete galvanic replacement. Figure 5.9 shows the diffraction patterns focused on the 1.9 – 2.6 Å region, where the (strongest) reflections of Au (111) [16], Au_3Cu (111) [15], AuCu (101) [17], $AuCu_3$ (111) [18] and Cu (111) [19] are reported. Cu/MWCNT shows the reflections of metallic copper (111), (200) and (220) at 2.09 Å, 1.81 Å and 1.28 Å, respectively [19]. Even though Cu (111) gives the strongest reflection of metallic copper, it strongly overlaps with the MWCNT (100) reflection. Therefore, reflections at around 2.1 Å cannot be used to confirm the presence of metallic Cu. A very weak reflection of the Cu_2O (111) crystal lattice is visible for Cu/MWCNT and $Cu_{97}Au_3$/MWCNT,

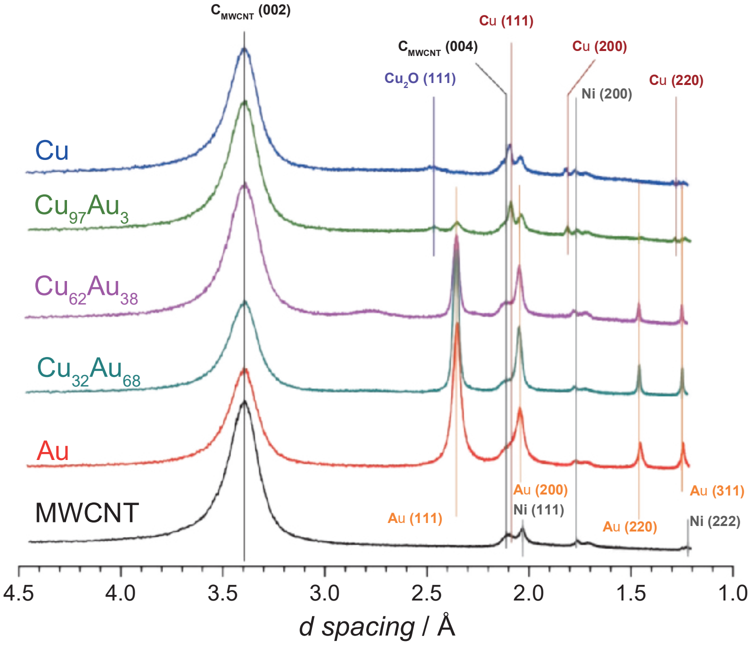

Figure 5.8: XRD diffraction patterns of (—) MWCNT, (—) Au/MWCNT, (—) $Cu_{32}Au_{68}$/MWCNT, (—) $Cu_{62}Au_{38}$, (—) $Cu_{97}Au_3$, (—) Cu/MWCNT. Reflections are indexed for (—) C_{MWCNT}, (—) Cu, (—) Au, (—) Cu_2O and (—) Ni.

confirming that the Cu nanoparticles are partly oxidized. The presence of Cu is evident for Cu/MWCNT and $Cu_{97}Au_3$/MWCNT with the Cu (220) and Cu_2O (111) reflections but cannot be concluded for $Cu_{62}Au_{38}$/MWCNT and $Cu_{32}Au_{68}$/MWCNT, since these reflections are no longer detected. In contrast, the presence of metallic Au is confirmed for all the bimetallic catalysts thanks to the strong reflections of Au (111), (200), (220) and (311) at 2.36 Å, 2.05 Å, 1.46 Å and 1.25 Å respectively [16]. Even though Au (200) is close to Ni (111) (at 2.03 Å), and Au (311) to Ni (222) (at 1.22 Å), the other reflections leave no doubt. In particular, Au (111) is clearly visible for $Cu_{97}Au_3$/MWCNT, which contains the lowest amount of Au. Au/MWCNT resulting from complete galvanic exchange of Cu does not show any sign of copper anymore, although some doubt remains due to the MWCNT (100) overlapping with the strongest reflection of Cu. Overall, no peak shift is observed on either metallic Cu reflections or Au metallic reflections. Besides, the most intense reflections of regular intermetallic compounds such as Au_3Cu (111), AuCu (101) or $AuCu_3$ (111) do not appear for any of the synthesized catalysts, ruling out the formation of these compounds. The two metals rather appear as separate phases. This leaves the hypotheses of Cu core-Au shell nanoparticles (Figure 5.4-c) and Janus-like CuAu nanoparticles (Figure 5.4-d).

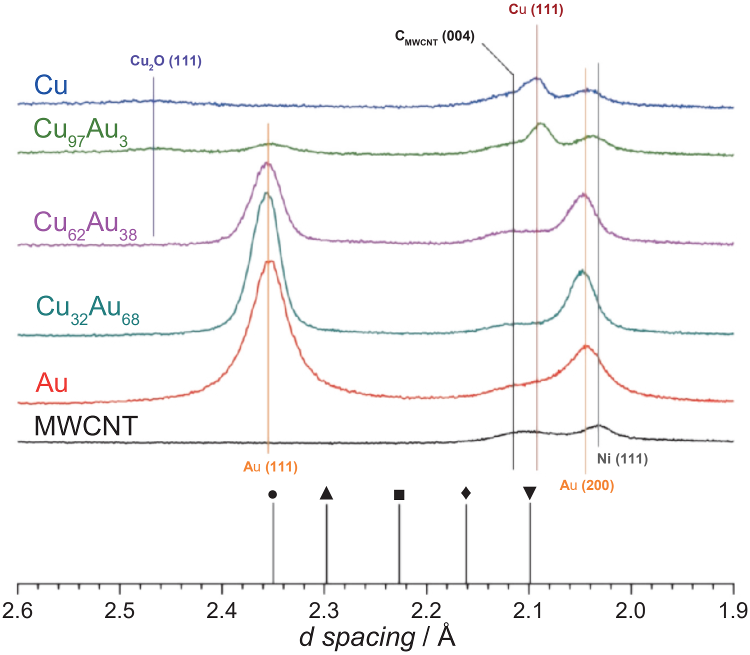

Figure 5.9: 1.9 – 2.6 Å region XRD diffraction patterns of (—) MWCNT, (—) Au/MWCNT, (—) $Cu_{32}Au_{68}$/MWCNT, (—) $Cu_{62}Au_{38}$, (—) $Cu_{97}Au_3$, (—) Cu/MWCNT. Reflections are indexed for (—) C_{MWCNT}, (—) Cu, (—) Au, (—) Cu_2O and (—) Ni. ICSD Reference reflections are given for (●) Au (111) [16], (▲) Au_3Cu (111) [15], (■) AuCu (101) [17], (♦) $AuCu_3$ (111) [18] and (▼) Cu (111) [19].

TEM images and particle size distributions are shown in Figure 5.10. Metal nanoparticles of 3 to 4 nm are present on the surface of the nanotubes for all the catalysts. The particle size distributions are rather similar across the different materials, except for the nanoparticles of the native Cu/MWCNT, which are smaller (2.8 nm on average) than the other samples (3.8, 4.6, 3.9 and 4.6 nm, respectively). Particle growth is not supposed to happen during galvanic exchange. It is possible that the smallest Cu nanoparticles (< 1 nm) preferentially leach during the process, explaining this consistently larger particle size. HRTEM analysis was attempted for some bimetallic catalysts, but this technique did not reveal whether the nanoparticles were intermetallic compounds, core-shell or segregated.

3 – 2 – Catalyst performance

The activity of the catalyst-loaded-GDEs was investigated at different potentials, and

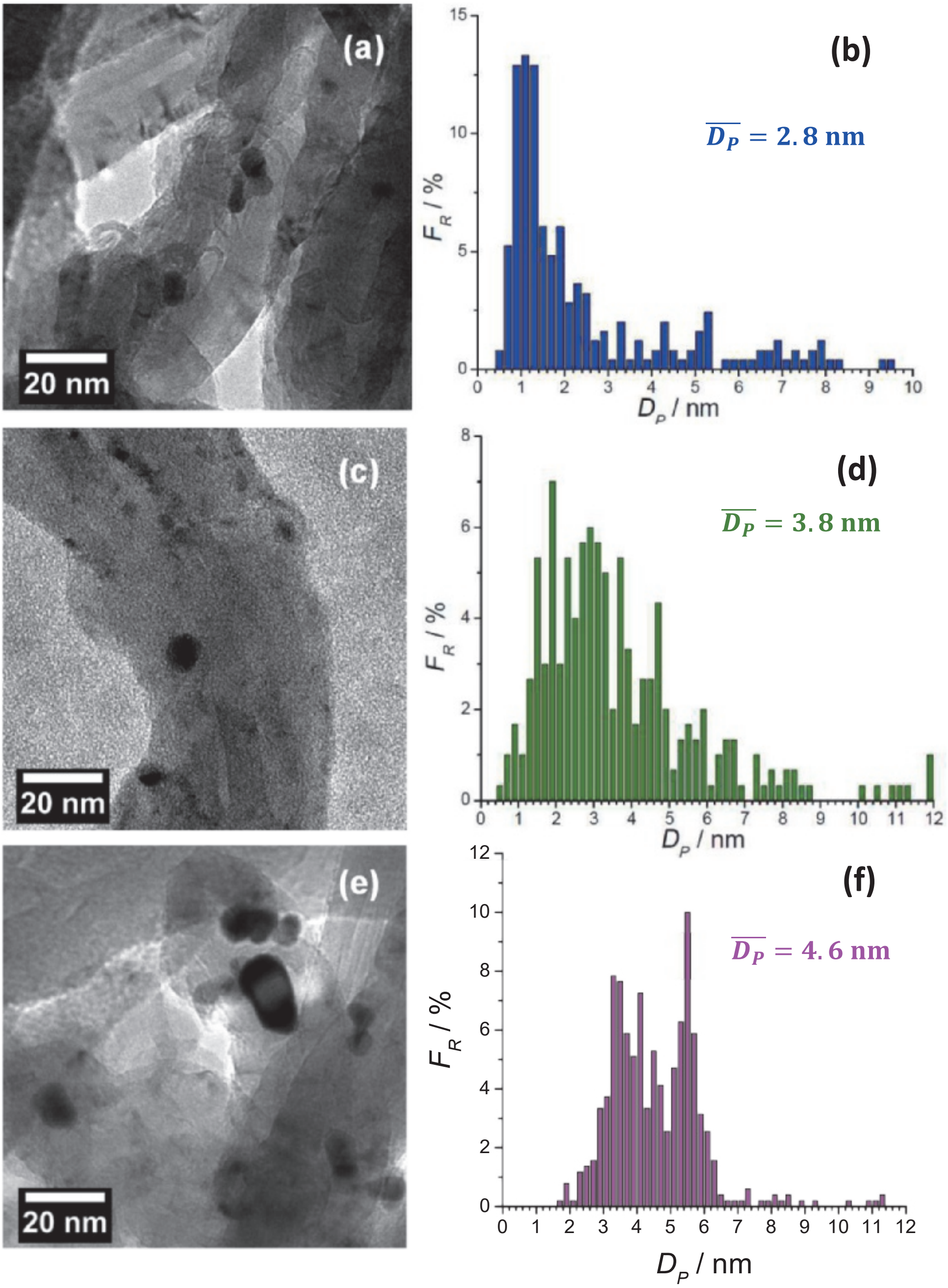

Figure 5.10 (1): Representative TEM images (*left*) and particle size distributions (*right*) of (a), (b) Cu/MWCNT, (c), (d) $Cu_{97}Au_3$/MWCNT, (e), (f) $Cu_{62}Au_{38}$/MWCNT, (g), (h) $Cu_{32}Au_{68}$/MWCNT, (i), (j) Au/MWCNT.

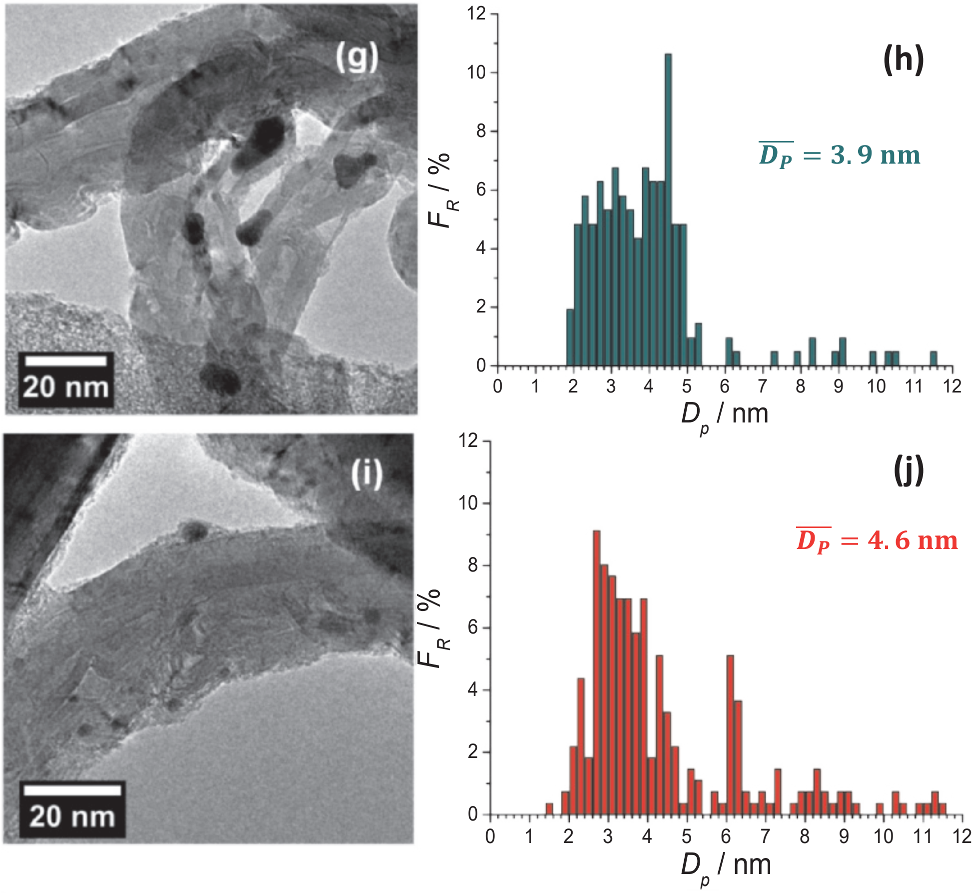

Figure 5.10 (2): Representative TEM images (*left*) and particle size distributions (*right*) of (a), (b) Cu/MWCNT, (c), (d) $Cu_{97}Au_3$/MWCNT, (e), (f) $Cu_{62}Au_{38}$/MWCNT, (g), (h) $Cu_{32}Au_{68}$/MWCNT, (i), (j) Au/MWCNT.

Figure 5.11 shows the applied potential profile and the resulting current density for the experiment involving Cu/MWCNT catalyst. The current density reaches a stable regime at all potentials within each 120 min potential step. Despite the stable current attained, the product concentration in the effluent of the cell takes much longer to stabilize, as can be seen in Figure 5.12. This could be due to the finite rates of all mass-transport and phase transfer phenomena occurring in combination with the capacity of the cell. Besides, other phenomena such as catalyst surface rearrangement or particle migration and coalescence as observed by Kim *et al.* [10] cannot be ruled out. The latter phenomena could take place without consequences for the current profile which mostly produces H_2 and the applied potential is always much more negative than the H_2

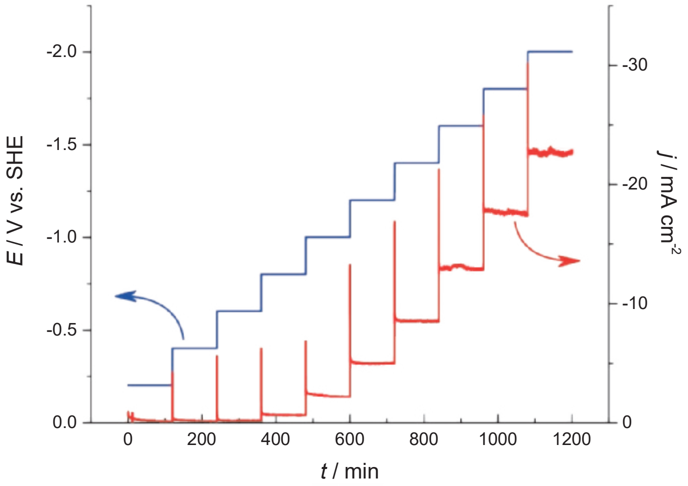

Figure 5.11: (—) Applied potential (*left, blue*) and (—) resulting current density profile (*right, red*) during the electrocatalytic reduction of CO_2 on the Cu/MWCNT gas diffusion cathode.

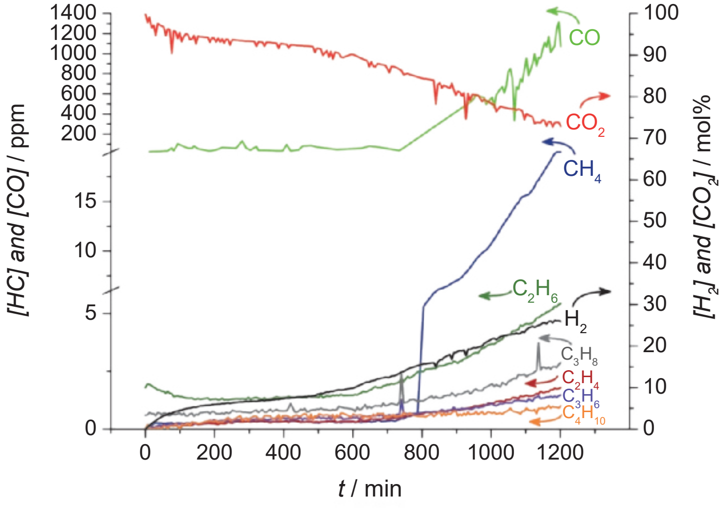

Figure 5.12: Concentrations of electrocatalytic CO_2 reduction products in the effluent of the set-up during the course of the catalytic experiment involving Cu/MWCNT catalyst. (—) H_2 (*right axis*), (—) CO_2 (*right axis*), (—) CO, (—) CH_4, (—) C_2H_4, (—) C_2H_6, (—) C_3H_6, (—) C_3H_8, (—) C_4H_{10}.

evolution potential.

In order to relate the productivities of the different compounds resulting from the reduction of CO_2, the molar fluxes are required. These can be converted to partial

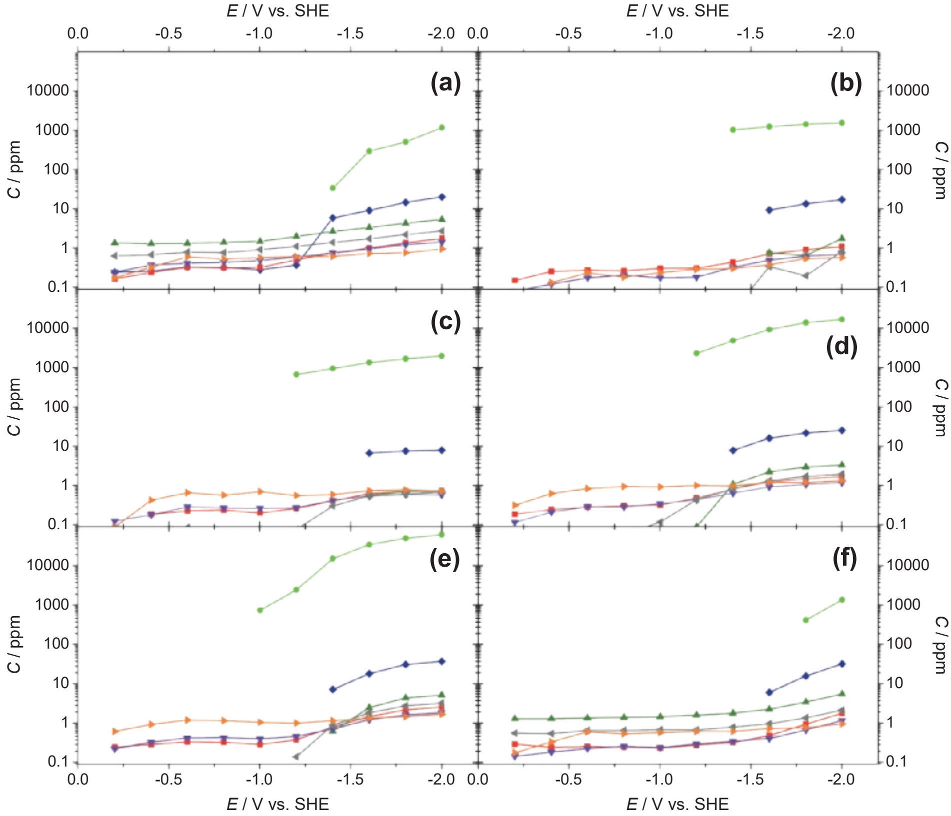

Figure 5.13: Product concentration in the effluent (CO *left* and hydrocarbons *right* axis) vs. applied potential for (a) Cu/MWCNT, (b) $Cu_{97}Au_3$/MWCNT, (c) $Cu_{62}Au_{38}$/MWCNT, (d) $Cu_{32}Au_{68}$/MWCNT, (e) Au/MWCNT, (f) MWCNT. Concentrations of (—●—) CO,(—♦—) CH_4,(—■—) C_2H_4,(—▲—) C_2H_6,(—▲—) C_3H_6,(—◀—) C_3H_8,(—▶—) C_4H_{10}.

currents and lead to Faraday efficiency estimations. Unfortunately, the volumetric outflow of the cell could not be determined with sufficient accuracy during the experiments, and no closed mass balance was reached. However, since the experimental protocol remains the same throughout, we can compare the relative data for the different catalysts. The concentrations in the effluent were averaged over each 120 min potential step and the results for the different catalysts are presented in Figure 5.13. The major CO_2 reduction product is always CO, followed by CH_4, but H_2 is by far the main electrolysis product. Higher hydrocarbons (C_3H_4, C_3H_6 and C_4H_{10}) are only produced in small amounts, yielding concentrations below 10 ppm. The famous selectivity profile of Cu for CH_4, C_2H_4 and CO, as first reported by Hori *et al.* [24], where CH_4 and C_2H_4 are produced with up to 40% of the FE, is not observed here. This is most likely because

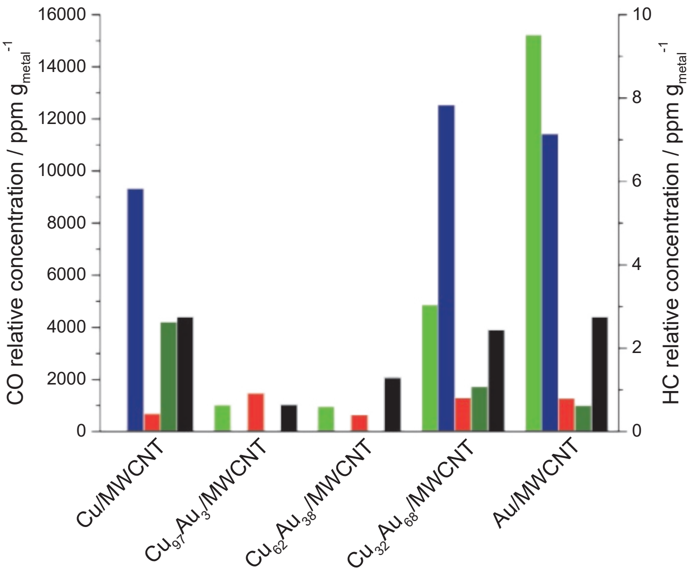

Figure 5.14: Comparison of CO_2 reduction product concentrations at -1.4 V vs. SHE of *left axis* (🟩) CO, and *right axis* (🟦) CH_4, (🟥) C_2H_4, (🟩) C_2H_6 and (⬛) C_{3+} for the studied catalyst series.

Hori *et al.* used a plain copper metallic electrode, whereas supported copper nanoparticles are studied here. The ensemble effects as observed recently by Kim *et al.* [10], which strongly depend on the initial catalyst morphology, are probably very different on the surface of a metallic Cu electrode compared to supported Cu nanoparticles. Also Centi *et al.* [25] report for gas diffusion electrodes loaded with supported catalysts hydrocarbons only in the ppm range, without a particular optimal potential window.

For easier activity comparison, the relative concentrations taking the metal loading into account are plotted for *E* = -1.4 V vs. SHE and *E* = -1.8 V vs. SHE in Figure 5.14 and Figure 5.15, respectively. At -1.4 V vs. SHE, not all catalysts are active. In particular, $Cu_{97}Au_3$/MWCNT and $Cu_{62}Au_{38}$/MWCNT only produce minute amounts of CO and hydrocarbons at this potential. In line with other reports [7, 8], CO is the major compound in practically all cases where Au is present, produced at 3 orders of magnitude more than CH_4. In contrast to other studies [7, 8] the CO production is the highest at -1.4 V vs. SHE and at -1.8 V vs. SHE for Au/MWCNT and not for a bimetallic catalyst. Au is well-known for being very selective to CO in this reaction [7, 8, 26]. Furthermore, the CO production at both -1.4 and -1.8 V vs. SHE increases as Cu:Au decreases, demonstrating the effect of Au addition. CH_4 is the second main reaction product except for $Cu_{97}Au_3$/MWCNT and $Cu_{62}Au_{38}$/MWCNT at -1.4 V vs.

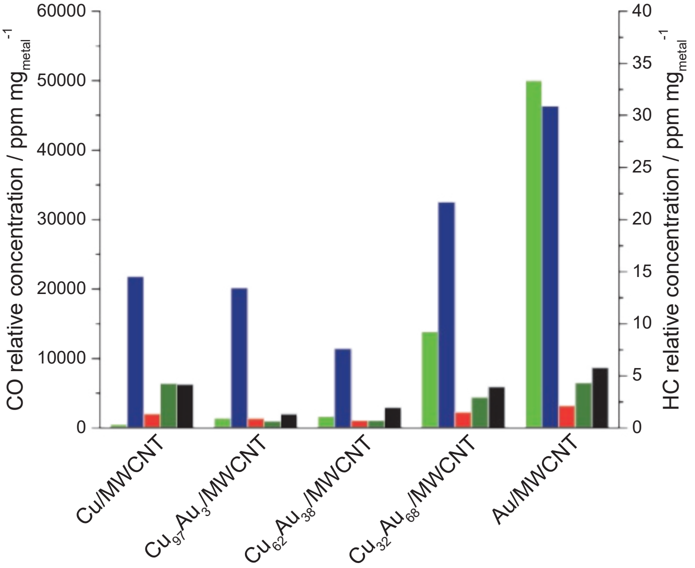

Figure 5.15: Relative product concentrations at -1.8 V vs. SHE of *left axis* (🟩) CO, and *right axis* (🟦) CH_4, (🟥) C_2H_4, (🟩) C_2H_6 and (⬛) Heavier HC for the studied catalyst series.

SHE, where it is below the detection limit. In the case of $Cu_{32}Au_{68}$/MWCNT, the CH_4 production is enhanced compared with that over monometallic Cu and Au catalysts, where other reports rather suggest that the overall hydrocarbon production decreases when Au is present [7, 8]. The Au/MWCNT catalyst shows a slightly lower production rate for CH_4 at this potential. This suggests a synergistic effect, albeit weak, of Cu and Au in the bimetallic catalyst $Cu_{32}Au_{68}$/MWCNT at -1.4 V vs. SHE. This is not the case at -1.8 V vs. SHE, where Au/MWCNT produces more CH_4 than $Cu_{32}Au_{68}$/MWCNT. The monometallic Cu/MWCNT catalyst remains the most selective one for higher hydrocarbons, but the differences with $Cu_{32}Au_{68}$/MWCNT and Au/MWCNT are small.

Apart from selectivities, it is also interesting to compare the catalysts on the energetic aspects. CO_2 reduction is known to require a high activation overpotential before products appear [1, 4, 5, 9, 27]. This is due to the multi-intermediate nature of the reaction, and scaling relations between the binding energies of these intermediates [1, 4]. Bimetallic catalysts are expected to remedy this by providing active site heterogeneity. The onset potential is the potential above which a particular compound starts being produced, and is an electrochemical measurement of the activation energy for that compound. Figure 5.16 shows the onset potentials of the two main CO_2 reduction products, CO and CH_4, on which the applied potential shows the strongest effect. The onset potential is then reported as the potential where CO and CH_4 appear

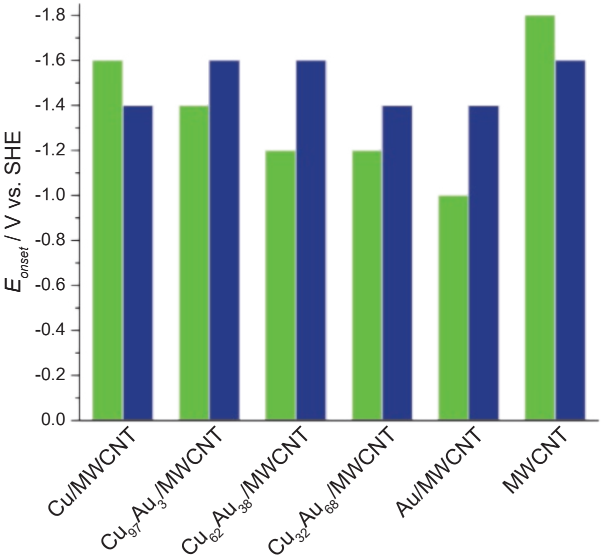

Figure 5.16: Onset potential for (🟩) CO and (🟦) CH_4 formation for the studied catalyst series.

as products of the reaction. No synergistic effect of Cu and Au can be seen on the onset potential of CO production. The onset potential for CO production decreases with decreasing Cu:Au ratio, and the monometallic Au/MWCNT has the least negative value (-1.0 V vs. SHE). Rather than a synergistic effect, this observation points to separate Au and Cu domains. Likewise, no benefit from Au incorporation could be observed on the onset potential for CH_4 production. The MWCNT support even shows a similar onset potential as some of the other catalyst samples, which questions the gain in energy efficiency that should be brought by the metal nanoparticles. This contrasts with the findings of Christophe *et al.* [7] and Kim *et al.* [8]. who both observed a synergistic effect with Au_1Cu_1 alloys producing more CO than the pure metals. The strong structure sensitivity of the CO_2 reduction reaction is probably responsible for these discrepancies. Combined with the strong sensitivity of the catalyst structure itself to the reaction conditions, this can account for the large discrepancies often reported in different studies. In particular, Kim *et al.* [10] reported Cu nanoparticle ensemble effects, where increasing the packing density of (monometallic) Cu nanoparticles showed a strong enhancement in FE for C_2 and C_3 products. In contrast, the nanoparticles in the present catalysts are much more dispersed on the catalyst support, and this could explain the low activities observed. Tackling these complex inter-related phenomena requires *operando* catalyst characterization studies such as X-ray techniques that should not interfere with the reaction.

Referring to the TGA results combined with the XRD observations allows us to conclude that Au was indeed incorporated in the catalysts when galvanic replacement was performed. The structure of the bimetallic nanoparticles could not be established clearly. In particular, no XRD feature was observed corresponding to the known Au_3Cu, AuCu or $AuCu_3$ regular intermetallic compounds. Nor could any shift of the Au (111) or Cu (111) reflections be observed when the Cu:Au ratio was changed, suggesting that Au did not atomically disperse in the Cu phase thus also suggesting that an alloyed intermetallic compound is not formed. The TEM observations did not allow drawing any conclusions on the structure of the bimetallic nanoparticles. From a characterization perspective, the bimetallic nanoparticles could be core-shell or segregated. Considering 6 nm nanoparticles, and the observation of separate Cu and Au phases under XRD with a domain size detection limit of 3 nm, the hypothesis of Janus-like particles is more likely. 6 nm Core-shell nanoparticles would have a core of at least 3 nm to be detected under XRD, which leaves 1.5 nm maximum of shell thickness which then cannot not be detected by XRD, as opposed to our XRD observations. The catalytic performance points to separate Au and Cu phases in the case of $Cu_{97}Au_3$/MWCNT and $Cu_{62}Au_{38}$/MWCNT, since no significant enhancement was observed in the synthesized bimetallic catalysts compared with the monometallic ones. $Cu_{32}Au_{68}$/MWCNT behaves somewhat differently, producing at least as much CH_4 and higher hydrocarbons as the monometallic Cu counterpart. The fact that the typical products observed on a copper electrode were still produced on the catalyst with the lowest Cu:Au ratio means that Cu is still present at the surface of the nanoparticles, thus ruling out the Au core-Cu shell structure.

To summarize, we conclude from combined characterization and catalytic performance perspectives that the bimetallic catalysts very likely contain segregated Au and Cu phases as depicted in Figure 5.5 (d). Overall, these observations point out that our attempt to break the scaling relationships by forming bimetallic active sites on the surface of the nanoparticles was not successful. The galvanic replacement we employed did not lead to an atomic dispersion of gold in or on copper nanoparticles (or vice versa). It is envisaged that in the course of the galvanic replacement, some metallic gold sites are first formed on the originally pure copper nanoparticles, but then it could be more energetically favourable for the remaining gold monomers to reduce on these gold sites rather than creating more interface with copper surfaces. This process would lead to nanoparticles with segregated domains of gold and copper, as our results suggest. Possibly, treatments such as annealing could provide the activation energy to form the stable regular intermetallic compounds from our nanoparticles with segregated Cu and Au phases. It remains to be seen if such an approach is successful because it holds the danger of sintering, resulting in loss of activity. Other approaches such as co-reduction of the two metals simultaneously during the colloidal synthesis, as employed by Kim *et al.* [8] look promising and avoid such temperature treatments.

4 – Conclusions

The colloidal synthesis of Cu nanoparticles using ethylene glycol combined with galvanic replacement resulted in the introduction of a controlled amount of Au, and a series of nanostructured CuAu bimetallic catalysts with similar particle size distributions could be prepared. The formation of intermetallic phases could not be confirmed by XRD; only reflections from the monometallic Cu and Au phases were observed. The galvanic replacement yielded lower Cu:Au ratios than expected, as revealed by TGA. This is attributed to the presence of copper (I) oxide on the parent monometallic Cu/MWCNT, requiring more copper replacement than for pure metallic Cu.

The catalysts were evaluated for the electrocatalytic reduction of CO_2 using gas diffusion electrodes. Despite the low CO_2 reduction activities (0 - 5% overall Faraday efficiency for CO_2 reduction), the large amount of molecular hydrogen being produced, and the material and charge balance not being fully closed, the catalytic activities could be compared mutually. Hydrogen is the major product in all cases, produced two orders of magnitude more than the CO_2 reduction products, with CO as the major product.

In particular, the CO production simply correlates with the amount of gold in the bimetallic catalysts, with pure gold showing the highest productivity. Implementing a bimetallic CuAu catalyst did not show any convincing benefit on the activation overpotential for CO and CH_4, it decreases with increasing gold content, being the lowest for the Au/MWCNT sample. $Cu_{32}Au_{68}$/MWCNT shows the highest activity for the production of CH_4 at -1.4 V vs. SHE, but not impressively more than Au/MWCNT or even MWCNT alone. The other catalyst compositions tested in this study at various potentials do not show synergistic effects either.

From a catalytic activity perspective, the catalysts behave as two separate Cu and Au phases.

References

1. Peterson, A.A.; Nørskov, J.K. *J Phys Chem Lett 3,* **2012**, 251-258.
2. Hansen, H.A.; Varley, J.B.; Peterson, A.A.; Nørskov, J.K. *J Phys Chem Lett 4,* **2013**,

388-392.
3. Nørskov, J.K.; Rossmeisl, J.; Logadottir, A.; Lindqvist, L.; Kitchin, J.R.; Bligaard, T.; Jónsson, H. *J Phys Chem B 108,* **2004**, 17886-17892.
4. Koper, M.T.M. *J Electroanal Chem 660,* **2011**, 254-260.
5. Koper, M.T.M. *Chem Sci 4,* **2013**, 2710-2723.
6. Santen, R.A.; van Leeuwen, P.W.N.M.; Averill, B.A.; Moulijn, J.A. *Catalysis: An Integrated Approach*; Elsevier: **2000**.
7. Christophe, J.; Doneux, T.; Buess-Herman, C. *Electrocatalysis 3,* **2012**, 139-146.
8. Kim, D.; Resasco, J.; Yu, Y.; Asiri, A.M.; Yang, P. *Nat Commun 5,* **2014**, 4948.
9. Jovanov, Z.P.; Hansen, H.A.; Varela, A.S.; Malacrida, P.; Peterson, A.A.; Nørskov, J.K.; Stephens, I.E.L.; Chorkendorff, I. *J Catal 343,* **2016**, 215-231.
10. Kim, D.; Kley, C.S.; Li, Y.; Yang, P. *P Natl Acad of Sci 114,* **2017**, 10560-10565.
11. Available online: https://www.cheaptubes.com/product/multi-walled-carbon-nanotubes-30-50nm/ (09/12/**2013**),
12. Simmons, T.J.; Bult, J.; Hashim, D.P.; Linhardt, R.J.; Ajayan, P.M. *ACS Nano 3,* **2009**, 865-870.
13. Oh, H.-S.; Kim, H. *Adv Funct Mat 21,* **2011**, 3954-3960.
14. Carroll, K.J.; Reveles, J.U.; Shultz, M.D.; Khanna, S.N.; Carpenter, E.E. *J Phys Chem C 115,* **2011**, 2656-2664.
15. Kubiak, R.; Janczak, J. *J Alloy Compd 176,* **1991**, 133-140.
16. Salamakha, L.P.; Bauer, E.; Mudryi, S.I.; Gonçalves, A.P.; Almeida, M.; Noël, H. *J Alloy Compd 479,* **2009**, 184-188.
17. Bjerkelund, E.; Pearson, W.B. *Acta Chem Scand 21,* **1967**, 2900-2902.
18. Sra, A.K.; Schaak, R.E. *J Am Chem Soc 126,* **2004**, 6667-6672.
19. Ramos de Debiaggi, S.; Cabeza, G.F.; Toro, C.D.; Monti, A.M.; Sommadossi, S.; Guillermet, A.F. *J Alloy Compd 509,* **2011**, 3238-3245.
20. Calvo, F. *Phys Chem Chem Phys 17,* **2015**, 27922-27939.
21. Kharton, V.V. *Solid State Electrochemistry II: Electrodes, Interfaces and Ceramic Membranes*; Wiley: **2012**.
22. Fayos, J. *J Solid State Chem 148,* **1999**, 278-285.
23. Endo, M.; Takeuchi, K.; Hiraoka, T.; Furuta, T.; Kasai, T.; Sun, X.; Kiang, C.H.; Dresselhaus, M.S. *J Phys Chem Solids 58,* **1997**, 1707-1712.
24. Hori, Y.; Murata, A.; Takahashi, R. *J Chem Soc Farad T 1 85,* **1989**, 2309-2326.
25. Centi, G.; Perathoner, S.; Winè, G.; Gangeri, M. *Green Chem 9,* **2007**, 671-678.
26. Zhu, W.; Michalsky, R.; Metin, O.; Lv, H.; Guo, S.; Wright, C.J.; Sun, X.; Peterson, A.A.; Sun, S. *J Am Chem Soc 135,* **2013**, 16833-16836.
27. Li, Y.; Sun, Q. *Adv Energy Mater 6,* **2016**, 1600463-1600488.

Summary

Bottom-up approaches for the synthesis of nanostructured heterogeneous (electro-) catalysts, via the colloidal deposition route combined with nanostructured catalyst supports, have been investigated in this thesis. Colloidal gold nanoparticles have been selected as a case study in view of their promising catalytic properties for oxidation reactions, as well as their ability to convert carbon dioxide to carbon monoxide under electrocatalytic conditions.

Benzyl alcohol aerobic oxidation was selected as a test reaction of choice to characterize the catalytic properties of the colloidal gold nanoparticles under investigation, in view of the extensive literature available on this topic. Furthermore, practical experience with this reaction and colloidal gold nanoparticles had already been gained in the Catalysis Engineering group, reflected by a previous publication involving dodecylamine-capped gold nanoparticles [1].

In the course of the investigations, while devising a catalytic performance test protocol for benzyl alcohol oxidation, it was realized that conversion rates did not follow the expected first order kinetics, even when a benchmark catalyst (AUROlite) was used. This led to Chapter 1 of this thesis, where it is established that the reaction products, in particular benzoic acid or an intermediate, are strongly inhibiting the catalytic reaction. When a basic compound such as potassium carbonate is present in the reaction medium, this inhibition is alleviated, supposedly because the inhibiting products are reacted away. This clears up the role of carbonates that are often encountered in literature for this reaction without a satisfying explanation of their role. Assuming a strong adsorption of benzoic acid in the absence of a base, and considering its enhanced condensation to benzyl benzoate in the presence of a base, a model was devised that satisfyingly predicts the inhibiting behaviour of benzoic acid and the alleviation by the base. The proper investigation of more complex catalysts, prepared by the above-mentioned methods, was then enabled. As future prospect, it could be envisioned to use a basic catalyst support in order to combine the effects of the catalyst and the potassium carbonate in a single solid compound. This should accelerate the kinetics of benzoic acid reaction to benzyl benzoate and thereby improve the catalytic performance even further.

In order to study the catalytic influence of the support free from nanoparticle size effects, a series of catalysts with the same gold nanoparticle size was realized and led to Chapter 2. This was made possible via the colloidal deposition method, wherein the gold nanoparticles are synthesized in the absence of the support. Catalytic activities for benzyl alcohol oxidation and carbon monoxide oxidation rank in opposite order,

underlining again the primacy of the elementary steps over the overall nature of the reaction. Catalyst support basicity promotes benzyl alcohol oxidation, consistent with the first elementary step being the deprotonation of the alcohol. In contrast, the carbon monoxide oxidation is promoted by catalyst support acidity, and more importantly, catalyst support reducibility. The high oxygen mobility and vacancies it provides on its surface promotes O_2 chemisorption, dissociation and surface diffusion. In benzyl alcohol oxidation, since O_2 reacts by oxidizing hydrides chemisorbed on the gold surface, support reducibility does not show a strong influence. The influence of the colloidal synthesis recipe remains to be assessed, as it is demonstrated in Chapter 3 that capping ligands remain on the surface of the gold nanoparticles. Alternative colloidal synthesis recipes could yield a better interaction of the gold particle with the catalyst support, in particular with silica where it was shown to be poor.

In their previous publication [1], the Catalysis Engineering team demonstrated that Au-DDA/Al_2O_3 was as active as the benchmark catalyst AUROlite, although the former contained larger gold nanoparticles (5 nm) than the latter (2 nm). Further investigations on the role of the capping ligand remaining on Au-DDA/Al_2O_3 in this remarkable observation led to Chapter 3 of this thesis. Ozonication at mild temperature was employed to clean the gold nanoparticles from dodecylamine, and this revealed a slight increase in catalytic activity for both benzyl alcohol oxidation and carbon monoxide oxidation. Ozonication at mild temperature is an effective alternative to high temperature treatment in air, which often causes sintering, and to solvent washing, which can cause leaching. Furthermore, the removal of dodecylamine did not yield less active catalysts, thus ruling out any promotional effect of the capping ligand on the catalytic activity. Concerning the carbon monoxide oxidation, catalytic activities are in line with the numerous observations reported in literature of the inversely proportional correlation of catalytic activity with gold particle size. This is however not the case for benzyl alcohol oxidation, where a catalyst with 5 nm gold nanoparticles exhibited a similar activity as a catalyst with 2 nm gold particles, even when neither contained capping ligands. This implies that the relation of catalytic activity with gold particle size usually observed for carbon monoxide oxidation does not apply for benzyl alcohol oxidation. Even though both reactions are oxidations in nature, the elementary steps of each reaction are quite different, and direct extrapolation of the activity ranking from one reaction type to another is incorrect. The ozonication enabled the complete removal of the remaining capping ligands at room temperature, which properly avoided the particle growth commonly observed with high temperature treatments in air. However, temperature treatment also allows to stabilize the gold-support interface, thereby increasing the gold-support interaction, which is usually positive for catalytic performance. It would be interesting to study the effect of mild temperature treatments (e.g. 100 – 200 °C) applied subsequently to the ozonication. Mild temperature treatments under more oxidizing atmospheres than air, such as 100% O_2 or even NO_2 or N_2O, could be a good compromise between temperature and chemical activity.

Next to the active phase nanoparticles, nanostructuring of the catalyst support was investigated in Chapter 4 of this thesis. Palladium nanoparticles were formed on various carbon supports with increasing complexity of nanostructure, from graphite to activated carbon to carbon black and to multi-walled carbon nanotubes (MWCNTs). Benzyl alcohol oxidation catalytic activities rank in the same order as the degree of nanostructure complexity of the carbon support, with Pd/MWCNT as the most active and Pd/Graphite the least active catalyst. This ranking should however be put into perspective, since the catalyst synthesis method (impregnation-reduction) yielded different palladium particle sizes. Functionalizing the surface of MWCNT with carboxylic moieties, via hot nitric acid treatment, yielded even smaller palladium nanoparticles (1.5 nm) compared to the non-functionalized Pd/MWCNT (5 nm), resulting in a two-fold increase in turn-over-frequency. Furthermore, the catalyst exhibited a stable activity over 6 consecutive batch reaction runs, suggesting a strong Pd-MWCNT interaction. Thus, tailoring the catalyst support at the nanoscale proved useful to control its nanostructure and to obtain high and stable activity. It would be interesting to combine the nanostructured support MWCNT with the colloidal deposition method. This would yield a fully nanostructured catalyst, and would allow the direct comparison of impregnation methods with the colloidal deposition method.

Finally, nanostructured bimetallic catalysts were employed in Chapter 5 for the electrocatalytic reduction of CO_2. This investigation was based on the theoretical studies from the groups of Nørskov [2-4] and of Koper [5, 6] who focused on the scaling relationships of binding reaction intermediates and predicted that these relationships were a main bottleneck in the reaction. Breaking these scaling relationships requires a sufficient heterogeneity of the active sites, *i.e.* active sites with different reactivities, adsorption strengths and adsorbate selectivities. Accordingly, copper-gold bimetallic catalysts were synthesized via reduction of a copper precursor by ethylene glycol followed by their immobilization on multi-walled carbon nanotubes and controlled galvanic replacement of (part of) the copper with chloroauric acid. The colloidal method for synthesizing the parent copper particles provided nanoparticles of similar size, whereas the galvanic replacement enabled the precise control of the composition of the bimetallics. Although it seemed that the scaling relationships were still holding, some variations in activity, selectivity and energy efficiency were recorded. However, these performances stayed within the order of magnitude of monometallic catalysts. Actually, the catalysts' performance and their characterization point to contributions of separate Cu and Au phases. A more intimate mixture of copper and gold (alloying) through alternative synthesis methods would seem necessary to provide the required active site heterogeneity, e.g. by using a mixture of metal precursors for the colloidal synthesis. A mild temperature post-treatment could also be employed on the resulting bimetallic catalysts to induce the formation of intermetallic crystals since some are thermodynamically favoured.

Overall, the aforementioned results demonstrate that the use of nanomaterials, in particular colloidal nanoparticles for catalyst synthesis, holds promises at least for fundamental catalysis research [7]. The colloidal deposition method improves the level of control in catalyst synthesis, providing particularly narrow nanoparticle size distributions and eliminating the influence of the support during synthesis. It constitutes an interface tool between theoretical and single crystal studies on the one hand and real catalysts on the other hand. Particle size-catalytic effects can be studied with a much higher level of detail than impregnation methods allow and can be used to verify theoretical predictions. The characteristics of the metal nanoparticles being independent from the surface chemistry of the catalyst support, in principle enables the study of chemical/catalytic properties of the latter without artefacts from the former. Active site engineering could also employ the control of exposed crystal facets via the control of the nanoparticle shape that is permitted in some instances by the colloidal deposition method. The latter aspect, however, presents serious limitations in the sense that the sought active site must be stable under reaction conditions, while it is known that catalytic surfaces can be very dynamic under exposure to the reaction environment. This is an additional challenge to that of achieving the self-assembly of atomic scale-tailored catalysts. Ideally, the desired active site could be formed under reaction conditions, thereby providing a better guarantee of its stability. To achieve this, *in-operando*/*in-situ* [8, 9] characterization tools must come into play. For instance *in-situ* TEM [10, 11] is of significant relevance as it provides the necessary atomic scale information under reaction conditions.

Tailoring materials at the atomic level via phenomena of self-assembly is the only realistic way to produce larger scale amounts of such sophisticated catalysts and thereby opening the way to industrial applications. For this sake, colloidal syntheses must be economical regarding the nature and amount of the necessary solvent and surfactant, and the gain in catalytic process improvement, primarily selectivity and stability.

In view of the advantages it is clear that the colloidal deposition route for catalyst synthesis will not only remain in the field of catalysis research [12], but will find commercial application as well [13].

References

1. Quintanilla, A.; Butselaar-Orthlieb, V.C.L.; Kwakernaak, C.; Sloof, W.G.; Kreutzer, M.T.; Kapteijn, F. *J Catal 271,* **2010**, 104-114.
2. Peterson, A.A.; Nørskov, J.K. *J Phys Chem Lett 3,* **2012**, 251-258.
3. Hansen, H.A.; Varley, J.B.; Peterson, A.A.; Nørskov, J.K. *J Phys Chem Lett 4,* **2013**, 388-392.
4. Nørskov, J.K.; Rossmeisl, J.; Logadottir, A.; Lindqvist, L.; Kitchin, J.R.; Bligaard, T.; Jónsson, H. *J Phys Chem B 108,* **2004**, 17886-17892.
5. Koper, M.T.M. *J Electroanal Chem 660,* **2011**, 254-260.
6. Koper, M.T.M. *Chem Sci 4,* **2013**, 2710-2723.
7. Narayanan, R.; El-Sayed, M.A. *J Phys Chem B 109,* **2005**, 12663-12676.
8. Topsøe, H. *J Catal 216,* **2003**, 155-164.
9. Weckhuysen, B.M. *Phys Chem Chem Phys 5,* **2003**, 4351-4360.
10. Vendelbo, S.B.; Elkjær, C.F.; Puspitasari, I.; Creemer, J.F.; Dona, P.; Mele, L.; Morana, B.; Nelissen, B.J.; Roobol, S.; van Rijn, R.; Helveg, S.; Kooyman, P.J. *Microsc Microanal 20,* **2014**, 1570-1571.
11. Vendelbo, S.B.; Elkjær, C.F.; Falsig, H.; Puspitasari, I.; Dona, P.; Mele, L.; Morana, B.; Nelissen, B.J.; van Rijn, R.; Creemer, J.F.; Kooyman, P.J.; Helveg, S. *Nat Mater 13,* **2014**, 884.
12. Zaera, F. *Chem Soc Rev 42,* **2013**, 2746-2762.
13. Witte, P.T.; Berben, P.H.; Boland, S.; Boymans, E.H.; Vogt, D.; Geus, J.W.; Donkervoort, J.G. *Top Catal 55,* **2012**, 505-511.

Samenvatting

In dit proefschrift zijn bottom-up benaderingen onderzocht voor de bereiding van nanogestructureerde heterogene (electro-)katalysatoren via colloïdale depositie in combinatie met nanogestructureerde dragers. Als case-study zijn colloïdale goud nanodeeltjes geselecteerd vanwege hun veelbelovende katalytische eigenschappen in oxidatiereacties en hun vermogen kooldioxide om te zetten in koolmonoxide onder electrokatalytische reactiecondities.

Aangezien al veel literatuur beschikbaar is over de aerobe oxidatie van benzylalcohol, werd deze gekozen als testreactie om de katalytische eigenschappen van de colloïdale goud nanodeeltjes te karakteriseren. Bovendien was er binnen de Catalysis Engineering groep reeds uitgebreide ervaring opgedaan met deze reactie gekatalyseerd door colloïdale goud nanodeeltjes gestabiliseerd met dodecylamine [1].

Tijdens het onderzoek om een testprotocol voor de benzylalcoholoxidatie te ontwikkelen bleek dat de reactiesnelheid niet de verwachte eerste-orde afhankelijkheid vertoonde, zelfs niet voor een referentiekatalysator (AUROlite). Dit resulteerde in Hoofdstuk 1 van dit proefschrift, waarin werd vastgesteld dat de reactieproducten, met name benzoëzuur of een intermediair ervan, de katalytische reactie sterk remmen. In aanwezigheid van een basische component in het reactiemedium wordt deze remming verminderd, en verondersteld wordt dat deze remmende componenten dan wegreageren. Dit verheldert de rol van carbonaten die in de literatuur vaak worden gebruikt bij deze reactie, zonder dat daar een bevredigende verklaring voor wordt gegeven. Op basis van de aannames dat benzoëzuur sterk adsorbeert in afwezigheid van een base, en wordt omgezet naar benzylbenzoaat in aanwezigheid van een base, is een model ontwikkeld dat de remming door benzoëzuur en de vermindering daarvan door een base bevredigend beschrijft. Dit maakte de weg vrij voor gericht verder onderzoek naar de meer complexere katalysatoren bereid volgens de hierboven beschreven methode. Op deze wijze bereide complexe katalysatoren konden nu goed onderzocht worden. In de toekomst zou een basisch drager materiaal gebruikt kunnen worden om het effect van het kalium carbonaat in de katalysator te integreren. Dit zou de kinetiek van de reactie van benzoëzuur naar benzyl benzoaat moeten versnellen en dus het katalytische effect nog verder moeten verbeteren.

In Hoofdstuk 2 is het effect van de drager op de katalyse onderzocht, waarbij het effect van de goud nanodeeltjesgrootte is uitgeschakeld. Goud nanodeeltjes van dezelfde grootte zijn bereid volgens de colloïdale depositiemethode in afwezigheid van een drager en vervolgens op verschillende dragers afgezet. De katalytische activiteit voor de benzylalcohol oxidatie en de oxidatie van koolmonoxide vertoonde een tegenovergestelde trend voor de verschillende dragers, wat het belang van de elementaire stappen voor de overall reactie onderstreept. Een basische drager bevorderd de oxidatie van benzylalcohol, wat consistent is met de deprotonering van het alcohol als eerste elementaire stap. Daartegenover wordt de oxidatie van koolmonoxide bevorderd door een zure drager en, nog belangrijker, de reduceerbaarheid van de drager. De hoge zuurstofmobiliteit en de oppervlaktevacatures bevorderen O_2 chemisorptie, dissociatie en oppervlaktediffusie. In de benzylalcoholoxidatie speelt reduceerbaarheid van de drager nauwelijks een rol, aangezien O_2 reageert met hydrides die via chemisorptie op het oppervlak van de gouddeeltjes geadsorbeerd zijn. De invloed van de exacte bereidingswijze van de colloidale deeltjes moet nog onderzocht worden, aangezien Hoofdstuk 3 aantoont dat er liganden achterblijven op het oppervlak van de goud nanodeeltjes. Andere colloïdale bereidingswijzen leiden wellicht tot een betere interactie van de goud deeltjes met het drager materiaal. Dit is vooral van belang bij gebruik van silica als dragermateriaal omdat daar geconstateerd is dat de interactie van de goud deeltjes met de drager slecht is.

In een eerdere publicatie [1] toonde het Catalysis Engineering team aan dat Au-DDA/Al_2O_3 even actief was als de referentiekatalysator AUROlite, terwijl de eerste grotere goud nanodeeltjes (5 nm) bevatte dan de laatste (2 nm). Verder onderzoek naar de rol van de nog aanwezige surfactant op Au-DDA/Al2O3 in deze opmerkelijke waarneming resulteerde in Hoofdstuk 3 van dit proefschrift. Ozonicatie (oxidatie met ozon) bij milde temperatuur is gebruikt om de dodecylamine te verwijderen van de goud nanodeeltjes. Voor beide reacties leverde dit een geringe toename in katalytische activiteit. Deze ozonbehandeling is een effectief alternatief voor de hoge temperatuurbehandeling in lucht, die vaak leidt tot sintering, en voor wassen met oplosmiddel, wat tot uitlogen kan leiden. Het verwijderen van dodecylamine resulteerde verder niet in minder actieve katalysatoren, wat een promoterende invloed van deze surfactant uitsluit. Voor wat betreft de koolmonoxide oxidatie zijn de katalytische activiteiten in lijn met literatuurrapportages over de inverse relatie tussen katalytische activiteit en grootte van de gouddeeltjes. Dit geldt echter niet voor de benzylalcoholoxidatie, waar een katalysator met 5 nm gouddeeltjes een vergelijkbare activiteit vertoonde als een katalysator met 2 nm gouddeeltjes, ook als geen van beide surfactant bevat. De deeltjesgrootte-activiteit relatie zoals normaliter waargenomen voor de koolmonoxide oxidatie geldt dus niet voor de benzylalcoholoxidatie. Hoewel beide reacties van nature oxidatiereacties zijn, zijn de elementaire stappen heel verschillend en is het incorrect de activiteitsrangschikking voor één reactietype rechtstreeks te extrapoleren naar een ander. De behandeling met ozon kan al bij kamertemperatuur de liganden volledig verwijderen en daarmee de groei van de gouddeeltjes, die meestal wordt waargenomen na hoge temperatuur behandeling in lucht, voorkomen. Het zou interessant zijn om het effect van milde temperatuur behandeling (bijv. 100 – 200 °C) na de ozonbehandeling te bestuderen. Milde temperatuurbehandelingen in een meer oxiderende atmosfeer dan lucht (bijv. 100% O_2, NO_2 of N_2O) vormen wellicht een goed compromis tussen behandelingstemperatuur en chemische reactiviteit.

In Hoofdstuk 4 van dit proefschrift is nanostructurering van de katalysatordrager onderzocht. Nanodeeltjes palladium zijn afgezet op diverse koolstof dragers met toenemende complexiteit van de nanostructuur: grafiet, actieve kool, carbon black en multi-walled carbon nanotubes (MWCNT's). De activiteit voor de benzylalcoholoxidatie vertoont een relatie met toenemende complexiteit van de kooldrager: Pd/MWCNT is de meest actieve en Pd/grafiet is de minst actieve katalysator. Hierbij moet wel de kanttekening gemaakt worden dat de katalysatorbereidingsmethode (impregnatie-reductie) verschillen in palladiumdeeltjesgrootte opleverde, wat meegenomen moet worden in de beschouwing. Functionalisering van het MWCNT oppervlak met carboxylgroepen door behandeling met heet salpeterzuur leverde nog kleinere Pd deeltjes (1.5 nm) dan zonder deze behandeling (5 nm), met als resultaat een verdubbeling van de turn-over-frequency. Verder vertoonde de katalysator een constante activiteit in 6 opeenvolgende batch experimenten, wat een sterke Pd-MWCNT interactie suggereert. Het op de nanoschaal gecontroleerd aanpassen van het katalysatordragermateriaal bleek dus effectief om de nanostructuur ervan te veranderen en zo een hoge en stabiele aktiviteit te verkrijgen. Het zou interessant zijn om de nanogesctructureerde drager MWCNT te combineren met de colloïdale bereiding van de metaalnanodeeltjes. Dit zou een volledig nanogestructureerde katalysator opleveren, en zou direkte vergelijking mogelijk maken tussen impregnatiemethodes en de colloïdale bereidingsmethode.

In Hoofdstuk 5 tenslotte zijn nanogestructureerde bimetallische katalysatoren toegepast voor de electrokatalytische reductie van CO_2. Dit onderzoek is gebaseerd op de uitkomsten van de theoretische studies van Nørskov [2-4] en Koper [5, 6] naar de schaalrelaties tussen de binding van reactieïntermediairen, waaruit volgde dat deze relaties het verdere verloop van deze reactie beperken. Het doorbreken van deze schaalrelaties vereist een voldoende heterogeniteit van de actieve centra, die moeten verschillen in activiteit, adsorptiesterkte en adsorptieselectiviteit. Daartoe werden bimetallische koper-goud katalysatoren bereid via reductie van een koperprecursor met ethyleenglycol, gevolgd door immobilisatie op multi-walled carbon nanotubes en een gecontroleerde galvanische uitwisseling van (een deel van) het koper door goud met chloor goudzuur. De colloïdale bereidingsmethode leverde kopernanodeeltjes op van gelijke grootte, terwijl de galvanische uitwisseling een gecontroleerde samenstelling van het bimetallische systeem mogelijk maakte. Hoewel de schaalrelaties nog steeds bleken te gelden, werd er toch enige variatie in activiteit, selectiviteit en energieëfficiëntie gemeten. Deze variaties bleven echter binnen de orde-grootte van die van de monometallische katalysatoren. De prestaties en karakteristieken van de katalysatoren wijzen eigenlijk op bijdragen van gescheiden aanwezige Cu en Au fasen. Andere bereidingsmethodes zijn waarschijnlijk nodig om tot beter gemengde koper-goud fasen te komen en de vereiste heterogeniteit van het actieve centrum te bereiken. Een nabehandeling van de resulterende bimetallische katalysatoren bij milde temperatuur zou wellicht tot intermetallische kristallen kunnen leiden, aangezien sommige daarvan thermodynamisch stabiel zijn.

Samenvattend laten de voornoemde resultaten zien dat het gebruik van nanomaterialen, en met name colloïdale nanodeeltjes in katalysatorbereiding, vooral in fundamenteel katalysatoronderzoek veelbelovend is [2]. De colloïdale depositiemethode verhoogt de mate van beheersing in katalysatorbereiding, wat een nauwe deeltjesgrootteverdeling in het nano bereik oplevert en de invloed van de drager tijdens de bereiding elimineert. Het vervult een brugfunctie tussen theoretische en éénkristal studies enerzijds en echte katalysatoren anderzijds. Deeltjesgrootte effecten kunnen veel gedetailleerder bestudeerd worden dan impregnatiemethoden toelaten, en kunnen worden gebruikt om theoretische voorspellingen te verifiëren. Dat de eigenschappen van metaalnanodeeltjes niet afhankelijk zijn van de oppervlaktechemie van de katalysatordrager maakt studie van de chemische/katalytische eigenschappen van de laatste mogelijk zonder beïnvloeding van de eerste. 'Active site engineering' zou zelfs bepaalde kristalvlakken kunnen exposeren door beheersing van de vorm van de nanodeeltjes, iets wat in sommige gevallen mogelijk is met de colloïdale depositiemethode. Het actieve centrum moet dan wel stabiel zijn onder reactiecondities: katalytische oppervlakken kunnen erg dynamisch zijn bij blootstelling aan het reactiemilieu. Dit is een bijkomende uitdaging naast die van de zelf-assemblage van katalysatoren op atomaire schaal. Idealiter wordt het actieve centrum gevormd onder reactiecondities, waardoor de stabiliteit ook gewaarborgd wordt. Om dit te bereiken zijn *operando/in-situ* [3, 4] karakteriseringsmethoden nodig zoals bijvoorbeeld *in-situ* TEM [5, 6] dat zeer relevant is aangezien het de benodigde atomaire resolutie onder reactiecondities kan verschaffen.

Het op maat vervaardigen van materialen met behulp van zelf-assemblage is de enige realistische manier om op grotere hoeveelheden van dergelijke geavanceerde katalysatoren te produceren, en daarmee te weg te openen naar industriële toepassing. Uiteraard moeten de kosten van bereiding en grondstoffen voor deze colloïdale route opwegen tegen de winst in procesverbetering, en met name selectiviteit en stabiliteit.Gezien de voordelen zal het duidelijk zijn dat de colloïdale depositieroute voor katalysatorsynthese niet alleen een blijvertje is in het veld van katalysatoronderzoek [7], maar ook commerciële toepassing zal vinden [8].

References

1. Quintanilla, A.; Butselaar-Orthlieb, V.C.L.; Kwakernaak, C.; Sloof, W.G.; Kreutzer, M.T.; Kapteijn, F. *J Catal 271,* **2010**, 104-114.
2. Peterson, A.A.; Nørskov, J.K. *J Phys Chem Lett 3,* **2012**, 251-258.
3. Hansen, H.A.; Varley, J.B.; Peterson, A.A.; Nørskov, J.K. *J Phys Chem Lett 4,* **2013**, 388-392.
4. Nørskov, J.K.; Rossmeisl, J.; Logadottir, A.; Lindqvist, L.; Kitchin, J.R.; Bligaard, T.; Jónsson, H. *J Phys Chem B 108,* **2004**, 17886-17892.
5. Koper, M.T.M. *J Electroanal Chem 660,* **2011**, 254-260.
6. Koper, M.T.M. *Chem Sci 4,* **2013**, 2710-2723.
7. Narayanan, R.; El-Sayed, M.A. *J Phys Chem B 109,* **2005**, 12663-12676.
8. Topsøe, H. *J Catal 216,* **2003**, 155-164.
9. Weckhuysen, B.M. *Phys Chem Chem Phys 5,* **2003**, 4351-4360.
10. Vendelbo, S.B.; Elkjær, C.F.; Puspitasari, I.; Creemer, J.F.; Dona, P.; Mele, L.; Morana, B.; Nelissen, B.J.; Roobol, S.; van Rijn, R.; Helveg, S.; Kooyman, P.J. *Microsc Microanal 20,* **2014**, 1570-1571.
11. Vendelbo, S.B.; Elkjær, C.F.; Falsig, H.; Puspitasari, I.; Dona, P.; Mele, L.; Morana, B.; Nelissen, B.J.; van Rijn, R.; Creemer, J.F.; Kooyman, P.J.; Helveg, S. *Nat Mater 13,* **2014**, 884.
12. Zaera, F. *Chem Soc Rev 42,* **2013**, 2746-2762.
13. Witte, P.T.; Berben, P.H.; Boland, S.; Boymans, E.H.; Vogt, D.; Geus, J.W.; Donkervoort, J.G. *Top Catal 55,* **2012**, 505-511.

Acknowledgements

The Dutch National Research School Combination Catalysis Controlled by Chemical Design (NRSC-Catalysis) is gratefully acknowledged for the financial support of this thesis.

The committee members of my PhD defence, including Prof. dr. Ernst J. R. Sudhölter, Prof. dr. Leon Lefferts, Prof. dr. Guido Mul, Prof. dr. ir. J. Ruud van Ommen are acknowledged for accepting our invitation and for reviewing this work.

I am very grateful to Prof. dr. Freek Kapteijn for giving me the opportunity to join Catalysis Engineering research group. Freek, I have enjoyed working with you, and learned a lot from your visionary spirit, always a step ahead with the next question to consider.

Many thanks to Prof. dr. Patricia J. Kooyman for your supervision throughout these years. I learned a lot about professional independence and human relations thanks to our collaboration. Your positive attitude, even during the most difficult phases, was really supportive.

Prof. dr. ir. Michiel T. Kreutzer is gratefully acknowledged for his support and feedback, particularly on conceptual designs and for transmitting his scientific rigorous style to me.

I also would like to express my deep gratitude to Em. prof. dr. Jacob A. Moulijn for your precious help with finishing this thesis. Jacob, I have always been impressed by your capacity to extract the brightest aspects of my work and turn them into chapters that I didn’t expect to realise. In particular, Chapter 1 of this thesis would have probably remained as ‘preliminary results’ without your support and pragmatism.

Chapter 1 would have also not been possible without the contribution of Dr. ir. Rob J. Berger on the modelling part of this work. Rob, working alongside you was a really enjoyable experience and the first true feeling for me of what professional collaboration is. I am sincerely thankful to you for this experience and the outcome of it.

I also want to thank Dr. ir. Michiel Makkee for his precious, albeit sharp remarks and feedback. Your down to earth attitude was very precious in the choice of which question to explore, which one is a dead end, and above all which one is really relevant and useful. You are a valuable asset to stay connected to the industrial realities.

The much-appreciated help of the technicians of the Catalysis Engineering section, Bart van der Linden, Harrie Jansma, Kevin Mouthaan and Willy Rook has been of crucial importance until the very end of my experimental work. Thanks to Willy for your help with texture studies and supervising students when I had so many to supervise. I particularly enjoyed learning with you about the new ammonia temperature programmed desorption apparatus that was used for Chapter 4 of this thesis. Kevin, sorry for having ruined your planning all the time with my GC emergencies, and thank you so much for teaching me all what could be done by myself in order to save time. Harrie I admire your professional attitude and availability, in particular on safety aspects of lab work. Your presence in the 'old building' until the very end of my stay allowed me step out of my bubble once in a while for a nice chat. Bart, I will remember you as "the man who can fix everything"! I have been impressed how you can step into a technical challenge, and how you were able to provide precious support in troubleshooting, even when it was outside your expertise. Many thanks to the technicians outside of the group, in particular Duco Bosma, Maarten Gorseling and Ben Norder.

Chapter 2 came out from the work of Boudewijn den Ouden during his MSc. thesis, whom I am very grateful for. Chapter 3 is the result of a collaboration with Indra Puspitasari who is sincerely acknowledged for her contribution. Many thanks to Sam Geschiere, who conducted the experiments of Chapter 5 with a remarkable independence during his MSc. thesis. I am also very grateful to Vijay Shinde for his huge contribution to Chapter 4. Furthermore, Karlijn Bezemer, Mark Meijerink, Mara de Zoete, Liam Borgers, Lisette Gijsbertsen, Lars van Gissen, Wouter 't Jong, Bram Bavelaar, Nancy Zhang, Jennifer Lanusse, Saashwath Swaminathan Tharakaraman, Vivian Karsten, Prya Jagai, Merijn de Boer and Tom Postma are sincerely acknowledged for their contribution through their LO1/2, BSc and MSc thesis projects.

Prof. dr. Marc T. M. Koper is gratefully acknowledged for the fruitful discussions about CO_2 electrocatalytic reduction in the beginning of my PhD. His input was very useful in drawing the scope of my contribution to this topic.

Furthermore, I would like to express my gratitude to the secretary team of Catalysis Engineering: Els Arkesteijn, Elly Hilkhuijsen and Caroline Monna for their support with the administration. My sincere appreciation to the PhDs/PostDocs of the Catalysis Engineering group for the nice working atmosphere they maintain all the time despite the work pressure. My greetings go to Jana, Barbara, Alberto, Enrique, Sina, Jasper, Vera, Søren, Abrar, Pablo, Tania, María-José, Eduardo, Anahid, Alla, Alma, Sonia,

Irina, Oscar, Sumit, Dmitrii, Ina, Rupali and all those whom I forget. Sometimes, professional relationships evolve into real friendships. This happened very quickly with Canan, whose generosity overflows to everybody. Canan, you were my best work buddy, and I can't thank you enough for your mental support when I needed it the most. I am looking forward that our paths cross each other again! Martijn, your sense of humour, even in the most annoying periods, is priceless! You are a great inspiration for having fun time in the most stressful situations. Vijay, you arrived when Canan was leaving, and somehow took over her mental support, something I really didn't expect! I value your advices very much on how to control one's own state of mind and keeping it healthy! I am also deeply grateful to you for providing me with the Indian Ayurvedic remedy for the eczema on my hands, that allowed me to continue the lab-work. I also can't forget Rajat; whom I met during my Master studies, and although we could not cross each other so often due to our busy schedules, I have no doubt on the sincerity of our friendship when I see the way we express it!

In the following section, I will take the freedom to write in my mother tongue to acknowledge my family, without whom this thesis would have probably not existed.

Je veux exprimer ma profonde gratitude envers ma mère, Dominique Skupien-Watel et mon père, Christian Skupien, qui ont rendu possible l'avènement de cette thèse. Vous avez tous les deux toujours cru en moi, et m'avez offert toutes les possibilités d'études que je souhaitais au prix de sacrifices que je n'oublierai jamais. Ce succès est aussi le vôtre! François et Rémi, mes frangins, nous auront été tous les trois dans des situations symétriques ces dernières années: se battre pour y arriver! Et finalement, nous allons nous en sortir à peu près en même temps. Félicitations pour la concrétisation de votre projet! On a réussi!

Also, because since July 2008, part of my family is German, I will write a piece in that language.

Esther, danke für all die Liebe, die du mir jeden Tag gibst und für all deine positiven Beiträge in mein Leben. Du warst an vorderster Front mit all der mentalen Unterstützung, die ich brauchte. Diese Doktorarbeit wäre ohne deine Hilfe und Liebe definitiv nicht herausgekommen. Ich bin dir sehr dankbar und werde es nie vergessen.

List of publications

List of publications

Peer-reviewed journal articles:

- Puspitasari, I.; Skupien, E.; Kapteijn, F.; Kooyman, P.J.; Au capping agent removal using plasma at mild temperature, *Catalysts 6*, **2016**, 179

- Shinde, V.M.; Skupien, E.; Makkee, M., Synthesis of highly dispersed Pd nanoparticles supported on multi-walled carbon nanotubes and their excellent catalytic performance for oxidation of benzyl alcohol. *Catal Sci Technol 5*, **2015**, 4144-4153

- Skupien, E.; Berger, R.J.; Santos, V.P.; Gascon, J.; Makkee, M.; Kreutzer, M.T.; Kooyman, P.J.; Moulijn, J.A.; Kapteijn, F., Inhibition of gold-based catalyst in benzyl alcohol oxidation: Understanding and remediation. *Catalysts 4*, **2014**, 89-115

- Juan-Alcañiz, J.; Ferrando-Soria, J.; Luz, I.; Serra-Crespo, P.; Skupien, E.; Santos, V.P.; Pardo, E.; Llabrés I Xamena, F.X.; Kapteijn, F.; Gascon, J., The oxamate route, a versatile post-functionalization for metal incorporation in MIL-101(Cr): Catalytic applications of Cu, Pd and Au. *J Catal 307*, **2013**, 295-304

Conferences/meetings:

- Skupien, E.; Berger, R.J.; Santos, V.P.; Gascon, J.; Makkee, M.; Kreutzer, M.T.; Kooyman, P.J.; Moulijn, J.A.; Kapteijn, F., Inhibition of gold-based catalyst in benzyl alcohol oxidation: Understanding and remediation. *Netherlands Catalysis and Chemistry Conference (NCCC XV)*, 10 – 12 March, **2014** *(oral)*

- Geschiere, S.D.; Skupien, E.; Kapteijn, F.; Kooyman, P.J., Electrocatalytic reduction of CO_2 to fuels with CuAu nanoparticles. *Netherlands Catalysis and Chemistry Conference (NCCC XV)*, 10 – 12 March, **2014** *(poster)*

- Skupien, E.; Berger, R.J.; Santos, V.P.; Gascon, J.; Makkee, M.; Kreutzer, M.T.; Kooyman, P.J.; Moulijn, J.A.; Kapteijn, F., Inhibition of gold-based catalyst in benzyl alcohol oxidation: Understanding and remediation. *National Research School Combination Catalysis Workshop (NRSCC Workshop 2014)*, Utrecht, The Netherlands, 13 February, **2014** *(oral)*

- den Ouden, B.B.A.; Skupien, E.; Kapteijn, F.; Kooyman, P.J., Investigating the effects of metal oxide supports on gold nanoparticle catalysis. *Netherlands Catalysis and Chemistry Conference (NCCC XIV)*, 11 – 13 March, **2013** *(poster)*

- Skupien, E.; Juan-Alcañiz, J.; Kooyman, P.J.; Kreutzer, M.T.; Gascon, J.; Kapteijn, F.; Gold catalysis – Total selectivity and alleviation of product inhibition in selective oxidation by support nanostructuring. *National Research School Combination Catalysis Workshop (NRSCC Workshop 2013)*, Utrecht, The Netherlands, 31 January, **2013** *(oral)*

- Boxhoorn, J.H.; Ros, C.H.; Skupien, E.; Kapteijn, F.; Kooyman, P.J., Tuning copper deposited catalysts for electrocatalytic CO_2 reduction. *CECAM Workshop "Future challenges in CO_2 reduction"*, Bremen, Germany, 8 – 12 October, **2012** *(poster)*

- Skupien, E.; Kampa, B.M.; Kooyman, P.J.; van Ommen, J.R.; Kreutzer, M.T.; Kapteijn, F., Engineering of nano-structured alloy catalysts and application in Electrocatalytic reduction of CO_2. *National Research School Combination Catalysis Workshop (NRSCC Workshop 2012)*, Utrecht, The Netherlands, 2 February, **2012** *(oral)*

- Kampa, B.M.; Skupien, E.; van Ommen, J.R.; Kooyman, P.J.; Kapteijn, F.; Kreutzer, M.T., Continuous flow synthesis of gold nanoparticles. *National Research School Combination Catalysis Workshop (NRSCC Workshop 2011)*, Utrecht, The Netherlands, 25 January, **2011** *(oral)*

- Van Ommen, J.R.; Skupien, E.; Mul, G., Controlled Manufacturing of Nanostructured Catalyst Particles Using Atomic Layer Deposition. *AIChE Annual Meeting,* Nashville, USA, 8-13 November, **2009** *(oral)*

About the Author

Emmanuel Skupien was born on May 28, 1985 in Bully les Mines, France. Having opted for the scientific branch during high school, he majored in Physics and Chemistry when he obtained his Baccalaureate in 2003 from André Malraux high school, in Béthune, France. He was then enrolled for a two-year training in the Integrated Preparatory Class of the Gay-Lussac Federation of National Chemistry Schools, in Lille, France. After this intense competition, he entered the National School of Chemistry of Mulhouse, France in 2005. His first international experience came in 2007, when he was enrolled for an internship with Albemarle Catalysts in Amsterdam, The Netherlands. Seduced both by Catalysis and by Esther Schötz he decided to stay in the Netherlands to finish his double MSc. diploma in Chemical Engineering and Materials Science with Delft University of Technology, which he obtained in 2009. Shortly after, in 2010, he started his PhD studies with Catalysis Engineering TU Delft, under the supervision of Freek Kapteijn, Patricia Kooyman and Michiel Kreutzer. Since September 2017, he works as Application Development Engineer for CarbonX, a startup company that was created in Delft University of Technology by Rutger van Raalten and Daniela Sordi. Emmanuel currently resides in The Hague, The Netherlands, where he shares a happy life with Esther whom he married on August 4, 2018.

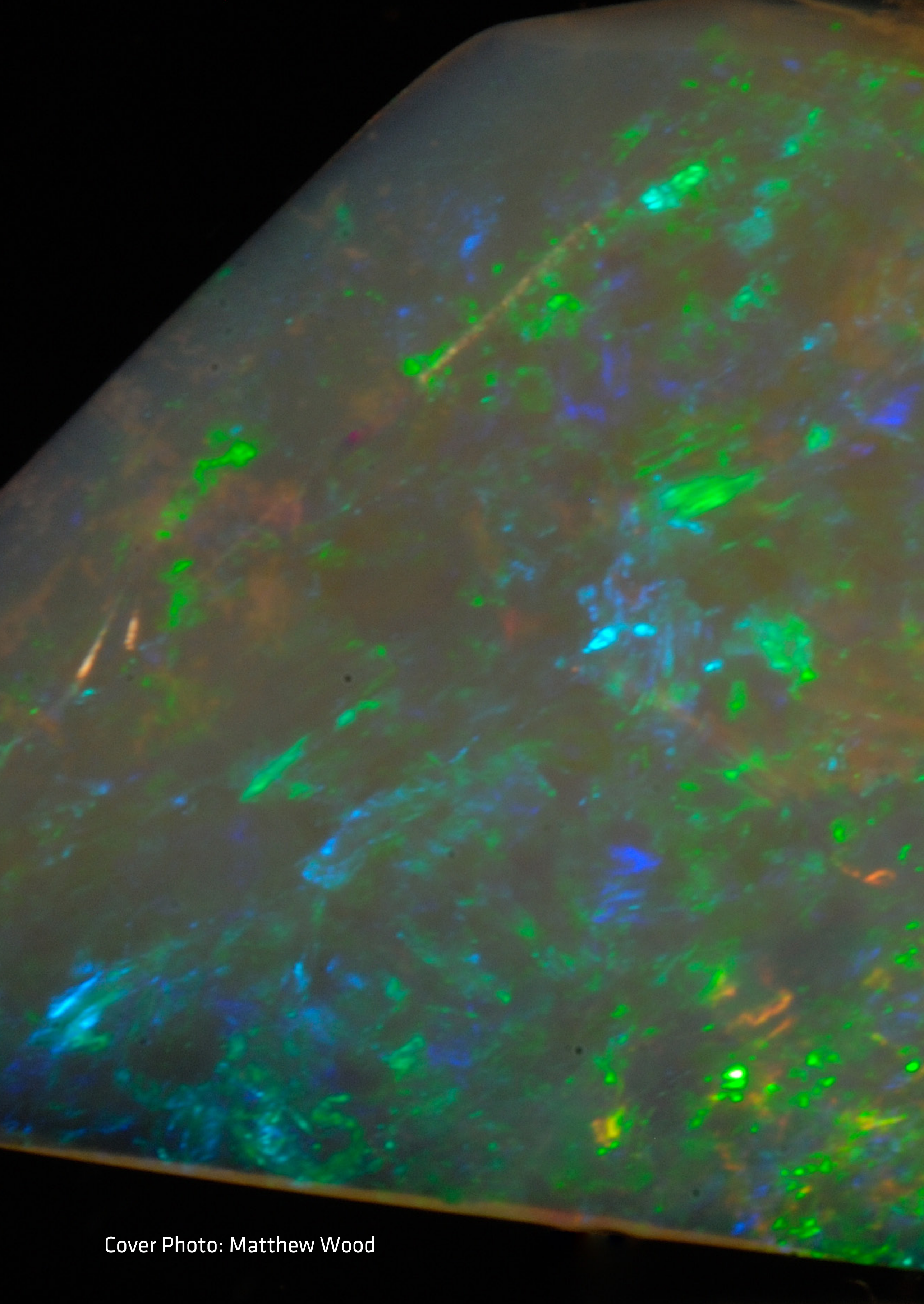

Cover Photo: Matthew Wood